issn 0065-3713

INSTITUT D'AERONOMIE SPATIALE DE BELGIQUE

3 - Avenue Circulaire
B - 1180 BRUXELLES

AERONOMICA ACTA

A – N° 403 – 1999

Wave phenomena in dusty space plasma

by

P. Meuris

BELGISCH INSTITUUT VOOR RUIMTE-AERONOMIE

3 - Ringlaan
B - 1180 BRUSSEL

Bedankt ...

Deze thesis zou onmogelijk zijn geweest zonder de niet-aflatende steun van Prof. Frank Verheest, die me kennis liet maken met het zeer interessante vakgebied van stofplasma's. Ik ben hem dankbaar voor de steeds positieve motivatie en het inpassen van de vele interessante discussies in zijn drukke agenda.

Mijn dank gaat ook uit naar Prof. Joseph Lemaire voor de initiële contacten met Prof. Donald Gurnett en Dr. Nicole Meyer-Vernet. Het vertrouwen en vooral de ruimte die hij me toevertrouwde worden erg gewaardeerd.

Ik hou er ook aan om al mijn collega's op het BIRA te bedanken voor hun steun. In het bijzonder Dr. Ir. Johan De Keyser, Ir. Olivier Hennen, Dr. Viviane Pierrard, Dr. Michel Roth, Tiny Steegmans en Jean-Marie Vandenberghe. Ook het ontvangst en de koffie in de vakgroep Wiskundige Natuurkunde en Sterrenkunde van de Universiteit Gent worden erg op prijs gesteld.

Verder gaat mijn dank ook uit naar de ere-directeur van het Belgisch Instituut voor Ruimte–Aëronomie, Dr. Marcel Baron Ackerman, en zijn opvolger Dr. Paul Simon, om mij in de mogelijkheid te stellen om dit doctoraat tot een goed einde te brengen, in het kader van de aktie ter versterking van het wetenschappelijk en technologisch potentieel van de federale wetenschappelijke instellingen.

Na het afwerken van een thesis zoals deze is het een plezier om die mensen uit het internationale vakgebied te bedanken die me met raad en daad hebben bijgestaan. Elektronische post doet immers heel wat grenzen vervagen, en hoewel het vakgebied van de stofplasmas aan belang wint, is het aantal mensen die er zich mee bezighouden nog verrassend beperkt. Ik denk daarbij speciaal aan Dr. Fran Bagenal, Prof. Ramesh Bharuthram, Dr. Jean-Louis Bougeret, Dr. Jeffrey Cuzzi, Dr. Viviane Chow, Dr. Roshan Daryanani, Prof. Ove Havnes, Prof. Jim Laframboise, Prof. Gurbax Lakhina, Prof. Mihâli Horányi, Dr. Frank Melandsø, Prof. Asoka Mendis, Dr. Nicole Meyer-Vernet, Dr. Richard Mace, Prof. Carol Nairn, Dr. Nagesha Rao, Dr. Mark Showalter, Dr. Padma Shukla en Dr. Hubertus Thomas.

Tenslotte wens ik mijn grote dankbaarheid uit te drukken voor die mensen die een belangrijke plaats in mijn leven innemen en die mee aan de basis liggen van de realisatie van dit werk. Zonder mijn ouders en mijn echtgenote zou dit alles onmogelijk zijn geweest en ze hebben me gesteund door dik en dun. Bedankt ...

Abstract

The plasma state is the fourth state of matter. Although we are especially familiar with solids, liquids and gases in our neighborhood, it is often said that 99 % of the universe consists of plasma (stars, interplanetary medium) and therefore space plasma physics is a well-developed field of research. One can ask oneself in what state we can find the remaining 1 % of matter. Well, dust would make up most of the remainder. Indeed, in almost all space plasma environments, including planetary magnetospheres, cometary environments and planetary rings, dust grains are found and a new field of research was introduced: the physics of dusty plasmas.

Because theoretical science must develop along with the available experiments and/or measurements, the first thing to do is to look at the available data. A review is given (chapter 2) for the three most promising dusty plasma environments in space physics (the rings of the outer planets, the cometary environment and interplanetary dust). As explained earlier, the dust charging process and the dusty plasma modes couple, and therefore the knowledge of the charging mechanism is essential in the description of dusty plasma waves. To evaluate the dust charging process correctly, it is essential that we use adequate information. The lack of availability of dust related data made it clear that new detection techniques are necessary to improve our knowledge of dusty plasma environments. In chapter 3, existing in situ detection techniques are reviewed and a new, promising one is examined in detail. This technique (Radio Dust Analyzer - RDA) makes it possible to analyze the dust grain characteristics (velocity, direction of propagation charge), by the use of wire dipole antenna. Chapter 4 briefly reviews the present status of the charging model, giving analytical expressions where they are available. The results of chapters 2 and 4 are used to indicate what processes are relevant in the charging of the dust grains in the different space plasma applications we have in mind (chapter 5). The chapter gives both the equilibrium potential and charging time, and the relative importance of the charging mechanisms for the different applications.

The remainder of this work describes waves and instabilities in dusty space plasmas. In chapter 6 we explain our multi-fluid model which includes sink/source terms for the plasma capture of the grains. In chapter 7 a general description of electrostatic modes in the presence of dust charge variations is carried out. The damping of low-frequency, dust-acoustic, ion-acoustic and Langmuir modes is quantified. Electromagnetic modes are described in Chapter 8, both at the linear and the nonlinear level. The influence of the dust on the pickup of cometary ions by the solar wind is examined, and the reductive perturbation method is used to treat the nonlinear evolution of parallel, perpendicular as well as oblique modes.

The influence of mass-distribution and self-gravitation is given in chapter 9, and a coupling between the Jeans instability and Alfvén and dust-acoustic modes is described. Chapter 10 the gives the general conclusions.

Samenvatting

Zoals bekend is de plasmatoestand de vierde aggregatietoestand van de materie. Alhoewel we vooral vertrouwd zijn met vaste stoffen, vloeistoffen en gassen, wordt er dikwijls beweerd dat 99 % van het heelal bestaat uit plasma. Hiermee worden dan voornamelijk de sterren en het interplanetaire milieu bedoelt en het is dan ook niet vreemd dat ruimteplasmafysica een goed uitgebouwde tak van de natuurkunde is geworden. Men kan zich natuurlijk de vraag stellen in welke toestand de overblijvende 1% van de materie zich bevindt. Stof is hiervoor een goede kandidaat. Aangezien in bijna alle ruimteplasma's stofdeeltjes zijn teruggevonden, werd er een nieuwe tak van de natuurkunde geïntroduceerd: de fysica van de stofplasma's.

Omdat theoretische benaderingen onmogelijk zonder een experimentele basis en/of verificatie kunnen, hebben we eerst en vooral de beschikbare gegevens op een rijtje gezet. In het tweede hoofdstuk werd een overzicht gegeven van de drie meest veelbelovende omgevingen: de ringen van de buitenplaneten, de omgeving van kometen en het interplanetaire medium. Voor de volledigheid werden de recente oplaadexperimenten en de stofplasmakristallen niet vergeten. Hieruit bleek duidelijk dat de stofplasma-gegevens beperkt zijn en dat zette ons aan om een nieuwe detectiemethode voor te stellen, die we "Radio Dust Analyzer" (RDA) hebben genoemd. Deze techniek maakt het mogelijk om met behulp van een dipoolantenne de karakteristieken van een langsvliegend stofdeeltje (snelheid, lading, richting) en van de omgeving (Debyelengte) te detecteren. Het signaal dat door een geladen deeltje wordt geïnduceerd en de bijbehorende ruisniveaus werden onderzocht voor enkele ruimtemissies: Rosetta, Wind, Casinni en Voyager. De mogelijkheid werd geopperd om de signalen die werden doorgestuurd door Voyager 2 en het PWS experiment te herbekijken met het oog op deze techniek. Hoofdstuk 4 geeft een kort overzicht van de huidige staat van het onderzoek naar het oplaadmodel. Het niet-lineaire oplaadproces kent verschillende oplaadmechanismen. Verder is de evenwichtslading niet uniek; het is immers mogelijk dat stofdeeltjes van dezelfde grootte en samenstelling een andere evenwichtslading bereiken vanwege hun verschillende oplaadgeschiedenis. Het vijfde hoofdstuk maakt duidelijk welke de belangrijkste oplaadmechanismen zijn in de ringen van Saturnus, en het interplanetaire medium.

Het vervolg van de thesis beschrijft golven en instabiliteiten in ruimteplasma's beschreven door een multi-fluïdum model waarin de stofcomponent wordt beschreven als een enkele fluïdum-populatie. Dit model is toereikend voor de toepassingen die we willen beschrijven en heeft het voordeel dat het makkelijk interpreteerbaar is. In tweede instantie zal het model worden uitgebreid door meerdere stofkomponenten met een massaverdeling en zelfgravitatie in te voeren (hoofdstuk 9). Het zevende hoofdstuk geeft de koppeling van elektrostatische golven met het oplaadmechanisme in een drie-komponenten plasma weer. We toonden aan dat de aanwezigheid van stofdeeltjes de klassieke Langmuir oscillaties zal dempen. Voor twee stofplasma-omgevingen werd de bekomen dispersierelatie opgelost. In hoofdstuk 8 worden dan de elektromagnetische golven behandeld. Een specifiek frequentiegebied waarvoor de stofdeeltjes als immobiel mogen worden beschouwd, terwijl de frequentie van de modes onder de gyrofrequentie van de plasmadeeltjes zit, werd behandeld. Dit laat ons toe om een nieuw soort whistlermode te beschrijven. Aan de andere kant laat de studie van dit frequentiegebied ook toe om te besluiten dat in de zonnewindinteraktie met kometaire

stofplasma's de stofdeeltjes geen rol van betekenis gaan spelen. Ook werd de niet-lineaire behandeling doorgevoerd van parallelle golven in een stofplasma waar het stof enkel uit een vaste achtergrond met fluctuerende lading bestaat.

De invloed van zelfgravitatie en massadistributie werd onderzocht in hoofdstuk 9. Alhoewel de gravitatiekrachten voor de deeltjes in een stofplasma veel kleiner zijn dan de elektrostatische krachten, zullen kleine afwijkingen van de evenwichtsoplossing van een stofplasma wel worden beïnvloed door de zelfgravitatie. Voor neutrale deeltjes kunnen enkel thermische effekten het systeem voor de Jeans instabiliteit behoeden. Voor een stofplasma met geladen deeltjes daarentegen, kunnen ook plasmagolven dit stabilizerend effect veroorzaken. Indien geen magnetische veld aanwezig is, zal de Jeans instabiliteit worden beperkt door stof-akoestische golven. Bij een uitwendig magnetisch veld blijkt dat we voor de beschrijving van de (loodrechte) magneto-akoestische golven we een Alfvén-Jeans lengte kunnen introduceren, die de grootte van de het stabiele systeem loodrecht op het magneetveld bepaalt.

Résumé

Les plasmas constituent le quatrième état de la matière. Bien que l'enseignement universitaire nous familiarise davantage avec la physique des solides, des liquides et des gaz neutres, les plasmas représente 99 % de l'Univers. En effet, les étoiles et l'environnement interplanétaire sont principalement constitués de plasmas. Aussi, il n'est guère étonnant que la physique des plasmas spatiaux soit devenue une branche très développée de la physique. On peut se poser la question de savoir dans quel état se trouve le dernier 1 % de la matière. L'état solide sous forme de grains de poussière pourrait s'avérer être le meilleur candidat. Or, étant donné que dans tous les plasmas spatiaux on détecte l'existence de grains de poussière, une nouvelle branche de la physique s'est créée : la physique des "dusty plasmas".

Sans recours aux observations et aux vérifications expérimentales, il est difficile de développer une approche théorique. Dès lors, nous commençons dans ce mémoire par répertorier les données d'observation actuellement disponibles. Au chapitre 2, nous donnons un aperçu des trois environnements ionisés les plus riches en grains de poussières : les anneaux des planètes extérieures, l'environnement cométaire et le milieu interplanétaire. En vue d'être aussi complet que possible, nous avons également décrit les récentes expériences relatives à l'électrisation des poussières et celles relatives aux propriétés des cristaux de particules exhibant les caractéristiques du plasma. Il ressort de cette première partie de notre étude que les données d'observations relatives au plasma contenant des grains de poussières solides sont relativement limitées.

Ceci nous a amené à proposer une nouvelle technique de détection des poussières. Nous avons appelé cette nouvelle technique « Radio Dust Analyzer » (RDA). Cette technique, basée sur l'utilisation d'une antenne dipôle, permet la détermination des caractéristiques d'une particule de poussière en mouvement (vitesse, charge, direction), ainsi que certaines propriétés de son environnement (longueur de Debye, température du plasma). Le signal induit par une particule chargée et les niveaux du bruit de fond qui l'accompagne pourraient être analysés par des sondes spatiales telles que : Rosetta, Wind, Casini et Voyager. La possibilité a été envisagée de réexaminer les signaux recueillis à bord de Voyager 2 par l'expérience PWS à l'aide d'une antenne dipolaire en appliquant cette nouvelle technique. Le chapitre 4 fournit un bref aperçu de l'état actuel des recherches concernant l'accumulation de charges électriques à la surface de grains de poussières. La charge à l'équilibre n'est pas nécessairement uniforme; en effet, il est possible que des particules de même grandeur et de composition identique aient une charge d'équilibre différente dépendant de l'histoire spécifique de leur chargement. Au chapitre 5 on explique clairement les principaux mécanismes de charge dans les anneaux de Saturne et dans le milieu interplanétaire.

La suite de ce texte décrit les ondes et les instabilités dans les plasmas spatiaux, représentés par un modèle multi-fluide dans lequel la population de poussières est décrite comme une des composantes fluides. Ce modèle est suffisant pour les applications que nous souhaitons décrire ici et offre l'avantage d'être facile à interpréter. En deuxième lieu, le modèle est étendu grâce à l'introduction de plusieurs composantes de poussières en tenant compte d'une répartition des masses et de l'autogravitation (chapitre 9). Le chapitre 7 explique le lien entre

les ondes électrostatiques et les mécanismes de charge dans un plasma à trois composantes. Nous avons démontré que la présence de particules solides atténue les oscillations classiques de Langmuir. La relation de dispersion obtenue a été résolue pour deux types d'environnements différents.

Le chapitre 8 traite ensuite des ondes électromagnétiques. Nous y avons examiné un domaine de fréquence spécifique dans lequel les particules peuvent être considérées comme immobiles alors que la fréquence des modes se situe en deçà de la fréquence cyclotron des particules du plasma. Ceci nous a permis de décrire un nouveau type d'émission à large bande de la magnétosphère. D 'autre part, l'étude de ce domaine de fréquences permet également de conclure que les particules de poussières ne jouent aucun rôle significatif dans l'interaction entre les vents solaires et les plasmas de particules cométaires. Nous y avons également réalisé le traitement non-linéaire d'ondes parallèles dans un plasma de particules où les poussières se composent d'un environnement à charge fluctuante.

Dans le chapitre 9, nous examinons l'influence de l'autogravitation et de la distribution de masses des grains de poussières. Bien que les forces gravitationnelles soient nettement plus faibles que les forces électrostatiques, la solution d'équilibre dans le cas d'un plasma contenant des grains solides est légèrement différente; elle est bel et bien influencée par l'autogravitation. Un système de particules neutres peut être stabilisé vis-a-vis de l'instabilité de Jeans par des effets thermiques. Dans le cas d'un plasma de particules chargées, par contre, des ondes de plasma sont également susceptibles de produire un effet stabilisateur. En l'absence de tout champ magnétique, l'instabilité de Jeans sera limitée par des ondes acoustiques des particules du plasma. En présence d'un champ magnétique extérieur, il semblerait que nous puissions introduire pour la description des ondes magnéto-acoustiques (perpendiculaires) une longueur Alfvén-Jeans qui détermine la dimension du système stable dans la direction perpendiculaire au champ magnétique.

Zusammenfassung

Beim Plasmazustand handelt es sich um den vierten Zustand der Materie. Obwohl wir mit Festkörpern, Flüssigkeiten und Gasen in unserer Nachbarschaft besonders vertraut sind, wird vielfach behauptet, daß 99 % des Universums aus Plasma besteht (Sterne, interplanetares Medium, usw.) und die Raumplasmaphysik deshalb als gut entwickelter Forschungsbereich zu betrachten ist. Man darf sich die Frage stellen, in welchem Zustand wir das verbleibende 1 % an Materie vorfinden können. Staub dürfte wohl den Hauptanteil am Restbestand bilden. In der Tat sind Staubkörner in nahezu allen Raumplasma Umgebungen, einschließlich der planetaren Magnetosphären, der kometaren Umgebungen und der Planetenringe an zu treffen und ein neuer Forschungsbereich wurde demzufolge eingeführt: Die Physik staubiger Plasmen.

Da die theoretische Wissenschaft sich gleichlaufend mit den verfügbaren Experimenten und/oder Messungen zu entwic keln hat, muß man sich in erster Linie die vorhandenen Daten ansehen. Eine Übersicht (Kapitel 2) wird für die drei vielversprechendsten Umgebungen mit staubigem Plasma in der Raumphysik gezeigt (Ringe der äußeren Planeten, kometare Umgebung und interplanetarer Staub). Wie bereits erläutert, ist der Staubbeladungsprozeß und das Schwingungsmoment des staubigen Plasmas und damit das Wissen um den Beladungsmechanismus bei der Beschreibung der staubigen Plasmawellen von wesentlicher Bedeutung. Zur richtigen Bewertung des Beladungsprozesses ist die Verwendung einer adäquaten Information von größter Wichtigkeit. Das Nichtvorhandensein von Daten in bezug auf Staub zeigt klar und deutlich, daß neue technische Ermittlungsverfahren im Hinblick auf eine bessere Kenntnis von Umgebungen mit staubigem Plasma erforderlich sind. Unter Kapitel 3 werden technische Ermittlungsverfahren in situ in Augenschein genommen und dabei wird ein neues, erfolgversprechendes Verfahren einer ausführlichen Prüfung unterzogen. Mit dieser Technik (Radio Dust Analyzer - RDA) wird es möglich, die Charakteristika der Staubkörner (Geschwindigkeit, Richtung der Propagationsladung) mit Hilfe einer Drahtdipolantenne zu analysieren. Kapitel 4 erläutert kurz den derzeitigen Status des Beladungsmodells, wobei analytische Ausdrücke gegeben werden, soweit sie verfügbar sind. Die Ergebnisse der Kapitel 2 und 4 werden zum Aufzeigen der Prozesse genutzt, die zum Beladen der Staubkörner bei den verschiedenen raumplasmatischen Anwendungen relevant sind, an die wir gedacht haben (Kapitel 5). Das Kapitel gibt sowohl das Ausgleichspotential und die Beladungszeit als auch die relative Bedeutung der Beladungsmechanismen für die verschiedenen Anwendungen an.

Im übrigen erläutert dieses Werk die Wellen und Unstabilitäten instaubigen Raumplasmen. Unter Kapitel 6 erläutern wir unser Mehrflüssigkeitsmodell, das Senk-/Quellenausdrücke für das plasmatische Einfangen der Körner umfaßt. Kapitel 7 vermittelt eine allgemeine Beschreibung elektrostatischer Schwingungstypen in der Gegenwart von Staubbeladungsänderungen. Das Dämpfen von Niederfrequenz-, von staubakustischen, ionakustischen und Langmuir-Schwingungstypen wird quantifiziert. Elektromagnetische Schwingungstypen werden unter Kapitel 8 beschrieben, und zwar sowohl auf der linearen als auch auf der nichtlinearen Ebene. Der Einfluß von Staub auf das Speichern kometarer Ionen durch den Solarwind wird untersucht und die reduktive Beeinflussungsmethode wird zum

Behandeln des nichtlinearen Verlaufs paralleler, lotrechter sowie diagonaler Schwingungstypen eingesetzt.

Der Einfluß der Massenverteilung und der Eigengravitation wird unter Kapitel 9 geschildert und eine Kopplung zwischen der Jeans-Unstabilität und Alfvén und staubakustischen Schwingungstypen wird beschrieben. Das Kapitel 10 enthält die allgemeinen Schlußfolgerungen

Contents

Bedankt . . . 1

Samenvatting . . . 3

1 Introduction **15**

1.1 What is a dusty plasma ? . . . 15

1.2 Waves in dusty plasmas . . . 17

1.3 Outline of this thesis . . . 18

2 Dusty plasma data **21**

2.1 Dusty plasmas in planetary rings . . . 22

2.1.1 Jupiter's ring system . . . 23

2.1.2 Saturn's ring system . . . 26

2.1.3 Uranus' ring system . . . 33

2.1.4 Neptune's ring system . . . 36

2.2 Cometary dusty plasmas . . . 39

2.3 Interplanetary dusty plasmas . . . 45

2.4 Dusty plasmas in laboratories . . . 48

2.4.1 Surface processing plasmas in RF-discharges . . . 48

2.4.2 Dust charging experiments . . . 49

2.4.3 Dusty crystals . . . 50

3 Detection methods **53**

3.1 Existing in situ detection methods 53

3.1.1 Pick-up of the ionization signal by electric antennae 53

3.1.2 Impact ionization detector 55

3.2 The radio dust analyzer (RDA) 56

3.2.1 Magnitude of the signals 57

3.2.2 Noise levels 61

3.2.3 Case studies 64

3.2.4 Conclusions 72

3.3 Appendix A: Geometrical Analysis 74

4 Charging model **75**

4.1 Continuous versus discontinuous charging 78

4.2 Grain charging mechanisms for isolated grains 78

4.2.1 Primary charging Standard model 78

4.2.2 Secondary electron emission 84

4.2.3 Photo-emission 88

4.2.4 Electrostatic disruption 89

4.2.5 Field emission 89

4.2.6 Centrifugal disruption 90

4.3 Charging model for a grain ensemble 90

4.3.1 The "Havnes model" 91

4.3.2 Dusty crystals 93

4.4 Influence of the magnetic field on the charging 93

5 Major charging mechanisms **97**

5.1 The charging model: a summary 98

5.1.1 Primary charging 98

5.1.2 Secondary electron emission 99

5.1.3 Reflection current 99

5.1.4 Photo-emission 100

5.1.5 Parameters 100

5.2 Saturn's ring system 101

5.2.1 Analysis and results 101

5.3 Interplanetary dusty plasmas 109

5.3.1 Analysis and results 109

6 Mathematical model **119**

6.1 Multi-fluid approach 120

6.1.1 Continuity equations 120

6.1.2 Momentum equations 121

6.1.3 Closure 122

6.1.4 Maxwell's equations 123

6.2 Calculation of the different parameters 123

6.3 Interpretation of the model parameters 125

7 Electrostatic modes **127**

7.1 Introduction 127

7.2 Mathematical description 128

7.2.1 Dispersion law 128

7.3 Modes in a non-magnetized plasma 131

7.3.1 Parameters 131

7.3.2 Langmuir modes 133

7.3.3 Dust ion-acoustic modes 135

7.3.4 Dust-acoustic modes 137

7.3.5 Zero-frequency modes 138

7.4 Modes in a magnetized plasma 138

7.4.1 Lower-hybrid modes 139

7.4.2 Upper-hybrid modes 139

7.5 Case studies 139

7.5.1 Saturn's E-ring: a dust-in-plasma 147

7.5.2 Saturn's spokes: a dusty plasma 148

7.6 Conclusions and new results 148

7.7 Appendix B: Tabulation of functions 150

8 Electromagnetic modes **153**

8.1 Introduction 153

8.2 Parallel modes 154

8.2.1 Linear parallel modes in an immobile background 155

8.2.2 Nonlinear parallel modes in an immobile background 161

8.3 Perpendicular and oblique modes 164

8.3.1 Linear magnetosonic mode 166

8.3.2 Nonlinear perpendicular modes in a warm magnetized multi-ion plasma 169

8.3.3 Nonlinear perpendicular modes in an anisotropic magnetized multi-ion plasmas 171

8.3.4 Nonlinear oblique modes in a cold magnetized multi-ion plasmas . . 173

9 Self-gravitation and mass distribution 179

9.1 Mass distribution and characteristic frequencies 181

9.2 Electrostatic modes 187

9.3 Electromagnetic modes 189

9.3.1 Driftless, unmagnetized plasma 190

9.3.2 Alfvén–Jeans modes 191

9.3.3 Influence of neutral dust or gas 192

9.3.4 Dust Alfvén modes 193

9.4 Conclusions and new results 195

9.5 Appendix C 196

10 General conclusions 197

11 References 201

12 Epilogue 213

Chapter 1

Introduction

The plasma state is the fourth state of matter. As a rule, by adding energy to a solid we can make a liquid, a gas and finally by adding even more energy we come to the plasma state, where the gas gets partially or fully ionized. When we follow the definition of Langmuir, a classical plasma is a quasi-neutral collection of charged and neutral particles (ions, electrons and neutrals) showing a collective behavior. Although we are especially familiar with solids, liquids and gases in our neigborhood, it is often said that 99 % of the universe consists of plasma (stars, interplanetary medium) and therefore space plasma physics is a well developed field of research.

One can ask oneself in what state we can find the remaining 1% of the matter. Well, dust would make up most of the remainder. Indeed, in almost all space plasma environments, including planetary magnetospheres, cometary environments, and planetary rings, dust grains are found and a new field of research was introduced: *the physics of dusty plasmas.*

1.1 What is a dusty plasma ?

A *dusty plasma* is the name given to a plasma heavily laden with a dispersed phase of charged solid objects (grains or dust particles). In space environments we see that the size transition from gas particles to large dust grains is almost continuous: from electrons and ions through macromolecules, clusters of molecules, very small or sub-micron sized grains, micron-sized grains, larger grains, boulders, asteroid remnants, etc. The size range we have in mind starts from the nanometer scale, extending to the centimeter scale, over seven orders of magnitude.

Dust grains embedded in an ambient plasma and a radiative environment will get electrically charged by various processes. In this way the relatively massive particles, with charges up to 10^4 elementary charges for micronsized grains, participate in the collective motion of the plasma particles. When the dust grain number density is small enough, the charging of the different dust grains takes place independently of each other and we prefer to call it a *dust-in-plasma*. In such a system, the charge of the grains can be calculated by a test-particle approach. On the other hand, when the different dust grains are closer to each other, the charging of the different grains influences each other, and we obtain a *dusty plasma*. Both *dust-in-plasma* and *dusty plasma* are encountered in astrophysical environments.

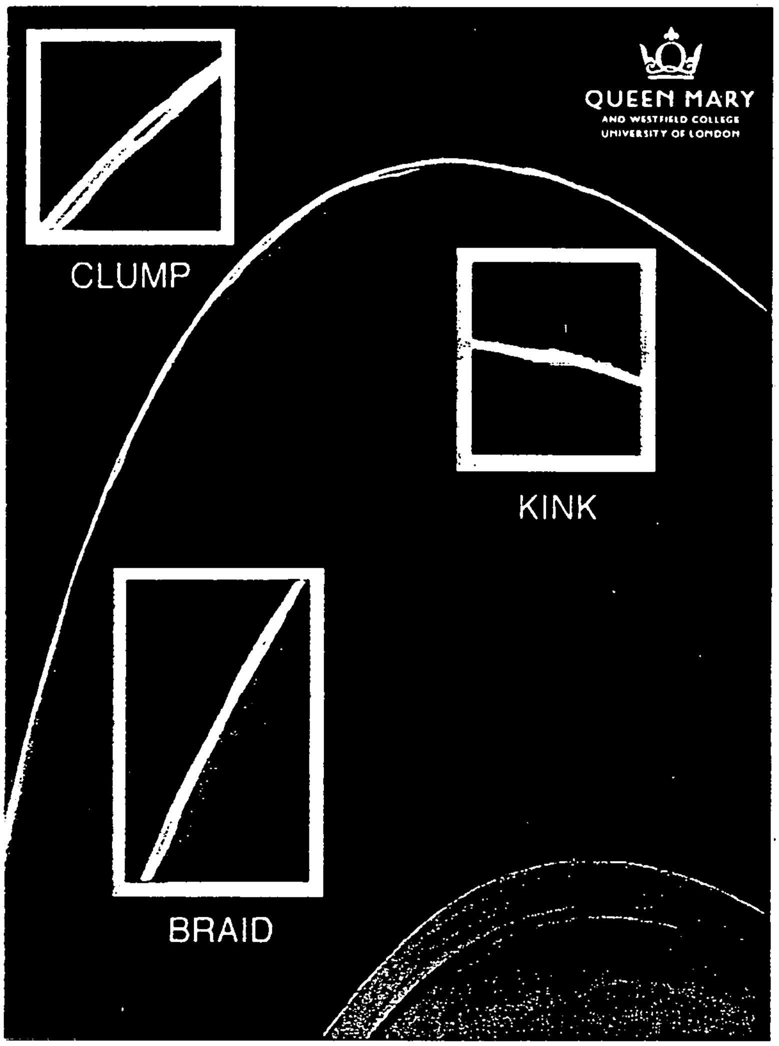

Figure 1.1: The F-ring of Saturn, and the typical braids, kinks and clumps

Despite the fact that the presence of dust grains in plasmas was already known for a long time, the study of the dust-plasma interactions is a relatively new field of investigation. Features observed in the Saturnian ring system by both Voyager 1 and 2, like the braids, kinks and clumps in the F-ring (Figure 1.1) and the spokes in the B-ring (Figure 2.3 infra), could not be explained by purely gravitational means. This renewed the interest in dust-plasma interaction which made it possible to explain the spoke feature.

Dusty plasmas have been investigated by diverse scientific communities, ranging all the way from astrophysicists to engineers involved in the fabrication of microchips for computers. Also, the scope of the processes involved go all the way from the physics of multicomponent plasmas, with varying degrees of collisionality, through surface physics to the physics of condensed matter. This last one arises from the most recent development of the field, namely the formation of crystals in dusty laboratory plasmas. When we embed dust grains in a RF-discharge, these charged grains will repel each other and they can crystalize as usual ions do in a Coulomb lattice. The study of these crystals makes it possible to examine the solid state and its phase transitions in a macroscopic system.

1.2 Waves in dusty plasmas

A straightforward and relatively easy way to study a collective system like a dusty plasma is to look at the characteristics of wave propagation through it. A zoo of modes can propagate in a plasma and the presence of dust grains will alter existing modes and create new ones. In this way waves and instabilities can be used as diagnostic tools in a dusty space plasma environment, although this research field is typically an area where theory is leading observations [Mendis and Rosenberg, 1994]. Also from a mathematical point of view the study of dusty plasmas is interesting and challenging. Indeed, there are at least four reasons why dusty plasmas are essentially different from classical plasmas.

1. **The charge of a dust grain is variable,** and is determined by the grain properties and the surrounding plasma. This changes the description of waves in the sense that plasma fluctuations related to a wave will induce grain charge fluctuations and a coupling between the wave and the charging mechanism occurs.

   Electrons and ions are given up or captured by the dust. This means that source/sink terms have to be incorporated in the plasma equations. The precise forms of these source/sink terms are highly nontrivial, but imply new (in)stabilities, both at the linear and nonlinear level. In a self-consistent theory, the dust grain charge becomes an additional, discontinuous, independent variable of the system. It would require a reconsideration of Boltzmann's equation coupled to the charging equation. This description is, however, beyond the scope of our work.

2. **The charge-to-mass ratio is usually much lower for dust grains than for plasma particles** and the dust characteristic frequencies (plasma frequency and gyrofrequency) are much smaller than those corresponding to the plasma particles. This makes it possible to examine a large, interesting frequency domain for phenomena faster than the dust characteristic frequencies but slower than the plasma characteristic frequencies. This implies also that it might be worthwhile to re-interpret low-frequency noise in dusty environments in this framework.

   Although for the usual plasma particles we can safely neglect the gravitational forces, this is no longer true for dust grains. Indeed it can be shown that the classical gravitational condensation of neutral grains is altered when we introduce dust grain charges and the corresponding plasma effects. The dusty plasma system can then be called *self-gravitational.*

3. **The ion charge density is different from the electron charge density** because charges are residing on the dust grains. These charges are immobilized and although the plasma *including* the dust is quasi-neutral, the collection of particles with a high mobility (electrons and ions) is not. The sign of the equilibrium charge of the grains determines the sign of the mobile charges. New wave phenomena occur for frequencies where the charged dust is just residing in the background.

4. **The dust grains possess a large range of grain sizes** and for a realistic description we would need to use a mass distribution. When we use as a simplification a mono-sized dust population for the dusty plasma, an appropriate value must be taken to derive adequate results.

1.3 Outline of this thesis

The choice between an analytical analysis and a computer simulation is always subtle. The first approach needs a simplification of the system and hence crucial system elements can get lost. However, an analytical description has the benefit of giving more insight in the system as it is. Computer simulations, on the other hand, can tell more on the *precise* evolution of the system, but the information is restricted to the case study. We think that in the dusty plasma research field our knowledge is not yet fully developed enough to start with detailed computer simulations. We restrict our approach to analytical models, without neglecting the applications, however.

Because theoretical science must develop along with the available experiments and/or measurements, the first thing to do is to look at the available data. A review is given (**chapter 2**) for the three most promising dusty plasma environments in space physics (the rings of the outer planets, the cometary environment and interplanetary dust). As explained earlier, the dust charging process and the dusty plasma modes couple, and therefore the knowledge of the charging mechanism is essential in the description of dusty plasma waves. To evaluate the dust charging process correctly, it is essential that we use adequate information. The lack of availability of dust related data made it clear that new detection techniques are necessary to improve our knowledge of dusty plasma environments. In **chapter 3**, existing in situ detection techniques are reviewed and a new, promising one is examined in detail. This technique (Radio Dust Analyzer - RDA) makes it possible to analyze the dust grain characteristics (velocity, direction of propagation, charge), by the use of wire dipole antenna. **Chapter 4** briefly reviews the present status of the charging model, giving analytical expressions where they are available. The results of chapters 2 and 4 are used to indicate what processes are relevant in the charging of the dust grains in the different space plasma applications we have in mind (**chapter 5**). This chapter gives both the equilibrium potential and charging time, and the relative importance of the charging mechanisms for the different applications.

The remainder of this work describes waves and instabilities in dusty space plasmas. In **chapter 6** we explain our multi-fluid model which includes sink/source terms for the plasma capture of the grains. In **chapter 7** a general description of electrostatic modes in the presence of dust charge variations is carried out. The damping of low-frequency, dust-acoustic, ion-acoustic and Langmuir modes is quantified. Electromagnetic modes are described in **Chapter 8**, both at the linear and the nonlinear level. The influence of the dust on the pickup of cometary ions by the solar wind is examined, and the reductive perturbation method is used to treat the nonlinear evolution of parallel, perpendicular as well as oblique modes.

The influence of mass-distribution and self-gravitation is given in **chapter 9**, and a coupling between the Jeans instability and Alfvén en dust-acoustic modes is described. **Chapter 10** then gives the general conclusions.

Chapter 2

Dusty plasma data

In the solar system, dusty plasmas can be found in the *Earth's magnetosphere*, *cometary tails and comae*, *planetary rings* as well as in the *interplanetary medium*. Although this has already been recognized for decades, much of the characteristics of dust grains in space plasma environments is still unknown. Our knowledge of these systems comes mainly from remote sensing methods and radiation reflected or emitted by the dust particles at wavelengths from ultraviolet to microwave. The latter method requires the inversion of the radiative transfer equation, which gives the collective behavior in terms of the individual particle properties. The solution of the inverse problem is not unique, and is dependent on the assumed plasma model, so the results have to be interpreted with care. More knowledge can be recovered from *in situ* measurements, although the availability of such kind of data is highly restricted.

In this chapter, the (mostly *in situ*) data on dusty plasmas in the solar system are reviewed and bundled. This is done mainly to bridge the gap that occurs between theoretical dusty plasma physics and their applications. Indeed, it happens that the same data are quoted over and over in literature without looking at the way in which they were obtained. An important example in the field of dusty plasma can be found in the well-known review article of Goertz [1989]. This otherwise so eminent article cites data without referring to the sources. Nevertheless, the numbers cited in this article are quoted very often in the literature, without the important warning that they are estimates at best. To correct this inaccuracy, a more profound study of the data sets is indispensable.

Another reason why we should re-examine the available data is that we want to study the dust charging process in the different dusty plasma environments (**chapter 4**). The relevant charging mechanisms are highly dependent on the local conditions. Therefore, we will not only be interested in *dust characteristics* (grain size distribution, grain composition, grain charge, ...) but also in *plasma characteristics* (plasma densities, plasma temperatures) and *environmental characteristics* (relative dust-plasma velocity, magnetic field strength, photon flux, ...). This is by no means an easy task, because both experimental and theoretical work are extremely intertwined.

Finally, a re-evaluation of the data sources can be used to quantify the mathematical models that were published in the last years. The interest in the physics of dusty plasmas has been increasing exponentially ever since, but most of the published papers use data from an unclear source, and hence a review like this could be very useful.

In the last few years, industrial dusty plasma applications became more and more important. Indeed, particulates suspended in plasmas were discovered to be a major cause of costly wafer contamination during semiconductor manufacturing. Much effort has been made to understand particle growth, charging, levitation, and transport in order to optimize the process.

A relatively new, exciting laboratory topic in dusty plasma physics is the growth of stable crystals consisting of charged dust grains embedded in a plasma. The possibility of this was predicted by Ikezi [1986], while today experimental set-ups are built.

We restrict this chapter to the most promising environments, i.e. the planetary rings (**section 1**), the cometary environment (**section 2**) and the interplanetary environment (**section 3**). Some of the data on dusty plasma in laboratories are also reviewed (**section 4**).

The concepts that might need some explanation are clarified at the end in a glossary. The occurrence of these words in the text is indicated with a superscript †.

2.1 Dusty plasmas in planetary rings

Each of the outer giant planets (Jupiter, Saturn, Uranus and Neptune) is known to be encircled by a system of rings. Some of these, such as the A, B and C rings of Saturn and the nine narrow Uranian rings, are rather optically thick and are composed primarily of large bodies (1 cm to 10 m). However, every other ring system has been found to contain a large population of micron-sized dust [Showalter, 1991].

While it has been recognized for more than a century that planetary rings must be composed of a myriad of particles, even in the post-Voyager era we have not yet seen a single one. So we must rely on indirect and incomplete evidence, supplemented by theoretical considerations.

To evaluate the dust-plasma velocity we follow Mendis et al. [1982]; the gyration frequency of a charged dust grain in a rotating magnetosphere lies between the Keplerian frequency (Ω_K) and the corotation frequency. Which of the two bounds will be closer to the actual gyration frequency depends on the charge to mass ratio of the grain. Highly charged grains are almost corotating, while massive grains are gyrating at the Keplerian frequency.

Often the magnetic field in the neighborhood of planetary rings is modeled by a stationary dipole field. This is valid in the plasmasphere of the planet where the magnetic field is not distorted by ring currents, in planets like the Earth, Jupiter and Saturn. However, for the planets Uranus and Neptune, the magnetic moments are offset and they have large tilt angles relative to the rotation angle and so their magnetic configuration in the ring plane is highly variable.

Radial distances are expressed by the magnetic dipole shell parameter (L) which corresponds to the distance from the magnetic axis of the planet in units of the planetary radius. The planetary radii can be found in Table 2.1.

Planet	Radius (m)	Mass (kg)
Jupiter	71.5×10^6	1.90×10^{27}
Saturn	60.3×10^6	5.69×10^{26}
Uranus	25.6×10^6	8.69×10^{25}
Neptune	24.8×10^6	1.03×10^{26}

Table 2.1: Planetary radii and masses

2.1.1 Jupiter's ring system

Jupiter's ring system (Figure 2.1) was discovered in a single image from the Voyager 1 flyby in 1979, and subsequently imaged in greater detail by Voyager 2. The data obtained from the spacecraft Ulysses and Galileo and their dust detectors are restricted. Due to the malfunctioning antenna, the low data rate of the Galileo orbiter restricts the images taken. The first Galileo images of Jupiter's ring system were acquired in November 1996. Another set will come about a year later [Showalter, private communication, 1997]. The closest approach for the Ulysses spacecraft is 6.3 Jovian radii from the center of the planet, outside the rings. For the Galileo spacecraft the closest approach is outside the rings as well, and therefore *in situ* measurements cannot be expected from these spacecraft.

The ring appears to contain three rather distinct components. The main ring is relatively thin. Near the main ring's boundary and the planet arises the halo, a vertically extended cloud of material. Finally, Showalter et al. [1985] were the first to note the presence of an even fainter ring extending outward from the main ring in a single Voyager image. The optical depth of this "gossamer" ring appears to have a peak near the location of the *synchronous*† orbit, which suggests a significant interaction with the local plasma.

Particles in Jupiter's rings probably don't stay there for long (due to atmospheric and magnetic drag). Therefore, if the rings are permanent features, they must be continuously resupplied. The small satellites Metis and Adrastea, which orbit within the ring, are the obvious candidate sources.

The only *in situ* data were obtained by the meteoroid penetration detectors on board the Pioneer 10 and 11 spacecraft. Pioneer 10 registered 11 impacts of dust particles with masses $m \geq 2 \times 10^{-12}$ kg and Pioneer 11 registered 2 dust particles with masses $m \geq 2 \times 10^{-11}$ kg [Humes, 1980].

A review of the Jupiter data can be found in Table 2.2.

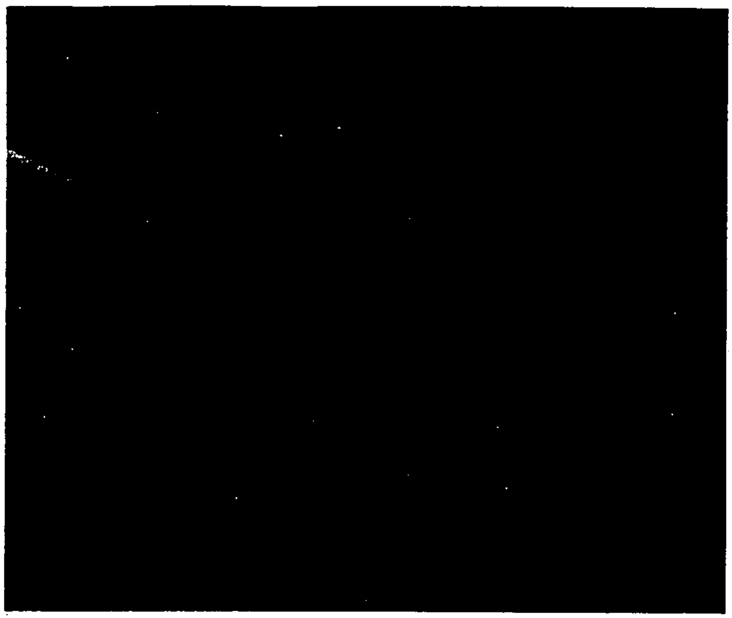

Figure 2.1: Voyager 2 image FDS 20693.02, looking back at the ring *ansa*† from inside Jupiter's shadow. Inside the main ring, we see the broad faint torus called the halo.

Dust characteristics

The main ring is scattering substantially more light into high phase angles than into small ones, indicating a considerable dust concentration. The interpretation of the photometric data of the Jovian system is difficult because each pixel in an image represents the intensity of a line of sight through both the ring and the halo. For the forward scattered component, a description by means of a *powerlaw*† integrated normal to the ring plane has been given: $N(a)_{\{m^{-2}\}} = (1.7 \pm 0.1 \times 10^{-11})\, a_{\{m\}}^{-2.5\pm0.5}$ for grains with radii $0.3\,\mu$m up to $100\,\mu$m. Backscattering information reveals a strikingly consistent similarity with the data taken from Amalthea and provides a good indication that there are rough, macroscopic bodies present, with surface properties quite similar to those of Amalthea [Showalter et al., 1987].

The halo, a broad faint torus, is even more difficult to analyze photometrically, because the intensity measured in any image pixel is a sum of contributions along a line of sight with sample points throughout the halo region. Variations in that intensity may therefore be the result of changes in geometry or phase angle, or both. Different arguments [Showalter et al., 1987] lead to the result that the halo consists of a dust distribution with a slightly steeper *powerlaw*†, or one in which some of the larger grains have been lost.

The *gossamer ring* has only been detected in *backscattering*† for a limited range of phase angles. Although the variance of the ring intensity suggests diffraction by grains of radius $a \approx 1.5\mu$m, it is not possible to exclude the presence of either larger or smaller particles based on these data [Showalter et al., 1985].

Earth based measurements of the Jovian ring reflectance spectrum have been performed [Burns et al., 1984]. The absence of absorption features rules out water, methane and

	Dust characteristics			Plasma characteristics				Environment characteristics			
	distribution	number density	nature	ne	ni	Te	Ti	Location	B	v	photonflux
Jupiter			[Burns et al., 1984]	[Intriligator et al., 1976]							9.24×10^{12} $m^{-2} s^{-1}$ [Goertz, 1989]
halo	Distribution similar to the distribution of the main ring, but a slightly steeper slope [Showalter et al., 1987] or with submicron sized grains [Burns et al., 1984]	?	Silicate, Carbonaceous	10^8 m^{-3}	10^8 m^{-3}	100 eV	100 eV	1.26-1.72 R_J	205-81 μT	21.7×10^3 m s^{-1} - 10.5×10^3 m s^{-1}	
main ring	Distribution around micron sizes with a power law (q=2-3, a_{min}=0.3 μm, a_{max}=100μm) [Burns et al., 1984] [Showalter et al., 1987]	The power law integrated normal to the ring plane: $(1.7 \pm 0.1) \times 10^{-11}\ a_{(m)}^{-2.5\pm0.5}\ m^{-2}$ [Showalter et al., 1987]	Silicate, Carbonaceous	10^8 m^{-3}	10^8 m^{-3}	100 eV	100 eV	1.72-1.81 R_J	81-69 μT	10.5×10^3 m s^{-1} - 8.5×10^3 m s^{-1}	
gossamer ring	micron sized radii [Showalter et al., 1985]	?	Silicate, Carbonaceous	10^8 m^{-3}	10^8 m^{-3}	100 eV	100 eV	1.81-2.94 R_J	69-16 μT	8.5×10^3 m s^{-1} - -12.4×10^3 m s^{-1}	

Table 2.2: Dust, plasma and environment characteristics of the Jovian ring system.

ammonia ice as major ring constituents. A silicate or carbonaceous composition has therefore been inferred.

Plasma characteristics

Intriligator et al. [1976] give an order of magnitude for the plasma characteristics in the plasmasphere: $N_e = N_p = 10^8\ \mathrm{m}^{-3}$, $T = 100$ eV. These values were quoted ever since (e.g. [Goertz, 1989]). There are no further plasma data available in the Jovian rings. $L = 5$ is the closest from in situ measurements [Bagenal, private communication, 1996].

Environmental characteristics

Jupiter's plasmasphere, extends to $L \sim 10$ and its dipole axis is tilted by 9.6°. The dipole moment is given by $M = 1.5 \times 10^{27}\mathrm{Am}^2$ [Parks, 1991].

We assume that the plasma rigidly rotates with a speed $v_\alpha(r) = \Omega_J \times r$, with $\Omega_J = 1.76 \times 10^{-4}\mathrm{rads}^{-1}$ [Ness, 1994].

The photoelectron flux from a metal surface at the orbit of Jupiter is given by $9.24 \times 10^{12}\mathrm{m}^{-2}s^{-1}$ [Goertz, 1989].

2.1.2 Saturn's ring system

Some peculiar features in the ring system of Saturn caused a major boost in the development of the physics of dusty plasmas. Indeed, during the Voyager spacecraft flybys, radial structures (*spokes*) in the B-ring, and braided structures in the F-ring (*braids*) were discovered. These features could not, contrary to general belief, be explained in purely gravitational terms, and hence a further development of the knowledge of the physics of dusty plasmas was necessary.

But dust is not only present in these features. The innermost D-ring seems to occupy most of the region between the C-ring and the planet's cloudtops. The distinct brightening of the ring at the highest phase angles clearly indicates diffraction by micron-sized dust. Traveling outward, local high dust densities are to be expected in the spokes (B-ring). The next ring to show a preponderance of dust is a narrow ringlet near the middle of the Encke gap in the A-ring. The F-ring itself was the first narrow and longitudinally variable ring observed. Finally Saturn has two very faint outer rings, designated G and E. Interest in these two rings has increased recently because of the potential hazard they may pose to the Casinni orbiter [Showalter, 1991]. The Saturn ring system is shown in Figure 2.2, while a review of Saturn dust data can be found in Table 2.3.

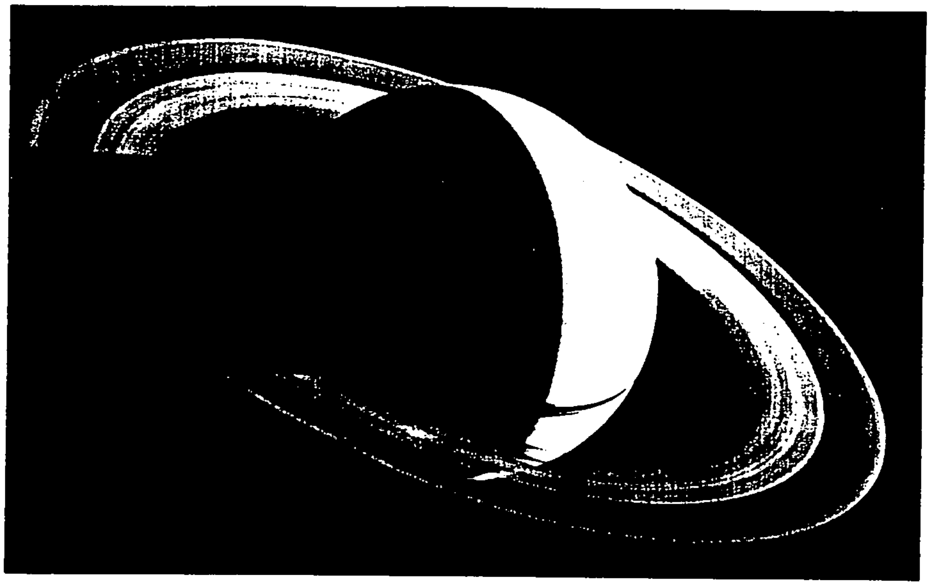

Figure 2.2: A picture of the Saturn ring system at a large phase angle

Dust characteristics

Our knowledge of particle properties has been greatly enhanced by spacecraft observations (Pioneer 11, 1-9-1979; Voyager 1, 12-11-1980; Voyager 2, 26-8-1981), which allow the rings to be viewed at a large range of phase angles extending to about 160°, fairly close to *forwardscattering*†. The main rings are typically *backscattering*†. This means that, overall, they contain at most only a small area fraction of dust. The photometric behavior of the optically thin rings is quite different from that of the main rings. These diffuse rings are brighter at high phase angles, demonstrating the presence of micron-sized dust particles.

All of the high-quality spectral reflectance data, needed to resolve the particle composition of the rings, were obtained for the A and B-rings [Esposito et. al, 1984]. These spectra have been used to establish that water ice is a major component of the ring material [Clark and McCord, 1980], [Clark, 1980]. The A and B-ring particles are probably primarily water ice, possibly containing clathrate hydrates, although minor amounts of colored material (possibly sulfur or iron-bearing silicate compounds) are also present. It is likely that an overall ring composition is not too different from that of the various icy satellites [Esposito et. al, 1984].

- The **D ring.**

  Little is known about the dust characteristics of the D-ring because of its low optical depths. This optical depth is uncertain, although it is very likely less than 10^{-3} everywhere [Wilson, 1991]. It could consist merely of dust grains, based on the few Voyager pictures where it can be seen [Showalter et al., 1991].

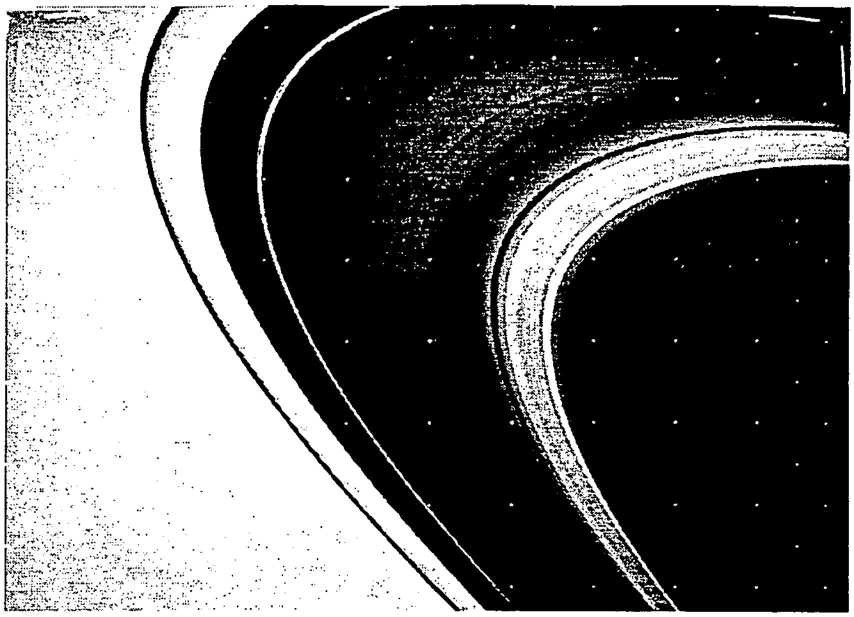

Figure 2.3: Voyager 2 image FDS 43643.34 shows a distinct pattern of "spokes" in the B Ring (in reversed grayscale in forward scattered light).

- The **Spokes**

One of the most intriguing features observed in the Saturnian ring system by both Voyagers 1 and 2 were the nearly-radial, wedge-shaped features in Saturn's B-ring. The wedge becomes wider towards the planet. Because of their radial extension these structures were called "spokes" [Collins et al., 1980]. The spokes have an inner boundary at $\sim$1.72 R_S and an outer boundary at approximately the outer edge of the B-ring. A typical spoke pattern is seen in Figure 2.3. High resolution images show that the leading and trailing edges of the spokes have distinctly different angular velocities, the leading edge has essentially the Keplerian velocity, whereas the trailing near-radial edge has approximately the corotational velocity [Grün et al., 1983].

Against the background of the B-ring they appear dark in backscattered light, and bright in forward scattered light, indicating that they are composed of micron and submicron-sized grains [Grün et al., 1983]. The observed deviation of the angular velocity of the spoke features from the Keplerian value can yield the charge-to-mass ratio of the spoke particles. A lower limit is given on the spoke particle size of about 0.01 μm [Thomsen et al., 1982].

The spokes were explained as follows. Consider a macroscopic ring particle in the neighborhood of which a dense plasma cloud develops. This cloud might be caused by meteor impact on the ring particles, however other mechanisms like lightning discharges cannot be ruled out. This dense plasma causes small dust grains that reside on the macroscopic ring particle to get electrostatically levitated. Due to the gravitational forces, these dust grains will drift relative to the plasma. Indeed, the plasma particles with their low charge-to-mass ratio will corotate with the planet and its magnetic field, while the dust grains have an angular velocity between the Keplerian and corotation velocity as explained earlier. This causes charge separation and hence an electric field **E** and a corresponding $\mathbf{E} \times \mathbf{B}$ drift in the plasma. Outside the *synchronous*[†] orbit, this results in a drift away from the planet, while inside the synchronous orbit, the $\mathbf{E} \times \mathbf{B}$ drift is directed to the planet. As long as the drifting plasma remains dense enough, dust can be levitated, which marks the radial trail of the plasma. An observer will see this dust trail very much like the dust cloud left behind by a car racing along a dusty road [Goertz and Morfill, 1983].

- The **Encke gap** brightens significantly at high phase angles, which indicates a preponderance of micron-sized dust. This ring has never received the investigation that it warrants, although an ample body of Voyager data exists [Showalter, 1991].

- The **F-ring** has been studied by the Voyager image instrument, occultation measurements of the rings and photopolarimeter instruments. Showalter et al. [1992] analyzed the photographic pictures using a semi-empirical theory for scattering by random oriented, nonspherical particles. The contribution of Saturn-shine was included to the incident radiation field. A power law index of the dust ($a_{min} = 0.001$ μm and $a_{max} = 20$ μm) and the fractional contribution f of the dust to the total optical depth were considered as free parameters. The analysis results in $q = 4.6 \pm 0.5$ and $f \geq 98\%$.

  The braids, kinks and clumps seen in only a few pictures of the F-ring (Figure 1.1) are the only features in the ring system which have up to this time defied a proper explanation. Avinash and Sen [1996] were to our knowledge the first to tackle the braid problem, giving an explanation based on the stability that occurs by the balance of the "pinch pressure" due to the dust ring current and the electrostatic pressure.

- The **G-ring** is very faint and narrow and has been studied photometrically [Showalter and Cuzzi, 1993]. The Voyager 2 spacecraft crossed the ring plane, very close to the G-ring, at 2.86 R_S and the local impacts could be recovered in the Voyager 2 data [Gurnett et al., 1983], [Tsintikidis, 1994], [Meyer-Vernet et al., 1997].

  There are only two Voyager photographic images available that show the G-ring as visible to the eye. Showalter and Cuzzi [1993] could find the G-ring for four different phase angles. They proposed a power law index of 6.0 ± 0.2 with a $a_{min} = 0.03$ μm, and $a_{max} \approx 0.5$ μm. Gurnett et al. [1983] proposed $q = 7$ for $a_{min} = 0.3$ μm and $a_{max} = 3$ μm. This result was revised by Tsintikidis [1994], and they obtained a dust number density of the order of 10^{-2} m^{-3}, with a mass threshold ranging from 10^{-14} to 5.4×10^{-12} kg. The results from the PRA-experiment given by Meyer-Vernet et al. [1997], give an indication that the slope flattens above 0.5 μm. They assumed a rough continuity between the distributions and inferred that $q < 3.5$ for grains between half a micron and a few microns.

  The dust distribution integrated normal to the ring plane, and radially along the G-ring, as derived by Showalter and Cuzzi [1993], is given by $N(a)_{\{m^{-1}\}} da_{\{\mu m\}} = (5.8 \pm 0.3) \times 10^9 a_{\{\mu m\}}^{-6} da_{\{\mu m\}}$.

- The **E-ring** has been studied photometrically [Showalter et al., 1991] and by local impact ionization analysis of the Voyager 1 data by Meyer-Vernet et al. [1996] (PRA-experiment) and Tsintikidis et al. [1995] (PWS-experiment).

  A very narrow distribution of slightly nonspherical particles $1.0 \pm 0.3\ \mu$m provides the best fit of the photometric data [Showalter et al., 1991]. This is in perfect agreement with the local analysis of Meyer-Vernet et al. [1996].

  From photometric data, only integrated densities along the line-of-sight can be obtained, while the number density of the dust for $L = 6.1$, is given by Meyer-Vernet et al. [1996] to be 4.3×10^{-3} m^{-3}. Tsintikidis et al. [1995] come to slightly larger grains, and a dust particle number density of the order of 10^{-3} m^{-3}.

Plasma characteristics

The ion characteristics deduced from the Pioneer data differ substantially from those reported by Voyager. Whether these differences are indicative of a real variation in Saturn's magnetosphere or a difficulty in analyzing the Pioneer data is uncertain. Therefore the plasma model from Richardson and Sittler [1990] used only Voyager data.

A two-dimensional map in the meridional plane of the plasma ion and electron densities for $L < 12$ is produced. Azimuthal symmetry was assumed; this is a reasonable assumption, since the time scales for ionization of neutrals and loss of ions are of the order of weeks and months, much longer than the 10-hour rotation period of Saturn. Outside $L = 12$, plasma spectra change rapidly [Richardson, 1995], but inside this limit, where we can find the rings, the plasma environment can be considered as steady state. Plasma densities are extrapolated along magnetic field lines using the equation for force balance parallel to the magnetic field.

The plasma consists of a heavy ion group (O^+, OH^+, H_2O^+, H_3O^+, N^+), all of which have mass near 16 m_p and which could not be resolved by the PLS-instrument, with a density of $1 - 100 \times 10^6$ m^{-3}. A light ion population was found consisting merely out of protons with a density of $0.1 - 10 \times 10^6$ m^{-3}. Over the full energy range of the Voyager PLS instrument, the electron distribution functions are clearly non-Maxwellian in character; they are composed of a cold (thermal) component with Maxwellian shape and a hot (suprathermal) non-Maxwellian component. In the neighborhood of the rings, the hot electrons are by far outnumbered by the thermal electrons [Sittler et al., 1983]. The total electron density in the ring plane is in the range of $1 - 100 \times 10^6$m^{-3}.

For the special case of the spokes in the B-ring the situation can be totally different. We can expect that the plasma density in the spokes is much higher than the surrounding plasma density (following the spoke formation model of Goertz and Morfill [1983]). These densities could be caused by meteor impacts on the larger B-ring particles and can be several orders of magnitude bigger than the general B-ring plasma density. Even densities of the order of $N_e = 10^{21}$ m^{-3} are not impossible [Goertz and Morfill, 1983].

	Dust characteristics			Plasma characteristics				Environment characteristics			
	distribution	density	nature	Ne	Ni	Te	Ti	Location	B	v	photonflux
Saturn			[Esposito et al., 1984]	[Richardson and Sittler, 1990]	[Richardson, 1995]	[Richardson and Sittler, 1990]	[Richardson, 1995]				$2.78 \times 10^{12}\ m^{-2} s^{-1}$ [Goertz, 1989]
D-ring	?	?	water ice	$\geq 10^8\ m^{-3}$	protons $5 \times 10^6\ m^{-3}$ heavy ions $1 \times 10^8\ m^{-3}$	thermal electrons 1 eV hot electrons 70 eV	protons 6 eV heavy ions 10eV	$1.11\ R_S$-$1.24\ R_S$	11-16 μT	$13 \times 10^3\ m\ s^{-1}$ - $10 \times 10^3\ m\ s^{-1}$	
Spokes in B-ring	micron and submicron sized grains [Mendis and Rosenberg, 1994]	?	water ice	$\geq 10^8\ m^{-3}$ even $10^{21}\ m^{-3}$ [Goertz and Morfill, 1994]	protons $5 \times 10^6\ m^{-3}$ heavy ions $1 \times 10^8\ m^{-3}$	thermal electrons 1 eV hot electrons 70 eV	protons 6 eV heavy ions 10eV	$1.52\ R_S$-$1.95\ R_S$	2.9-6.1 μT	$5.3 \times 10^3\ m\ s^{-1}$ - $-1.3 \times 10^3\ m\ s^{-1}$	
Encke gap	?	?	water ice	$\geq 10^8\ m^{-3}$	protons $5 \times 10^6\ m^{-3}$ heavy ions $1 \times 10^8\ m^{-3}$	thermal electrons 1 eV hot electrons 70 eV	protons 6 eV heavy ions 10eV	$2.21\ R_S$	2.0 μT	$-5.0 \times 10^3\ m\ s^{-1}$	

Table 2.3: Dust, plasma and environment characteristics of the Saturn ring system. (1/2)

	Dust characteristics			Plasma characteristics				Environment characteristics			
	distribution	density	nature	ne	ni	Te	Ti	Location	B	v	photonflux
F-ring	power law distribution (q=4.6±0.5, a_{min}=0.001 μm, amax=20μm) [Showalter et al., 1992]	?	water ice	≥ 10^8 m^{-3}	protons 5 × 10^6 m^{-3} heavy ions 1 × 10^8 m^{-3}	thermal electrons 1 eV hot electrons 70 eV	protons 6 eV heavy ions 10eV	2.32 R_S	1.7 μT	-6.5 × 10^3 m s^{-1}	
G-ring	power law distribution (q=6, a_{min} ≤ 0.03 μm, a_{max} ≈ 0.5 μm) [Showalter and Cuzzi, 1993] (q=7, a_{min}=0.3 μm, a_{max}=10μm) [Gurnett et al., 1983] (q<3.5, a_{min}=0.5 μm, a_{max}=10μm) [Meyer-Vernet et al., 1997]	N_d=10^{-2} m^{-3} with a mass threshold ranging 10^{-14}- 5.4 × 10^{-12} kg [Tsintikidis et al., 1984] The power law integrated normal to the ring plane, and radially along the ring: $N(a)_{(m-1)}\, da_{(\mu m)} = (5.8 \pm 0.3) \times 10^9\ a_{(\mu m)}^{-6}\, da_{(\mu m)}$ [Showalter et al., 1993]	water ice	≥ 10^8 m^{-3}	protons 5 × 10^6 m^{-3} heavy ions 1 × 10^8 m^{-3}	thermal electrons 1 eV hot electrons 70 eV	protons 6 eV heavy ions 10eV	2.8 R_S	0.98 μT	-13 × 10^3 m s^{-1}	
E-ring	A narrow size distribution of micron-sized grains [Showalter et al., 1991] [Meyer-Vernet et al., 1995]	N_d=10^{-3} m^{-3} [Tsintikidis et al., 1995] [Meyer-Vernet et al., 1995]	water ice	10^7 - 10^8 m^{-3}	protons 0.8 × 10^6 m^{-3} - 2 ×10^7 m^{-3} heavy ions 4 × 10^6 - 1 ×10^8 m^{-3}	thermal electrons 1-11 eV hot electrons 80-200 eV	protons 8-20 eV heavy ions 13-180 eV	3-8 R_S	0.042-0.8 μT	-15 × 10^3 m s^{-1} - -70 × 10^3 m s^{-1}	

Table 2.3: Dust, plasma and environment characteristics of the Saturn ring system. (2/2)

Environmental characteristics

Saturn's plasmasphere extends to $L \sim 10$ and its dipole axis is within 1° of being parallel to the rotation axis. The dipole moment is given by $M = 4.7 \times 10^{25}\mathrm{Am}^2$ and the field is very well described using that model [Ness, 1994].

We assume that the plasma rigidly rotates with a speed $v_\alpha(r) = \Omega_S \times r$, with $\Omega_S = 1.64 \times 10^{-4}\,\mathrm{rads}^{-1}$ [Ness, 1994].

The photoelectron flux from a metal surface at the orbit of Saturn is given by $2.74 \times 10^{12}\mathrm{m}^{-2}\mathrm{s}^{-1}$ [Goertz, 1989].

2.1.3 Uranus' ring system

The nine "classical" rings of Uranus have high optical depths, and hence very little dust (Figure 2.4). The narrow ring (λ or 1986U1R) discovered in the backscattered Voyager images, have been found to be somewhat of an exception. In a single Voyager image at high phase angles, these rings were found to be far brighter than their environment, indicating that dust is the major constituent. One additional broad ring, designated 1986U2R is visible in a single Voyager image at a 90° phase angle. This ring is interior to all other rings. Unfortunately, very little can be determined about the particle properties of this ring from a single view, although a predominance of dust is strongly suspected [Showalter, 1991]. Between the δ and λ ring, a region is encountered which is mostly forward scattering. This region is called the dust belt, as can be seen on Figure 2.5 [Esposito et al., 1991].

A review of the Uranus data is given in Table 2.4.

Dust characteristics

Local impact ionization analysis of the Voyager 2 data was done for the PWS-experiment [Gurnett et al., 1987] and for the PRA-experiment [Meyer-Vernet et al., 1986]. The ring plane crossing took place at $L = 4.40$, which is farther away from the planet than the rings. The results from the two instruments are roughly the same but differ in detail. Grains of a few μm (1 to 4 μm according to PRA and 4 to 8 μm according to PWS), having a maximum number density of about 10^{-4} to $10^{-3}\,\mathrm{m}^{-3}$ struck the spacecraft.

A photometric analysis was made by Ockert et al. [1987]. The brightness distribution is dominated by *backscattering*†, which means that mostly macroscopic grains are present. The fractional area in dust-sized particles in and around the nine main rings was analyzed and found to be less than 2×10^{-3}. Furthermore the observations were consistent with an average dust particle size of $1.0 \pm 0.3\ \mu$m, with a power law with index $q = 2.5 \pm 0.5$.

Figure 2.4: August, 1994 image of Uranus and its rings was acquired by the Wide Field/Planetary Camera on Hubble Space Telescope.

The particles are quite dark and scatter light like rough dark bodies such as the Moon or Callisto. The gray color of the ring particles could be explained by chondrites with a coating of carbon [Esposito et al., 1991].

Plasma characteristics

The closest encounter with the planet took place in January 1986, when Voyager 2 passed the planet at a magnetic L-shell $L = 4.59$, so the rings were not visited. The plasma population at locations $L = 4.59$ and farther away from the planet is modeled by a thermal Maxwellian and a hot non-Maxwellian distribution for the electrons, and by a hot, an intermediate and a warm ion population. Any extrapolation of these data has to be carried out carefully, because of the different orientations of the spinning and magnetic axes [Belcher et al., 1991].

Environmental characteristics

Uranus' plasmasphere dipole axis is tilted by 58.6°. The dipole moment is given by $M = 3.8 \times 10^{24}\mathrm{Am}^2$. Furthermore the dipole offset (planet center to dipole center) equals $L = 0.3$ [Parks, 1991].

	Dust characteristics			Plasma characteristics				Environment characteristics			
	distribution	density	nature	ne	ni	Te	Ti	Location	B	v	photonflux
Uranus			[Esposito et. al, 1991]	[Belcher et. al, 1991] at 4.40 R_U					[Ness, 1994]		679×10^9 $m^{-2} s^{-1}$ [Goertz, 1989]
1986U2R	?	?	Carbonaceous chondrites	hot $10^4 m^{-3}$	hot $10^5 m^{-3}$	hot 20-50 eV	hot 100-1000 eV	1.45-1.54 R_U	6.5-27 μT	8.1×10^3 m s^{-1} - 10×10^3 m s^{-1}	
dust belt	?	?		cold ?	intermediate 10^5-$10^6 m^{-3}$	cold ?	intermediate 50-100 eV	1.88-1.95 R_U	3.9-10 μT	5.9×10^3 m s^{-1} - 7.5×10^3 m s^{-1}	
1986U1R	at R_U=4.40 micrometer-sized grains [Gurnett et al., 1987] [Meyer-Vernet et al., 1987]	at R_U=4.40 10^{-3}-10^{-4} m^{-3} [Gurnett et al., 1987] [Meyer-Vernet et al., 1987]			warm $10^6 m^{-3}$		warm 8-10 eV	1.95 R_U	3.5-9.0 μT	5.9×10^3 m s^{-1} - 7.2×10^3 m s^{-1}	

Table 2.4: Dust, plasma and environment characteristics of the Uranus ring system.

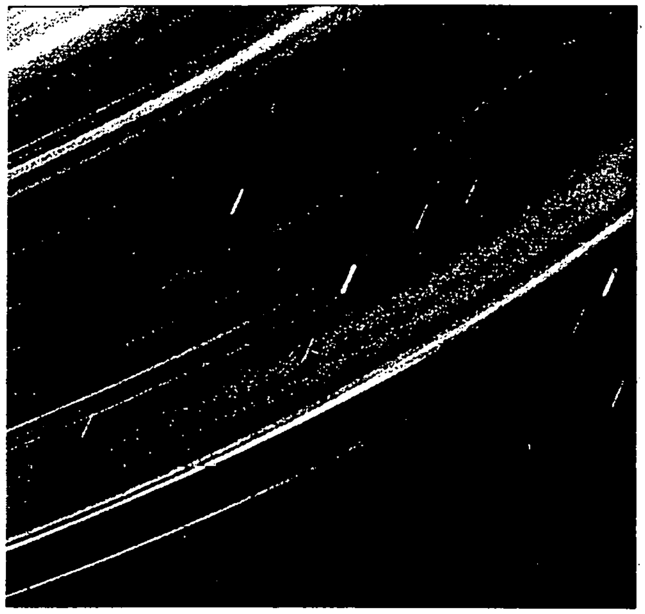

Figure 2.5: A 96 second wide-angle image, FDS 26852.19, taken by Voyager 2 looking back at the planet from inside the shadow of Uranus. The high phase angle dramatically enhances the visibility of the micron-sized dust particles.

We assume that the plasma rigidly rotates with a speed $v_\alpha(r) = \Omega_U\, r$, with $\Omega_U = 1.01 \times 10^{-4}\,\mathrm{rads}^{-1}$ [Ness, 1994].

The photoelectron flux from a metal surface at the orbit of Uranus is given by $679 \times 10^9 \mathrm{m}^{-2} s^{-1}$ [Goertz, 1989].

2.1.4 Neptune's ring system

The Voyager cameras revealed a number of new dusty rings in orbit about Neptune. The largest set of data available on the rings of Neptune, are the $\sim$ 800 images collected by Voyager 2. The handful of positive detections by groundbased observations during the 1980s, the Voyager Photopolarimeter (PPS) and Ultraviolet Spectrometer (UVS), the Voyager Plasma Wave (PWA), Planetary Radio Astronomy (PRA) constitute additional sources of data. Note that the Voyager 2 spacecraft ring plane crossing took place outside the rings.

Very preliminary photometric modeling indicates that all of these rings contain a mixture of dust and larger bodies representing comparable optical dust. Especially the Adams rings and the Le Verrier rings contain a significant fraction of dust, comparable to that observed in Saturn's F ring. The Lassell ring appears to have a different mix of particle sizes than Le Verrier or Adams. Azimuthal arcs on scales of the order of 1° to 10° were found in the Adams ring and within these arcs several long linear features were found. These are believed to be discrete clumps or denser-than-average regions of the arc. It was proposed that they represent an accumulation of dust-sized particles, although they can be explained in a pure gravitational way [Porco et al., 1995].

The reader must bear in mind that much work remains to be accomplished and what is presented here is more a statement of progress than a complete and final assessment. Indeed, the low light levels at Neptune, and the extremely low albedo of the rings required uncommonly long exposures for imaging the rings with the Voyager cameras. This causes the photo's to be badly smeared and so photometric analysis results need to be taken with a grain of salt.

The expected symmetry plane for particles on gravitationally dominated orbits is called the Laplace plane, and is not generally coincident with Neptune's equator because of the perturbations from a massive moon Triton on an inclined orbit. A review of Neptune data can be found in Table 2.5.

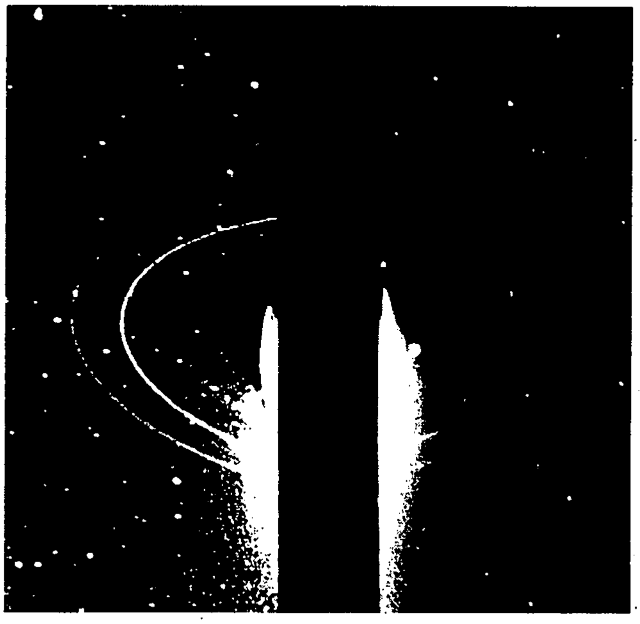

Figure 2.6: Pair of Voyager 2 images, FDS 11446.21 and 11448.10, showing the full ring system with the highest sensitivity. Both images are 591 second exposures obtained through the clear filter of the wide angle camera.

	Dust characteristics			Plasma characteristics				Environment characteristics			
	distribution	density	nature	ne	ni	Te	Ti	Location	B	v	photonflux
Neptune			[Ferrari and Brahic, 1994]	[Richardson et al., 1995] at 3.45 R_N					[Ness et al., 1995]		276×10^9 $m^{-2} s^{-1}$ [Goert, 1989]
Adams	5-10 µm [Gurnett et al., 1991]	$Nd=10^{-2}$ m^{-3} at $R_N=3.45$ $Nd=10^{-3}$ m^{-3} at $R_N=4.26$ [Gurnett et al., 1991]	dirty ice	3×10^5 - 10^6 m^{-3}	N^+ 10^5 - 10^6 m^{-3} H^+ 10^5 m^{-3}	20 - 100 eV	N^+ 300-1000 eV H^+ 30-100 eV	2.54 R_N	0.71-2.7 µT	4.8×10^3 m s^{-1} - 6.8×10^3 m s^{-1}	
Unnamed	power law distribution (q=4, amin=1.6 µm, amax=10µm) [Pedersen et al., 1991]	$N_{m>m0} \approx 7 \times 10^{-17}/m_0$ at $R_N=4.26$ $N_{m>m0} \approx 7 \times 10^{-16}/m_0$ at $R_N=3.45$ [Pedersen et al., 1991]						2.50 R_N	0.75-2.9 µT	5.0×10^3 m s^{-1} - 7.0×10^3 m s^{-1}	
Arago								2.31 R_N	0.90-3.9 µT	5.7×10^3 m s^{-1} - 7.7×10^3 m s^{-1}	
Lassell								2.15 R_N-2.31 R_N	0.90-5.2 µT	5.7×10^3 m s^{-1} - 8.5×10^3 m s^{-1}	
Le Verrier								2.15 R_N	1.1-5.2 µT	6.4×10^3 m s^{-1} - 8.4×10^3 m s^{-1}	
Galle								1.65 R_N-1.73 R_N	1.8-16 µT	8.5×10^3 m s^{-1} - 11×10^3 m s^{-1}	

Table 2.5: Dust, plasma and environment characteristics of the Neptune ring system.

Dust characteristics

The results from the PRA and PWS experiments (respectively given by Pedersen et al. [1991] and Gurnett et al. [1991]) differ for the precise peak locations, vertical thicknesses and the dust volume densities. The first paper derives a power law for the dust grain distribution around $R_N = 4.26$, with $q = 4$, a_{min}=1.6 μm, a_{max}=10 μm. Furthermore the cumulative number density is given by $N_{m>m_0\{\mathrm{m}^{-3}\}} \approx 7 \times 10^{-17}/m_{0\{\mathrm{kg}\}}$. At $R_N = 3.45$, this cumulative density is given by $N_{m>m_0\{\mathrm{m}^{-3}\}} \approx 7 \times 10^{-16}/m_{0\{\mathrm{kg}\}}$. The PWS-experiment detected grains in the range of 5-10 μm with an uncertainty of a factor of 2 to 3. The densities are given by 10^{-2} m^{-3} for the outbound crossing at $R_N = 4.26$ and 10^{-3} m^{-3} for the inbound crossing at $R_N = 3.45$.

Data on the ring optical depth has been used by Ferrari and Brahic [1994] to derive added constraints on the refractive indices of the ring particles. Their conclusion is that the ring particle refractive indices best match "dirty ice" composition, rather than a highly absorbing carbon-rich material. We must add that a refractive index of this magnitude is appropriate for a large variety of silicates as well. Even though the specific set of refractive indices does not provide a good fit to the data, the occurrence of silicates cannot be ruled out.

Plasma characteristics

The analysis of the Voyager data is given by Richardson et al. [1995]. The spacecraft crossed the ring plane in the magnetic shell parameter of 3.45 R_N, and hence outside the ring plane.

Environmental characteristics

The overall magnetic field can be characterized by an offset tilted dipole model (OTD) with dipole moment 2×10^{24}Am^2, with a dipole offset (planet center to dipole center) of $L = 0.55$ and a dipole axis tilted by 47° [Ness et al., 1995].

We assume that the plasma rigidly rotates with a speed $v_\alpha(r) = \Omega_N \times r$, with $\Omega_N = 1.08 \times 10^{-4}$ rads^{-1} [Ness, 1994].

The photoelectron flux from a metal surface at the orbit of Neptune is given by 276×10^9 m$^{-2}s^{-1}$ [Goertz, 1989].

2.2 Cometary dusty plasmas

Other intriguing objects containing solar system dust are cometary environments. The appearance of dust grains is very obvious in one of the optically largest structures that can be seen in the sky: the cometary dust tail. This tail, pushed away from the sun by the solar pressure, is nowadays quite well understood and can reveal lots of important scientific information on the dust characteristics.

To have an idea of the global morphology of the cometary environment, the interaction with the solar wind should be discussed briefly. Heavy cometary neutral species are ionized by solar ultraviolet radiation or charge exchange with the solar wind ions and are assimilated into the magnetized solar wind. The continuous mass loading of the inflowing solar wind by the newly created ions causes the solar wind to decelerate and heat up. Continuous deceleration of the solar wind by mass loading is possible only as long as the mean molecular weight of the plasma remains less than a critical value. Before that critical value is reached, a weak *bow shock* forms ahead of the comet. Downstream from the shock, the mass-loaded subsonic solar wind continues to interact with the cometary atmosphere, penetrating into a region of ever increasing neutral density. Strong deceleration occurs at a boundary we label the *collisionopause* or *cometopause*, where significant momentum is transferred by collisions from the outflowing cometary neutrals to the solar wind ions. Inside this transition region, collisions dominate and the solar wind decelerates rapidly and cools due to charge exchange processes with the less energetic cometary neutrals, while the magnetic field compresses to form a magnetic barrier region. A tangential discontinuity interface (*ionopause*) forms at the inner edge of the magnetic barrier region and separates the two plasmas: the purely cometary plasma and the mass-loaded solar wind plasma. Inside the ionopause is a magnetic field-free cavity [Flammer, 1991].

Prior to the 1986 apparition of comet Halley, all attempts to determine the physical properties of cometary dust were limited to remote observations and the analysis of various particles captured by the Earth's magnetosphere. This introduces difficulties related to the inverse problem. Deconvolution of, for example, the observed brightness into the local dust number density involves knowledge of the size distribution, which is changing perhaps both spatially and temporally. It is difficult to separate these spatial and temporal effects. Within a period of less than three weeks in March 1986, Halley's comet was encountered by six spacecraft belonging to four space agencies and carrying a total complement of 50 experiments [Mendis, 1988]. Three of the spacecraft passed within 10 000 km of the nucleus, providing us with the first opportunity to investigate the full size-range of dust particles. From all those spacecraft, Giotto was the only one going through the entire cometosheath including the inner cometosheath and the ionopause.

Dust characteristics

The dynamics of dust grains in the comet coma has been explained by the *fountain model.* Dust particles that are ejected by the cometary nucleus will get accelerated by the expanding gas coma, until they reach a final expanding velocity (v_{out}) that increases with decreasing particle size. This expanding velocity depends also on the heliocentric distance (r_h), increasing for decreasing r_h. Once a dust grain leaves the region of dust-gas interaction, the only forces acting on it in the heliocentric frame are the solar radiation (pressure) force F_{rad} and the solar gravity F_{grav}, since the gravitational force of the cometary nucleus itself is negligible. As illustrated in Figure 2.7 in cometocentric bipolar coordinates (nucleus at the origin, an axis along the heliocentric radius vector), the particle trajectories are parabolic, the envelope of which is a paraboloid of revolution with focus at the nucleus [Divine et al., 1993], [Horányi and Mendis, 1991].

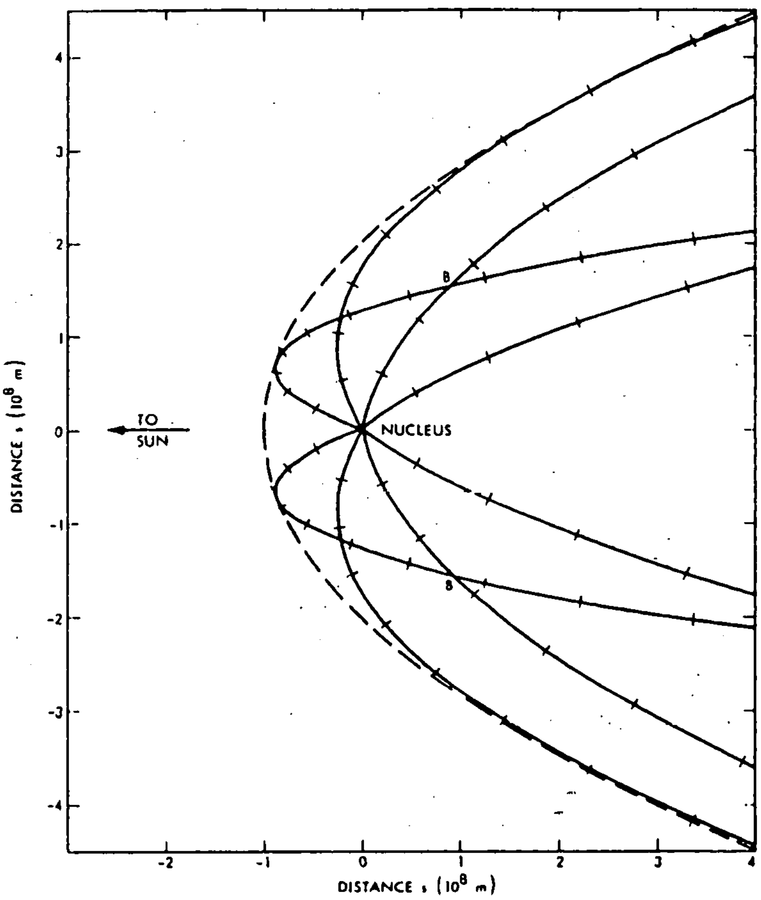

Figure 2.7: Fountain model trajectories (solid lines) for dust particles with $v_{out} = 347$ ms^{-1} at r=0.89 AU. Time ticks are indicated every two days. The envelope, with apex distance $A=10^8$ m for those particles with mass near 10^{-12} kg is shown by a dashed line [Divine et al., 1993].

As a first approximation, the order of magnitude of the number density of the dust grains is proportional to:

$$N_d(r_h, a, r) \propto \frac{Q(r_h, a)}{r^2} \qquad r < A(r_h, a) \tag{2.1}$$

where r is the distance dust grains-comet, $Q(r_h, a)$ is the dust production rate and $A(r_h, a)$ the apex distance for a grain with radius a. It was found that the dust release rates in the coma decreases with the increase of heliocentric distance as a power law:

$$Q(r_h, a) \propto r_h^{-q}, \tag{2.2}$$

with $q = 3.0 \pm 0.7$. This is in agreement with other models although the precise value of the power index q varies in the neighborhood of $q = 4$ ([Singh et al., 1997] and references therein). The fountain model does not include any orbital motion by the comet, but can give suitable predictions of dust grain flux magnitudes [McDonnell et al., 1992].

Although for a first estimate the fountain model seems to match the available data [Mazets et al., 1986], the reality is more complicated and other effects play a role, indicated by the following measurements.

- Both the VEGA [Simpson et al., 1986] and the GIOTTO [McDonnell et al., 1986] spacecraft detected *dust-packets.* They discovered small dust particles arriving in sequences of events preceded and followed by relatively long time intervals (time gaps) during which no events were measured.

- There exists a large quantity of small dust grains and the dust mass spectrum seems to increase downward to $a = 0.01$ μm. The smallest particles were detected much farther away than expected by the fountain model. They were well outside their bounding paraboloids, if we assume that they were slightly absorbing as detected by the VEGA dust detectors [Mendis, 1988].

- It was detected [Mazets et al., 1986] that in the inner regions of the coma, the dust particle number density varies substantially stronger than r^{-2}, and the apex boundaries, expected from modeling to be drastic, were not as sharp as anticipated [McDonnell et al., 1991].

- There is a tendency for the mass density of the dust grains to decrease with increasing size. For these very small particles, the electromagnetic forces will play an important role. The density of the grains can be given by [McDonnell et al, 1991]:

$$\rho_{\{\mathrm{kgm}^{-3}\}} = 3000 - 2200\frac{a}{a+a_0}, \tag{2.3}$$

  which results in densities in the range of 1000 to 2500 kgm^{-3}, with $a_0 = 2$ μm. Indeed grains with atomic (C+O)/(Mg+Si+Fe)-ratios in the range of 0.01 to 10 (silicate dominated) have densities around 2500 kgm^{-3}, while those with larger ratios (CHON-dominated) have a mean density of 1000 kgm^{-3}. Hence the CHON dominated grains are fluffy, while the silicate-dominated ones are more compact [Jessberger and Kissel, 1991]. Most dust particles recorded by PUMA-1 (VEGA 1), consist of a fluffy silicate core, covered by refractory, icy fluffy organics [McDonnell et al., 1991].

The real dust size distribution is best fitted by a *powerlaw*†. The measured *fluences*† show clearly the variation of the power law index over both mass and time. Measured values range from $q = 3.3$ for VEGA 2, to $q = 4.1$ for GIOTTO, although model values have $q = 3.6$ from 10^{-13} to 10^{-19} kg in the coma. For larger dust particles (m $\geq 10^{-9}$ kg), the spectrum is much flatter, and we recover $q = 2.7$ [McDonnell et al., 1991]. At small distances from the nucleus, the relative number of small submicron particles is high. The relative contribution of such particles decreases with increasing distance from the nucleus. Furthermore, the slope of the mass spectrum decreases for small masses. At large distances from the nucleus, one observes a clearly pronounced separation of two dust groups, namely of the smallest ($< 10^{-17}$ kg) and fairly large ($< 10^{-13}$ kg) particles [Mazets et al., 1986].

Another dust size distribution has been constructed too [Singh et al., 1992] that looks like

$$n(a)da = g_0 \left[1 - \frac{a_0}{a}\right]^M \left[\frac{a_0}{a}\right]^N, \quad a \geq a_0, \tag{2.4}$$

$$n(a)da = 0, \qquad a < a_0. \tag{2.5}$$

Here a_0 is the radius of the smallest grain (taken to be 0.1 μm), and g_0 is a normalization constant, with $N(=4.2)$ defining the slope of the largest grains (N plays the role of power law index for grains for which $a \gg a_0$), and $\log M = 1.13 + 0.62 \log r_{h\{AU\}}$.

It is commonly believed that comets were formed within the solar system from the same initial dust and gas nebula as were the larger bodies, such as the planets. But because of the small size of the comet, which implies the absence of large-scale mixing processes, one may expect that the isotopic, chemical and molecular characteristics of the presolar material are best preserved in comets. It were the mass spectrometers on board GIOTTO and the VEGA's that revealed the chemical properties of individual dust grains. Jessberger and Kissel [1991] conclude that Halley's comet is composed of two end-member components: a refractory organic phase (mostly low-mass elements like C, H, O, N, and therefore named *chondrites*) and a Mg-rich silicate phase. The CHON component is probably coating the silicate cores. However, because the experiments cannot be reproduced, the data must be interpreted cautiously and models with too far reaching consequences should be avoided.

The dust densities are given for distances up to 2×10^8 m, for the different mass channels ranging from 10^{-13} to 10^{-20} kg. The dust population consists mainly out of submicron grains, with number densities of the order of $10^{-3}\mathrm{m}^{-3}$ at a distance of 10^8m. Note that the first dust particles were detected by VEGA 1 at 260×10^6 m and by VEGA 2 at 320×10^6 m [Vaisberg et al., 1986].

Data of the ICE-flyby at P/Giacobini-Zinner were discussed by Boehnhardt and Fechtig [1987]. For silicate grains the equilibrium potentials vary between +6 and +10 V within the bow shock and outside the cometopause. Within the cometopause, these potentials are steadily decreasing to slightly negative numbers (-0.1 V), due to the high density of the low-energy plasma electrons. Carbon grains charge to a potential between +5 V and -19 V outside the cometopause. Inside of it, they quickly achieve negative potentials (-0.1 V). This paper discusses equally the Giotto flyby at P/Halley. Outside the cometopause, the grains are dominated by photoelectrons. Silicate grains charge in the range $6 - 10$ V, while carbon grains have an equilibrium potential of $4 - 5$ V. The spacecraft potentials are typically +7 V in the solar wind, reduce to about 2.5 V in the outer coma, and 1 V at closest approach [Grard et al., 1989]. It must be stressed as is discussed in chapter 5, that the numerical calculation of the equilibrium potential depends on a large amount of a large-range parameters.

Plasma characteristics

We can find plasma parameters from VEGA, GIOTTO and SUISEI in Grard et al. [1989], Amata et al. [1991] and Mukai et al. [1986], respectively, but only the GIOTTO spacecraft was the only one going through the entire cometosheath and the ionopause.

- The kinetic energy of the electrons, measured in the range 80×10^6–800×10^6 m, can only be given as a mean value 0.53 eV and 0.49 eV for VEGA-1 and 2 respectively [Grard et al., 1989], due to the large dispersion inherent to the diagnostic technique. This electron mean kinetic energy is not typical of the solar wind, where values 30 times larger are generally observed. After correction of spurious effects caused by photo-emission and nitrogen releases, the electron density for VEGA-1 has an average value of 60×10^6 m^{-3} at distances of 300×10^6–1000×10^6 m (roughly between the bow shock and the cometopause). In the same distance range, the VEGA-2 measurements give a density of 40×10^6 m^{-3}. Both spacecraft indicate an electron density of 10^9 m^{-3}, closer to the nucleus (16×10^6 m).
- Amata et al. [1991] consider four different plasma populations. Besides the electron population, a hot and a cold water group population and a proton population are recovered for distances between 10^8 and 10^9 m from the nucleus, which is inside the bow shock. The proton density is rather constant and assumed to be $20 - 30 \times 10^6$ m^{-3}, with a temperature of ≈ 35 eV. Also the high energy water group ions have a rather constant number density of $0.3 - 0.7 \times 10^6$ m^{-3}, and a temperature of ≈ 4.3 keV. The low energy water group population on the contrary changes considerably with the cometocentric distance. The number density at 10^8 m is of the order of 5×10^9m^{-3}, decreasing for larger distances to 10^6 m^{-3}. The energy for these cases are 1.7 keV and 80 eV respectively.
- In the plasma density inside and outside the bow shock an abrupt change of the plasma parameters occurred around 450×10^6 m away from the nucleus, which probably represents the bow-shock. Just after the bow-shock they recovered a density of 35×10^6 m^{-3}. At a distance of 10^9 m, a density of 15×10^6 m^{-3} was found [Mukai et al., 1986].

Environmental characteristics

The Giotto data for the magnetic field during the ionopause crossing of comet Halley, can be found in Neubauer [1991] (Figure 7). Outside the cometary ionopause (which separates the outflowing cometary ions from the inflowing, contaminated solar wind plasma), the plasma is magnetized ($B \approx 20\, nT$), while inside the ionopause the magnetic field vanishes. This interplanetary magnetic field varies near Earth's orbit from a few nanoteslas at quiet times to more than 10 to 20 nanoteslas accompanying solar disturbances [Parks, 1991].

The relative dust-plasma velocity is of the order of several meters per second to 100 ms^{-1} [Richter et al., 1991].

The photoelectron flux Γ is given by $\Gamma = \eta \times 2.5 \times 10^{14}\, r_{A.U.}^{-2}$, with $r_{A.U.}$ the distance grain-sun in astronomical units, and η the photoemission efficiency [Goertz, 1989].

2.3 Interplanetary dusty plasmas

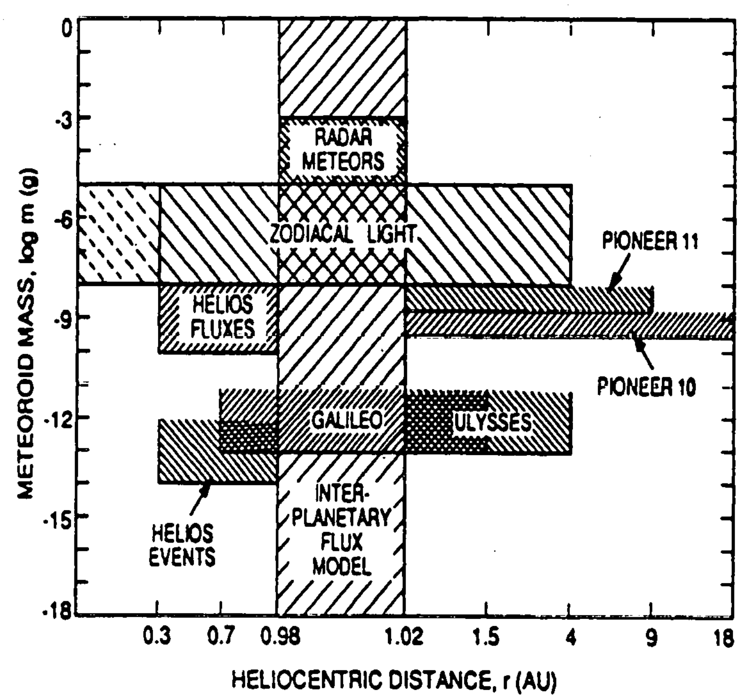

Figure 2.8: The coverage in mass and heliospheric distance for the data sets used. [Divine, 1993]

The dust population in interplanetary space has been studied intensively by a number of detection methods. Several models were worked out, but the most comprehensive one is given by Divine [1993]. He presents the most complete model for the interplanetary dust grains in the solar system. The coverage in mass and heliospheric distance is shown in Figure 2.8. In this paper the assumptions were made that solar gravitation is the only operative force, and that the system is symmetric both in ecliptic latitude and longitude. He proposes five distinct Keplerian dust populations to match successfully all data. They span ranges from 10^{-21} kg to 10^{-3} kg, in mass, and from < 0.1 AU to 20 AU in heliocentric distance. No time dependencies are considered, although for the submicron dust flux a 22-year cycle has been suggested [Grün et al. 1997].

Although we are going to follow the treatment of Divine [1993], recently some improvements were made by Grün et al. [1997]. They modified the Divine model to make it applicable to the complete Galileo and Ulysses data sets. Divine employs purely gravitational (Keplerian) dynamics to derive impact rates. However, for micron-sized dust Grün et al. [1997] added the effect of radiation pressure on the dynamics. They also added an interstellar dust population which penetrates the solar system on hyperbolic trajectories.

Dust characteristics

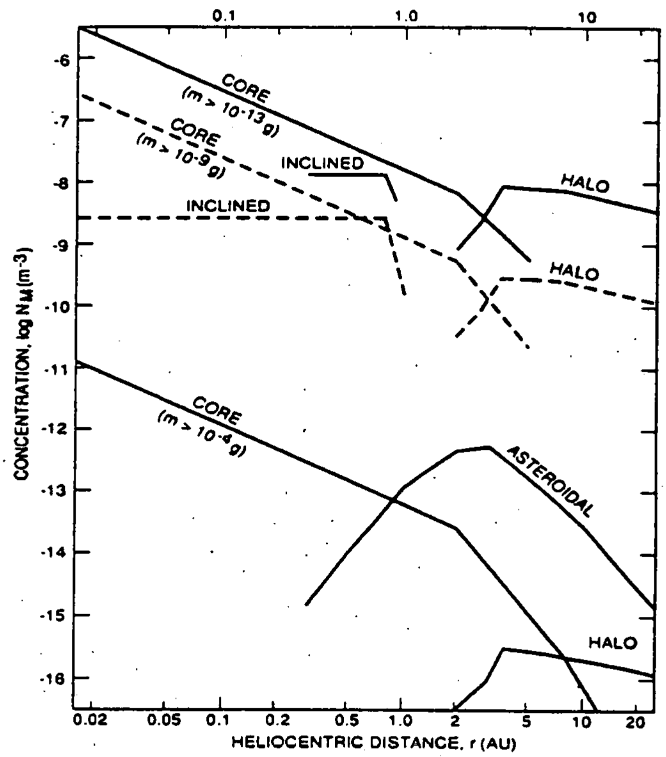

Figure 2.9: Cumulative number concentration as a function of heliocentric distance in the ecliptic plane at three mass thresholds. [Divine, 1993]

The relevant data sets are the following:

- Interplanetary flux model: The first knowledge of the properties of interplanetary dust grains comes from meteor and meteorite observations, as well as lunar cratering records and from impact detectors aboard several spacecraft orbiting the Earth. A review of the available data, was given by [Grün et al., 1985]. The threshold mass ranges from 10^{-21} to 0.1 kg, and the flux is presented as the average over a spinning flat plate.

- Pioneer 10 and Pioneer 11 Meteoroid Experiment: The data for the impact detectors aboard Pioneer 10 and Pioneer 11, are given by Humes [1980]. These data are represented as spin-averaged penetration fluxes, averaged over unequal intervals in heliospheric distance between 1 and 18 AU within 3.1° of the ecliptic plane for Pioneer 10, and 1 and 9 AU within 15° of the ecliptic plane for Pioneer 11. There were 95 penetrations recorded by Pioneer 10, and 87 penetrations by Pioneer 11.

- Helios data: Part of the available data on dust grain characteristics of the Helios space mission can be found in Grün et al. [1980]. The range between 0.31 and 0.98 AU is studied in the ecliptic plane, and the grain flux is given averaged over intervals of 0.1 AU.
- Galileo Dust Detector: These data are represented as spin-averaged penetration fluxes, averaged over unequal intervals in heliospheric distance between 0.88 and 2.3 AU in the ecliptic plane.
- Ulysses Dust Detector: These data are represented as spin-averaged penetration fluxes, averaged over unequal intervals in heliospheric distance between 1.0 and 5.4 AU, over a wide range of ecliptic latitudes $(-80°, 80°)$.
- Furthermore, there are radar observations and observation of zodiacal light in the range 0.3–4.0 AU.

The nature of the five populations proposed by Divine [1993] (core, eccentric, asteroidal, inclined and halo) can be seen in his figures 4-6. The dust density, mass and area concentration for the whole heliocentric range are given in Figure 2.9 and Figure 2.10. The dust number density for grains with sizes between [0.46 μm–10 μm] decreases roughly as an $1/r_h^2$-law for $r_h < 2AU$. The dust number density is of the order of 10^{-8} m^{-3} in the neighborhood of the Earth. For $r_h > 2AU$, the halo-population comes into play, and the power law is less steep.

Plasma characteristics

The plasma in the interplanetary medium is provided by the solar wind. Since the discovery of this plasma population by the spacecraft Lunik 2 and Lunik 3 in 1960, several models were proposed. It is known that the solar wind parameters are highly variable. However, we can assume that the electron, proton and helium ion densities for *low*, *average* and *high* solar activity are respectively given by $N_e = (0.4; 6.5; 100) \times 10^6$ m^{-3}, $N_p = (0.4; 6.2; 75) \times 10^6$ m^{-3} and $N_\alpha = (0; 0.3; 25) \times 10^6$ m^{-3} at 1 AU in the ecliptic plane [Mukai, 1981]. These densities decrease by an inverse square law with the heliocentric distance. The electron temperature can be taken to be $(5 \times 10^3; 2 \times 10^6; 10^6)$ K. This temperature will vary with the heliocentric distances according to a *powerlaw*†. The power index at high latitudes was measured by the Ulysses spacecraft ($q = 0.81 - 1.03$) [Goldstein et al., 1996], while $q = 1.22$ was used by Mukai [1981] in the ecliptic plane. The solar wind velocity is of the order of $(200 \times 10^3; 400 \times 10^3; 900 \times 10^3)$ ms^{-1}.

Environmental characteristics

The interplanetary magnetic field varies near Earth's orbit from a few nanoteslas at quiet times to more than 10 to 20 nanoteslas accompanying solar disturbances. The magnetic

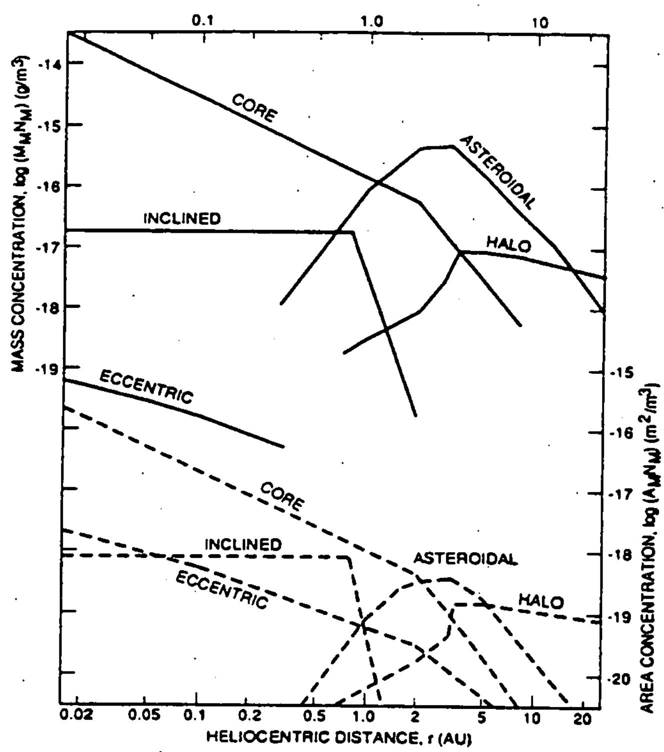

Figure 2.10: Mass (solid lines) and area (dashed lines) concentrations as functions of heliocentric distance in the ecliptic plane for the five populations. [Divine, 1993]

field can be considered to vary as $|\mathbf{B}| = 4.75 \times 10^{-9}\sqrt{(1 + r_{h\{AU\}}^2)/r_{h\{AU\}}^4}$ which is the expression given by the Parker spiral field model and recovered by the Voyager spacecraft [Burlaga et al., 1984]. The magnetic field for $r_{h\{AU\}} \gg 1$ will change as $r_{h\{AU\}}^{-1}$.

The photoelectron flux Γ is given by $\Gamma = \eta \times 2.5 \times 10^{14}\, r_{h\{AU\}}^{-2}$, and η the photoemission efficiency [Goertz, 1989].

2.4 Dusty plasmas in laboratories

2.4.1 Surface processing plasmas in RF-discharges

A RF-discharge plasma is weakly ionized: the density of the free electrons is typically 10^{15} m^{-3}, which makes up about 0.0001 % of the neutral density. The average electron energy is of the order of a few electronvolts (20 000-40 000 K), which is much higher than the energy of the neutrals ($\sim$ 300 K). For a typical RF discharge the driving frequency has a value between the ion and electron plasma frequency. This means that the electrons oscillate in the high frequency field, while the ions *feel* mainly the time averaged field. The plasma consist of distinct regions: a dark space near the electrodes, which is called *the* *sheath* and a radiating zone in the middle called *the plasma glow.* One of the major applications of RF-discharges involves the plasma-surface interactions. RF-discharges are very efficient sources for deposition of various layers, e.g. amorphous silicon in the fabrication of solar cells, transistors and color televisions, carbon layers used as antireflection and/or protective coatings and hard coatings. Furthermore, the plasma chemistry in combination with the high energy ions allows for anisotropic etching of different substrates. This kind of etching allows to produce narrow and deep structures, which cannot be obtained by wet chemical etching [Stoffels and Stoffels, 1994].

In these RF-discharges, macroscopic dust particles were produced. In the beginning, these dust grains were solely considered harmful, as they contaminated the substrate, and therefore the dusty research aimed at avoiding the particle formation and/or contamination. The formation of macroscopic clusters in surface processing plasmas was first reported in 1986. Since then this field has been rapidly evolving [Stoffels and Stoffels, 1994].

An important source of small dust particles are the reactor and substrate surface. The negative charge on the particles is responsible for their trapping in the positive plasma glow. The trapped particles will grow and coalescence producing cauliflower like grains [Stoffels and Stoffels, 1994].

Despite the extensive precautions, such as clean rooms, and sophisticated handling procedures in order to avoid processed wafer contamination by dust, particle formation and/or trapping, leads to pollution effects. Indeed, particles can be formed from wafer material, and hence improvement of the quality of the vacuum, does not prevent nucleation and growth of dust particle in the clean room. The greatest fraction of yield killing contaminants land on the wafer not during handling in the ambient atmosphere of the clean room, but under vacuum conditions during plasma processing [Daryanani, 1996].

2.4.2 Dust charging experiments

Although a lot of work has been done on the charging mechanism of dust grains from a theoretical point of view, there have been only a few experimental efforts [Hazelton and Yadlowsky, 1994], [Walch et al., 1994], [Barkan et al., 1994], [Walsh et al., 1995]. The plasma parameters for the experiment described in the last three publications are:

$$\begin{aligned} \kappa T_e &= 0.2 - 5\text{eV}, \\ n_i &= 10^{11} - 10^{16}\text{m}^{-3}. \end{aligned}$$

The dust grains in this experiment are made of silicon, graphite (low secondary emission coefficient), cupper (metallic conductor) and glass (high secondary emission coefficient). The mean value of the size distribution of the grains is situated in the range $(1 - 125\mu\text{m})$. The dust density was low enough, so the grains could be considered as not interacting and the number density of the dust was not specified. Only in Barkan et al. [1994], a value of $N_d = 10^{10}\text{m}^{-3}$ was used.

Experiments on wave phenomena were described by Barkan et al. [1995, 1996].

The effect of closely packed grains on the charging can be found in [Xu et al., 1993], for

$$\kappa T_e = 0.2\text{eV},$$
$$n_i = 10^{13}\text{m}^{-3}.$$

and for $\sim 1\mu$m and $\sim 50\mu$m kaolin, and aluminum oxide with nominal sizes of 0.3 μm and 0.01μm.

2.4.3 Dusty crystals

Hiroyuki Ikezi considered a system of dust grains embedded in a plasma [Ikezi, 1986]. He predicted that the system crystallizes when the nearest-neighbor potential energy of the grains is large compared to the grain's thermal energy, as can be accomplished by using large particles and cooling them by drag on a neutral gas background. The dusty plasma crystal itself is formed in the sheath of the RF-discharge because there the electric field can balance the gravity force of the grains. The modeling of a dusty plasma in a RF-discharge becomes a complicated task, because of the alternating currents involved. Some experimental setups were built, and in all of them Coulomb lattices were formed with lattice constants of the order of 10^{-4} m.

- **Max-planck-Institut für Extraterrestrische Physik, Garching, Germany**

  This experiment was described by Thomas et al. [1994]. They use 7.0 μm diameter melamine/formaldehyde spheres embedded in a weakly ionized plasma generated by a RF-discharge. Based on frame-by-frame measurements of the mean particle velocity, the particle kinetic temperature was estimated as $T_d = 310$ K, which is close to room temperature. Furthermore, $\kappa T_e = 3 \pm 1$ eV, and the plasma density $N_0 = 10^{15}$ m^{-3}. Using these parameters and an appropriate charging theory will lead to equilibrium charges of $-9.8 \times 10^3 e \geq Q_d \geq -27.3 \times 10^3 e$.

- **Department of physics, National Central University, Chungli, Taiwan, Republic of China**

  In the experiment [Chu and I, 1994; I et al., 1996], micrometer-sized (a few microns to hundreds of microns) SiO_2 particles are used in a RF-discharge with plasma densities of the order of $N_0 = 1 - 10 \times 10^{15}$ m^{-3}.

- **Institut für Experimentalphysik, Cristian-Albrechts-Universität Kiel, Germany**

  In the experiment, described by Meltzer et al. [1994] TIO_2 particles are used, with a size up to 30 μm and later highly monodispersive melamin formaldehyde particles of diameter $a = 9.4 \pm 0.3\mu$m. They reach a dust density of $N_d = 10^9 - 10^{10}$ m^{-3} and a plasma density of $N_0 = 2 - 5 \times 10^{14}$ m^{-3}.

Glossary

- *albedo* — Fraction of the total incident light reflected by a spherical body. Bolometric Bond albedo refers to the reflectivity over all wavelengths.

- *ansa* — Portion of the ring that appears farthest from the disk of a planet.

- *backscattering:* — Situation where most of the incident light is scattered in low *phase angles.* This means that most of the ring material consists of super micron sized grains, and there is only a low dust fraction present.

- *fluence:* — The time integral of the flux, including missing data. (in m^{-2})

- *forward scattering:* — Situation where most of the incident light is scattered in high *phase angles.* This means that most of the ring material consists of micron sized grains and smaller. The dust fraction is high.

- *synchronous orbit* — The *synchronous orbit* of a planet is defined as the orbit for which the Keplerian angular velocity $\sqrt{GM_P/R^3}$ (with G, M_P and R, the gravitational constant, the mass and distance from the planet's center respectively) equals the rotation angular velocity of the planet Ω_P. At this distance, dust grains and plasma rotate with the same angular velocity.

- *optical depth:* — The intensity of light passing through a medium consisting of a field of particles decreases exponentially with distance through the medium. The depth of penetration into the medium can be expressed in terms of the number of factors of e of diminishment. That number is called the *optical depth.* The number of factors of e of diminishment through the entire medium is called the *optical thickness.* Strictly speaking, optical thickness depends on the direction of propagation relative to the normal to the surface. In practice the term optical thickness is often used synonymously with *normal optical thickness.*

- *optical thickness:* — see *optical depth.*

- *phase angle:* — The angle between the sun, the object (i.e. rings) and the observer (i.e. the camera)

- *Poynting-Robertson drag:* A loss of orbital angular momentum by orbiting particles associated with their absorption and reemission of solar radiation
- *power law:* A way to describe the grain size distribution, which is used throughout this chapter is the 4 parameter power law $n_d(a)\, da = C\, a^{-q}\, da$ in a restricted radius domain $[a_{min}, a_{max}]$. Here $n_d(a)\, da$ denotes the number of grains with a radius within $(a, a + da)$ per unit volume, q is the power law index and C a normalization constant.

Chapter 3

Detection methods

A new method for the detection of dust grains is proposed in **section 2** of this chapter. In order to give a realistic view on the relevance of this method, a short description of existing in situ dust detection methods is given in **section 1**.

3.1 Existing in situ detection methods

3.1.1 Pick-up of the ionization signal by electric antennae

This technique proposed by Gurnett et al. [1983] and Aubier et al. [1983] has been used to analyze data in the ring plane passage of Jupiter, Saturn [Meyer-Vernet et al., 1996], [Tsintikidis et al., 1994], Uranus and Neptune for the Voyager missions and during the ICE flyby of P/Giacobini-Zinner [Gurnett et al., 1986].

When a dust grain with mass m strikes a spacecraft at a relative velocity larger than a few kilometers per second, the grain is instantly vaporized together with a part of the target material, and heated to a temperature higher than 10^5K (Figure 3.1). A small, partially ionized cloud of gas (with an overall charge $Q(m)$ larger than the initial charge before impact) is produced, expanding outwardly from the point of impact. Initially this cloud is collision-dominated. But when the density of the expanding cloud decreases, a point is reached where collisions are no longer dominant. At this point, recombination ceases and the residual ionization escapes as an expanding cloud of plasma, picked up by the antenna. When we invert the relation $Q(m)$, the mass of the impacting particle can be obtained from the signal recorded by the antenna receiver (*ionization signal*). In this way the local dust number density and mass distribution of a dusty environment can be obtained.

The determination of the amplitude of the ionization signal is very complex. As indicated by Meyer-Vernet et al. [1996], the charge released by a dust grain bombarding a

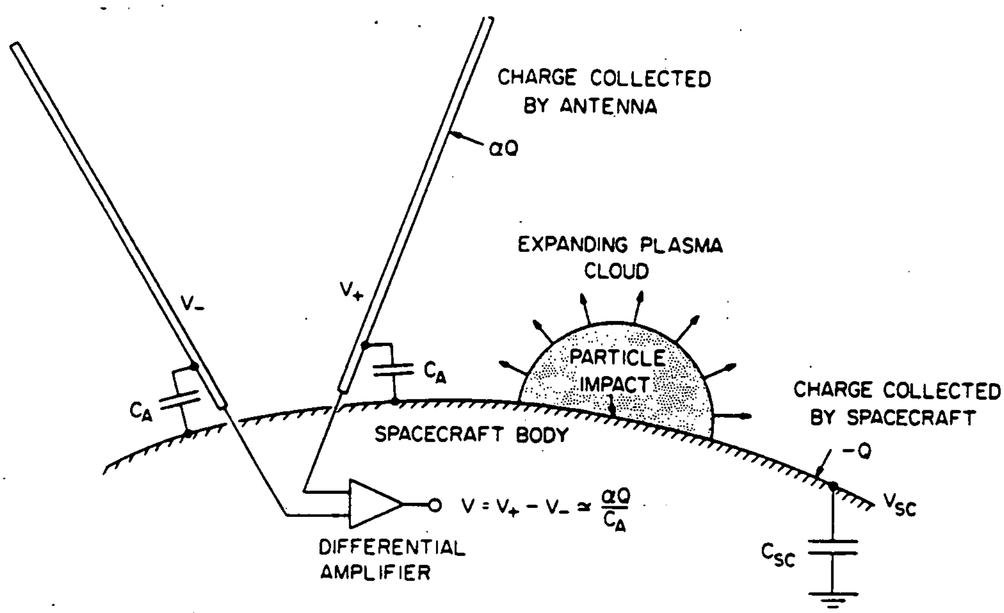

Figure 3.1: Detecting dust grains by means of impact ionization [Gurnett et al., 1983]

spacecraft has not a simple proportionality. Although a lot of work is done in calibration measurements for the direct impact dust detectors, $Q(m)$ is not easy to assess since little is known about the composition and surface state of the dust particles in the space plasma environments we have in mind. The released charge as a function of the mass of the impacting particle for silicate, carbon and iron grains was given for different impact velocities by Göller and Grün [1989]. For realistic velocities, $Q(m)$ is proportional to the grain mass and only weakly dependent on the incidence angle, and we assume that it obeys the relation:

$$Q_{\{\mathrm{C}\}}(m) \approx 10^3 m_{\{\mathrm{kg}\}}. \tag{3.1}$$

The maximum amplitude of the signal is then given by $\Delta_{ION\{V\}} = 10^3 m_{\{\mathrm{kg}\}}/C_{\{\mathrm{F}\}}$, with C denoting the antenna capacitance. As stated by Tsintikidis et al. [1994] and Meyer-Vernet et al. [1996], the value of Δ_{ION} is an upper bound. We can expect that only a fraction α of the dust cloud will be collected. Indeed, the antenna surface is small, and hence most of the released charge will not get collected by it. For a dipole antenna, where the voltage is measured by the difference between two antenna arms, we may expect that $\alpha \ll 1$. The derivation of the parameter α is by no means an easy task and can only be carried out statistically if enough events are available, because it depends highly on the place of impact. However, for a monopole configuration, where the voltage between spacecraft and antenna is measured, α will be close to the upper bound 1, because the spacecraft body can be a very efficient collector of charge, since the plasma is formed very near to its surface. We may conclude that the monopole configuration is preferable, because the resulting signal is much larger and easier to interpret. As we shall see in section 3.2, the dipole configuration has other and new possibilities for the detection of dust grains.

3.1.2 Impact ionization detector

The impact ionization detector detects individual particles impacting on the sensor and measures their mass, impact speed and electric charge. Although people were building dust detectors based on impact ionization already in the early 1970s for the Pioneer spacecraft, in this section we describe briefly the latest generation of detectors on board the Galileo/Ulysses spacecraft [Grün et al., 1992] (Figure 3.2).

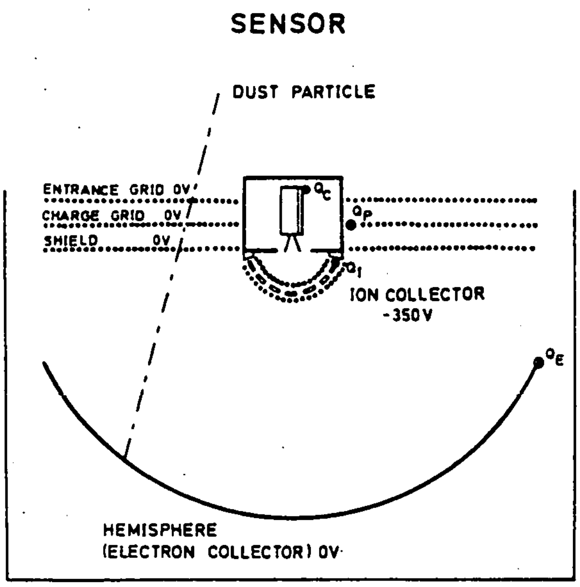

Figure 3.2: Detecting dust grains by means of the direct impact detector [Grün et al., 1992]

Positively or negatively charged particles entering the sensor are first detected via the charge which they induce on the charge grid while flying between the entrance and shield grids. All dust particles — charged or uncharged — are detected by the ionization they produce during the impact on the hemispherical impact sensor. After separation by an electric field, the ions and electrons of the plasma are accumulated by charge sensitive amplifiers, thus delivering two coincident pulses of opposite polarity. The rise times of the pulses, which are independent of the particle mass, decrease with increasing particle speed. From both the pulse heights and rise times, the mass and impact speed of the dust particle are derived by using empirical correlations between these four quantities.

The sensor consists of a grid system for the measurement of the particle charge, an electrically grounded target (hemisphere) and a negatively biased ion collector. A charged dust particle entering the sensor will induce a charge to the charge grid, which is connected to a charge sensitive amplifier. The output voltage of this amplifier rises until the particle passes this grid, and falls off to zero when it reaches the shield grid. The peak value (Q_p) is stored for a maximum of 600 microseconds and is only processed if an impact is detected by the impact ionization detector within this time. A dust particle hitting the hemispherical target produces electrons and ions, which are separated by the electric field between the hemisphere and ion collector into negative charges (electrons and negative ions) and positive ions. The negative charges are collected at the hemisphere and measured by a charge sensitive amplifier (Q_e). Positive ions are collected and measured at the negatively biased ion collector with a charge sensitive amplifier (Q_i). Some of the ions penetrate the ion collector, which is partly transparent (total transmission approximately 40 %), are further accelerated, and hit the entrance cone of an electron multiplier (channeltron). Secondary electrons are produced, amplified, and measured by a charge sensitive amplifier (Q_c). Other quantities measured are the rise times of both the positive and negative charge pulses (Q_i and Q_e). The measurement of the time delay between electron pulse and ion pulse serves as a means for distinguishing impact events from noise. Impact events have time delays of 2-50 microseconds, while mechanical noise has a time delay of milliseconds. These signal amplitudes and times of a single recorded event are digitized and stored in an Experiment Data Frame.

This detector neither determines the chemical composition nor the impact angle of an impinging particle, and therefore calibration can be carried out by averaging over impact angle and an assumed compositional distribution. This introduces uncertainties of factors 1.6 for impact speed, and 6 for the grain mass. These kind of uncertainties are connected with the detection process itself, and cannot be ruled out by building a better instrument [Göller and Grün, 1989]. For the Galileo/Ulysses dust detectors, there is an additional problem in getting the charge of the dust grains and no reliable dust grain charge data are available [Landgraf, personal communciation, 1996].

3.2 The radio dust analyzer (RDA)

Recently, Meuris et al. [1996] proposed a new technique to derive dust grain characteristics with the help of a simple wire dipole antenna, elaborating on earlier results [Lesceux et al. 1996]. Charged dust grains passing by the antenna induce an electric potential change for the time of the flyby. This dust-detection technique has been called the Radio Dust Analyzer (RDA). The induced "waveforms", called the *RDA signals*, are studied as a function of the characteristics of the dust grain (its charge and velocity vector) and the plasma parameters. The amplitude of the noises due to flyby, emission and impacts of the ambient plasma electrons is compared with the expected amplitude of the RDA-signal. In order to use the method, the noise levels must be at least an order of magnitude smaller. Furthermore the ionization signal which is produced when a dust grain strikes the spacecraft will be larger but less frequent than the RDA-signal and therefore the event rates of both signals play a crucial role.

3.2.1 Magnitude of the signals

RDA signal

We consider a maxwellian two-component plasma, with electron and ion temperature $T_e = T_i = T$ and plasma density N. The electron Debye length is given by

$$\lambda_D^2 = \frac{\varepsilon_0 \kappa T}{N e^2}, \tag{3.2}$$

where ε_0 is the vacuum permittivity and κ is Boltzmann's constant. A spherical dust grain with radius $a \ll \lambda_D$ and scalar velocity v embedded in the plasma acquires an equilibrium charge Q, given by the standard charging model (Section 4.2.1). In all cases of practical interest, the velocity satisfies $v \ll c_{se}$ ($c_{s\alpha}$ denotes the thermal velocity of species α), so that the electrons contribute fully to the shielding. When $c_{si} \ll v \ll c_{se}$, the ions do not contribute at all and the relevant Debye length is λ_D (this would remain true when v is of order of magnitude c_{si} provided that $T_e \ll T_i$). If, on the other hand $v \ll c_{si} \ll c_{se}$, the ions and electrons fully shield the charge and the relevant Debye length becomes $\lambda_D/\sqrt{2}$. In intermediate cases, the plasma temporal dispersion cannot be neglected and the problem is more complicated. The grain charge is taken to be constant, because the charge variation timescale is much larger than the dust signature width. The well-known Debye-shielded potential around one single dust grain is then given by

$$\Phi(r) = \Phi_0 \frac{a}{r} e^{-(r-a)/\lambda_D}, \tag{3.3}$$

$$\Phi_0 = \Phi(a) = \frac{Q}{4\pi\varepsilon_0 a}, \tag{3.4}$$

keeping in mind that when $v \ll c_{si}$, λ_D must be replaced by $\lambda_D/\sqrt{2}$ and that we have implicitly assumed linear shielding, i.e., $\Phi(r) \ll \kappa T/e$, which is always satisfied in practice.

We consider a Cartesian (x, y, z) frame and a wire dipole antenna (with radius r_a) positioned along the z axis, with the two arms (each arm with length L) meeting each other in the origin (Figure 3.3). For the calculations presented here, the opening angle between the two antenna arms is $\alpha = 180°$, but an analogous reasoning can be held for other α-values as we will see later on. Furthermore we assume that the response time of the receiver antenna system is much smaller than the dust flyby time, and that the antenna is thin enough ($r_a \ll L$ and $r_a \ll \lambda_D$). The dust signature width has a value intermediate between the time for a grain moving parallel to the antenna $(L + \lambda_D)/v$ and that for a grain moving perpendicular to the antenna (λ_D/v).

The orbit of a dust grain in uniform motion is given by

$$x(t) = x_0 + v\ \sin(\theta)\cos(\varphi + \varphi_0)\ t \tag{3.5}$$

$$y(t) = y_0 + v\ \sin(\theta)\sin(\varphi + \varphi_0)\ t \tag{3.6}$$

$$z(t) = z_0 + v\ \cos(\theta)\ t, \tag{3.7}$$

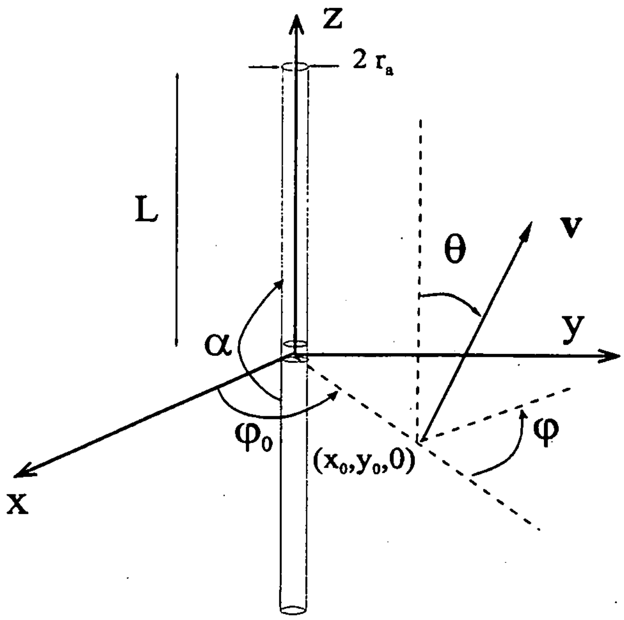

Figure 3.3: Antenna geometry of a wire dipole antenna and the coordinates used.

where (v, θ, φ) are the spherical coordinates of the velocity of the grain relative to the antenna, as indicated in Figure 3.3.

The potential at a point (x, y, z) on the antenna is given by

$$\Phi[x, y, z, t] = \frac{a}{R}\,\Phi_0\, e^{-\frac{R}{\lambda_D}}, \tag{3.8}$$

with

$$R = \sqrt{[x(t) - x]^2 + [y(t) - y]^2 + [z(t) - z]^2}. \tag{3.9}$$

The voltage measured by a wire dipole antenna is the difference between the voltages averaged over each arm; hence the antenna response is

$$\Delta\Phi(t) = \frac{1}{L}\int_{-L}^{0} \Phi[0, 0, z, t]dz - \frac{1}{L}\int_{0}^{L} \Phi[0, 0, z, t]dz. \tag{3.10}$$

According to (3.10), the antenna response $\Delta\Phi(t)$ is proportional to $\Phi_0 \times a$ and hence to Q. We introduce the shape function

$$\xi(t) = \frac{\Delta\Phi(t)}{a\Phi_0}, \tag{3.11}$$

with dimensions m^{-1}. The problem depends on the six geometrical parameters v, θ, φ, φ_0, $r_0 = \sqrt{x_0^2 + y_0^2}$, z_0 of the grain's orbit. Changing φ_0 will not change the antenna response due to the cylindrical symmetry. Since v is only present in the expression $v \times t$, changing v will only stretch the timescale and will not change the shape of the shape function. When we take $t = 0$ when $z = 0$, there are just three parameters left to determine the shape: θ, φ, and r_0.

Given a response profile, it is theoretically possible to fit the parameters v, θ, φ, r_0, and $\Phi_0 \times a \propto Q$. Furthermore, in most of the cases we already know the direction of the dust-antenna velocity and even its magnitude. In that case the problem becomes a fit for r_0, φ, and $\Phi_0 \times a \propto Q$. Here we are only giving some indications of the relations between the features of the waveform and the values of those parameters. The results might be generalized to a more complex antenna system (triple or quadrupole), in order to refine the diagnostics.

In Figure 3.4 the shape function for a grain moving parallel to the antenna is shown for different antenna lengths. Increasing the antenna length increases the width of the signal, as expected. We see that for long antenna lengths ($L \gg \lambda_D$), the maximum value of the signal (detected only by one arm) can be found at $|v \times t| \approx L/2$. When the antenna length gets smaller the maximum is recovered near $|v \times t| \geq L/2$. The response reaches a maximum for a specific antenna length in the neighborhood of $L = 3$m, for this particular choice of grain orbits.

Figure 3.5 shows the influence of the Debye length for a grain moving parallel to the antenna. It is readily understood that the regime where $\lambda_D \ll r_0$ gives no response at all, because of Debye shielding of the grain charge. However, when we increase the Debye length, the maximum response increases and eventually reaches a constant value.

Figure 3.6 shows the influence of the orbit's orientation with θ in the first quadrant. For θ in the other quadrants, these results can be used by taking into account the transformations $\theta \rightarrow \theta + \pi \Leftrightarrow t \rightarrow -t$ and $\theta \rightarrow \pi - \theta \Leftrightarrow \xi(t) \rightarrow -\xi(t)$. The influence of φ is shown in Figure 3.7 with values taken in the first quadrant.

Figure 3.8 shows the influence of r_0. When $r_0 \gg \lambda_D$, the antenna response becomes very small.

The practical use of antennae as a grain detector has several limitations: first of all, the random voltage induced by the plasma particles passing near the antenna and secondly the random voltage induced on the antenna by particle impacts and/or emissions. Both noises have to be smaller than the dust signal for it to be detectable.

3.2.2 Noise levels

Noise level due to plasma particle flyby

Together with the grain signature on the antenna we would expect a contribution $\Phi_P(t)$ due to the flyby of the plasma particles. Owing to the nonzero time constant of the receiver, the antenna does not "see" individual electrons but a mean over a large number of passages. The signal produced by a single flyby for a plasma particle of velocity $\mathbf{v}$ is an odd function of $\mathbf{v}$. The average of such a signal over a Maxwellian distribution yields $< \Phi_P(t) >= 0$.

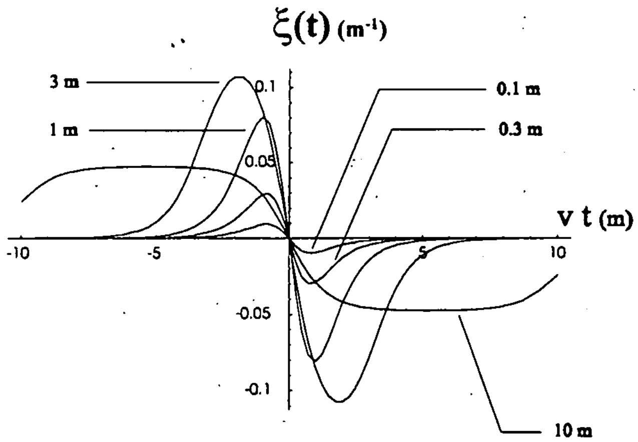

Figure 3.4: Antenna response for a grain moving parallel to the antenna as a function of $v\,t$ for different antenna lengths, Here r_0=1.41 m, λ_d=1m.

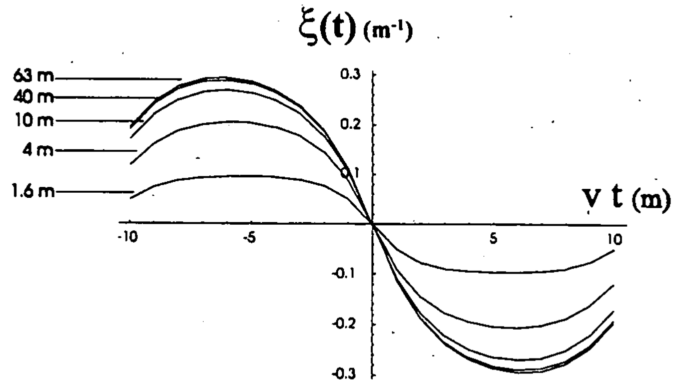

Figure 3.5: Antenna response for a grain moving parallel the antenna as a function of $v\,t$ for different Debye lengths. Here r_0=1.41 m, L=10m.

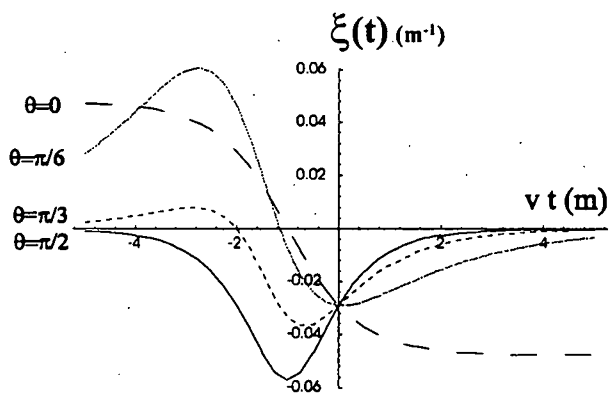

Figure 3.6: Antenna response as a function of $v\,t$ for different θ. Here r_0=1.41 m, ϕ=−π/4, L=10 m, λ_d=1m.

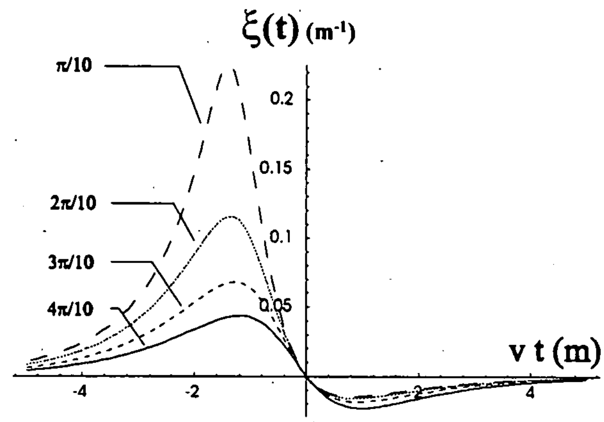

Figure 3.7: Antenna response as a function of $v\,t$ for different ϕ. Here r_0=1.41 m, θ=π/2, L=10 m, λ_d=1m.

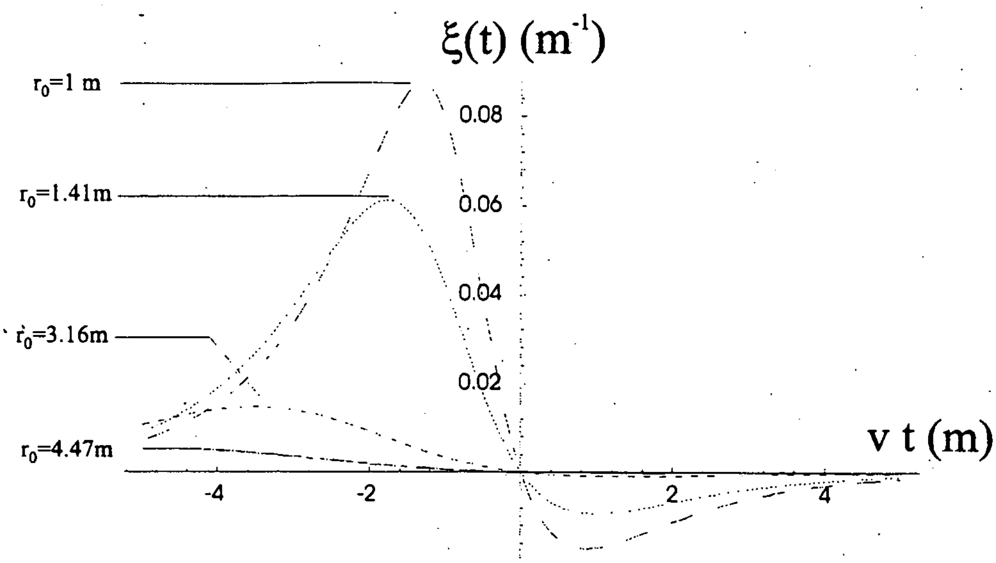

Figure 3.8: Antenna response as a function of vt for different r_0. Here $\varphi = -\pi/4, \theta = \pi/4, L = 10\text{m}, \lambda_D = 1\text{m}$.

So we calculate the variance $< \Phi_P^2(t) >$, given for Maxwellian electrons and ions, by Meyer-Vernet and Perche [1989]

$$< \Phi_P^2(t) >= \int_0^\infty < \Phi_P^2(f) > df, \tag{3.12}$$

where $\Phi_P^2(f)$ is the noise spectral density:

$$< \Phi_P^2(f) > = 4\kappa T \, Re(Z), \tag{3.13}$$

$$Z = \frac{4i}{\pi^2 \varepsilon_0 \omega} \int_0^\infty \frac{F(k)}{\varepsilon_L(k,\omega)} dk, \tag{3.14}$$

$$F(k) = \frac{1}{32\pi} \int |\mathbf{k} \cdot \mathbf{J}(\mathbf{k})|^2 d\Omega \tag{3.15}$$

$$= \frac{\text{Si}(kL)}{kL} - \frac{\text{Si}(2kL)}{2kL} - \frac{2\sin^4(kL/2)}{k^2L^2}. \tag{3.16}$$

Here ε_L is the longitudinal permittivity, ε_0 is the vacuum permittivity and Z is the antenna impedance. Si denotes the sine integral function. In (3.15) the integration is over the direction of $\mathbf{k}$.

To evaluate these integrals, we assumed a linear current distribution:

$$\mathbf{J}(\mathbf{k}) = \frac{4}{k_z^2 L} \sin^2(k_z L/2)[J_0(k_r r_a)]\mathbf{e_z}, \tag{3.17}$$

with $k^2 = k_z^2 + k_r^2$. The noise variance is then given (for $r_a \ll L$ and $r_a \ll \lambda_D$):

$$< \Phi_P^2(t) >= \frac{4\kappa T}{\pi^2 \varepsilon_0} \int_0^\infty \frac{F(k)}{1 + k^2\lambda_D^2/2} dk. \tag{3.18}$$

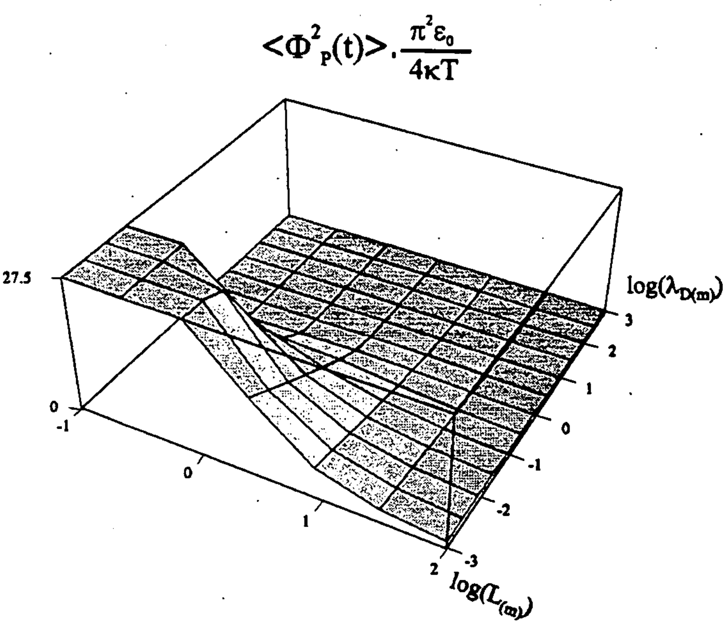

Figure 3.9: Normalized noise variance due to plasma particles flyby, as a function of the antenna length and Debye length, T being constant.

Unlike the case of a spherical dipole antenna, evaluating this integral analytically is not easy. We restrict ourselves to a numerical evaluation of (3.18). With the help of a change of variables $y = k\lambda_D/\sqrt{2}$, the noise variance due to plasma particle flyby can be put in the form

$$< \Phi_P^2(t) >= \frac{4\sqrt{2}\kappa T}{\pi^2 \varepsilon_0 \lambda_D}\, G(L/\lambda_D). \tag{3.19}$$

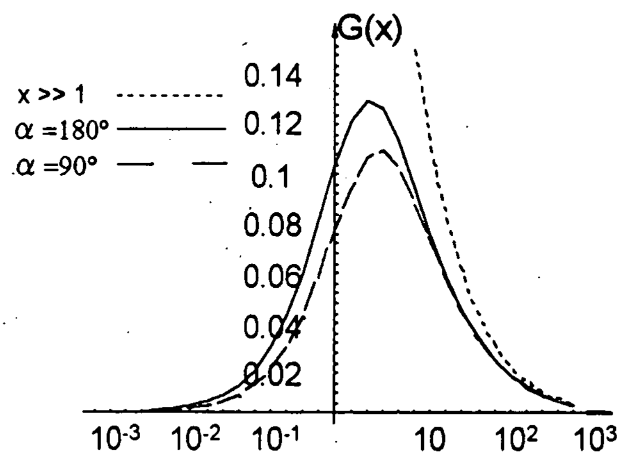

Figure 3.10: Plot of the function $G(x)$ in full line. The dashed line indicates the analytical result for $x \gg 1$.

Figure 3.9 shows the normalized noise as a function of L and λ_D. The effect of the antenna length is illustrated in Figure 3.10, which shows the function $G(x)$ for parallel as well as for perpendicular dipole antennas. The response of a wire dipole antenna reaches a maximum for wave vectors satisfying $k_z \approx 3/L$. This results in a variance that reaches a maximum for a specific antenna length L_M, given by the maximum of the function $G(x)$ located at $L_M = 2.74\ \lambda_D$.

The analytical result for the case $\lambda_D \ll L$,

$$< \Phi_P^2(t) >= \frac{\kappa T}{\pi \varepsilon_0 L} \ln(\sqrt{2}L/\lambda_D), \tag{3.20}$$

is shown in Figure 3.10 as a dashed line.

Increasing the Debye length decreases the noise. Indeed, when the Debye length increases, three phenomena occur. The timescale for a single plasma particle flyby and the number of relevant plasma particles both increase because of the bigger Debye sphere around the particle. However, the amplitude of the mean plasma particle signal decreases. This is due to the decrease of the average magnitude of the responses, which is proportional to the inverse of the mean distance of the flyby's, given by the Debye length.

Noise level due to plasma particle impacts or emissions

If the antenna is not meshed, it can collect or emit particles, which gives rise to a noise $\Phi_{i/e}(t)$. In general, the problem is very complicated [Calder and Laframboise, 1985]. The number of impacts or emissions cannot be determined exactly, because it depends on the unknown floating potential and surface state of the antenna. However, an order of magnitude of the resulting noise variance can be calculated as follows.

One event, i.e., one electron impact (or emission), on one antenna arm produces the voltage maximum amplitude given by $[e/(2C)]^2$, where C stands for the capacitance of the antenna given by

$$C = \frac{\pi \varepsilon_0 L}{\ln(\lambda_D/r_a)}. \tag{3.21}$$

This voltage squared has to be multiplied by the number of events per time unit and by a typical timescale in order to obtain the variance. The number of events per time unit is given by $2I_e/e$, where I_e stands for the electron current to the antenna. The factor 2 takes into account the return current.

Indeed, the equilibrium potential is a result of the balance ($|I_p|+|I_i|=|I_e|$) between electron, ion and photoelectron currents, I_e, I_i and I_p respectively, so that the number of events ($|I_e|+|I_i|+|I_p|)/e$ can be simplified to $2|I_e|/e$.

A typical timescale is the decay time of the signal given by $\tau = RC$. Since the antenna is not meshed, the resistance R is mainly due to the dc current. In order of magnitude, this dc resistance R_{dc} is given by the inverse of the derivative of the dc current on the antenna:

$$\frac{1}{R_{dc}} \approx \left|\frac{dI}{d\Phi}\right| \approx \frac{I_e e}{\kappa T_{eff}}. \tag{3.22}$$

For a negative antenna potential, only the direct plasma current contributes to R_{dc} and $T_{eff} = T$, while for a positive antenna potential, the photoelectron current contributes and the order of magnitude of the effective temperature is then given by $1/T_{eff} = 1/T + 1/T_p$, where T_p is the temperature of the photoelectrons ($\sim$ 1 eV) [Goertz, 1989].

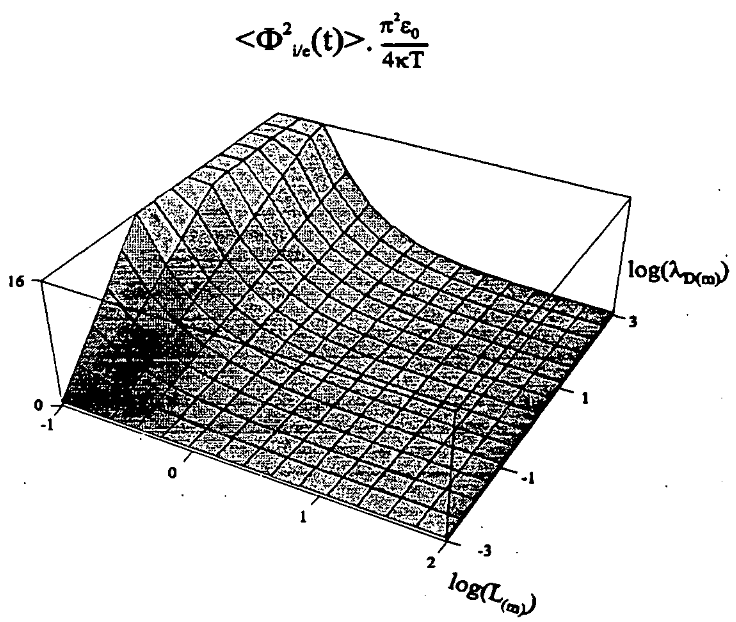

Figure 3.11: Normalized noise variance due to plasma particles impact and/or emission, as a function of the antenna length and Debye length, T being constant.

Hence the order of magnitude of the noise variance is given by

$$\begin{aligned} < \Phi^2_{i/e}(t) > &\approx \left(\frac{e}{2C}\right)^2 \frac{2I_e}{e} C \frac{\kappa T_{eff}}{eI_e} \\ &= \frac{\kappa T_{eff}}{2C} \\ &= \frac{\kappa T_{eff} \ln(\lambda_D/r_a)}{2\pi\varepsilon_0 L}. \end{aligned} \tag{3.23}$$

Figure 3.11 shows this noise level as a function of L and λ_D.

3.2.3 Case studies

To be able to detect grains with RDA, the grain signal has to be larger than the noise levels. Also, for the response to be detectable, the signal should be larger than the sensitivity of the receiver. The first condition gives a minimum detectable grain size:

$$a_m = \frac{\mathrm{Max}\left[\sqrt{< \Phi^2_{i/e}(t) >}, \sqrt{< \Phi^2_P(t) >}\right]}{\xi_M \Phi_0}, \tag{3.24}$$

ξ_M being the maximum value of the shape function for a typical grain flyby (at a distance $r_0 = \lambda_D$, for $\theta = \varphi = \pi/4$). The second condition gives the sensitivity needed to detect the smallest detectable grains:

$$\Delta\Phi_s = a_m \, \Phi_0 \, \xi_M \tag{3.25}$$

$$= \text{Max}\left[\sqrt{< \Phi_{i/e}^2(t) >}\sqrt{< \Phi_P^2(t) >}\right]. \tag{3.26}$$

The number of detectable events per time unit is given by $R_{RDA} = vN_dS$, where N_d denotes the number density of detectable grains and S is the cross section of the detector. The latter is given by

$$S = 4\,\lambda_D\,[\lambda_D\pi\cos\theta + L\sin\theta]\,. \tag{3.27}$$

	Case 1 ROSETTA	Case 2 ROSETTA	Case 3 WIND	Case 4 CASSINI	Case 5 VOYAGER
λ_D, m	10	0.1	7.5	10	5
T, K	100×10^3	100	100×10^3	100×10^3	100×10^3
Φ_0, V	10	10	7.5	-20	-10
N_d, m^{-3}	$10^{-5}(a)$	$3 \times 10^{-2}(a)$	$1.5 \times 10^{-14}(b)$	–	–
v, $\mathrm{m\,s}^{-1}$	100	100	20×10^3	10×10^3	14×10^3
L, m	5	5	40	10	10
r_a, m	1.0×10^{-3}	1.0×10^{-3}	2.0×10^{-3}	14×10^{-3}	6.3×10^{-3}
S_{RDA}, m^2	1.1×10^3	2.0	1.4×10^3	1.2×10^3	180
ξ_M, m^{-1}	0.03	0.2	0.04	0.1	0.03
$\sqrt{< \Phi_{i/e}^2(t) >}$, V	70×10^{-6}	5×10^{-6}	20×10^{-6}	40×10^{-6}	40×10^{-6}
$\sqrt{< \Phi_P^2(t) >}$, V	20×10^{-6}	6×10^{-6}	40×10^{-6}	30×10^{-6}	40×10^{-6}
a_m, (μm)	250	3	150	20	130
$\Delta\Phi_s$, μ V	70	6	40	40	40
R_{RDA}, s^{-1}	1	6	4×10^{-7}	$12 \times 10^6\,N_d$	$2.5 \times 10^6\,N_d$

Table 3.1: The equivalent cross section of the detector (S), the noise levels, the minimum detectable grain radius (a_m), the minimum antenna sensitivity required to detect the smallest detectable grains ($\Delta\Phi_s$) and the event rate (R_{RDA}) given for different types of environments, with typical plasma (λ_D, T), grain (Φ_0, N_d, v) and antenna (L, r_a) parameters. The value of ξ_{max} is given for a grain flyby at a distance $r_0 = \lambda_D$, for $\theta = \varphi = \pi/4$ except for case 5 where the direction of the grains is known. Case 1, Cometary environment, outside the contact surface. Case 2, Cometary environment, inside the contact surface. Case 3, Interplanetary medium at 1 AU heliospheric distance. Case 4, Planetary environment, Saturn's dilute E-ring. Case 5, The Voyager 2 Saturn ring plane crossing. (a) Cumulative density for grains larger than a_m; adapted from *McDonnell et al.* [1992]. (b) [*Grün et al.*, 1985].

Results are shown in Table 3.1 for a selection of cases in cometary, interplanetary, and planetary media, which might be useful in the Rosetta, Wind, Cassini and Voyager missions respectively.

Case 1 and 2: Cometary Medium

To get estimates for a cometary medium, we use results for comet P/Hartley 2 near perihelion ($\sim$1 AU) from McDonnell et al. [1992] and extrapolate them for comet P/Wirtaken, which will be visited by the Rosetta mission. We take a gas production rate typically 3 times lower, assume the same dust to gas ratio, and consider a distance from the nucleus of 100 km. The flux of particles of mass $m \approx 10^{-10} - 10^{-9}$ kg (corresponding to a_m of case 2 in Table 1) is then $F = 3\,\mathrm{m}^{-2}\,\mathrm{s}^{-1}$. This corresponds to a dust density of $N_d \sim 0.03\,\mathrm{m}^{-3}$. The corresponding event rate R_{RDA} is of the order of one event per second.

To get an estimate for particles of mass $m > 10^{-6}$ kg (corresponding to a_m of case 1), we assume a grain mass distribution such that the flux of particles with mass $m > m_0$, is proportional to $m_0^{-4/5}$. This exponent is close to the mean value measured in situ for comet P/Halley [McDonnell et al., 1987], and to recent measurements for large grains in two other comets [Fulle, 1992; Fulle et al., 1992]. The flux is then $F \sim 10^{-3}\,\mathrm{m}^{-2}\,\mathrm{s}^{-1}$ and the corresponding dust density is $N_d \sim 10^{-5}\,\mathrm{m}^{-3}$. Again, the corresponding event rate is of the order of one event per second. Note that if the grains are fluffy, the charge mass ratio is larger, which would significantly decrease the minimum size of detectable grains and thus increase the event rate.

Cases 3: Interplanetary Medium

Table 1 of Grün et al. [1985] gives the cumulative lunar flux for different models. This flux is close to the average interplanetary flux at 1 AU, for the particle sizes considered. With the value of a_m given in case 3, the minimum mass of detectable particles is of the order of 10^{-7} kg, for a grain density of 2.5×10^3 kg m^{-3}. This corresponds to an event rate of $R_{RDA} = 4 \times 10^{-7}$ s^{-1} and a typical time between the events of about a month.

However, if the grain mass density, like often suggested for large grains, is smaller than 2.5×10^3 kg m^{-3}, R_{RDA} would increase. The same happens within sporadic meteoroid streams.

Case 4 and 5: Planetary Medium

Typical parameters are given for the Cassini mission in Case 4. We must be careful on the interpretation of these results. In the ring plane one encounters a high dust density and therefore, we can expect a higher frequency of ionization signals. This requires a more detailed analysis, and a precise description of the spacecraft's orbit. This is not yet available for the Cassini mission, but in Case 5, for the Voyager 2 ring plane crossing the analysis is carried out.

We consider the time domain data from the PWS experiment Voyager 2 ring plane crossing, on August 26, 1981, at a radial distance of 2.86 R_S, very close to the G-ring. These data were already studied by Gurnett et al. [1983], Tsintikidis [1994] and recently by Meyer-Vernet et al. [1997], in the framework of the ionization signal.

- The two antennas (length $L = 10$ m and radius $r_a = 6.3 \times 10^{-3}$ m) on board the Voyager spacecraft, were used for both the radioastronomy instrument (PRA) and the plasma wave experiment (PWS) (Figure 3.12). The first uses a monopole configuration, measuring the voltage between one arm and the spacecraft, while the second uses a dipole configuration, measuring the difference of potential between the two antenna arms. Where the PRA consists only of a spectrum analyzer, the PWS data includes besides the spectrum analyzer, a wideband receiver (10 Hz to 56.2 kHz) which provides waveforms of the received signals with a time resolution of about 30 μs. This wideband receiver can provide us with the required waveform data.

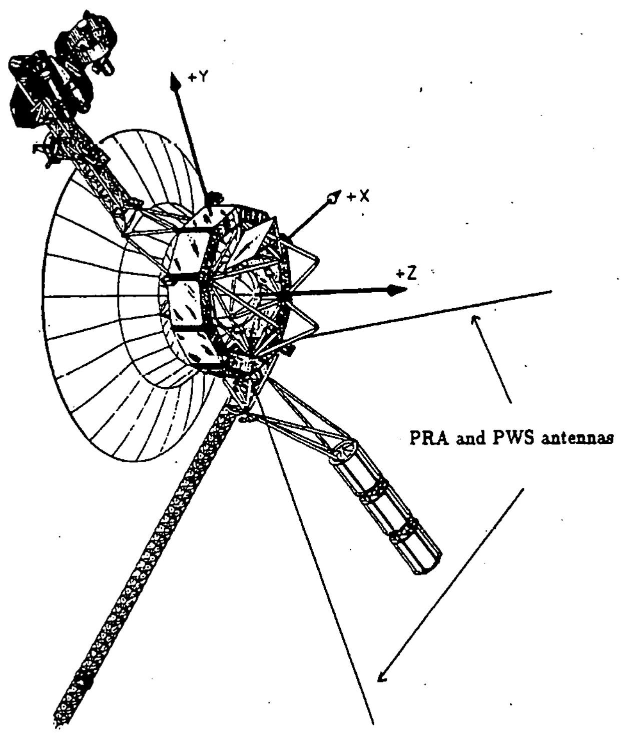

Figure 3.12: The Voyager spacecraft. The wire dipole antennae are used in monopole configuration by PRA, and in dipole configuration by PWS; they are mutually orthogonal and perpendicular to the 13-m length magnetometer boom, which is tilted by 50° from the -z axis, and contained in the y-z plane.

The wideband receiver includes an automatic gain control that maintains an approximately constant output amplitude with a feedback time constant of 0.5 s. In this way the output signal will have a suitable dynamic range for the high-rate telemetry system, which has only 4-bit resolution [Gurnett et al., 1983]. The spacecraft coordinate system was shown in Figure 3.12.

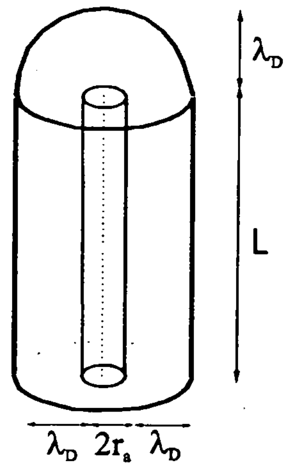

Figure 3.13: The active volume for the Radio Dust Analyzer for one of the antennas.

The relative dust-spacecraft velocity is v=13.8 km s^{-1} during the ring plane crossing and so the time the grain resides in the active volume (Figure 3.13) is of the order of Δt_{RDA}=0.5–10 ms for realistic Debye lengths. This results in 17–300 samples for each RDA-signal. The time width of the ionization signal is between 0.5 and several ms, but the mean value is about 1.6 ms [Gurnett et al., 1983].

- For the case considered, the noise level due to plasma particle impact on the antenna can be directly calculated by (3.23).

  The noise level due to plasma particle flyby on the other hand has to be recalculated for the specific geometry (perpendicular antennas) using Meyer-Vernet and Perche [1989]. When we assume a linear distribution, we get:

$$\mathbf{J}(\mathbf{k}) = G(k_x)\mathbf{e_x} - G(k_y)\mathbf{e_y}, \tag{3.28}$$

$$G(x) = \frac{1}{ix} - \frac{e^{-ixL} - 1}{x^2 L}, \tag{3.29}$$

and calculate

$$F(k) = \frac{1}{32\pi} \int |\mathbf{k} \cdot \mathbf{J}(\mathbf{k})|^2 d\Omega, \tag{3.30}$$

where the integration is carried out over the direction of $\mathbf{k}$. The noise variance is then given by:

$$< \Phi_p^2(t) >= \frac{4\kappa T}{\pi^2 \varepsilon_0} \int_0^\infty \frac{F(k)}{1 + k^2 \lambda_D^2/2} dk. \tag{3.31}$$

Equation (3.31) was evaluated numerically, given by:

$$< \Phi_p^2(t) >= \frac{4\sqrt{2}\kappa T}{\pi^2 \varepsilon_0 \lambda_D} G(L/\lambda_D), \tag{3.32}$$

and the results for different Debye lengths and a temperature of $T = 100 \times 10^3 K$, can be seen in Table 3.2. The function $G(x)$ is drawn in Figure 3.10 (dashed line), where the case for parallel and perpendicular arms can be compared.

λ_D	(m)	1	2	5	10	20
S_{RDA}	(m^2)	30	62	180	430	1200
$\sqrt{<\Phi^2_{i/e}>}$	(μV)	35	38	41	43	46
$\sqrt{<\Phi^2_p>}$	(μV)	87	68	42	26	14

Table 3.2: The variance of the noise due to impact/emission of plasma particles, the variance of the noise due to plasma particle flyby and the effective cross section of the RDA, for different Debye lengths for the Saturn ring plane crossing of Voyager 2. This noise level is given for T_{eff}=1 eV.

- The geometrical analysis of the spacecraft's orbit was carried out in Appendix A. Because we already know the relative dust grains-antennae direction, the RDA-signal becomes a function of only 4 parameters: x_0, y_0, λ_D and Q, where (x_0,y_0) is the coordinate of the intersection of the orbit of a grain and the x-y plane (Figure 3.12), while Q stands for the charge of the grain.

- The plasma environment in the Saturn rings [Richardson, 1995], consists of protons, heavy ions (with mass $\approx$ 16 m_p), and two populations of electrons (hot and cold). The environment in the neighborhood of the Voyager ring plane crossing is shown in Table 3.3. With a dust-spacecraft velocity of $13.8 \times 10^3 ms^{-1}$, we can conclude that protons and electrons will contribute in the plasma shielding, while the heavy ions cannot react fast enough to do so. Furthermore to keep the analysis tractable we also neglect the cold electron component, keeping only the proton and hot electron population. With this assumption, the overall shielding length $\lambda_D \approx$ 5m.

	N (m^{-3})	T (K)	c_s (ms^{-1})
protons	8×10^6	9×10^4	3×10^4
heavy ions	1×10^8	2×10^5	8×10^3
cold electrons	2×10^5	1×10^4	4×10^5
hot electrons	1×10^8	9×10^5	4×10^6

Table 3.3: The number densities, the temperature and the sound velocity of the different plasma constituents at $L = 3$ near the Voyager 2 ring plane crossing at Saturn [Richardson, 1996]

The knowledge of the dust density in the G-ring of Saturn is very poor. In the paper of Tsintikidis et al. [1994], the mass threshold for the dust particle sizes is of the order of 1–10 μm, with number densities in the range 10^{-3}–10^{-2} m^{-3}. The dust size distribution for the G-ring has been described by the photometric analysis of Showalter et al. [1992], and is assumed to be a power law distribution, with a power index q = 6 for grains between a_{min} = 0.03 μm and a_{max} = 0.5 μm. The analysis recently made by Meyer-Vernet et al. [1997], assumed a less steep power law for micron sized grains.

- We can make a more detailed analysis of the signal frequency R_{RDA}. We expect that the RDA signal is smaller but more frequent than the ionization signal (section 3.1.1). In order to resolve RDA-signals between the ionization signals, a more thorough analysis of the event rates for the two kind of signals must be carried out.

			$< N_d >$ (m^{-3})				
			10^{-6}	10^{-4}	10^{-2}	10^{0}	10^{2}
T_{RDA}	λ_D(m)	1	40×10^{-6}	4.1×10^{-3}	0.41	41	4.1×10^{3}
		2	860×10^{-6}	86×10^{-3}	8.6	860	86×10^{3}
		5	2.4×10^{-3}	240×10^{-3}	24	2.4×10^{3}	240×10^{3}
		10	5.9×10^{-3}	590×10^{-3}	59	5.9×10^{3}	590×10^{3}
		20	16×10^{-3}	1.6	160	16×10^{3}	1.6×10^{6}
T_{ION}			22×10^{-6}	2.2×10^{-3}	0.22	22	2.2×10^{3}

Table 3.4: The ratio T_{RDA} for different Debye lengths and different $< N_d >_{RDA}$ for δt_{RDA}=1 ms and δt_{ION}=1.6 ms. The ratio T_{ION} is given for different $< N_d >_{ION}$.

The event rates (R) for the ionization and RDA signal are given respectively by:

$$R_{RDA} = v \ S_{RDA} < N_d >_{RDA}, \tag{3.33}$$

$$R_{ION} = v \ S_{ION} < N_d >_{ION}, \tag{3.34}$$

in which S stands for the effective cross section of the different signals and $< N_d >$ denotes the *effective grain densities* i.e. the number densities of the grains that give rise to a signal that exceeds the noise levels. The height of the RDA signal depends only on the two geometrical parameters x_0 and y_0.

S_{RDA} is given by the projection perpendicular to the direction of the grains of the active volume (Figure 3.13). For the ionization signal on the contrary, we assume that only the metallic part of the spacecraft contribute to this cross section, and the rest of the spacecraft is expected to have a low unknown yield for the ionization signal [Meyer-Vernet et al., 1996]. From Gurnett et al. [1983] we recover that $S_{ION} = 1.7\mathrm{m}^2$. Furthermore, the projected cross section for the RDA signal, depends on the Debye length (λ_D). The order of magnitude for the cross section for different Debye lengths is given in Table 3.2.

The next parameters to determine are the effective signal densities. These densities depend on the number density of the dust particles, which is often given by a power law distribution $n(a)da = Ka^{-\beta}da$, with radii a in a given range $[a_{min}, a_{max}]$ (see chapter 2). This is believed to be the case in most planetary rings and cometary environments. However, not all of these particles will give rise to signals exceeding the noise levels. The height of the signals, and hence the effective grain densities will depend on the geometry of the dust grain orbit. Bigger (smaller) grains, passing closer to (farther away from) the antenna will produce a larger (smaller) RDA signal. Hence to recover the effective grain densities, we need estimates for the height of the signal as a function of the grain orbit. We can write:

$$S_{RDA} < N_d >_{RDA} = \int_{S_{RDA}} N_d \left[a > a^*(x_0, y_0)\right] dx_0 dy_0, \tag{3.35}$$

with

$$N_d \left[a > a^*(x_0, y_0)\right] = \int_{a^*(x_0,y_0)}^{a_{max}} n(a)da, \tag{3.36}$$

with $a^*(x_0, y_0)$ the minimum grain radius the grain must have for it to pass through the point $(x_0, y_0, 0)$ and causing a RDA-signal bigger than the noise level. This can be calculated with the help of equation (3.10) and is shown in Figure 3.14.

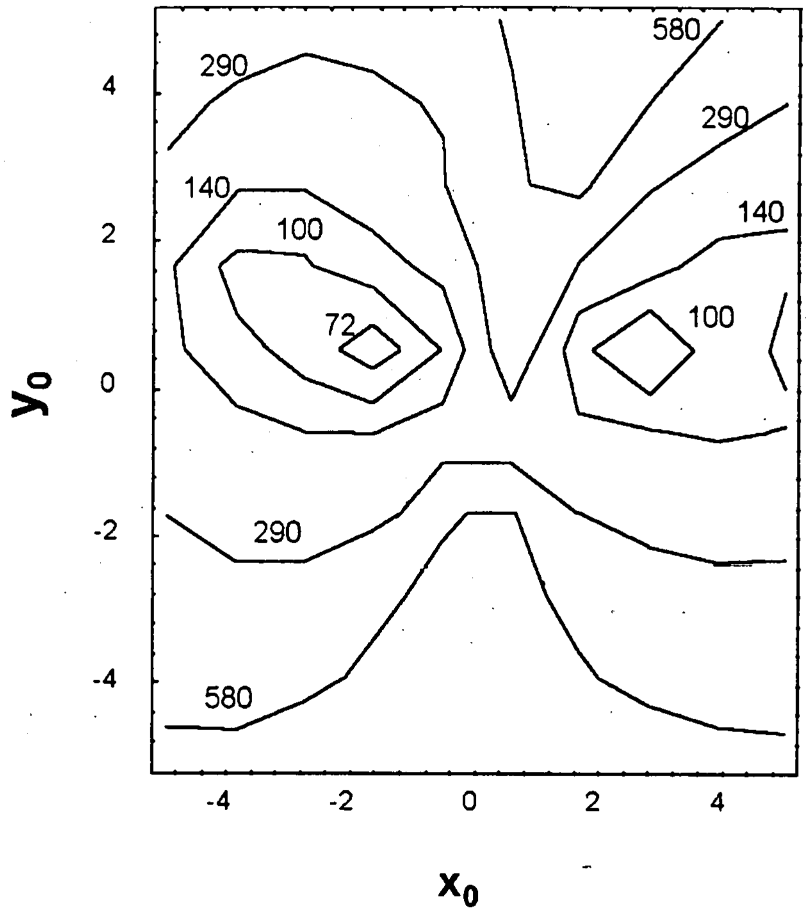

Figure 3.14: The minimal grain size $a^*(x_0, y_0)$ (in μm) for the dust particle to cause a RDA signal that exceeds the noise levels for $\lambda_D = 5$m and a maximum noise level of 40μV.

When the timewidth of the signals are denoted by Δt we define the following diagnostic parameters (Figure 3.15):

$$T_{RDA} = \Delta t_{RDA} R_{RDA}, \tag{3.37}$$
$$T_{ION} = \Delta t_{ION} R_{ION}. \tag{3.38}$$

These parameters stand for the ratio of the time width of an individual detectable RDA(ION)-signal and the mean time between two such events. It is a measure for the possibility to resolve individual detectable RDA (ION) signals, as can be seen in Figure 3.15. When $T \ll 1$, one recovers mostly individual signals. When $T \geq 1$ the different signals will overlap most of the time. The parameter gives the percentage of time for which signals can be seen. We conclude that in order to use the RDA technique, we require $T_{ION} \ll T_{RDA} < 1$.

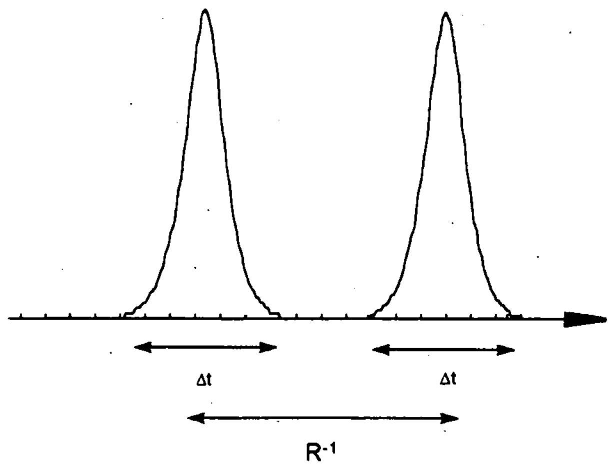

Figure 3.15: The definition of the characteristic time scales Δt and R^{-1}.

Table 3.4 gives different values for T_{RDA} and T_{ION}, as a function of the effective grain densities. We assume that $\Delta_{ION\{V\}} = 10^3 \times \alpha \times m_{\{\mathrm{kg}\}}/C_{\{\mathrm{F}\}}$ as indicated in section 3.1.1. The capacitance of the spacecraft is given by $C = 3 \times 10^{-10}$ F [Meyer-Vernet et al., 1997] and $\alpha = 0.0078$ [Tsintikidis et al., 1994]. The minimum grain size that induces an ionization signal therefore becomes $\approx 7\mu$m. From Figure 3.14 we see that the minimum grain size to produce RDA signals is at least an order of magnitude larger, and combined with a typical grain size distribution [Meyer-Vernet et al., 1997], we come to $< N_d >_{ION} \geq 10^3 \times < N_d >_{RDA}$. Introducing these values in Table 3.4 give us $T_{RDA} \ll T_{ION}$, and mostly ionization signals will be seen.

3.2.4 Conclusions

A new method for the detection of dust grains by the use of a simple wire dipole antenna is analyzed and presented. To use the method with a high precision we must try to reduce the noise levels. As is shown in Figures 3.9 and 3.11 we must preferably use the method in a neighborhood with a large Debye length and using large antennas.

Advantages

- The RDA-method has a big cross-section ($\approx 10^3$m^2), because in contrast with the two other methods discussed in the beginning of this chapter, the cross-sectional area is not a physical surface.

- The RDA-method provides us with a method that does not need detailed assumptions on the nature of the grains. This is needed in the classical dust detectors to recover the amount of charge released by impact vaporization of the grain and the released charge as a function of the impacting grain mass.

- There is a low extra cost to implement the method, because on interplanetary missions, antennas are easily available by a plasma wave-experiment or for the detection of the plasma population by antenna noise analysis. The same antennas can be used, and only a Data Processing Unit (DPU) must be built. This unit must be programmed in such a way that it recognizes the signals, processes them and sends back the characteristics of the signal.

Disadvantages

- Although the number of RDA-signals will exceed the number of ionization signals, the amplitude of the RDA-signal is expected to be weak. This means that the noise levels that can be expected such as noise due to plasma particle flyby, and impact, are critical parameters to look at. It has however been shown that the magnitude of the RDA-signal will exceed the noise levels for realistic grain sizes in four case studies.
- To derive the dust grain characteristics starting from the RDA signals, we must solve the inverse problem, i.e. starting from the antenna signal, recovering the characteristics of the grain's orbit.
- In order to be able to make the proper analysis of the signals, we need the signals in the time-domain.

Our results for different space missions were summarized in Table 3.1.

3.3 Appendix A: Geometrical analysis for the Voyager 2 ring plane crossing

In the spacecraft x, y, z coordinate system (Figure 3.12) the velocity of the particles is given by $\mathbf{V}$= (4.005, 9.996, -8.640) km s^{-1}. Using the geometry of the spacecraft as explained by Meyer-Vernet et al. [1996], the endpoints of the antennas in the same coordinate system are given by $\mathbf{A}_1$= (7.07, -4.55, 5.42) m and $\mathbf{A}_2$= (-7.07, -4.55, 5.42) m. The ratio of the projected area of the two antennas on the direction of the grain velocities turns out to be 1.82, and therefore we expect to have 1.82 more grains which impact directly on antenna 1 compared to the impacts on antenna 2 as indicated by Gurnett et al. [1983].

The volume in which a grain is detectable for one of the antennas is shown in Figure 3.13. It consists of a cilinder with radius λ_D and length L and a hemisphere with radius λ_D. The projection of the endpoints $\mathbf{A}_1$ and $\mathbf{A}_2$ on the plane perpendicular to the velocity vector $\mathbf{V}$, are given by $\mathbf{P}_1$=(8.41, -1.20, 2.52) and $\mathbf{P}_2$=(-4.54, 1.77, -0.050).

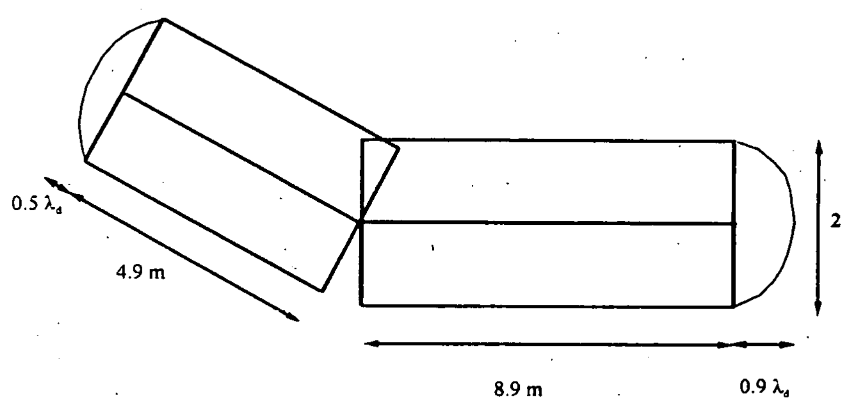

Figure 3.16: The effective cross section for the Radio Dust Analyzer in the plane perpendicular to the grain-spacecraft velocity for the Voyager 2 dipole antenna during the ring plane crossing

With this knowledge, one can derive the lengths of the projection of the antennas, and the angle between them (160°). This gives us the projection as indicated in Figure 3.16. The effective cross section becomes therefore in order of magnitude $S_{RDA} = 28 \times \lambda_D + 1.5 \times \lambda_D^2$.

The velocity vector can be described in spherical coordinates using the spacecraft coordinate system. We know that $\mathbf{V} = (4.005, 9.996, -8.640)$, and therefore the angle θ with the positive z-axis, is 129°. On the other hand, the projection on the x-y plane gives us the angle ϕ=68°.

Chapter 4

Charging model

The charging of a dust grain embedded in a plasma is a very fascinating, easily posed problem: when we put a dust grain (typically micron sized) in a plasma, what charge will it obtain, and how will this charge depend on the local plasma parameters ? The problem is rather old and was first tackled by Mott-Smith and Langmuir [1926] in the framework of probe theory. Indeed, the analysis of the floating potential of a plasma probe is parallel to the calculation of the equilibrium potential of a dust grain in a plasma. A dust grain can be considered as a probe at the floating potential, because no net current can be drawn by the grain. As we will see, solving this charging problem can become quite difficult, and the solution is even nowadays not yet clear in some domains.

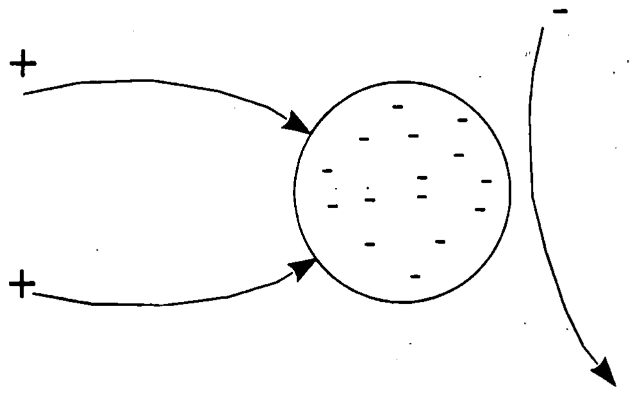

Figure 4.1: A dust grain becomes negatively charged by plasma.

Let us look at a single dust grain exposed to a plasma environment (Figure 4.1). Its surface will continually be bombarded by incident charged particles and photons. Some of the particles can be captured by the dust grain, resulting in a change of the object's charge (*primary charging*) at random intervals with probabilities that depend on the grain's potential. Indeed, when a grain becomes more and more negatively charged, the chance that it is hit by an electron decreases, because of the repulsion by electrostatic forces, whereas the probability to be hit by a positively charged ion will increase. Since the electrons are far more mobile than the ions, there is an immediate build up of negative charge and hence negative potential with respect to the plasma. Immediately the random motions of the ions and electrons in the region of the particle are disturbed. Since the particle charges negatively, electrons are repelled and ions are attracted. Thus the electron flux is reduced by repulsion just enough to balance the ion flux.

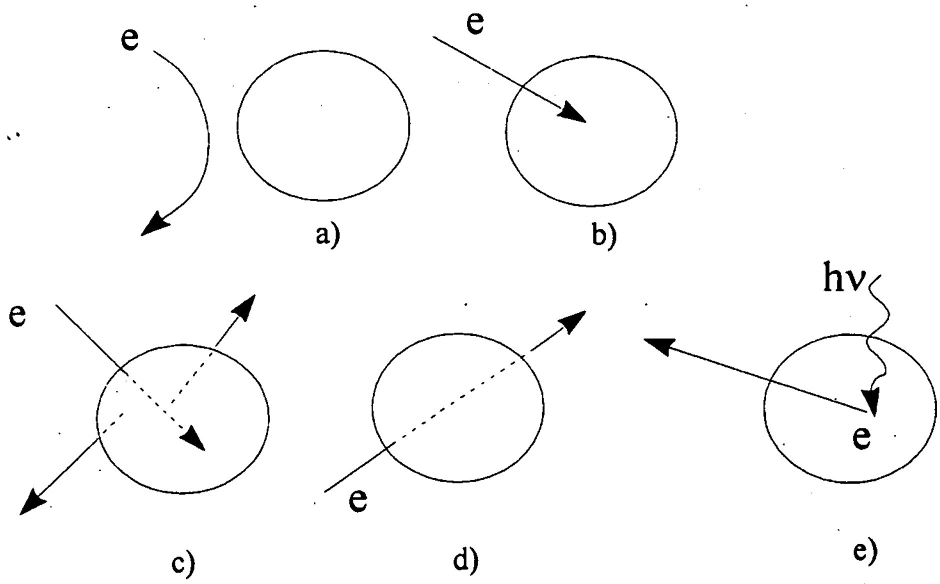

Figure 4.2: The different charging mechanisms a) reflection b) primary charging, c) true secondary electron emission, d) tunneling, e) photo-emission

But in reality the situation becomes more complicated (Figure 4.2). Some of the incident electrons, especially those with a high enough energy, can pass through the grain, before being stopped (*tunneling*). Furthermore, particles can reflect (*elastic and inelastic electron reflection*) or liberate secondary electrons (*true secondary electron emission*), while incident energetic photons can cause the emission of photoelectrons (*photo-emission*). All these processes result in a charge transfer between the plasma and the grain.

When the dust grain acquires a high enough potential, the electrostatic repulsion of the surface charges produces an electrostatic tension in the grain. If the grain's stability is insufficient this tension can cause its breakdown by *electrostatic disruption*. When a critical surface electric field is exceeded, electrons can be emitted by a negatively charged grain, *electron field emission*, or ions by a positively charged grain (*ion field emission*). When the grain is spinning, there will be a centrifugal stress, which can cause *centrifugal disruption*.

The rate (number of exchanged charges per time unit) at which the charge transfer occurs depends on the grain (its charge, geometry, ...), as well as on the plasma characteristics (number densities, temperatures, ...) and environmental characteristics (relative grain-plasma velocity, ambient magnetic field, ...). The rates for the different charging mechanisms, are denoted by $I_\alpha, I_t, I_s, I_r, I_p$, for the primary current due to capture of species α (e.g. e, i for electrons and ions), the electron tunneling current, the secondary electron current, the reflected electron current and the photo-emission current respectively.

Furthermore, we denote the grain surface potential, the grain charge and the normalized surface potential as V, Q and $\chi_\alpha = q_\alpha V/(\kappa T_\alpha)$, with q_α, T_α and κ the particle charge, temperature and Boltzmann's constant. Equilibrium values will be denoted by adding a subscript 0.

Throughout this chapter, we assume that a steady state exists for the charging process. This state is eventually reached, when the sum of all currents to the grain surface is zero, and this is given by a non-linear equation in V_0

$$\frac{dQ_0}{dt} = \sum_\beta I_\beta(V_0, ...) = 0. \tag{4.1}$$

It needs to be stressed that, depending on the specific form of the different charging currents, the solution of (4.1) might not be unique. Especially when secondary charging becomes important [Meyer-Vernet, 1982], it can be shown, that hysteresis can appear: in that case the equilibrium potential of a grain depends on its history, producing both positively and negatively charged particles in the same plasma. Recently these results were confirmed experimentally by Walsh et al. [1995].

An interesting parameter to deal with is the characteristic charging time t_{ch}, defined as the time needed for a neutral grain to reach 90 % of its equilibrium value. This parameter may be regarded as a time constant for the charging mechanism, although the charging process is nonlinear.

Even though in most of the cases the charging process is described as a continuous process, the real charging is discontinuous. Plasma particles are absorbed at the grain surface at random times and in a random sequence, resulting in an equilibrium charge fluctuation. The effect of this phenomena is discussed in **section 1**. A review of the charging currents is given in **section 2**. When there is a unique equilibrium potential and multiple grains are injected into or formed in an initially neutral plasma, they become negatively (positively) charged, leaving excess ions (electrons) in the plasma. Therefore the ion (electron) flux decreases and the grain does not have to become so negative (positive) in order to equalize the ion and electron currents to its surface. The resulting equilibrium charge is lower in absolute magnitude, than its "isolated" value. The influence of the interaction of the different grains on the grain charging is examined in **section 3**. It is easy to understand that the resulting charging current has to be adapted when a considerable magnetic field is present. As an example, we could expect that for strong magnetic fields, the geometrical cross section of the grain becomes $2 \times \pi a^2$ instead of $4\pi a^2$, because the charging will take place only by grains moving parallel to the magnetic field lines. A further analysis is given in **section 4**.

4.1 Continuous versus discontinuous charging

The effect of the discontinuous character of the charging process was studied by Cui and Goree [1994] for the primary charging currents. They find that the fractional rms fluctuation level is given by the simple law:

$$\frac{< (Q - Q_0)^2 >^{1/2}}{Q_0} = \frac{1}{2}\sqrt{\frac{e}{Q_0}}, \tag{4.2}$$

where < ... > stands for the average over the different charge levels. For a large object (carrying a large equilibrium charge) in a plasma (e.g. a spacecraft) the fluctuations are negligible. On the other hand, for a tiny dust grain with an average of only a few electrons, the fluctuations are enormous, and the grains can have a positive charge momentarily, even in the absence of electron emission. In the rest of this chapter we assume that the charging process is continuous.

4.2 Grain charging mechanisms for isolated grains

4.2.1 Primary charging Standard model

The primary charging mechanism, described by the standard model, was first derived by Mott-Smith and Langmuir [1926]. Suppose that we can neglect all other charging mechanisms for a single neutral grain, at rest in a Maxwellian two-component plasma with $\sqrt{\kappa T_e/m_e} \gg \sqrt{\kappa T_i/m_i}$. The initial ion flux is smaller than the initial electron flux and mostly electrons will hit the grain. As the grain becomes more and more negative, the ion flux increases, and the electron flux decreases, until an equilibrium value is reached. At this point the frequency of negative charges hitting the grain equals the frequency of positive hits, a dynamic equilibrium is reached and the floating potential of the grain is smaller than the plasma potential (V_p). Note that only the potential difference has a physical meaning and hence we have to consider the difference $V - V_p$ instead of the grain potential V. For the moment we consider isolated grains, and so the plasma potential equals the potential at infinity. The latter is taken to be zero and we set $V_p = 0$ for the rest of this section. The process of charging is driven by the difference between the instantaneous surface potential and the equilibrium potential ($\Delta V = V - V_0$).

Although the standard charging theory is maybe too simple for some applications, it is a good starting point, to see what the consequences are of the different assumptions made:

- A steady state for the charging process exists.
- No magnetic field is present.
- Only the primary charging mechanisms are considered.
- The grains are considered as perfectly absorbing, spherical and conducting.
- The velocity distribution of the plasma species at infinity is given by a Maxwellian distribution.

- The currents are *orbital motion limited.* This theory contains the assumption that some particles (of every energy range) graze the probe surface. Implicitly this includes that there are no trapped orbits for the particles.

When $f_\alpha(\mathbf{v})$ is the velocity distribution at infinity, the charging current I_α due to the plasma species α is given by:

$$I_\alpha = n_\alpha q_\alpha \int_{v_0}^{|\mathbf{v}|=\infty} v\sigma_\alpha f_\alpha(\mathbf{v}) d^3\mathbf{v}. \tag{4.3}$$

Here σ_α is the charging cross section, v_0 is the smallest particle velocity required to hit the grain.

Furthermore, the capacitance (C) for a spherical grain, is equal to [Houpis and Whipple, 1987]

$$C = 4\pi\varepsilon_0 a, \tag{4.4}$$

provided that $a \ll \lambda_D$.

The charging cross section can be found as follows (Figure 4.3). A plasma particle starts with a velocity v_α outside the Debye sphere of a dust grain, with impact parameter b_c. When it enters the Debye sphere, the particle is going to "feel" the influence of the grain, and the path of the particle changes due to electrostatical forces. We consider a plasma particle grazing at the dust grain's surface with a velocity $v_{\alpha g}$. When we decrease the impact parameter, for a constant start velocity, the plasma particle is going to hit the grain, therefore the collision cross section will be given by πb_c^2, where b_c is the impact parameter for grazing impact. The laws of conservation of momentum and energy require that:

$$\frac{1}{2}m_\alpha v_\alpha^2 = \frac{1}{2}m_\alpha v_{\alpha g}^2 + \frac{Qq_\alpha}{4\pi\varepsilon_0 a}, \tag{4.5}$$

$$m_\alpha v_{\alpha g} a = m_\alpha v_\alpha b_c. \tag{4.6}$$

We eliminate $v_{\alpha g}$ from the above equations and use (4.4). The cross section is given by:

$$\begin{aligned} \sigma_\alpha &= \pi b_c^2 \\ &= \pi a^2 \left[1 - \frac{q_\alpha Q}{2m_\alpha \pi\varepsilon_0 a v^2}\right] \\ &= \pi a^2 \left[1 - \frac{2q_\alpha V}{m_\alpha v^2}\right] \end{aligned} \tag{4.7}$$

When $q_\alpha V < 0$, the particle and the grain attract each other, the integration in (4.3) is over the complete v domain and so $v_0 = 0$. On the other hand, for $q_\alpha V > 0$, plasma particles with too low velocities will not reach the grain, being repelled by the electrostatic force. The limiting orbit which just reaches the grain's surface, will start with a velocity v_0. This velocity is given by the solution of the equation of conservation of energy: $E = 1/2m_\alpha v_0^2 + q_\alpha V = 0$.

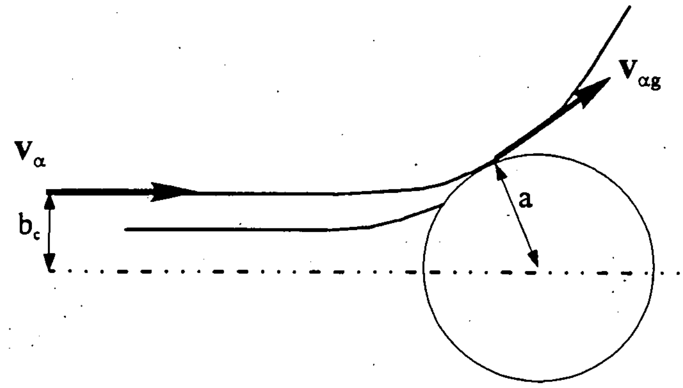

Figure 4.3: A grazing collision between an electron and a charged particle

Furthermore, the velocity distribution is taken to be Maxwellian at infinity:

$$f_\alpha(v) = n_\alpha \left(\frac{m_\alpha}{2\pi\kappa T_\alpha}\right)^{\frac{3}{2}} \exp\left[-\frac{mv^2}{2\kappa T_\alpha}\right]. \tag{4.8}$$

Substituting (4.8) and (4.7) in (4.3) and using spherical coordinates, we get [Whipple, 1981] for an attractive potential $q_\alpha V < 0$:

$$I_\alpha = \pi a^2 n_\alpha q_\alpha \sqrt{\frac{8\kappa T_\alpha}{\pi m_\alpha}} \left(1 - \frac{q_\alpha V}{\kappa T_\alpha}\right), \tag{4.9}$$

and for a repulsive potential $q_\alpha V > 0$:

$$I_\alpha = \pi a^2 n_\alpha q_\alpha \sqrt{\frac{8\kappa T_\alpha}{\pi m_\alpha}} \exp\left[-\frac{q_\alpha V}{\kappa T_\alpha}\right]. \tag{4.10}$$

An isothermal electron-ion plasma

When the plasma is isothermal ($T_e = T_i = T$), and consists only of two plasma species ($n_e = Z_i n_i = n_0$), the grain will be negatively charged, and we can rewrite the expressions (4.9) and (4.10) as:

$$I_i = \pi a^2 n_0 e \sqrt{\frac{8\kappa T}{\pi m_i}} \left(1 - \frac{Z_i eV}{\kappa T}\right), \tag{4.11}$$

and

$$I_e = -\pi a^2 n_0 e \sqrt{\frac{8\kappa T}{\pi m_e}} \exp\left[\frac{eV}{\kappa T}\right]. \tag{4.12}$$

In this case the evolution of the normalized surface potential $\chi = eV/(\kappa T)$ will be given by:

$$\frac{d\chi}{dt} = \frac{a\,\omega_{pe}^2}{\sqrt{2\pi}\,c_{se}} \left\{ \sqrt{\frac{m_e}{m_i}}(1 - Z_i\chi) - \exp[\chi] \right\}, \tag{4.13}$$

and we can conclude from (4.11), (4.12) and (4.13) that:

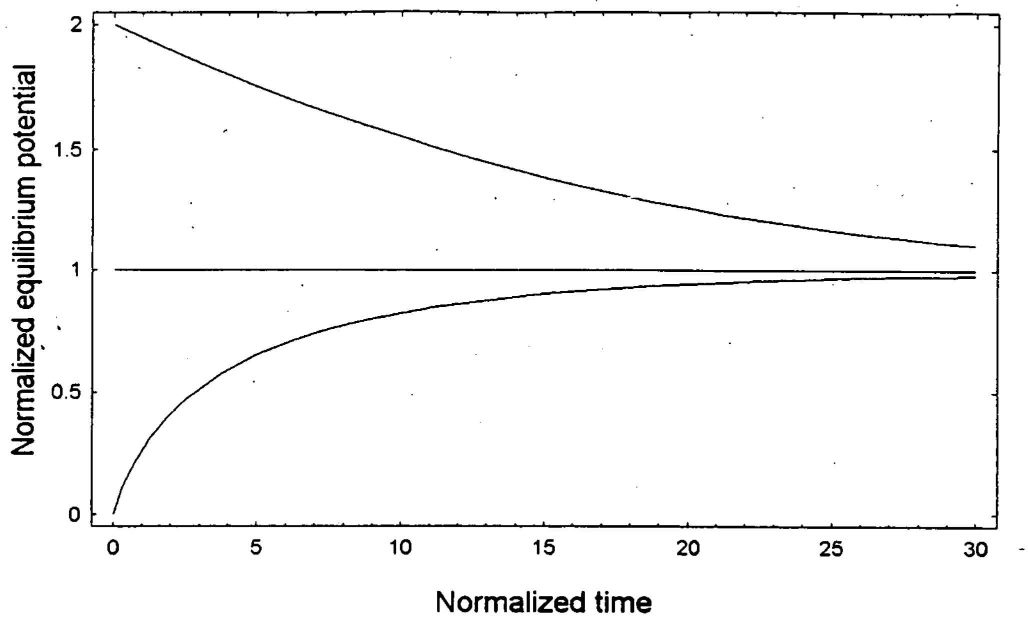

Figure 4.4: Charge evolution for a single dust grain embedded in a proton-electron plasma described by (4.13). The times is normalized by t_0 and the potential by its equilibrium value.

- The equilibrium solution of (4.13) is independent of the plasma density n_0 and the grain size a, as it depends only on the variables between the curly brackets.

- The natural time scale for the charging is given by

$$t_0 = \sqrt{2\pi} c_{se}/(a\omega_{pe}^2), \tag{4.14}$$

  The charging time for a neutral grain, given by $t_{ch} = 14.7 \times t_0 = 37 \times c_{se}/(a\omega_{pe}^2)$, is proportional to $\sqrt{T}/(n_0 a)$, therefore larger grains, or grains embedded in a denser or colder plasma, will reach equilibrium faster. This can be readily explained [Choi and Kushner, 1994]. Small dust particles charge slowly because they are small targets, and less plasma particles are going to hit them. Dust particles in very hot plasmas charge slowly because the final equilibrium potential is large. Dust particles in dense plasmas charge quickly because of the high plasma flux.

- From the numerical solution, for a proton-electron plasma (Figure 4.4), we can see that the equilibrium charge is obtained faster for grains that obey $|V| < |V_0|$. When a grain is "not negative enough", the charging will be faster than for a grain that is "too negative". This is due to the higher electron mobility.

For a hydrogen plasma the equilibrium potential is given by $\chi_0 = -2.51$, while for a singly ionized oxygen plasma $\chi_0 = -3.61$.

A drifting electron-ion plasma

In most of the cases however, drift velocities have to be included allowing the different species to have different equilibrium drifts (U_α) in the reference frame of the body [Whipple, 1981]. The velocity distribution is taken to be a Doppler-shifted Maxwellian

$$f_\alpha(\mathbf{v}) = \left(\frac{m_\alpha}{2\pi\kappa T_\alpha}\right)^{\frac{3}{2}} \exp\left[-\frac{m(\mathbf{v}-\mathbf{U}_\alpha)^2}{2\kappa T_\alpha}\right]. \tag{4.15}$$

Substituting (4.15) in (4.3) and using spherical coordinates, we get [Whipple, 1981] for an attractive potential $q_\alpha V < 0$:

$$\begin{aligned} I_{\alpha,att.} &= \pi a^2 n_\alpha q_\alpha c_{s\alpha} \mathcal{F}_\alpha \left[\frac{U_\alpha}{\sqrt{2}c_{s\alpha}}\right], \\ \mathcal{F}_\alpha(x) &= \sqrt{2}x \left\{\left(1 + \frac{1}{2x^2} - \frac{q_\alpha V}{\kappa T_\alpha}\frac{1}{x^2}\right) \mathrm{erf}\,[\mathrm{x}] + \frac{1}{\mathrm{x}\sqrt{\pi}} \exp\left[-\mathrm{x}^2\right]\right\}. \end{aligned} \tag{4.16}$$

and for a repulsive potential $q_\alpha V > 0$:

$$\begin{aligned} I_{\alpha,rep.} &= \pi a^2 n_\alpha q_\alpha c_{s\alpha} \mathcal{G}_\alpha \left[\frac{U_\alpha}{\sqrt{2}c_{s\alpha}}, \sqrt{\frac{q_\alpha V}{\kappa T_\alpha}}\right], \\ \mathcal{G}_\alpha(x,y) &= \frac{x}{\sqrt{2}} \left\{\left(1 + \frac{1}{2x^2} - \frac{y^2}{x^2}\right)(\mathrm{erf}\,[\mathrm{x}+\mathrm{y}] + \mathrm{erf}\,[\mathrm{x}-\mathrm{y}])\right\} \\ &\quad + \frac{1}{\sqrt{2\pi}} \left\{\left(\frac{y}{x}+1\right) \exp\left[-(x-y)^2\right] - \left(\frac{y}{x}-1\right) \exp\left[-(x+y)^2\right]\right\}. \end{aligned} \tag{4.17}$$

As we can see in expressions (4.16) and (4.17) the influence of the drift velocity is expressed as a function of $U_\alpha/c_{s\alpha}$. In most applications, this ratio becomes negligible for the electrons and hence we can use (4.10) for the electron charging current. For the ion charging current, however, the thermal velocity is much smaller, so it is more prudent to use (4.16).

In Figure 4.5, we can see the variation of the equilibrium grain potential, as a function of the drift velocity relative to the ion thermal velocity. One would expect the grain to sweep up more ions per time unit when moving than at rest, and therefore to be less negatively charged. This is indeed the case for high values of U_i/c_{si}. However, for low values of this parameter, the grain becomes more negative because the increase in ion flux to the front side due to the motion is more than offset by reduction in the flux to the backside.

Discussion of the assumptions

- The grains are modeled as spherical, for reasons of mathematical treatability. However, as will be shown later on, nonspherical grains show a tendency to become more spherical by electrostatic disruption.

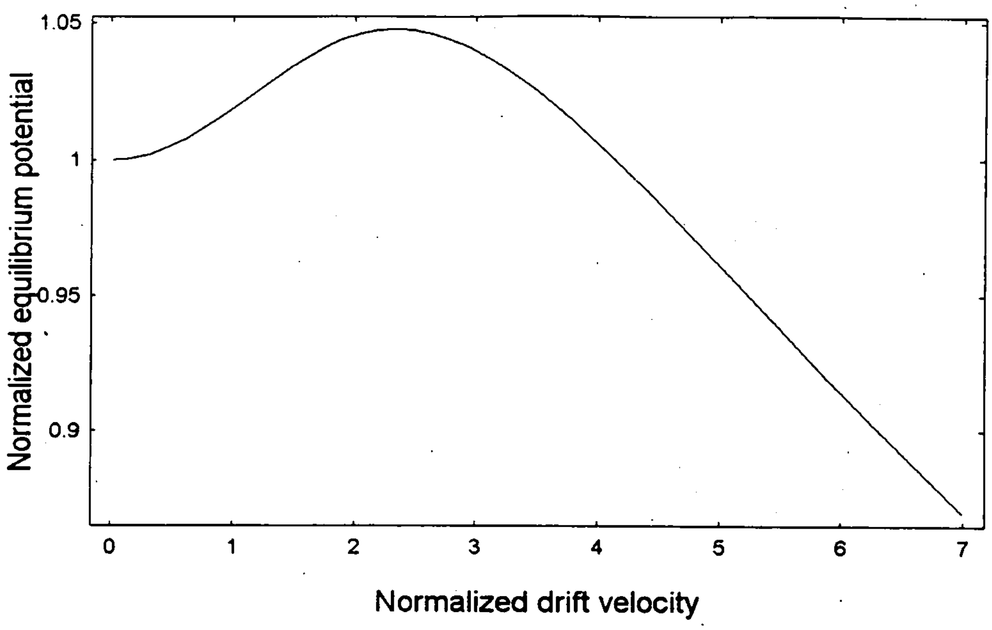

Figure 4.5: The equilibrium potential of a single dust grain embedded in a proton-electron plasma. The potential is normalized by its equilibrium value, while the drift velocity is normalized by the ion thermal velocity c_{si}.

- For a perfect isolator, the charges will not be redistributed over the grain's surface. The current density on the grain surface as a function of position would be needed. The surface would not be an equipotential surface, the electric field near the surface would need to be known to obtain the currents, and the problem becomes very complex.

- **The orbital motion assumption (OML):** We assumed that particles can graze the grain. This includes implicitly that there are no trapped orbits for the particles. In reality however, some of the plasma particles can be trapped by the grain. This is often included in the theory by assuming that an absorption radius exists outside the probe, which in a sense replaces the probe radius: particles which cross this absorption radius are destined to hit the probe and be collected [Allen, 1992]. The discussion of the validity of the orbit-limited motion approach is still going on [Allen, 1992], [de Angelis, 1992], [Daryanani, 1996]. Ideally, we should solve together the equations of motion and Poisson's equation for a considerable amount of plasma particles.

  To examine whether or not trapped orbits can exist, we give a brief analysis using spherical coordinates with the origin taken in the center of the grain. For the total energy E_α of a particle of species α (attracted or repelled) in a plasma we get:

$$E_\alpha = \frac{1}{2} m_\alpha \left(v_r^2 + v_\theta^2 \right) + q_\alpha V(r). \tag{4.18}$$

  The canonical angular momentum component J_α about any z-axis is conserved and given by:

$$J_\alpha = m_\alpha r v_\theta. \tag{4.19}$$

Combining these equations, gives us:

$$\begin{aligned} E_\alpha &= \frac{1}{2}m_\alpha v_r^2 + U_\alpha(r) \\ U_\alpha(r) &= q_\alpha V(r) + \frac{J_\alpha^2}{2m_\alpha r^2}. \end{aligned} \tag{4.20}$$

These equations describe a particle motion in one dimension with an effective potential $U_\alpha(r)$. The analysis of the problem goes as follows:

- **No collisions:** Although it is possible that the effective potential has a local minimum, which can cause trapped orbits, particles will not populate such orbits. Indeed, particles coming from $r = \infty$, with a positive energy, will be collected or reflected, but they keep their initial energy and therefore trapped orbits will be empty.
- **Collisional plasma:** Collisions will scatter particles, and the possibility of trapped particles exist, if a local minimum is reached by the effective potential. It is easily verified that if potential $V(r)$ decays faster with r than r^{-2} such minimum can exist. If trapped orbits exist than they will be populated due to collisions, and the OML-theory will not hold in that particular case.

4.2.2 Secondary electron emission

When an electron is absorbed into the material, it may be stopped by the grains (*primary charging*), pass through the grain before being stopped (*tunneling*) or release secondary electrons (*true secondary emission*). On the other hand, the electrons may get reflected (*elastic and inelastic reflection*).

Tunneling

Tunneling is distinguished experimentally from true secondary emission primarily by the energy of the emitted electrons. It is only recently recognized that this phenomenon might be important to explain the charging of very small dust grains [Chow et al., 1993]. Assuming that the primary electron current density is conserved within the grain and neglecting drift velocities, one can express the electron tunnel current as follows :

$$I_t = \frac{8\pi^2 a^2 e}{m_e^2}\int_{\max[E_{min}, E_{min}-eV]}^{\infty} E\, f_e(E + eV)dE. \tag{4.21}$$

E_{min} denotes the minimum energy required for an electron, to tunnel through the grain and f_e the electron velocity distribution. In Chow et al. [1993] this energy is given by $E_{min} = \sqrt{K_W a}$, with K_W Whiddington's constant. This constant is of the order of 10^{14} eV^{2}m^{-1}, both for insulators and for conductors.

Evaluating this integral (4.21) over the usual Maxwellian distribution yields for negatively charged grains ($V \leq 0$)

$$I_t = -\pi a^2 n_e e \sqrt{\frac{8\kappa T}{\pi m_e}} \exp\left[\frac{eV}{\kappa T}\right] \exp\left[-\frac{E_{min}}{\kappa T_e}\right] \left(1 + \frac{E_{min}}{\kappa T_e}\right), \tag{4.22}$$

and for positively charged grains particles ($0 \leq V$)

$$I_t = -\pi a^2 n_e e \sqrt{\frac{8\kappa T}{\pi m_e}} \left(1 + \frac{E_{min} + eV}{\kappa T_e}\right) \exp\left[-\frac{E_{min}}{\kappa T_e}\right]. \tag{4.23}$$

This tunneling effect can only play for very small grains, as the number of electrons with energy $E \geq 10^4 eV\sqrt{a_{\{\mu\mathrm{m}\}}}$, is usually negligible. Only for very small grains this current must be taken into account.

True secondary emission

If sufficiently energetic particles are present, true secondary emission becomes important. Electrons are usually the most energetic plasma particles, and therefore mostly electron driven secondary electron emission has been carried out.

We define the secondary yield $\delta(E)$ as the ratio of emitted electrons to incident electrons with energy E. The secondary electron emission charging current can be written [Meyer-Vernet, 1982; Chow et. al, 1993], for negative grains ($V \leq 0$)

$$I_s = \frac{8\pi^2 a^2 e}{m_e^2} \int_0^\infty E\, \delta(E)\, f_e(E - eV) dE, \tag{4.24}$$

and for positively charged grains particles ($0 \leq V$)

$$I_s = \frac{8\pi^2 a^2 e}{m_e^2} \exp\left[-\frac{eV}{\kappa T_s}\right] \left(1 + \frac{eV}{\kappa T_s}\right) \int_{eV}^\infty E\, \delta(E)\, f_e(E - eV) dE. \tag{4.25}$$

T_s stands for the temperature of the emitted secondary electrons, which can adequately be described by a Maxwellian velocity distribution [Meyer-Vernet, 1982], with T_s in the range (1-5 eV). This assumes tacitly that the escaping electron flux is independent of the incident electron energy. For plasma temperatures of the order of T_s, this means that a (significant) portion of the secondary electrons can escape with energies greater than the incident energy which is clearly unphysical, and the results need to be modified. A better point of view is the approximation of the emitted secondary electrons by the same Maxwellian with a cutoff at the incident electron energy [Jurac et al., 1995].

For explicit expressions of δ we refer to the papers mentioned above and the references therein. In general $\delta(E)$ exhibits a maximum (δ_m) at an optimum incident energy E_m, indicating that low-energy primary electrons will not produce secondaries, because their lack of energy, while energetic primaries penetrate deep in the grain and the produced secondaries cannot escape. Laboratory data are available, but the yield for dust grains can differ appreciably from these values, due to the known high dependence of the yield on the physical and chemical structure of the surface. The result from Sternglass [1954] is widely spread, but the model of Draine and Salpeter [1979] is also used [Jurac et al., 1995]. Both models were obtained for a semi-infinite slab of material and for normal incidence. To account for both the assumed spherical shape of the dust particle and isotropic incidence, some papers used a multiplication factor of 2 for δ_m. It was observed, however, that in that case not only the secondary electron emission increases with incident angle but that also the value of E_m shifts towards higher energies. Whipple [1981] gives expressions for these effects.

Also, secondary emission starts at some threshold energy (E_{th}) for the impacting electrons and not at zero energy which is almost always assumed in derivations of $\delta(E)$. The surface barrier for insulators is determined by the electron affinity (E_A), which is the energy difference between the vacuum level and the bottom of the conduction band. Only those electrons for which the component of kinetic energy perpendicular to the surface is greater than E_A will escape from the material. The resulting function for $\delta(E)$ corresponds to replacing E with E_{th} and E_m with $E_m - E_{th}$ in the Sternglass or Draine and Salpeter expression. This threshold energy is usually between 5 and 10 eV for insulators, and therefore especially in plasmas where the temperature is in the same range, one can make significant mistakes by ignoring this effect [Jurac et al., 1995].

It has been shown by [Chow et al., 1993] that two grains with the same history can become oppositely charged, depending on their sizes. This is the case when besides the primary currents, the secondary electron current and the tunnel current are taken into account. The effects of tunneling and secondary electron current are therefore strongly related to the grain size distribution.

Elastic and inelastic reflection

Figure 4.6 shows the total electron fluxes from tungsten for 10 and 20 eV at normal incidence measured by Harrower [1956]. We see the expected peak due to the true secondary emission electrons, and a second peak at the incident electron energy corresponds to the reflected electrons. The maximum corresponds to elastic reflection while inelastic reflected electrons, which lose some of their energy in the interaction with the grain, correspond to energies below the elastic maximum. The distinction between the inelastically scattered electrons and the secondary electrons is somewhat arbitrary, but when we model the true secondaries as a (truncated) Maxwellian, the rest of the flux can be considered as reflected electrons.

For *negative* grain potentials all emitted electrons can escape, that is, regardless of their energy and the reflected current can be calculated using:

$$I_r = \frac{8\pi^2 a^2 e}{m_e^2} \int_0^\infty E R(E) f_e(E - eV) dE. \tag{4.26}$$

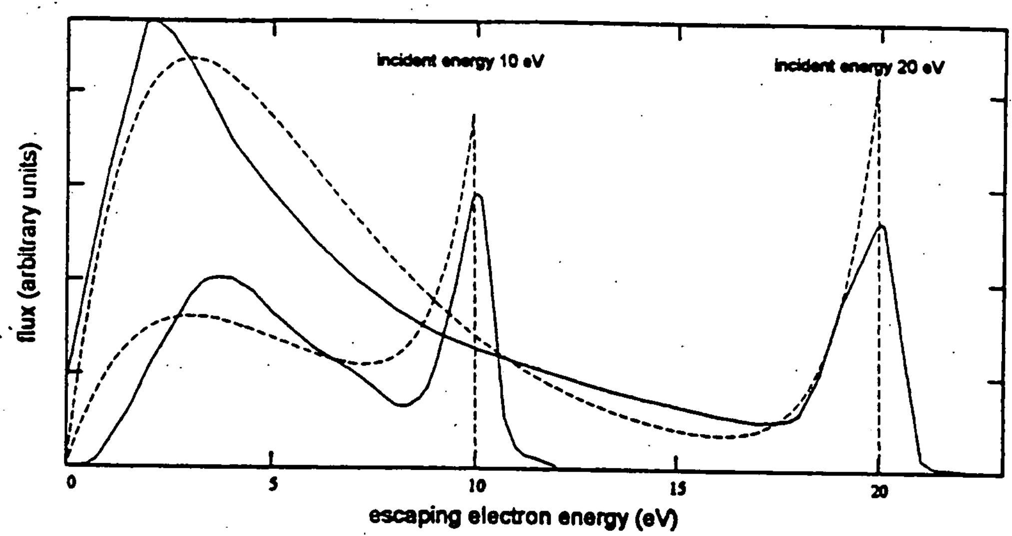

Figure 4.6: Total electron fluxes from tungsten for 10 eV and 20 eV primary electrons at normal incidence (solid lines) and the modeled flux distributions (dashed lines) as a sum of a Maxwellian around 3 eV for the true secondary electrons and a truncated Maxwellian for the reflected electrons [Jurac et al., 1995].

The *reflection coefficient* $R(E)$ denotes the mean number of ejected electrons per emitted electron by inelastically as well as by elastically backscattered primaries.

For *positive* grains only electrons with sufficient energies escape. Therefore a model is needed for the reflected current as a function of the escaping electron energy. A half-Gaussian velocity distribution (with a spread measured by T_{ref} of the order of 1 eV) up to the elastic peak at incident electron energy can be used (Figure 4.6, dashed line which includes the true secondary electrons). The resulting current is given by Jurac et al. [1995]:

$$I_r = \frac{8\pi^2 a^2 e}{m_e^2} \int_{eV}^{\infty} \left[\frac{1 + (eV/\kappa T_{ref} - 1)\exp(-(E - eV)/\kappa T_{ref}) - E/\kappa T_{ref}}{1 - \exp(-E/\kappa T_{ref}) - E/\kappa T_{ref}} \right] \times E f_e(E - eV) R(E) dE. \quad (4.27)$$

The reflection coefficient approaches zero as $E \rightarrow 0$, reaches a maximum below ≈ 20 eV and decreases slowly at higher energies. Typically, for metals the maximum value reaches 0.1-0.4, whereas for dielectrics it attains 0.5-0.8 [Jurac et al. 1995]. The number of available measurements on the reflection coefficient especially at low energies is however very limited.

Ion induced secondary electron emission

Impact of high energetic ions on a target material (*sputtering*) is extensively examined in laboratory simulation due to its use for the production of integrated circuits. Sputtering causes erosion of the target material, and releases secondary electrons. It is shown [Whipple, 1981] that secondary emission due to ion impact is important for ion energies above several keV and therefore less relevant for the space applications we are interested in.

4.2.3 Photo-emission

The absorption of photons can release photoelectrons and contribute to a positive charging current. For regularly shaped grains, the absorption characteristics of electromagnetic radiation may be calculated by Mie theory, while for irregular shaped grains such calculation may be a poor representation of the actual absorption characteristics. The absorption characteristics are strongly dependent on the grain size, its type and the radiation wavelength [Havnes, 1984].

The general expression for the photo-emission current for a negatively charged grain is given by:

$$I_p = e\pi a^2 \int \xi(E_\nu) S(E_\nu) dE_\nu \tag{4.28}$$

where $\xi(E_\nu)$ is the photo-electric efficiency, $S(E_\nu)$ is the flux of photons of energy E_ν onto the dust particle. High values of I_p can be found as a result of rather large photo-electric yields for many materials in the extreme ultraviolet range of wavelengths, together with significant energy in the same region of the energy distribution of the solar photons. We can carry out the integration, using a typical solar spectrum and a typical photo-efficiency. The spectrum of the photo-electrons released is often assumed to be a Maxwellian with a temperature T_p in the range 1–3 eV. The area of the grain illuminated by the Sun emits photo-electrons which all escape in the plasma when the grain potential is negative. In this case the associated current is constant:

$$I_p = e\pi a^2 \Gamma, \tag{4.29}$$

where Γ denotes the number of photo-electrons per square meter, per second. When the potential is positive, a fraction of these electrons return to the surface, and only the most energetic ones overcome the retarding potential and escape, contributing to a current:

$$I_p = e\pi a^2 \exp\left[-eV/(\kappa T_p)\right] \Gamma. \tag{4.30}$$

For photons originating from the sun $\Gamma = \eta\, 2.5 \times 10^{14}\, r_{h\{A.U.\}}^{-2}$ m^{-2}s^{-1}, with $r_{h\{A.U.\}}$ the distance grain-sun in astronomical units and η the photo-emission efficiency ($\eta \approx 1$ for metals and $\eta \approx 0.1$ for dielectrics).

The importance of the photo-emission for the charging can be quantified [Havnes et al., 1990] by the ratio between the photo-electron flux and the electron flux:

$$R_{p/e} = \eta \frac{40 \times 10^9}{r_{h\{A.U.\}}^2 N_{e\{m^{-3}\}} \sqrt{T_{e\{K\}}}}. \tag{4.31}$$

4.2.4 Electrostatic disruption

When dust grains acquire a very high potential, the electrostatic repulsion of like surface charges produces an electrostatic tension in the grain. Öpik [1956] was the first to calculate this electrostatic tension in a charged spherical *conducting* grain, and showed that it would blow apart if its tensile strength F_t is exceeded by the electrostatic repulsive force at a surface potential V_0:

$$F_t \leq \varepsilon_0 \frac{V_0^2}{a^2}. \tag{4.32}$$

The tensile strength and the maximum surface field can be found in Table 4.1 for different materials. It is important to note that the above expressions probably underestimate the importance of the process, since they do not take into account the irregularities in the grain's geometry or surface condition [Grün et al., 1984].

	F_t (Pa)	$E_{max}(\mathrm{Vm}^{-1})$
fluffy aggregates	10^3	10^7
ice	$10^5 - 10^7$	$10^8 - 10^9$
silicates	$10^6 - 10^8$	$3 \times 10^8 - 3 \times 10^9$
glass	7×10^8	10^{10}
metals	2×10^9	2×10^{10}

Table 4.1: The tensile strength and corresponding maximum surface field strength of some dust grain materials [Grün et al., 1984].

Hill and Mendis [1981] examined the disruption of *conducting* ellipsoid grains. They showed that the electrostatic pressure increases monotonically from a minimum at the center to maxima at the ends of the ellipsoid axis. When a grain is charged to equilibrium, and the tensile strength is everywhere in the grain larger than the electrostatic pressure the grain remains intact. However, as a grain with a uniform tensile strength is charged, it will continue to chip off at its ends where the electrostatic pressure exceeds the uniform tensile strength of the grain, resulting in a more spherical grain.

It is clear that when the grain breaks down, its size a in (4.32) becomes smaller, and the value of F_t required to prevent grain disruption increases rapidly. This implies that when a grain begins to disrupt electrostatically, it will continue to do so until it reaches the smallest fragments for which the macroscopic condition (4.32) is no longer fulfilled.

4.2.5 Field emission

For micron- and submicron-sized particles, the tensile strength can be much larger than in Table 4.1, because they may consist of monocrystals. For these particles the maximum electric field attainable at the surface is limited by ion field emission for positively charged grains, and electron field emission for negatively charged grains. The critical surface electric field for ion and electron field emission is $E_{ec} = 5 \times 10^{10}$ V/m and $E_{ic} = 10^9$ V/m respectively [Draine and Salpeter, 1979].

When a highly negatively charged grain breaks down, the grain radius decreases, and the surface electric field increases to the critical value E_{ec}. At this value, electron emission occurs and the absolute value of the grain potential decreases to a value that is given by the size alone: $V_0 = E_{ec}a$. With the help of (4.32), we find that materials with a tensile strength larger than $(\varepsilon_0 E_{ce}^2)/2 \approx 4 \times 10^6$ Pa are stabilized against electrostatic destruction by electron field emission. As can be seen in Table 4.1, silicates, glasses and metals are in this case.

4.2.6 Centrifugal disruption

For spherical particles in an isothermal plasma, assuming that the maximum tensile stress is independent of the grain size, a spinning grain will be disrupted if [Meyer-Vernet, 1984]:

$$F_t \leq \frac{\pi}{8}\rho a^2 \omega^2, \tag{4.33}$$

with ρ the grain's mass per unit volume and ω the angular rotation frequency. If equipartition holds, the rms angular speed due to the random collisions with plasma particles, satisfies $I\omega^2 = 3\kappa T$, where $I = 8\pi\rho a^5/15$. This yields the condition:

$$F_t \leq \frac{45}{64}\frac{\kappa T}{a^3}. \tag{4.34}$$

Due to its cubic dependence on the grain size, this mechanism becomes relevant for submicron sized grains.

4.3 Charging model for a grain ensemble

As we increase the dust density in a dusty plasma (and decrease the average dust grain distance d), the equilibrium charge on the dust grains will decrease dramatically. Two effects will play a role [Goertz, 1989].

- When we increase the dust density, the capacitance of the grains is going to increase [Houpis and Whipple, 1987]. Indeed, the grain with its Debye shield is qualitatively like a spherical capacitor, the outer shell being replaced by the sheath. As grain spacing becomes comparable to or less than the Debye length, the positive sheath of each grain is forced closer to the grain surface, thus decreasing the capacitor's gap and increasing its capacitance.

- There is however a strong countereffect. When there is a unique equilibrium potential and the grains are injected into or formed in an initially neutral plasma, they become negatively (positively) charged, leaving excess ions (electrons) in the plasma. So the grain does not have to become so negative (positive) in order to equalize the ion and electron currents to its surface. The absolute value of the equilibrium charge obtained by the grain ensemble is smaller than the value obtained for a single grain.

  This effect was experimentally described by Barkan et al. [1994]. If the equilibrium potential of the grain is not unique, the role of ensemble effects is not yet clear and needs further investigation.

So when we increase the dust density, the grains "appetite" for electrons will increase but the number of available electrons will decrease. The latter effect takes over from the former, and the mean charge for each grain decreases, when we compare to the equilibrium charge of a single grain. For a plasma where only the primary charging and the photoemission are relevant, the influence of high dust densities has been quantified by Havnes [1986].

4.3.1 The "Havnes model"

Let us consider a dusty plasma with one mono-sized dust population, in which only primary charging takes place. The primary charging currents are given by (4.9) and (4.10) and the system is described the charge neutrality condition at equilibrium:

$$-en_e + q_i n_i + Q_0 N_d = 0. \tag{4.35}$$

The total current vanishes at equilibrium:

$$I_e(Q_0) + I_i(Q_0) = 0, \tag{4.36}$$

and the plasma is considered as thermalized, so the plasma number densities are given by Boltzmann relations:

$$n_\alpha = N_0 \exp\left[-\frac{q_\alpha U}{\kappa T_\alpha}\right], \tag{4.37}$$

with N_0 the plasma density outside the dust cloud.

This leads to two equations that can be solved for U (cloud potential) and $V - V_p$. The results are shown in Figure 4.7 for a proton-electron plasma as a function of the Havnes-parameter P

$$P = \frac{4\pi\kappa\varepsilon_0}{e^2}\frac{N_d a T}{N_0} = 60 \times 10^3 \frac{N_d a T}{N_0}. \tag{4.38}$$

When $P \ll 1$ the grains can be considered as isolated, and the previous results are valid. However, when P is increased, the cloud potential increases because of the imbalance of electron and ion charges in the surrounding plasma. As a result, the surface potential

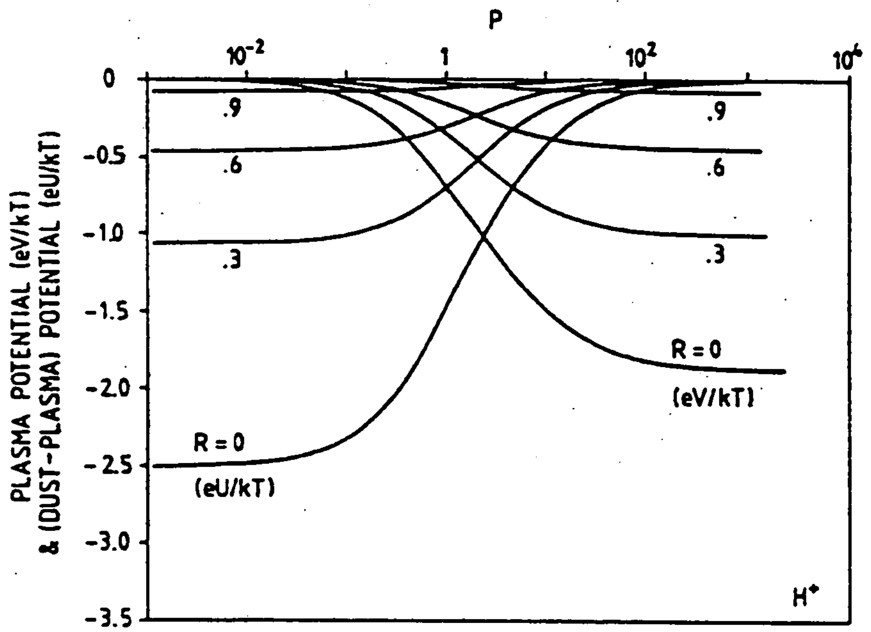

Figure 4.7: The cloud potential and the dust minus cloud potential versus the Havnes parameter P for an isothermal proton-electron plasma for different $R_{p/e}$ [Havnes et al., 1990].

decreases because there are less free electrons left to charge the grain. This effect has been verified experimentally [Xu et al., 1993].

One drawback to this model was given by Wilson [1991]. It ignores the effect of absorption of charged particles. Indeed, both the ions and electrons were assumed to be Boltzmann distributed, and eventual sink/source terms occurring in continuity and momentum equations due to the charging process are not included in the model. When the densities of particles in the cloud are not too high and the loss of plasma particles due to the charging process is rather small, such assumptions are reasonable.

It is important to note that the number of dust particles in a Debye cube can be written as:

$$N_D \lambda_D^3 = \frac{P}{4\pi} \frac{\lambda_D}{a}. \tag{4.39}$$

It can be readily verified, that even when $P \ll 1$ (considered as isolated), the number of grains in a Debye cube can be large, provided that $\lambda_D \gg a$, which is usually the case in dusty plasma environments. Often ensemble effects are explained by Debye spheres of different grains that overlap [Goertz, 1989]. This picture however is clearly not valid, because ensemble effects can be neglected ($P \ll 1$) even when the number of grains in a Debye cube is large. This is due to the fact that this model does not use any information on the charge of the grain. For low equilibrium charge, grain ensemble effects will occur for higher dust densities than in the case of high equilibrium charges [Melandsø, private communication, 1996].

4.3.2 Dusty crystals

It was predicted by Ikezi [1986] that when $Q^2/(dT)$ (d stands for the average dust grain distance), exceeds a critical value, a lattice can be formed by the charged dust grains. This paper was the start of some successful *dusty plasma crystal* experiments. These experiments make it possible to examine wave phenomena, the structure of crystals and the charging of grains in strongly coupled systems. However the latter is beyond the scope of this thesis.

4.4 Influence of the magnetic field on the charging

We can expect that the presence of a magnetic field alters the charging currents. Indeed, the paths of the plasma particles change when an ambient magnetic field is introduced. A review on the charging of a spherical conducting probe in a laboratory magnetoplasma is given by Laframboise and Sonmor [1993].

The relevant length scales for this problem are the grain radius a, the length scale of the electric potential $V(\mathbf{r})$ variation (denoted as λ_D^* because for a Debye shielded potential this length is equal to the Debye length), the mean gyration radius $\overline{r_{\alpha g}}$ and the mean free path length r_{mfp}. For a collisionless plasma, we assume that $r_{mfp} \to \infty$, while for all relevant dusty plasma applications, $a \ll \lambda_D^*$.

A calculation for a spherical conducting grain in a collisionless magnetoplasma, for an infinitely large Debye length, was addressed by Sonmor and Laframboise [1991], while upper and lower bounds for the charging currents were given by Rubinstein and Laframboise [1982]. For this approach, the charging current is shown to be a function of the normalized magnetic field and electric potential denoted respectively by $\beta_\alpha = a/\overline{r_{\alpha g}}$ and $\chi_\alpha = q_\alpha V/(\kappa T_\alpha)$.

Collisionless theory for infinite Debye lengths

Following the same outline as before (Section 4.2.1), the motion of the particles can now be seen as a particle motion in the (r, z)-plane with an effective potential $U_\alpha(r, z)$, using cylindrical coordinates. The effective potential becomes in the presence of a magnetic field:

$$U_\alpha(r, z) = q_\alpha V(r, z) + \frac{1}{2} m_\alpha r^2 \left[\frac{J_\alpha}{m_\alpha r^2} - \frac{\Omega_\alpha}{2}\right]^2. \tag{4.40}$$

Since the kinetic energy must be nonnegative, it follows that a particle having a particular E_α and J_α, is confined in the region of the (r, z)-plane for which, $E_\alpha \geq U(r, z)$, i.e., inside the particle's magnetic bottle (Figure 4.8).

These bottles have rotational symmetry about the z-axis. For the collisionless limit, particles cannot cross magnetic bottle borders. When we assume that any particle whose

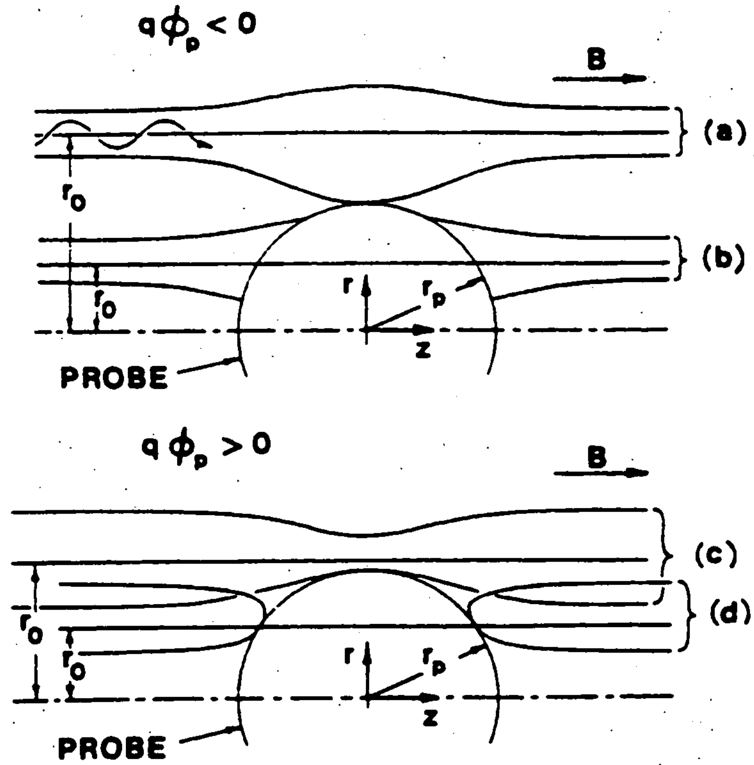

Figure 4.8: The magnetic bottles in the neighborhood of a grain [Rubinstein and Laframboise, 1982].

magnetic bottle intersects the probe is collected, an upper-bound of the actual charging current can be derived when one ignores the effects of a particle's thermal motion at infinity [Parker and Murphy, 1967]. When the thermal motion at infinity is taken into account, Laframboise and Sonmor [1993] derived an upper bound (I_α^{max}) for the current.

Another attempt was made by Sonmor and Laframboise [1991]. They calculated a large amount of particle orbits by integrating Newton's equation of motion, with a Coulomb potential ($\lambda_D^* \to \infty$), and derived the currents as a function of β_α and χ_α. They concluded that:

- when $\beta_\alpha \to 0$, magnetical effects can be neglected and we recover the orbital motion limited theory.
- when χ_α increases, the collected current asymptotically approaches the upper-bound value I_α^{max}, but very slowly. Hence this value will never be obtained for real dusty plasma conditions.

It has to be stressed that this kind of calculation is not self-consistent. A self-consistent calculation should solve together the equations of motion and Poisson's equation, but is notoriously intractable. The number of papers dealing with the self-consistent solution of the problem is very restricted [Laframboise, private communication, 1996]. However, a numerical three-dimensional particle-in-cell analysis has been carried out for a cylindrical probe [Singh et al., 1994]. They recovered that the actual current was adequately described by the upper-bound limit, when the electric field gradient λ_D^* is sufficiently large, and this happens even for realistic grain potentials as low as a few volts.

Combined effects of space charge and collisions

In a *collisionless* plasma, depending on the explicit expression of the electric potential, some of the magnetic bottles will be unpopulated. This is the case for the bottles not connected to $|z| \to \infty$. For a *collisional* plasma, however all bottles will contain particles due collisional scattering.

It can be shown [Laframboise and Sonmor, 1993] that effects of collisions and space charge cannot be separated, even in the limit of a large mean free path. It turns out that a strictly collisionless theory cannot be exact in cases of finite Debye length. To explain why, we consider the depletion of particles at large distances from a spherical probe, caused by the probe's current collection. If $\mathbf{B}_0 = \mathbf{0}$, this depletion occurs equally in all directions for both ions and electrons, and therefore results in a spherically symmetric distribution of net space charge and therefore of potential.

If $\mathbf{B}_0 \neq \mathbf{0}$, this depletion occurs predominantly along, and adjacent to the probe's "magnetic shadow". In other words, in the collisionless limit we expect that for plasma particles far away from the probe, both ion and electron density disturbances will become functions only of the cylindrical radius r. In contrast with the nonmagnetic case, however, these disturbances will have a different dependence on r for the ions and electrons, because the much smaller gyroradius of the electrons will cause the electron depletion to be confined much more closely to the magnetic shadow itself, whereas the ion depletion will be more widespread.

The resulting charge imbalances will produce a potential disturbance which will also depend only on r, even far away from the grain. In the absence of collisions, no mechanism exists to cause the charge density disturbances to decay with increasing $|z|$, and the resulting potential disturbances must therefore also extend to infinity in both directions along the magnetic shadow. However, if the mean free path lengths are finite, no matter how large they are, collisions will ultimately repopulate the depleted regions.

So the effects of finite Debye length and an ambient magnetic field are coupled, and the problem becomes more complex. Until now, this problem has never been treated in a self-consistent way [Laframboise, private communication, 1996].

Chapter 5

Major charging mechanisms for different space plasma applications

In order to quantify the physical characteristics of the dust grain charging process (equilibrium potential, charging time, relevance of the different charging mechanisms, ...), we need to combine the appropriate data sets (**chapter 2**) and the latest charging models (**chapter 4**). Part of this calculation has been given for planetary rings [Jurac et al., 1995], [Horányi, 1996] and for the interplanetary medium [Mukai, 1981], but using either a less complete charging model, or a less appropriate set of data. Additionally, we will analyze the magnitude of the charging times and the relevance of the different charging processes.

The interpretation of our results must be carried out carefully. The charging problem is highly nonlinear and hence small changes in the parameters (some of which are very uncertain) can result in serious differences in the results. Therefore it cannot be our ambition to give *the* solution for the charging equation, but we will give an indication what processes might be important in the charging of the grains in the space plasma environment that were studied in **chapter 2**. For that, we use a broad, well chosen parameter range for the charging parameters and look at the sensitivity of the model to these values.

We deliberately did not include the analysis for the cometary environment, because we believe that the availability of the data is restricted to "snapshots" taken by *in situ* spacecraft at a limited number of comets. An additional problem is that the plasma parameters vary from comet to comet depending on the nucleus size, composition and structure, and for a given comet with solar distance, with time, and with distance to the nucleus and hence the range of variation of the parameters is large. There were attempts to explain the charging of dust grains in comets (e.g. [Boenhardt en Fechtig, 1987]), but they were based on a rather simplified model, taking only the primary electrons and the photo-emission into account, without specifying quantitatively why the other charging mechanisms where neglected. We believe that a detailed analysis of the charging mechanism in cometary dusty plasmas is still premature.

The influence of the magnetic field has been neglected. As we have seen before (Section 4.4), this might be valid as long as the grain size is smaller than the mean gyration radius. The gyration radius in the rings of the giant planets and in the interplanetary medium is of the orders of meters and kilometers respectively and therefore this choice can be considered reasonable. However, our results must be re-examined when an adequate theory for grain charging in a magnetized plasma becomes available. Furthermore, we did not take into account the tunneling current and this rules out very small grains with radii $a \ll 1\mu$m. The uniqueness of the solution of the charging equation has been verified. We assumed that the dust density is low enough so that the charging of the different grains can be considered as independent. As explained earlier, this implies that the magnitude of the equilibrium potential calculated here is assumed to be an upper bound for the real situation.

The chapter is structured as follows. In the first section, a summary is given of the model equations. The details and notation follow **chapter 4**. We apply this model to Saturn's rings and the interplanetary medium.

5.1 The charging model: a summary

For a good understanding a summary of the different charging model equations is given. The charge evolution of a dust grain is described by (4.1):

$$\frac{dQ_0}{dt} = \sum_\beta I_\beta(V_0, ...) = 0, \qquad (5.1)$$

where the summation is over the different charging mechanisms. As we know, the solution of (5.1) is not necessarily unique. The characteristic timescale t_{ch} is the time needed for a neutral grain to reach 90 % of its equilibrium value. This value was calculated for a micron sized grain. It is clear that this parameter changes as $t_{ch} \sim Q_0/\sum_\beta I_\beta \sim a^{-1}$ and so bigger grains reach their equilibrium faster.

5.1.1 Primary charging

We use equations (4.16) and (4.17). This gives for an attractive potential $q_\alpha V < 0$:

$$I_{\alpha,att.} = \pi a^2 n_\alpha q_\alpha c_{s\alpha} \mathcal{F}_\alpha \left[\frac{U_\alpha}{\sqrt{2}c_{s\alpha}}\right],$$
$$\mathcal{F}_\alpha(x) = \sqrt{2}x \left\{ \left(1 + \frac{1}{2x^2} - \frac{q_\alpha V}{\kappa T_\alpha}\frac{1}{x^2}\right) \mathrm{erf}\,[\mathrm{x}] + \frac{1}{\mathrm{x}\sqrt{\pi}} \exp\left[-\mathrm{x}^2\right] \right\},$$

and for a repulsive potential $q_\alpha V > 0$:

$$
\begin{aligned}
I_{\alpha,rep.} &= \pi a^2 n_\alpha q_\alpha c_{s\alpha} \mathcal{G}_\alpha \left[\frac{U_\alpha}{\sqrt{2}c_{s\alpha}}, \sqrt{\frac{q_\alpha V}{\kappa T_\alpha}}\right], \\
\mathcal{G}_\alpha(x,y) &= \frac{x}{\sqrt{2}}\left\{\left(1+\frac{1}{2x^2}-\frac{y^2}{x^2}\right)(\mathrm{erf}\,[\mathrm{x}+\mathrm{y}]+\mathrm{erf}\,[\mathrm{x}-\mathrm{y}])\right\} \\
&+ \frac{1}{\sqrt{2\pi}}\left\{\left(\frac{y}{x}+1\right)\exp\left[-(x-y)^2\right]-\left(\frac{y}{x}-1\right)\exp\left[-(x+y)^2\right]\right\}.
\end{aligned}
$$

5.1.2 Secondary electron emission

For negative grains ($V \leq 0$) the secondary current is given by (4.24) and (4.25). With the use of the Sternglass equation [Sternglass, 1954]:

$$
\delta(E) = e^2 \times \delta_m E/E_m \exp\left[-2\sqrt{E/E_m}\right],
$$

where e stands for Euler's number, these expressions become for negative grains ($V \leq 0$):

$$
\begin{aligned}
I_s &= e^2 \delta_m n_e \sqrt{\frac{\kappa T_e}{2\pi m_e}} \exp\left(eV/\kappa T_e\right) F_5(E_m/4\kappa T_e), \\
F_5(x) &= x^2 \int_0^\infty u^5 \exp\left[-(xu^2+u)\right] du.
\end{aligned}
$$

For positively charged grains particles ($V \geq 0$) on the other hand we get:

$$
\begin{aligned}
I_s &= e^2 \delta_m n_e \sqrt{\frac{\kappa T_e}{2\pi m_e}} \exp\left(eV/\kappa T_e - eV/\kappa T_s\right)\left(1+eV/\kappa T_s\right) G_5(E_m/4\kappa T_e), \\
G_5(x) &= x^2 \int_{4eV/E_m}^\infty u^5 \exp\left[-(xu^2+u)\right] du.
\end{aligned}
$$

5.1.3 Reflection current

We use equations (4.26) and (4.27) and obtain for positive grains:

$$
\begin{aligned}
I_r = \frac{8\pi^2 a^2 e}{m_e^2} \int_{eV}^\infty & \left[\frac{1+(eV/\kappa T_{ref}-1)\exp(-(E-eV)/\kappa T_{ref}) - E/\kappa T_{ref}}{1-\exp(-E/\kappa T_{ref}) - E/\kappa T_{ref}}\right] \\
& \times E f_e(E-eV) R(E) dE,
\end{aligned}
$$

and for negative grains:

$$
I_r = \frac{8\pi^2 a^2 e}{m_e^2} \int_0^\infty E R(E) f_e(E-eV) dE.
$$

The reflection coefficient $R(E)$ will be taken from Jurac et al. [1995] who propose:

$$R(E) = 103.9 \frac{E^{5.23}}{(1+1.93E)^{5.66}},$$

based on laboratory experiments on ice. The parameter T_{ref} is taken to be 1 eV.

As indicated in **chapter 4**, the difference between true secondary electrons and reflected electrons is difficult to establish. Especially in the determination of the secondary yield parameters in laboratory experiments, all electrons coming away from a grain are measured (true secondaries as well as reflected ones) and the two parameters (δ_m,E_m) are fitted to the measurements. This is why, for example, "secondary production" occurs even for incoming electron energies below the ionization threshold. The data available on the secondary emission effect for low energetic electrons is very restricted and does not resolve the different secondary electron populations, especially at low electron energies. In fact, the only reliable data on the magnitude of the reflected current are based on laboratory experiments for rather large values of the incident energy. We use the reflection current for Saturn's rings where we can expect to find icy dust grains. For the interplanetary medium we choose to neglect the reflection current and use a more broader (δ_m,E_m)-space instead, in order to include the effect of the reflected currents [Horányi, personal communication, 1997].

5.1.4 Photo-emission

Equations (4.29) and (4.30) are used. For negative grains ($V < 0$), we get:

$$I_p = e\pi a^2 \Gamma,$$

while for positive grains

$$I_p = e\pi a^2 \exp\left[-eV/(\kappa T_p)\right] \Gamma$$

is used, where $\Gamma = \eta \times 2.5 \times 10^{14} r_{h\{A.U.\}}^{-2}$ $\mathrm{m^{-2}s^{-1}}$.

5.1.5 Parameters

The charging mechanism depends on environmental parameters and the following dust-related parameters: δ_m, E_m, T_s, T_p, η and T_{ref}. Some of them can be fixed because there is agreement on their value

$$\begin{aligned} T_s &= 2.5\,\mathrm{eV}, \\ T_p &= 2\,\mathrm{eV}, \\ T_{ref} &= 1\,\mathrm{eV}, \\ \eta &= 0.1, \end{aligned}$$

while (δ_m,E_m) are far from sure. The secondary yield parameters for ice were determined to be (δ_m,E_m)=(2.35, 340 eV) for normal incidence on a semi-infinite slab [Jurac et al., 1995]. This corresponds to a yield function with (δ_m,E_m)=(3.43, 575 eV) for isotropic incidence, using results from Whipple [1981]. The parameters for lunar dust were given by Draine and Salpeter [1979] (δ_m,E_m)=(1.5, 500 eV), but these parameters were derived for normal incidence on a semi-infinite slab. If the latter is the case, the parameters to use are (δ_m,E_m)=(2.19, 846 eV). As indicated by Chow [1996], isotropic and parallel incidence on a spherical target are identical from the point of view of secondary electron emission. Although this gives us an order of magnitude for these parameters, we must proceed with care because it is known that they depend on the number of lattice defects, and the physical and chemical structure of the surface [Meyer-Vernet, 1982].

5.2 Saturn's ring system

We use the magnetospheric plasma data of Richardson [1995] with a plasma consisting of hot and thermal electrons, protons and heavy (water group) ions. An order of magnitude for the actual densities and temperatures can be found in Table 2.3, but for the details we refer to Richardson [1995].

The charging current consists of

- Primary current due to cold electrons
- Primary current due to hot electrons
- Primary current due to protons
- Primary current due to heavy ions
- Secondary current due to thermal electrons
- Secondary current due to hot electrons
- Reflected current due to thermal electrons
- Reflected current due to hot electrons
- Photo-emission current

5.2.1 Analysis and results

Figures 5.1-5.3 show the equilibrium potential for different values of the secondary parameters. We used the values for ice-like particles and the values for lunar dust, including the reflected particles with the data available for ice. Three cases were considered. To

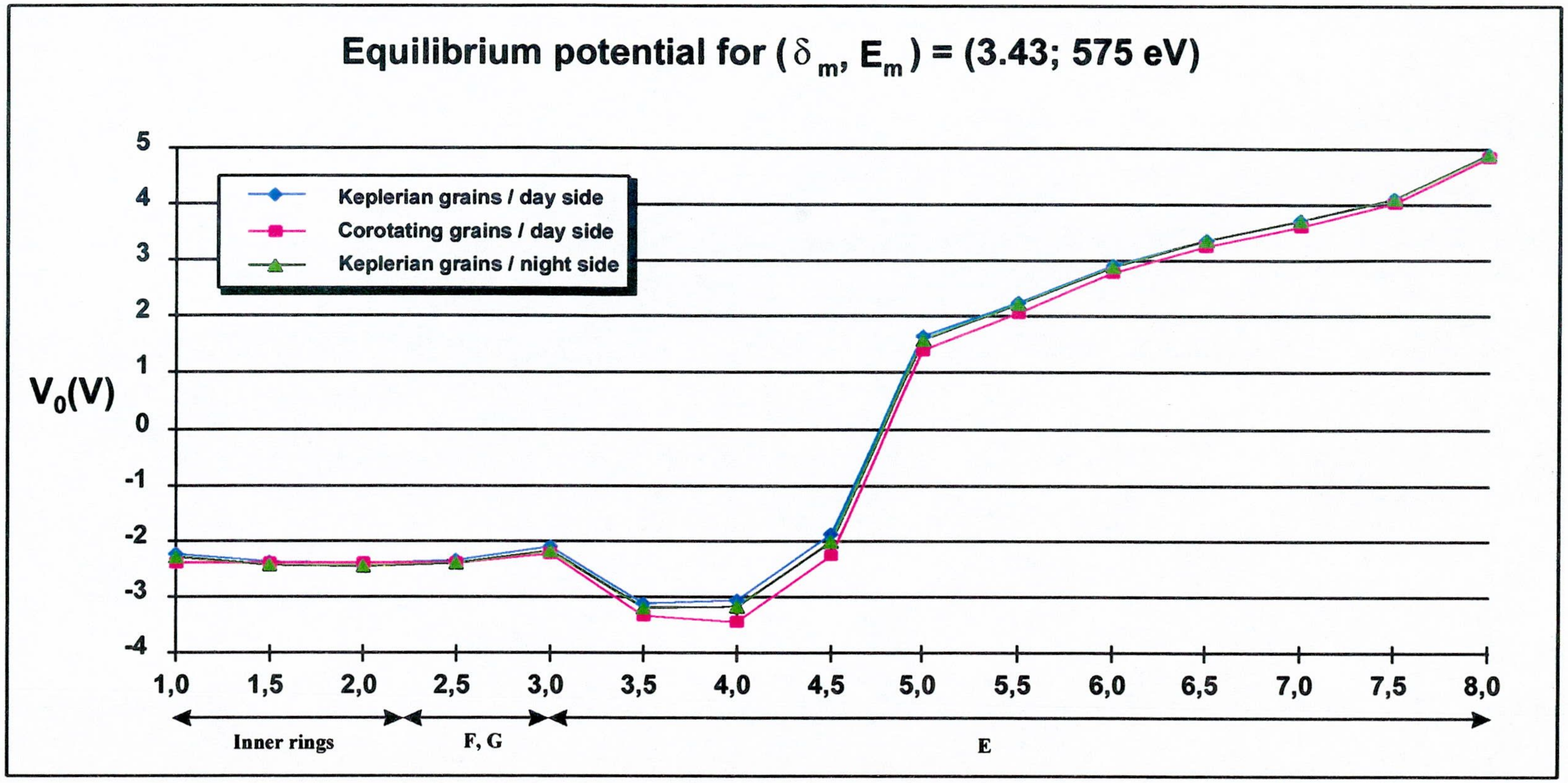

Figure 5.1: The equilibrium potential for different *L*-values in Saturn's rings. The grains are considered to have a velocity between the corotating and the Keplerian velocity. The influence of the day/night side is also evaluated.

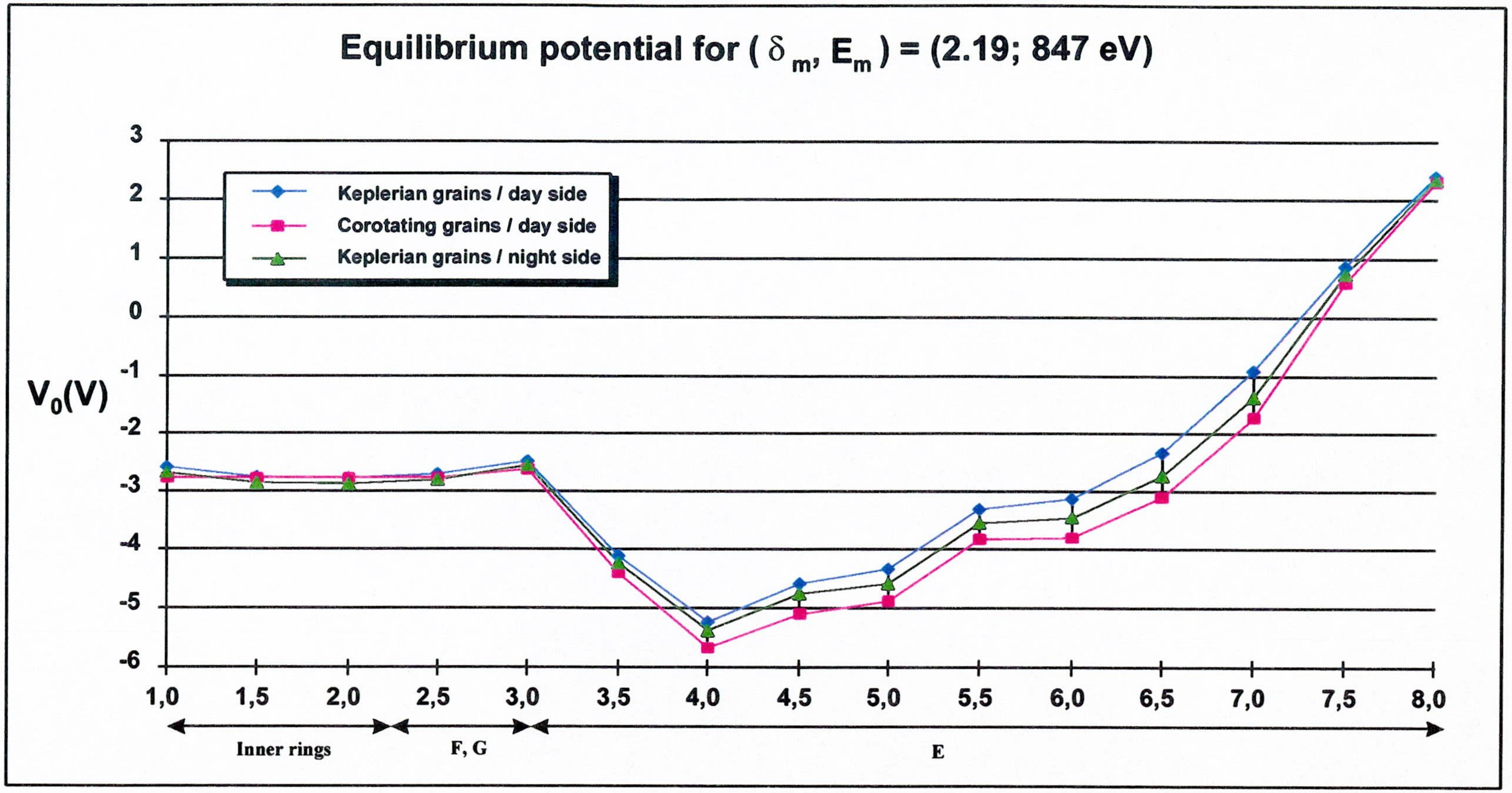

Figure 5.2: The equilibrium potential for different *L*-values in Saturn's rings. The grains are considered to have a velocity between the corotating and the Keplerian velocity. The influence of the day/night side is also evaluated.

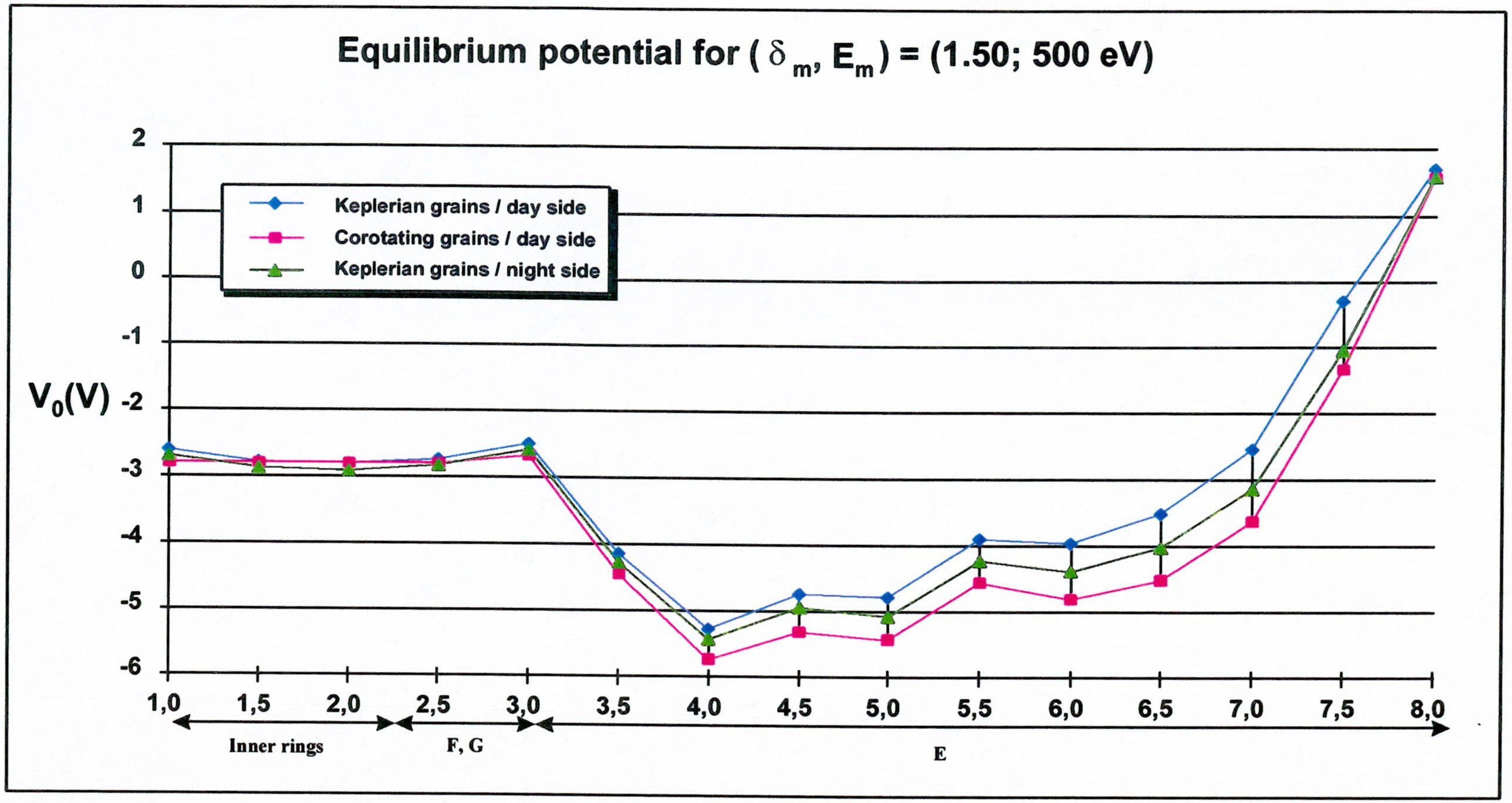

Figure 5.3: The equilibrium potential for different *L*-values in Saturn's rings. The grains are considered to have a velocity between the corotating and the Keplerian velocity. The influence of the day/night side is also evaluated.

see the influence of the dust-plasma drift, caused by the difference in angular velocity of the grains and the plasma, we looked at two limiting cases. First we considered Keplerian grains (blue diamonds) and then the case for which the grains are corotating (pink squares). The real grain angular velocity can be found in between. As we can expect, the equilibrium potential decreases when a drift velocity is taken into account. This happens, as explained in section 4.2.1, for drift velocities exceeding the thermal velocity of the ions. For the synchronous orbit at $L = 1.86$ the rotation and Keplerian periods are equal and the effect disappears. We expect that the effect will increase when we go father away from the planet, because the relative drift-plasma velocity increases. However, as we can verify in Figure 5.6, the relative importance for the ion charging currents (the only currents influenced by the plasma-grain drift) decreases with increaseing L-value. These two effects result in a maximum difference of about 1 V, for the parameters considered.

The influence of the photo-emission effect on the equilibrium potential is also shown in Figures 5.1-5.3. The charging equation was solved with (blue diamonds) and without (green triangles) the photo-emission effect. The photo-emission effect makes the grains more positive as can be verified in Figures 5.1-5.3. The influence of the day/night side on the charging of the grains is rather small.

Figure 5.4 shows the equilibrium potential for Keplerian grains and different secondary yield parameters. As we see, the influence of the secondary yield parameters in the inner, F and G-rings is rather small, and increases when we go father away from the planet. This is due to the fact that the importance of the secondary charging mechanism increases with increasing L (Figure 5.6). Depending on the parameter set we use, the equilibrium charge can even change sign, in the outer E-ring.

The charging time for the different cases is shown in Figure 5.5. It ranges roughly from minutes to hours and is smaller than the rotation period of the planet ($\approx$ 11 hours). A big decrease in the charging time occurs, when the equilibrium charge changes sign. This effect can be found for a simple grain in a proton-electron plasma as well (Figure 4.4). The charging time for grains for which $q_d(0) < q_d(\infty) = Q_0$ is much smaller than the charging time for grains with $q_d(0) > q_d(\infty) = Q_0$, due to the higher mobility of the electrons. This holds even in the presence of other charging mechanisms as can be verified in Figure 5.5.

The relevance of the different charging mechanisms are shown in Figure 5.6. We see that close to the planet the primary electron current is balanced by the reflected thermal electrons, the secondary current due to the thermal electrons and the heavy ion current. However as we move away from the planet, the secondary currents together with the reflected thermal electrons will balance the primary electron current. The heavy ion current decreases, because the heavy ion density decreases away from the planet (see the Richardson data).

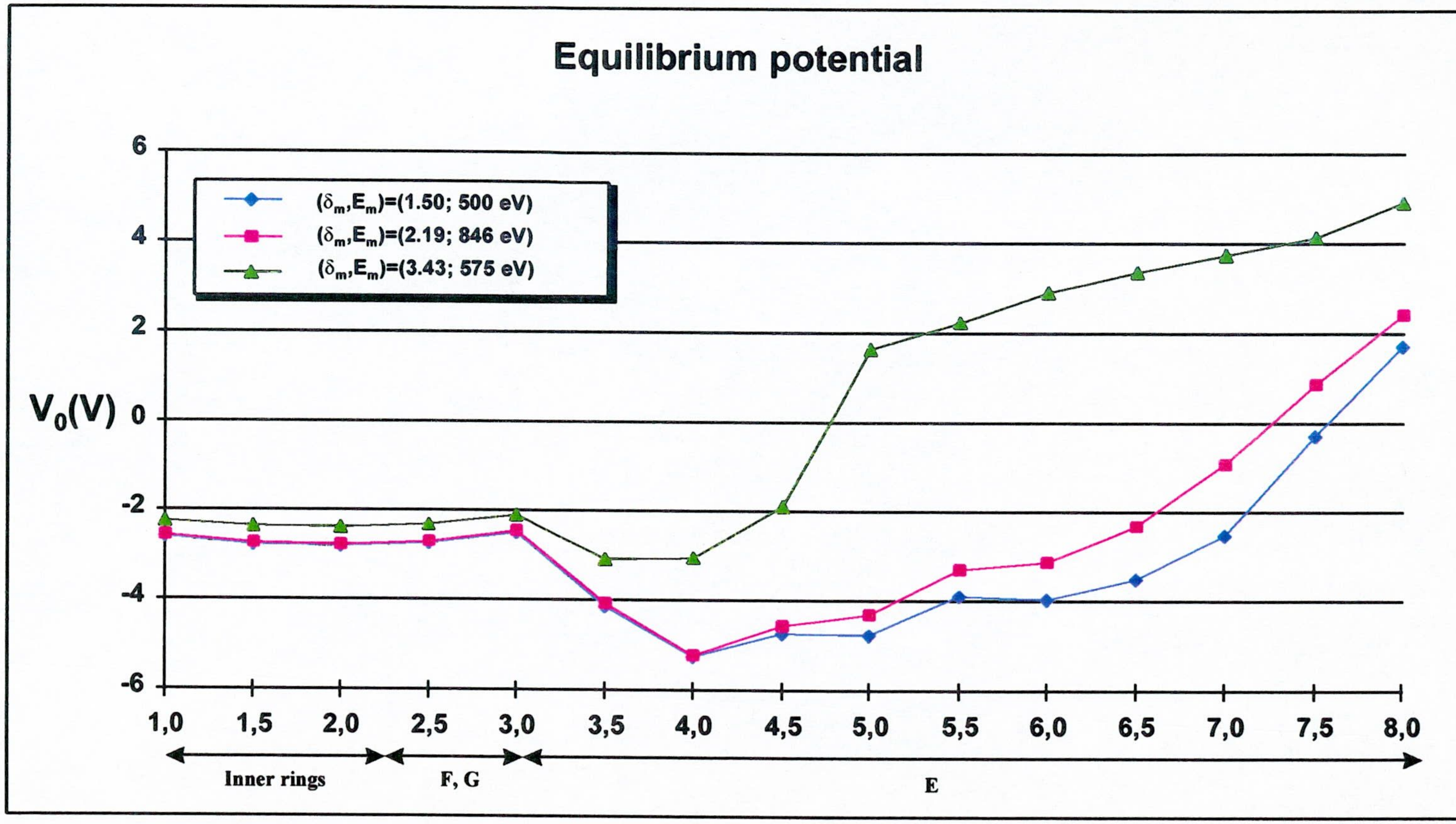

Figure 5.4: The equilibrium potential for different *L*-values in Saturn's rings and different secondary yield parameters.

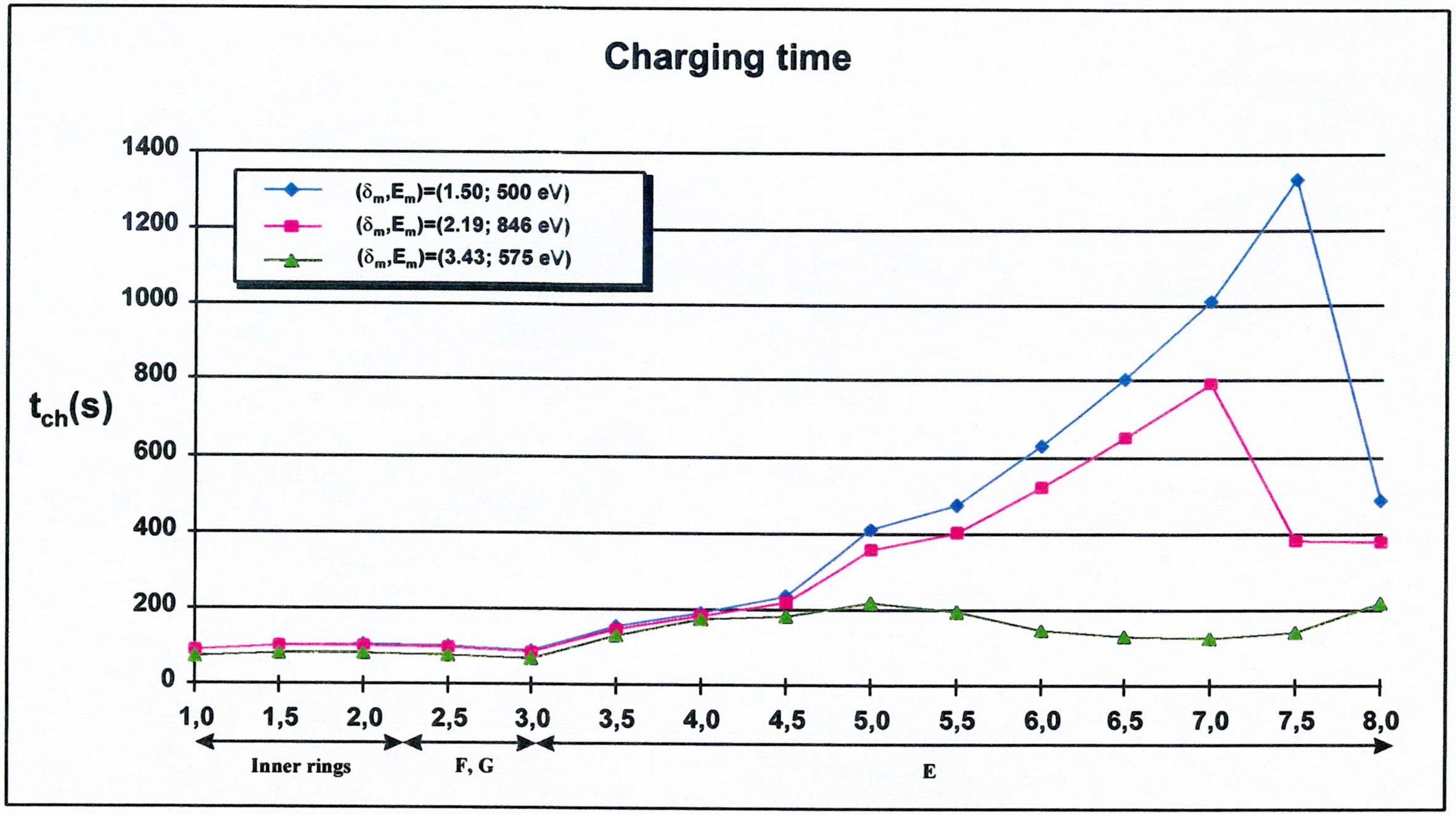

Figure 5.5: The charging time of a dust grain for different *L*-values in Saturn's rings and different sets of secondary yield parameters

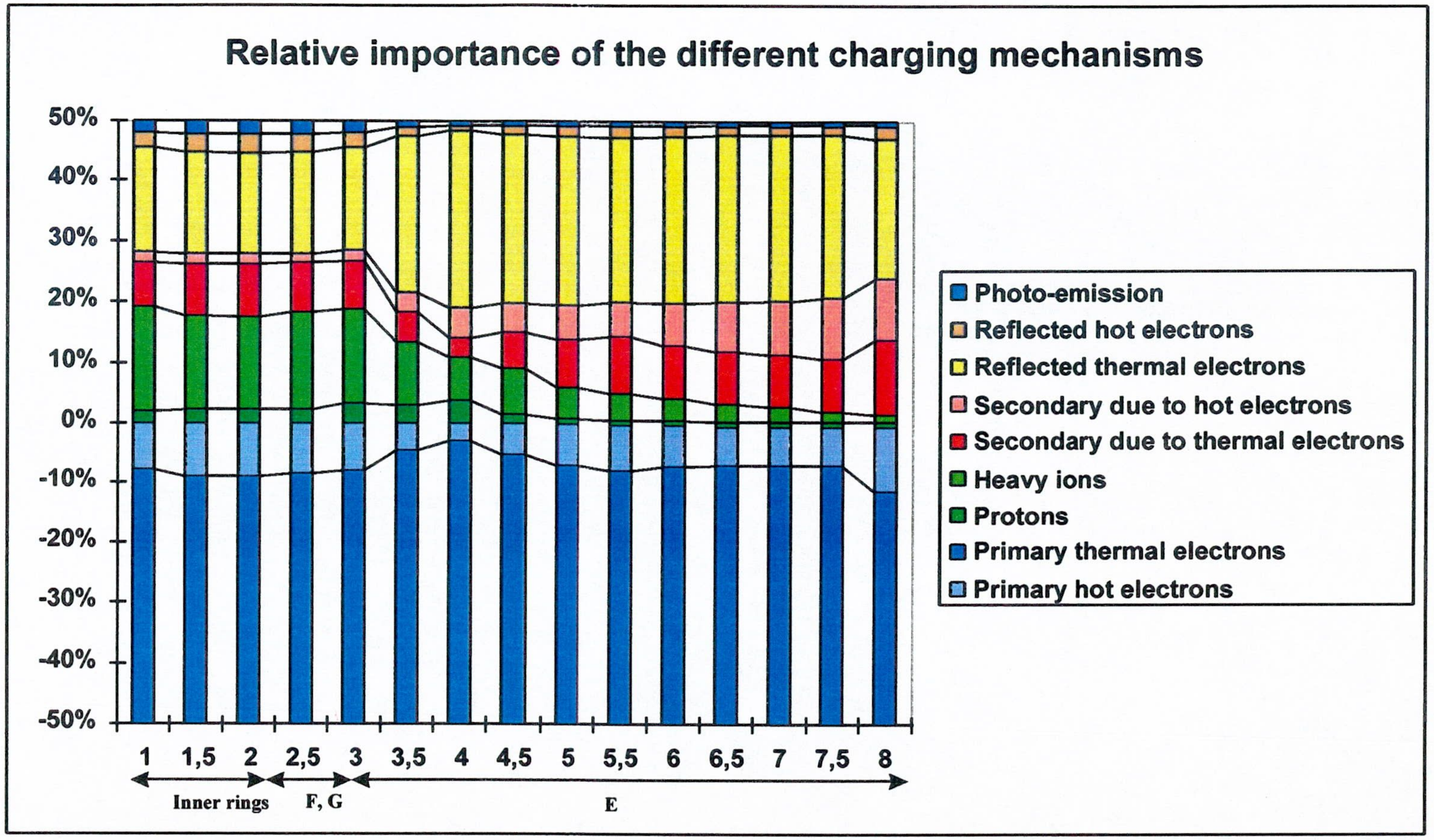

Figure 5.6: The relative importance of the different charging mechanisms for different *L*-values in Saturn's rings, for the secondary parameters (δ_m, E_m)=(1.5, 500 eV).

5.3 Interplanetary dusty plasmas

Because of the high variability of the solar wind plasma, we will consider three cases of solar wind activity: a minimum, average and maximum solar wind phase. The characterization of these phases and the evolution of the plasma with the heliocentric distance can be found in **chapter 2**. We are restricting the analysis to the ecliptic plane.

The charging current consist of

- Primary current due to electrons
- Primary current due to protons
- Primary current due to alpha particles
- Secondary current due to electrons
- Photo-emission current

The grains are assumed to have Keplerian orbits around the sun. The angular velocity of the grains is therefore given by

$$v_{\{\mathrm{ms}^{-1}\}} = \frac{29.8 \times 10^3}{\sqrt{r_{h\{AU\}}}}, \tag{5.2}$$

and unless we look close to the sun ($r_{h\{AU\}} \ll 0.5$), the relative plasma-grain velocity is given by the solar wind velocity. As explained earlier, instead of taking the reflected electrons into account, we will examine a broad (δ_m, E_m) space to account for the reflected current as well. We considered $\delta_m \in [1, 10]$ and $E_m \in [100, 1000]$ eV.

5.3.1 Analysis and results

Figure 5.7 shows the *unique* equilibrium potential V_0 as a function of the heliocentric distance for four typical cases of the secondary yield parameters. The ordinary behavior shows a decreasing equilibrium potential V_0 with increasing heliocentric distance (r_h). For large values of r_h, V_0 reaches a constant value almost independent of r_h. However, for a maximum solar wind activity, there is a possibility for the formation of a maximum equilibrium potential at a distance $r_h < 1$ AU, e.g. (δ_m, E_m)=(3, 300 eV), (δ_m, E_m)=(3, 500 eV). Furthermore for specific values of the secondary yield parameters, especially for small values of δ_m and large values of E_m e.g. (δ_m, E_m)=(1, 500 eV), very negative values of the equilibrium potential and a strong dependence on r_h occur.

Figures 5.8–5.10 show the equilibrium potential as a function of the secondary yield parameters. As can be expected, the equilibrium potential increases with increasing δ_m,

Equilibrium potentials as a function of the heliocentric distance

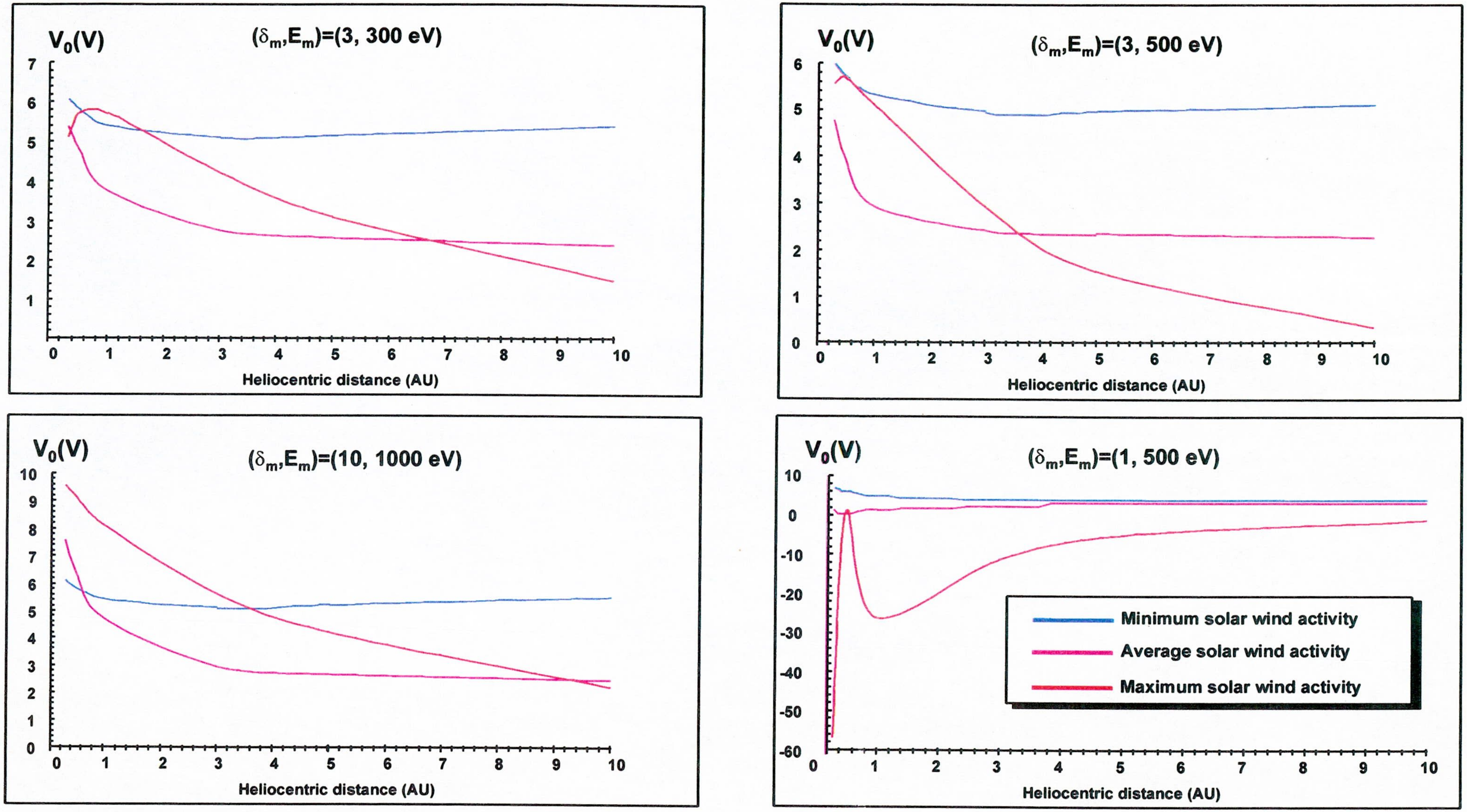

Figure 5.7: The influence of the secondary yield parameters on the equilibrium potential of interplanetary dust particles at 1 AU

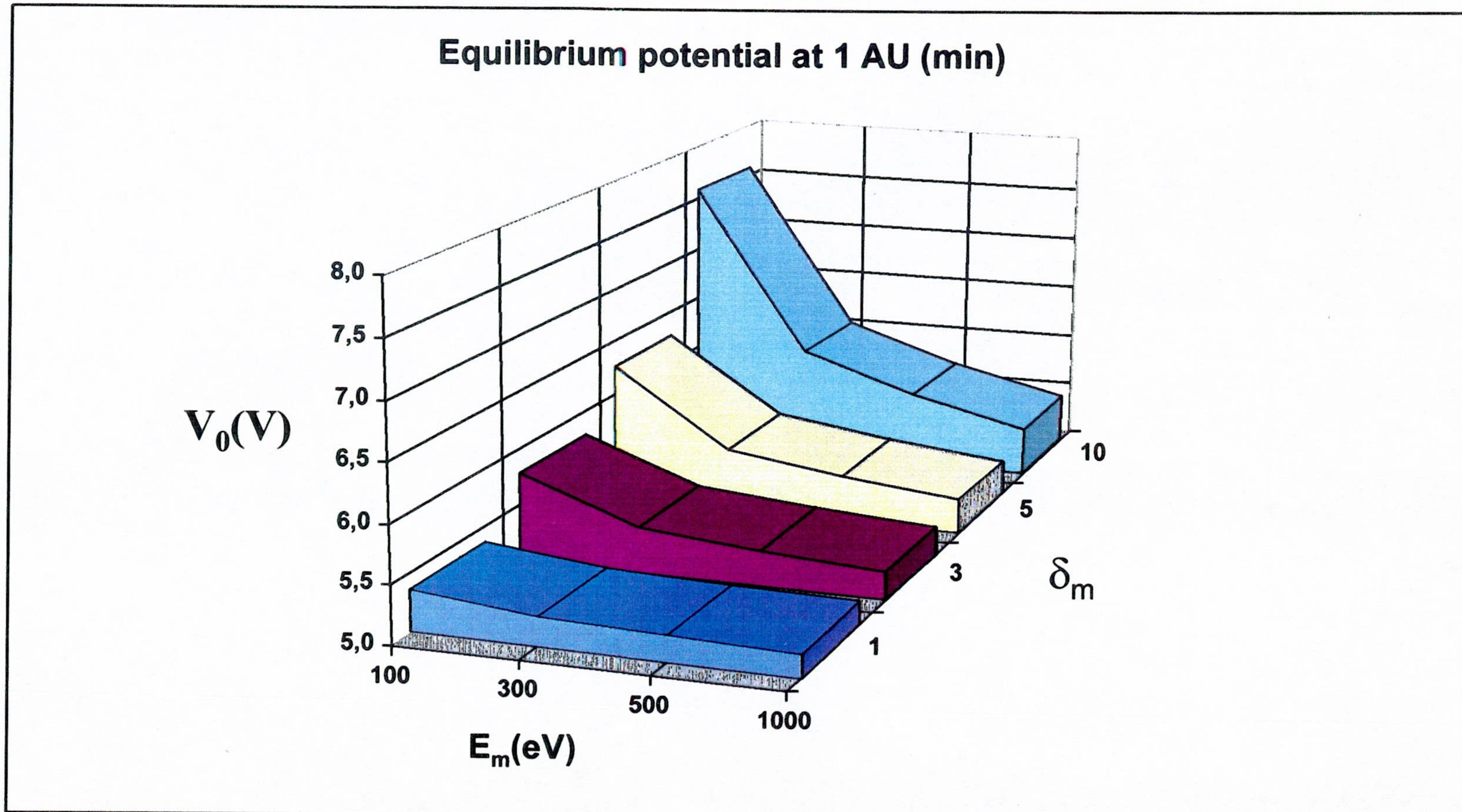

Figure 5.8: The influence of the secondary yield parameters on the equilibrium potential of interplanetary dust particles at 1 AU and for minimum solar wind activity.

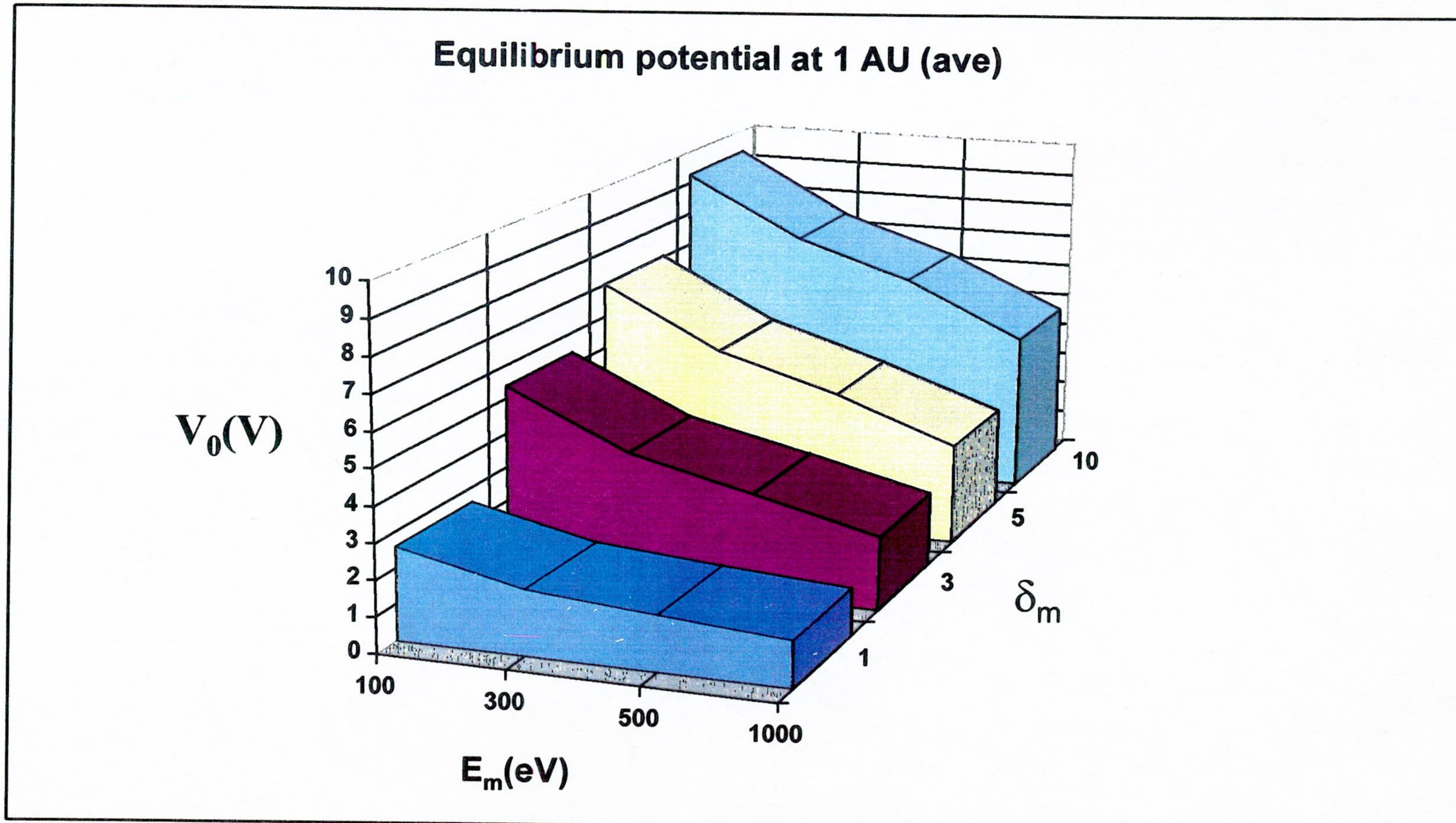

Figure 5.9: The influence of the secondary yield parameters on the equilibrium potential of interplanetary dust particles at 1 AU and for an average solar wind activity.

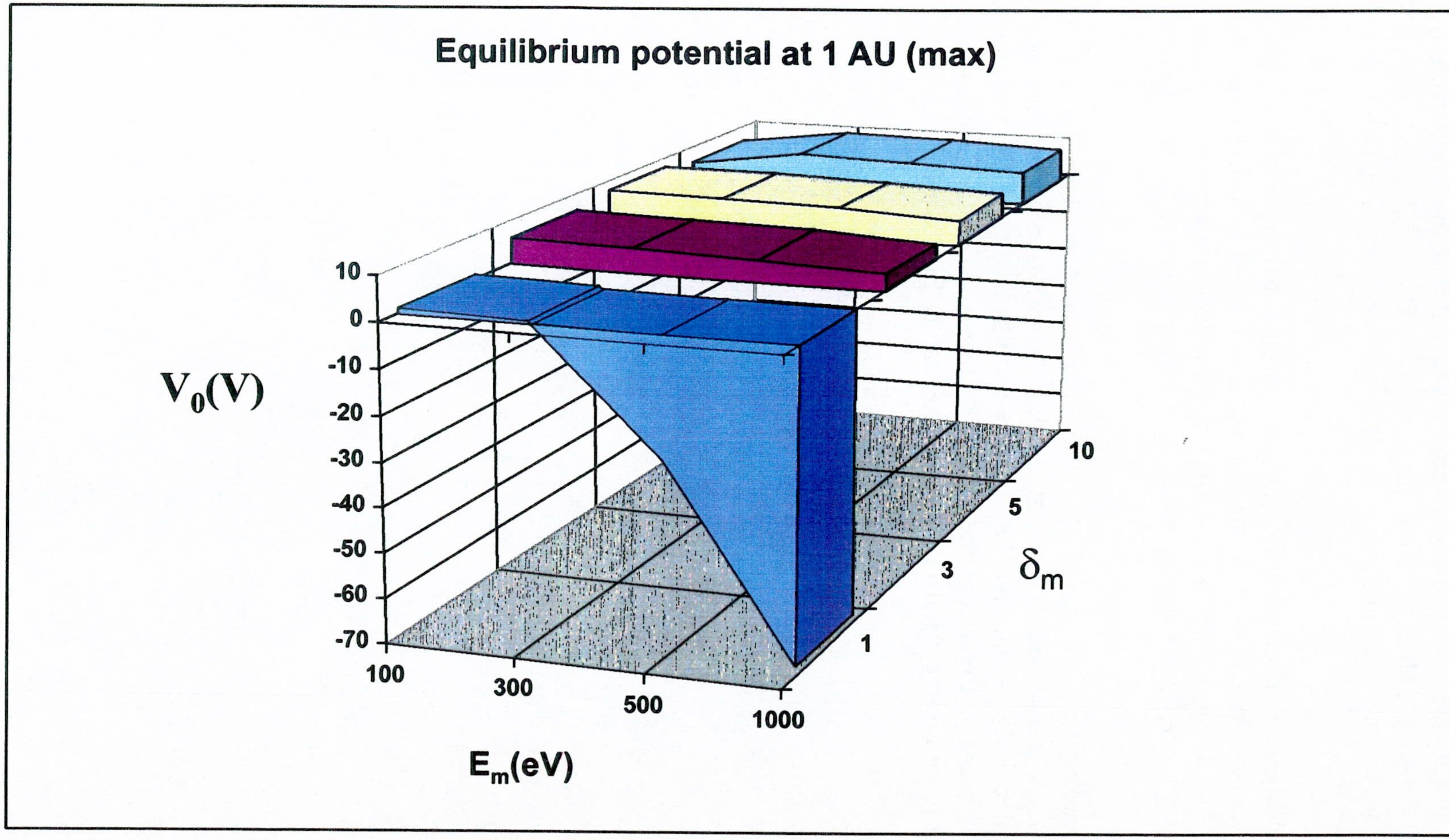

Figure 5.10: The influence of the secondary yield parameters on the equilibrium potential of interplanetary dust particles at 1 AU and for an average solar wind activity.

but decreases when E_m is increased. The former is because the total secondary charging current is proportional to δ_m, while the latter is due to the fact that the equilibrium potential is smaller than the grain potential that maximizes the secondary charging current. Indeed, when this is the case, increasing E_m will decrease the secondary electron current in the neighborhood of the equilibrium potential, and the equilibrium potential will decrease. For small values of δ_m and large values of E_m, e.g. (δ_m, E_m)=(1, 500 eV), negative grains occur, and the equilibrium solution becomes very sensitive to the secondary yield parameters.

The relative importance of the different charging mechanisms is shown in Figures 5.11–5.13. For average and maximum solar wind activity we see that both the relative photoemission and the relative primary ion currents increase with increasing r_h. The relative secondary current however decreases. The opposite is true for minimum solar wind activity.

The charging times (Figure 5.14) range from seconds to several hours. The dependence of t_{ch} on r_h is complex. The densities and therefore the particle fluxes change inversely proportional to the square of the heliocentric distance (r_h), but the energy of the population changes in a more complicated way. However the dependence of the charging time is close to an inverse square law, as can be seen in Figure 5.14.

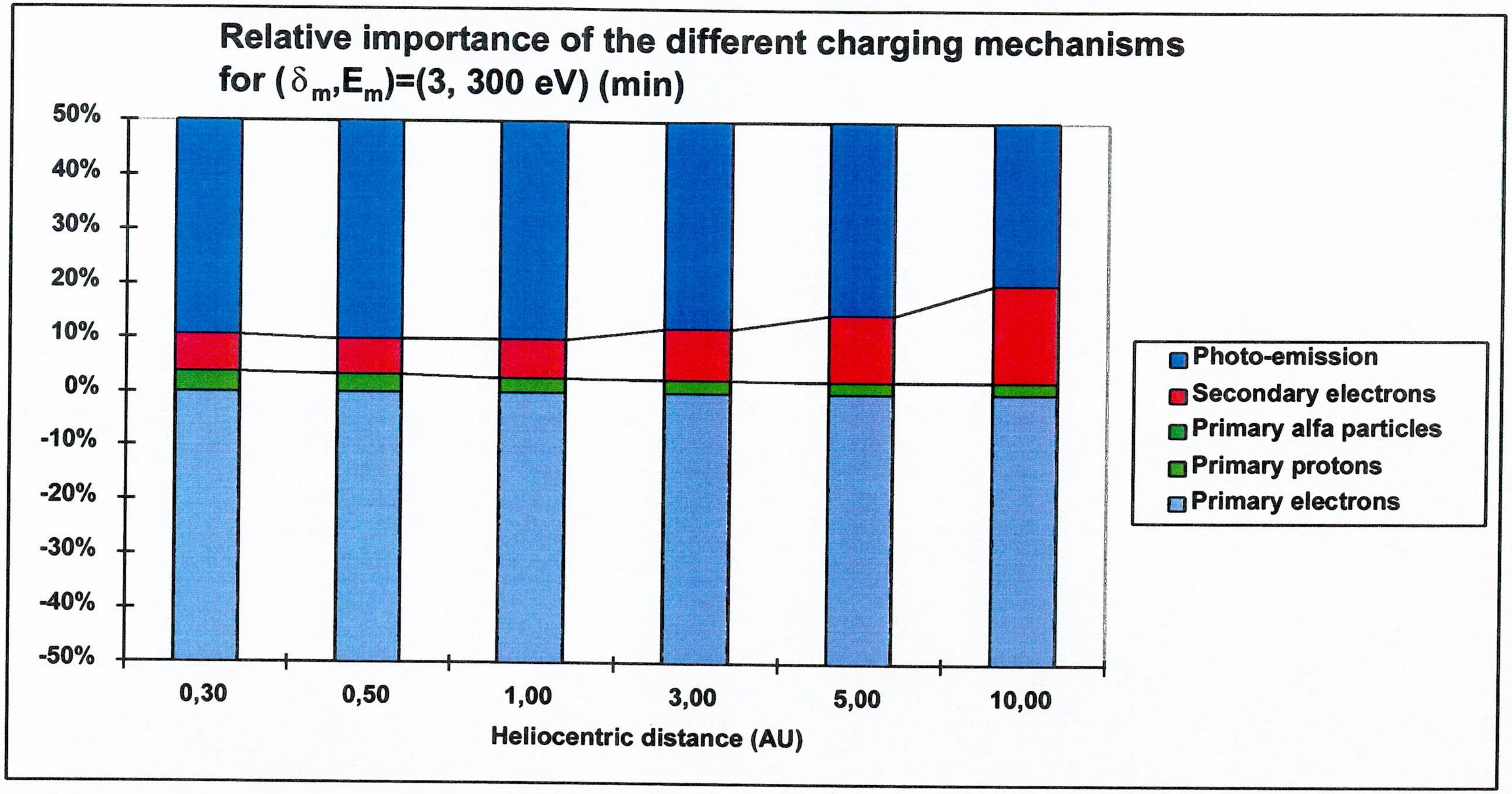

Figure 5.11: The relative importance of the different charging mechanisms in the interplantery medium as a function of heliocentric distance for minimum solar wind activity.

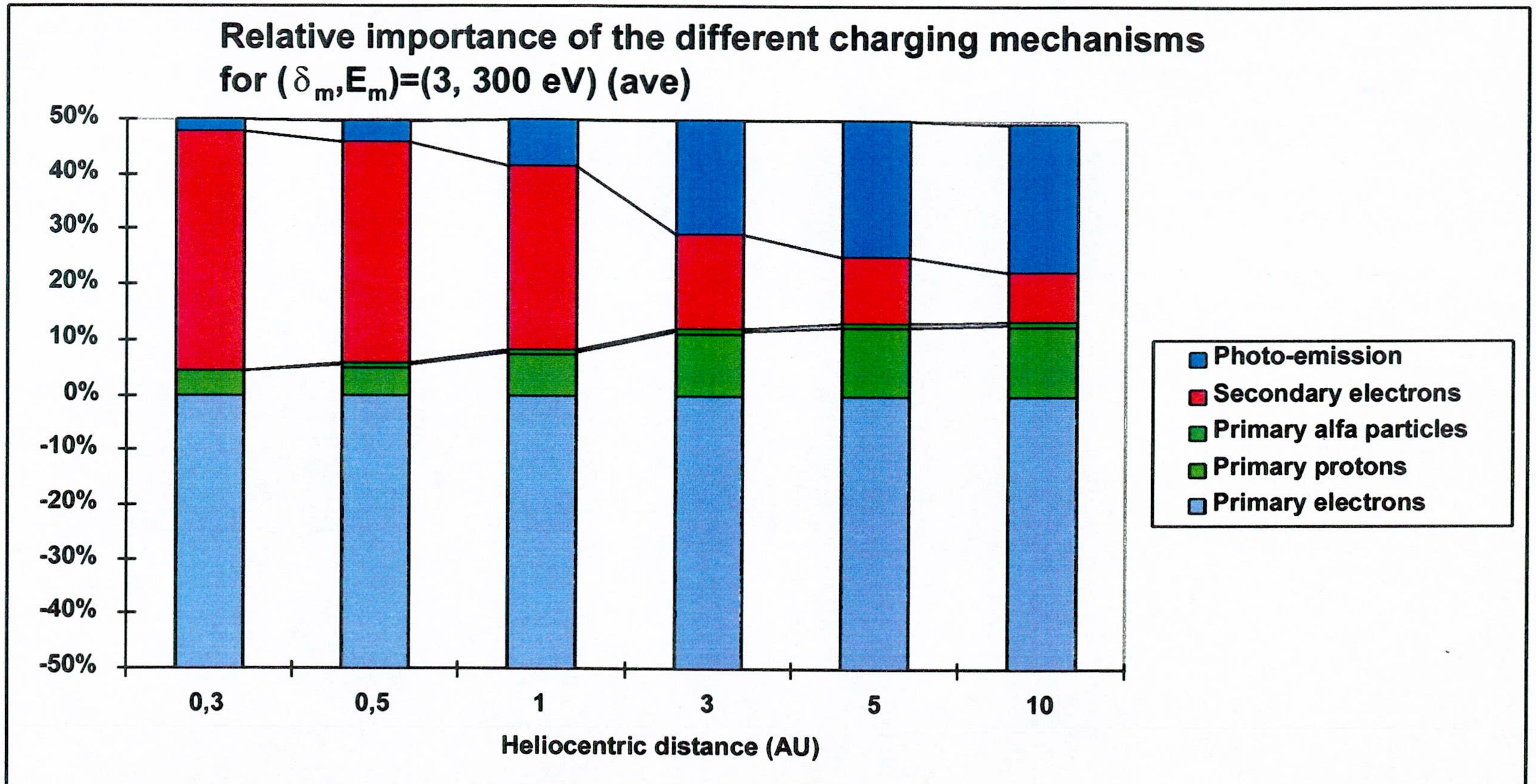

Figure 5.12: The relative importance of the different charging mechanisms in the interplantery medium as a function of heliocentric distance for an average solar wind activity.

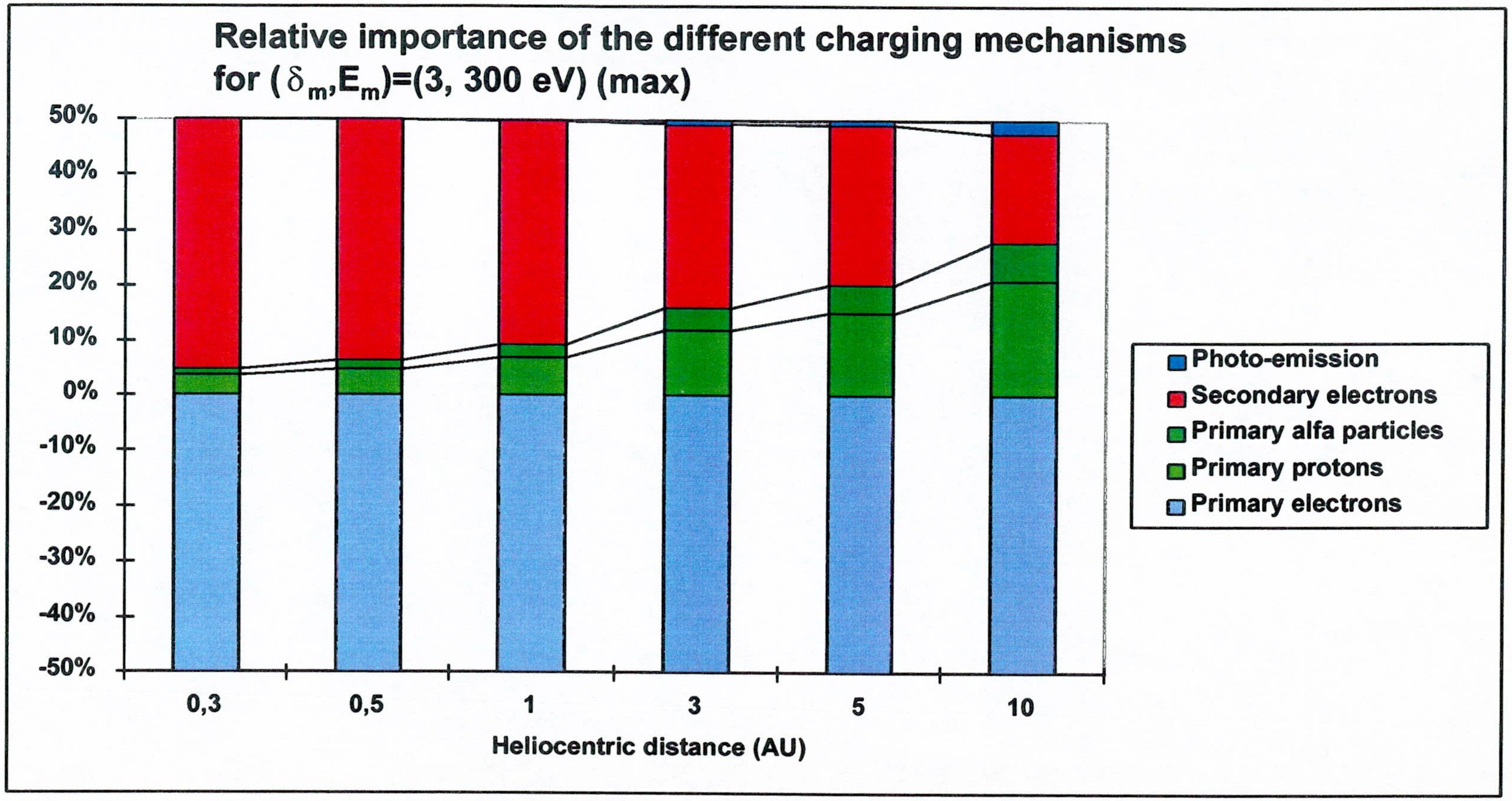

Figure 5.13: The relative importance of the different charging mechanisms in the interplantery medium as a function of heliocentric distance for a maximum solar wind activity.

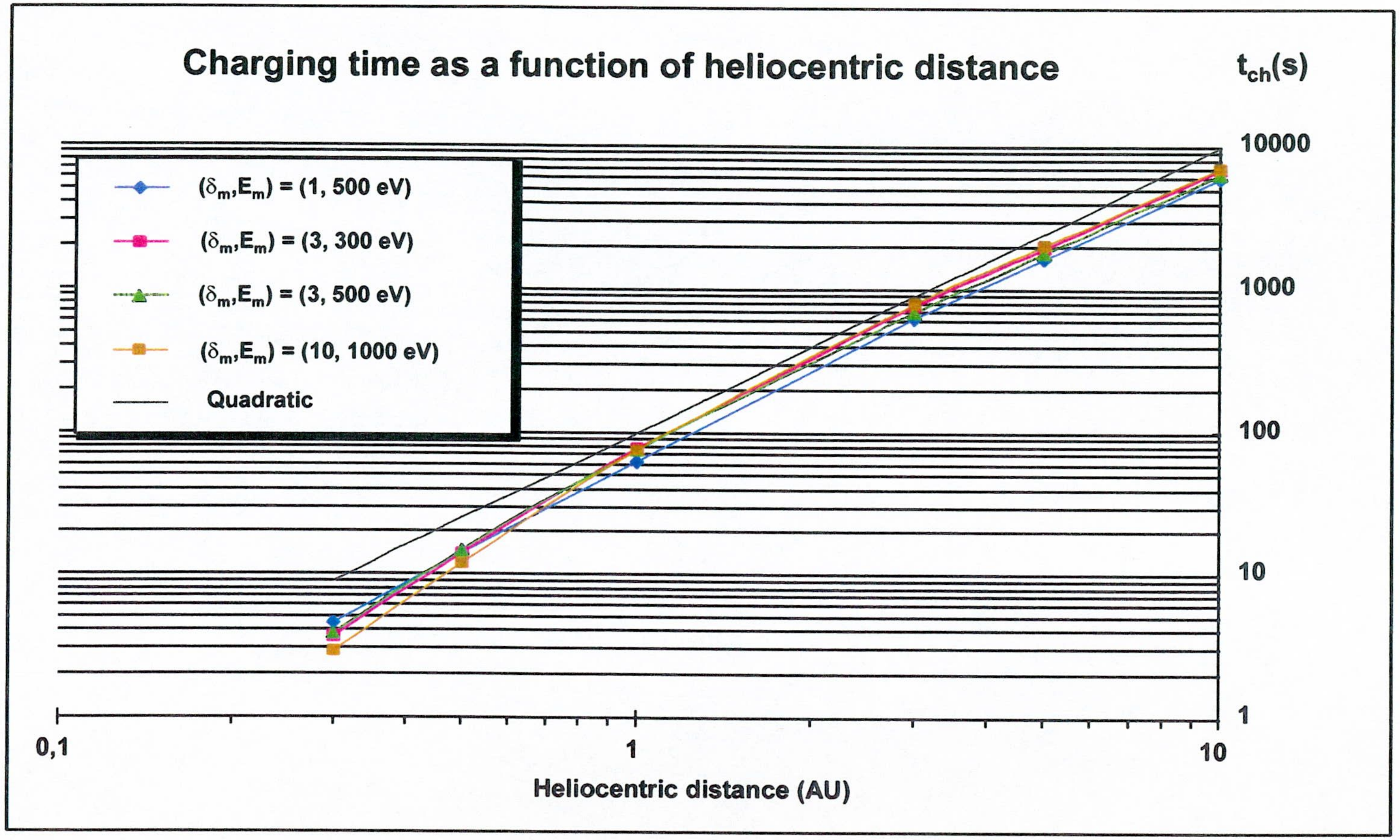

Figure 5.14: The influence of the secondary yield parameters on the charging time of interplanetary dust particles at 1 AU for an average solar wind activity.

Chapter 6

Mathematical model

We consider an infinite dusty plasma, consisting of a number of plasma species with subscript α and a single dust species of dust particles with equal radius a. In **chapter 9** however, we expand the model, including a grain size-distribution and self-gravitation. The plasma is assumed to be collisionless, except for the dust grain charging collisions. To model such a system, one can use different mathematical models. But besides of returning verifiable results, an appropriate model must be calculable as well, and in plasma physics the subtle choice of combining these two model features has been the object of study for a long time. When we start with Boltzmann's equation, and introduce the different velocity moments, an infinite set of evolution equations for the velocity moments can be derived. Although the momentum approach is totally equivalent to the Boltzmann equation, this infinite set is unmanageable. The solution for this problem is to close the system by a reasonable assumption, so that we can neglect the higher moments in the evolution equations.

It is common to assume that one is dealing with an "infinite" plasma. While not often explicitly stated the infiniteness of the system is tacitly assumed. To put the idea on a semi-quantitative foundation we can define an infinite plasma to be a spherical plasma, whose radius R is very much larger than the maximum wavelength under study:

$$\lambda_{\text{max}} \ll R \quad \text{or} \quad k_{\text{min}} R \gg 1, \tag{6.1}$$

where λ_{max} is the maximum wavelength under consideration, k_{min} is the equivalent wavenumber and R_p is the radius of the plasma. The implication of (6.1) is that physical plasma boundary effects/conditions can, to a good approximation, be ignored for the important wavelengths under consideration. As the wavelength λ approaches R boundary effects have an increasing effect on the allowable waveform and can no longer be neglected [Mace et al., 1997].

The plasma-dust interaction in a dusty plasma will cause a direct change in the multifluid model, introducing sink/source terms in continuity and momentum equations. In **section 1**, we give a short overview of the model used and how we adapted the classical multi-species approach. The explicit expressions for the source/sink terms are given in **section 2**, while the interpretation and results will be given in **section 3**.

6.1 Multi-fluid approach

6.1.1 Continuity equations

There are first the continuity equations where for the ordinary species we use a model based on the model of Bhatt and Pandey [1994], incorporating the fact that the number densities of these species are not conserved. Extra source/sink terms are due to fluctuations in the charges of the dust grains, which liberate or capture electrons and protons and hence influence their number densities:

$$\frac{\partial n_\alpha}{\partial t} + \nabla \cdot (n_\alpha \mathbf{u}_\alpha) = S_\alpha. \tag{6.2}$$

Here n_α and $\mathbf{u}_\alpha$ denote the number density and fluid velocity of population α. The source/sink terms S_α are not further specified for the time being, but are assumed to vanish in equilibrium for all species. This argument means that at equilibrium there are as much plasma particles created as collected by dust grains per time unit. This creation process can be a consequence of the emission of plasma particles by the grain, charge exchange at the grain's surface and/or ionization of neutrals in the plasma.

For the dust grains, there is no sink/source term present. The argument for this statement is that the dust number density is not affected by the dust loosing or picking up some charges. Coalescing or breaking up of the dust could be important but has not been incorporated in the treatments discussed further on. So the continuity equation for the dust remains as usual:

$$\frac{\partial n_d}{\partial t} + \nabla \cdot (n_d \mathbf{u}_d) = 0. \tag{6.3}$$

The equation expressing conservation of charge in the plasma as a whole,

$$\frac{\partial}{\partial t}\left(\sum_\alpha n_\alpha q_\alpha + n_d q_d\right) + \nabla \cdot \left(\sum_\alpha n_\alpha q_\alpha \mathbf{u}_\alpha + n_d q_d \mathbf{u}_d\right) = 0, \tag{6.4}$$

can be rewritten with the help of the continuity equations (6.2) as:

$$n_d \left(\frac{\partial}{\partial t} + u_d \cdot \nabla\right) q_d = -\sum_\alpha q_\alpha S_\alpha. \tag{6.5}$$

On the other hand the charge fluctuations are given by

$$\frac{dq_d}{dt} = \left(\frac{\partial}{\partial t} + u_d \cdot \nabla\right) q_d = \sum_\alpha I_\alpha(n_\alpha, q_d), \tag{6.6}$$

where I_α stands for the charging current that involves species α. When we combine (6.6) and (6.5), we get:

$$-\sum_\alpha q_\alpha S_\alpha = \sum_\alpha n_d I_\alpha(n_\alpha, q_d). \tag{6.7}$$

To obtain this equation no specific assumptions were needed, but to proceed we will assume that there exists a homogeneous equilibrium state, for which the total current vanishes

$$\sum_\alpha I_{\alpha 0} = 0, \tag{6.8}$$

and that the system is close to it. In that case one can linearize (6.7) and we get:

$$\begin{aligned} -\sum_\alpha q_\alpha S_\alpha \approx \sum_\alpha N_d \left.\frac{\partial I_\alpha}{\partial n_\alpha}\right|_{(N_\alpha Q_d)} & (n_\alpha - N_\alpha) \\ + \sum_\alpha N_d \left.\frac{\partial I_\alpha}{\partial q_d}\right|_{(N_\alpha Q_d)} & (q_d - Q_d) \qquad (6.9) \\ + \sum_\alpha (n_d - N_d) I_{\alpha 0}. & \qquad (6.10) \end{aligned}$$

The last term vanishes because of (6.8). Inspired by the previous result, we will introduce a form for S_α, vanishing at equilibrium for all species as stated before:

$$S_\alpha = -\nu_\alpha (n_\alpha - N_\alpha) - \mu_\alpha (q_d - Q_d), \tag{6.11}$$

keeping in mind that this expression is only valid close to equilibrium.

With this form for S_α:

$$\sum_\alpha q_\alpha \nu_\alpha (n_\alpha - N_\alpha) = \sum_\alpha N_d \left.\frac{\partial I_\alpha}{\partial n_\alpha}\right|_{(N_\alpha Q_d)} (n_\alpha - N_\alpha), \tag{6.12}$$

$$\sum_\alpha q_\alpha \mu_{\alpha d} (q_d - Q_d) = \sum_\alpha N_d \left.\frac{\partial I_\alpha}{\partial q_d}\right|_{(N_\alpha Q_d)} (q_d - Q_d). \tag{6.13}$$

This reasoning holds for any number of plasma species and therefore the coefficients ν_α and $\mu_{\alpha d}$ are given by:

$$\nu_\alpha = \frac{N_d}{q_\alpha} \left.\frac{\partial I_\alpha}{\partial n_\alpha}\right|_{(N_\alpha Q_d)}, \tag{6.14}$$

$$\mu_{\alpha d} = \frac{N_d}{q_\alpha} \left.\frac{\partial I_\alpha}{\partial q_d}\right|_{(N_\alpha Q_d)}. \tag{6.15}$$

6.1.2 Momentum equations

The momentum equations are also altered by the presence of dust. The equations of motion can be written by:

$$\left(\frac{\partial}{\partial t} + \mathbf{u}_\alpha \cdot \nabla\right) \mathbf{u}_\alpha + \frac{1}{n_\alpha m_\alpha} (\nabla \cdot \mathsf{P}_\alpha) = \frac{q_\alpha}{m_\alpha} (\mathbf{E} + \mathbf{u}_\alpha \times \mathbf{B}) - \mathbf{M}_{\alpha d} \tag{6.16}$$

$$\left(\frac{\partial}{\partial t} + \mathbf{u}_d \cdot \nabla\right) \mathbf{u}_d + \frac{1}{n_d m_d} (\nabla \cdot \mathsf{P}_d) = \frac{q_d}{m_d} (\mathbf{E} + \mathbf{u}_d \times \mathbf{B}) - \sum_\alpha \mathbf{M}_{d\alpha}, \tag{6.17}$$

where P_α stands for the pressure tensor of species α. For the specific form of the momentum exchanges due to the charging process, we were inspired by the linearized expressions usually written for ordinary collisional exchanges:

$$\mathbf{M}_{\alpha d} = \gamma_{\alpha d}(\mathbf{u}_\alpha - \mathbf{U}_\alpha - \mathbf{u}_d + \mathbf{U}_d), \tag{6.18}$$
$$\mathbf{M}_{d\alpha} = \gamma_{d\alpha}(\mathbf{u}_d - \mathbf{U}_d - \mathbf{u}_\alpha + \mathbf{U}_\alpha). \tag{6.19}$$

The coefficients $\gamma_{\alpha d}$ denote the frequency characterizing the rate of capture of plasma particles by dust particles, and they should be computed from an appropriate and self-consisting theory, as outlined further in this chapter. This frequency is assumed to be constant, unlike the model of Bhatt and Pandey [1994], where the variation of $\gamma_{\alpha d}$ is taken into account. Note that for a non-drifting plasma our model corresponds to theirs.

6.1.3 Closure

- The evolution of the pressure tensor is given by:

$$\frac{\partial \mathsf{P}_\alpha}{\partial t} + \nabla \cdot (\mathbf{u}_\alpha \mathsf{P}_\alpha) + \mathsf{P}_\alpha \cdot \nabla \mathbf{u}_\alpha + [\mathsf{P}_\alpha \cdot \nabla \mathbf{u}_\alpha]^T + \nabla \cdot \mathsf{Q}_\alpha + \frac{q_\alpha}{m_\alpha}\left[\mathbf{B} \times \mathsf{P}_\alpha + (\mathbf{B} \times \mathsf{P}_\alpha)^T\right] = \mathsf{S}_\alpha, \tag{6.20}$$

  in which Q_α stands for the heat tensor for species α. Herein we neglected the heat flow term and all velocity-flow tensor terms involving the average velocity compared to the thermal-pressure tensor terms [Shkarkofsky et al., 1966, pp473]. The heat flow tensor may be neglected provided that the phase velocity is greater than the thermal plasma velocity. Also the influence of the capture/release of plasma particles by the grains is taken into account by using the sink/source tensor S_α.

- For an isotropic plasma this tensor becomes diagonal $\mathsf{P}_\alpha = p_\alpha \mathsf{1}$. In that case, we can use an appropriate polytropic law, of the form:

$$p_\alpha \sim n_\alpha^{\gamma_\alpha}, \tag{6.21}$$

  where γ_α stands for the polytropic exponent. This is a general equation that includes e.g. adiabatic ($\gamma_\alpha = 5/3$) equations of state. Note that the isotropic assumption is *not* a special case of the anisotropic case, as might be thought. Indeed an isotropic tensor (different from zero) cannot be a solution of (6.20).

- Furthermore if the plasma pressure can totally be neglected, the cold plasma approximation can be used, for which $\mathsf{P}_\alpha = 0$. This is valid if the plasma thermal velocities are much smaller than the phase velocity of the waves, and hence the cold plasma approximations might be seen as the zeroth order approximation for the other models.

6.1.4 Maxwell's equations

The system is closed by using the equations of Maxwell:

$$\nabla \times \mathbf{E} + \frac{\partial \mathbf{B}}{\partial t} = \mathbf{0}, \tag{6.22}$$

$$\varepsilon_0 \nabla \cdot \mathbf{E} = \sum_\alpha n_\alpha q_\alpha + n_d q_d, \tag{6.23}$$

$$c^2 \nabla \times \mathbf{B} = \frac{\partial \mathbf{E}}{\partial t} + \frac{1}{\varepsilon_0}\left[\sum_\alpha n_\alpha q_\alpha \mathbf{u}_\alpha + n_d q_d \mathbf{u}_d\right], \tag{6.24}$$

$$\nabla \cdot \mathbf{B} = 0. \tag{6.25}$$

However for electrostatic modes we do not need the full Maxwell set, and Poisson's equation is sufficient:

$$\varepsilon_0 \nabla^2 U = -\sum_\alpha n_\alpha q_\alpha - n_d q_d, \tag{6.26}$$

with U standing for the electrostatic potential, for which $\mathbf{E} = -\nabla U$.

6.2 Calculation of the different parameters

The calculation for the different dust related parameters ν_α, $\mu_{\alpha d}$, $\gamma_{d\alpha}$ and $\gamma_{\alpha d}$ was given by Meuris and Verheest [1996], assuming that the charging of the grains takes place solely due to the attachment of electrons and ions to the dust grains, and that the effects of secondary charging, radiation, etc. can be ignored. We consider spherical dust grains with radius a. The charging current perturbation, as well as the dust charge perturbation, are assumed to be small, so that we can consider the different charging frequencies to be independent of these perturbations. The current on a dust particle can be described in an orbit-limited theory for an unmagnetized plasma by

$$I_\alpha(\Gamma_\alpha) = n_\alpha q_\alpha \int_{|\mathbf{v}|=\eta\sqrt{\Gamma_\alpha}}^{|\mathbf{v}|=\infty} v \sigma_\alpha f_\alpha(\mathbf{v}) d^3\mathbf{v}, \tag{6.27}$$

where the subscript α stands for electrons ($\alpha = e$) or ions ($\alpha = i$), $\mathbf{v}$ is the relative grain-plasma particle velocity, $v = |\mathbf{v}|$, while $f_\alpha(\mathbf{v})$ is the equilibrium distribution function for species α, which can be Maxwellian or shifted Maxwellian, but its form need not be specified. Then σ_α is the charging cross section, given by

$$\sigma_\alpha = \pi a^2 \left(1 - \frac{\Gamma_\alpha}{v^2}\right), \tag{6.28}$$

and $\eta = 1$ for negative particles, because only sufficiently fast negative particles can charge the dust grains. For positive particles, $\eta = 0$. Γ_α was introduced to make the notation easier:

$$\Gamma_\alpha = \frac{2q_\alpha(V - V_p)}{m_\alpha} = \frac{2q_\alpha q_d}{m_\alpha C}, \tag{6.29}$$

with V the grains' constant surface potential and V_p the average potential of the ambient plasma. C stands for the capacitance of the grain which we can find in Whipple [1981] or Houpis and Whipple [1987]. Note that the use of their orbit-limited theory implies that the dust grains are considered as point particles, and hence $a \ll \lambda_D$.

We split all quantities in equilibrium and fluctuating (not necessarily small) parts, where the latter are denoted by superposed carets:

$$n_\alpha = N_\alpha + \widehat{n}_\alpha, \tag{6.30}$$
$$I_\alpha = I_{\alpha 0} + \widehat{I}_\alpha, \tag{6.31}$$
$$\Gamma_\alpha = \Gamma_{\alpha 0} + \widehat{\Gamma}_\alpha, \tag{6.32}$$
$$\phi = \phi_0 + \widehat{\phi}. \tag{6.33}$$

The charging currents, due to the collisions of plasma particles of species α with dust grains, can be written as:

$$I_\alpha = n_\alpha(I_1(\Gamma_\alpha) - \Gamma_\alpha I_2(\Gamma_\alpha)), \tag{6.34}$$

with

$$I_1(\Gamma_\alpha) = q_\alpha \pi a^2 \int_{|v|=\eta\sqrt{\Gamma_\alpha}}^{|v|=\infty} v f_\alpha(\mathbf{v}) d^3\mathbf{v}, \tag{6.35}$$
$$I_2(\Gamma_\alpha) = q_\alpha \pi a^2 \int_{|v|=\eta\sqrt{\Gamma_\alpha}}^{|v|=\infty} \frac{f_\alpha(\mathbf{v})}{v} d^3\mathbf{v}. \tag{6.36}$$

This becomes to first order in the grain charge perturbation:

$$\begin{aligned} I_{\alpha 0} + \widehat{I}_\alpha &= N_\alpha \left(1 + \frac{\widehat{n}_\alpha}{N_\alpha}\right) (I_1(\Gamma_{\alpha 0}) - \Gamma_{\alpha 0} I_2(\Gamma_{\alpha 0})) \\ &\times \left\{1 + \frac{\frac{dI_1}{d\Gamma}(\Gamma_{\alpha 0}) - \Gamma_{\alpha 0}\frac{dI_2}{d\Gamma}(\Gamma_{\alpha 0}) - I_2(\Gamma_{\alpha 0})}{I_1(\Gamma_{\alpha 0}) - \Gamma_{\alpha 0} I_2(\Gamma_{\alpha 0})}\widehat{\Gamma}_\alpha\right\}. \end{aligned} \tag{6.37}$$

It is readily verified, however, with the help of the definitions (6.35) and (6.36), that

$$\frac{dI_1}{d\Gamma}(\Gamma_{\alpha 0}) - \Gamma_{\alpha 0}\frac{dI_2}{d\Gamma}(\Gamma_{\alpha 0}) = 0. \tag{6.38}$$

The charge fluctuations are given by

$$\frac{dq_d}{dt} = \sum_\alpha I_\alpha, \tag{6.39}$$

resulting in

$$n_d \frac{dq_d}{dt} = n_d \sum_\alpha \frac{I_{\alpha 0}}{N_\alpha}(n_\alpha - N_\alpha) - \sum_\alpha \frac{2 n_d q_\alpha}{m_\alpha C} \frac{I_{\alpha 0} I_2(\Gamma_{\alpha 0})}{I_1(\Gamma_{\alpha 0}) - \Gamma_{\alpha 0} I_2(\Gamma_{\alpha 0})}(q_d - Q_d). \tag{6.40}$$

When we compare this result with (6.5) and (6.11), we can find in zeroth-order approximation that

$$\nu_\alpha = \frac{N_d I_{\alpha 0}}{q_\alpha N_\alpha}, \tag{6.41}$$
$$\mu_\alpha = -\frac{2N_d}{m_\alpha C} \frac{I_{\alpha 0} I_2(\Gamma_{\alpha 0})}{I_1(\Gamma_{\alpha 0}) - \Gamma_{\alpha 0} I_2(\Gamma_{\alpha 0})}. \tag{6.42}$$

Furthermore, the frequency $\gamma_{\alpha d}$ characterizing the rate of capture of plasma particles by dust particles can be calculated to zeroth order as

$$\gamma_{\alpha d} = N_d \int_{|\mathbf{v}|=\eta\sqrt{\Gamma_\alpha}}^{|\mathbf{v}|=\infty} v\sigma_\alpha f_\alpha(\mathbf{v}) d^3\mathbf{v} = \frac{N_d I_{\alpha 0}}{N_\alpha q_\alpha}, \tag{6.43}$$

and we verify readily that $\gamma_{\alpha d} = \nu_\alpha$. Assuming conservation of momentum between any two species, as true collisions would do, then yields an expression for $\gamma_{d\alpha}$ as well:

$$\gamma_{d\alpha} = \gamma_{\alpha d} \frac{N_\alpha m_\alpha}{N_d m_d}. \tag{6.44}$$

To find expressions for μ_α, we assume a shifted Maxwellian distribution function:

$$f_\alpha(\mathbf{v}) = \left(\frac{m_\alpha}{2\pi k T_\alpha}\right)^{\frac{3}{2}} \exp\left[-\frac{m(\mathbf{v}-\mathbf{U}_\alpha)^2}{2kT_\alpha}\right]. \tag{6.45}$$

The equilibrium charging currents for an electron-proton plasma are given by Whipple [1981] With this distribution function it is easy to calculate the ratio I_1/I_2. We define $b_\alpha = \eta\sqrt{\Gamma_{\alpha 0}}/(\sqrt{2}c_{s\alpha})$, and $w_\alpha = U_\alpha/(\sqrt{2}c_{s\alpha})$, and then calculate the ratio in a more compact form. For electrons ($\eta = 1$) the thermal velocity is usually much higher than the drift velocity in the dust frame, hence we take the limit $w_e \to 0$ and find

$$\left\{\frac{I_1}{I_2}\right\}_e = \frac{2kT_e}{m_e} + \Gamma_{e0}. \tag{6.46}$$

On the other hand for the ions we have to take the limit $b_i \to 0$:

$$\left\{\frac{I_1}{I_2}\right\}_i = \frac{2kT_i}{m_i}\left(\frac{1}{2} + w_i^2 + \frac{w_i e^{-w_i^2}}{\sqrt{\pi}\mathrm{Erf}(w_i)}\right), \tag{6.47}$$

which becomes

$$\left\{\frac{I_1}{I_2}\right\}_i = \frac{2kT_i}{m_i} \tag{6.48}$$

for driftless ions ($w_i \to 0$).

6.3 Interpretation of the model parameters

We can derive from (6.5) and (6.11) that charge fluctuations are driven by the difference of the plasma densities and their equilibrium values, with a natural decay rate

$$t_{ch}^{-1} = -\sum_\alpha q_\alpha \mu_\alpha / N_d. \tag{6.49}$$

This rate is hence the *charge-relaxation frequency.*

The continuity equation for the plasma particles can be written for dust grains at equilibrium charge as:

$$\frac{dn_\alpha}{dt} = -\nu_\alpha(n_\alpha - N_\alpha). \tag{6.50}$$

Therefore the coefficients ν_α describe the density relaxation due to capture/emission of plasma particles by the dust grains, and therefore we will call them *continuity attachment frequencies*. As we saw in the previous section, the coefficients $\gamma_{\alpha d} = \nu_\alpha$ for a Maxwellian plasma. Because there is no reason why a fully self-consistent calculation of these coefficients would confirm this, we keep the different notation for these coefficients. The coefficients $\gamma_{\alpha d}$ can be regarded as *momentum attachment frequencies*.

Chapter 7

Electrostatic modes

7.1 Introduction

The classification of the zoo of waves that exist in a plasma is by no means an easy nor a straightforward task. It is known that when one introduces collisions among the plasma species, the different modes are going to couple. This coupling exists in dusty plasmas even in the *collisionless model* due to the grain charging mechanism. We will address *electrostatic* modes in **chapter 7** while in **chapter 8** *electromagnetic* modes are analyzed. The former involve no oscillating magnetic field, while the latter cover all modes that are not electrostatic. Eminent reviews of waves and instabilities in dusty plasmas are given by Shukla [1992, 1996] and Verheest [1996].

Electrostatic waves are generated, for example, when a perturbation creates a charge imbalance in a neutral fluid element. This charge imbalance will accelerate electrons (ions) in the neighborhood of the charged fluid element, resulting in charges oscillating back and forth. These oscillations involve only the electric field and they are defined as electrostatic waves (the oscillating magnetic field is zero). The equation of Faraday shows that the electric field $\mathbf{E}$ is then parallel to the direction of the wave vector $\mathbf{k}$.

When there is no magnetic field, or when the propagation of the waves is parallel to the field lines, we recover Langmuir modes, dust ion-acoustic modes, dust-acoustic modes, and zero frequency modes related to the dust charging. All those modes will couple with the charging mechanism. Indeed, as we have seen in **chapter 4**, the charging of the grains depends on the local plasma characteristics. If a wave disturbs these characteristics, the charging status of the grains is affected and the grain charging couples to the wave mode. When the propagation is perpendicular to the ambient magnetic field electrostatic modes couple also to the cyclotron motion and cyclotron resonances may appear. We must stress, however, that the description of these resonances requires a self-consisting charging theory in a magnetized plasma, which is not yet available.

The description of electrostatic waves, including dust charge variation, has been investigated before. The first to do so were Melandsø et al. [1993] who analyzed the damping of the dust-acoustic mode. However, their treatment was not really self-consistent because they used a Boltzmann distribution for the plasma particles from the start, and we will see that this neglects some essential elements for both small and long wavelengths [Meuris and Verheest, 1996]. Independently Varma et al. [1993] analyzed also Langmuir and dust ion-acoustic modes, but again without using source/sink terms in the continuity equations. Similarly, Jana et al. [1993] discussed the whole range of electrostatic modes using a comparable model. The first fully self-consistent approaches were carried out by Bhatt and Pandey [1994], Meuris and Verheest [1996] and Bhatt [1997].

In this chapter, we are giving a more systematic treatment along the lines of Bhatt and Pandey [1994], starting with a minimum of assumptions. This makes it possible to see the relevance of the different assumptions made by other authors.

This chapter is organized as follows. In section 2, we derive the dispersion law, while in section 3 modes in a non magnetized plasma are analyzed. The influence of a magnetic field on the wave propagation is the subject of section 4. Case studies are carried out in section 5, and section 6 states the conclusions.

7.2 Mathematical description

7.2.1 Dispersion law

For a good understanding the model equations are repeated here:

$$\begin{aligned}
\frac{\partial n_e}{\partial t} + \frac{\partial}{\partial z}(n_e u_e) &= -\nu_e(n_e - N_e) - \mu_e(q_d - Q_d), \\
\frac{\partial n_i}{\partial t} + \frac{\partial}{\partial z}(n_i u_i) &= -\nu_i(n_i - N_i) - \mu_i(q_d - Q_d),
\end{aligned} \tag{7.1}$$

$$\frac{\partial n_d}{\partial t} + \frac{\partial}{\partial z}(n_d u_d) = 0 \tag{7.2}$$

$$\begin{aligned}
\left(\frac{\partial}{\partial t} + u_e\frac{\partial}{\partial z}\right) u_e + \frac{\kappa T_e}{m_e n_e}\frac{\partial n_e}{\partial z} &= -\frac{q_e}{m_e}\frac{\partial \varphi}{\partial z} - \gamma_{ed}(u_e - U_e - u_d + U_d), \\
\left(\frac{\partial}{\partial t} + u_i\frac{\partial}{\partial z}\right) u_i + \frac{\kappa T_i}{m_i n_i}\frac{\partial n_i}{\partial z} &= -\frac{q_i}{m_i}\frac{\partial \varphi}{\partial z} - \gamma_{id}(u_i - U_i - u_d + U_d),
\end{aligned} \tag{7.3}$$

$$\begin{aligned}
\left(\frac{\partial}{\partial t} + u_d\frac{\partial}{\partial z}\right) u_d &= -\frac{q_d}{m_d}\frac{\partial \varphi}{\partial z} - (\gamma_{de} + \gamma_{di})(u_d - U_d) \\
&\quad + \gamma_{de}(u_e - U_e) + \gamma_{di}(u_i - U_i),
\end{aligned} \tag{7.4}$$

$$0 = \varepsilon_0 \frac{\partial^2 U}{\partial z^2} + n_e q_e + n_i q_i + n_d q_d, \tag{7.5}$$

$$\frac{\partial}{\partial t}\left(n_e q_e + n_i q_i + n_d q_d\right) = -\frac{\partial}{\partial z}\left(n_e q_e u_e + n_i q_i u_i + n_d q_d u_d\right) \tag{7.6}$$

When we assume that all quantities are going like $\exp[i(\omega t - kx)]$, we can Fourier transform and linearize the equations (7.1–7.6) following the outline of Meuris and Verheest [1996]. This implies that there exists a local equilibrium solution, homogeneous in the space-coordinates. This assumption is valid when a typical wavelength is much smaller than a typical length scale for the variations of the plasma parameters.

Since the plasma and dust equations are coupled by the charge exchange terms, we have to proceed carefully. We will introduce some short notations, in order to write the resulting expressions in a compact form:

$$\begin{aligned}
\omega_{\nu e} &= \omega - kU_e + i\nu_e, & \omega_{\gamma e} &= \omega - kU_e + i\gamma_{ed}, \\
\omega_{\nu i} &= \omega - kU_i + i\nu_i, & \omega_{\gamma i} &= \omega - kU_i + i\gamma_{id}, \\
\omega_d &= \omega - kU_d, & \omega_{\gamma d} &= \omega - kU_d + i\gamma_{de} + i\gamma_{di}.
\end{aligned} \tag{7.7}$$

After linearization and Fourier analysis we find from (7.1) and (7.3) that

$$\delta n_e = \frac{kN_e}{\omega_{\nu e}}\delta u_e - i\frac{\mu_e}{\omega_{\nu e}}\delta q_d, \tag{7.8}$$

$$\delta u_e = \frac{kc_{se}^2}{N_e\omega_{\gamma e}}\delta n_e + \frac{kq_e}{m_e\omega_{\gamma e}}\delta U + i\frac{\gamma_{ed}}{\omega_{\gamma e}}\delta u_d, \tag{7.9}$$

$$\delta n_i = \frac{kN_i}{\omega_{\nu i}}\delta u_i - i\frac{\mu_i}{\omega_{\nu i}}\delta q_d, \tag{7.10}$$

$$\delta u_i = \frac{kc_{si}^2}{N_i\omega_{\gamma i}}\delta n_i + \frac{kq_i}{m_i\omega_{\gamma i}}\delta U + i\frac{\gamma_{id}}{\omega_{\gamma i}}\delta u_d. \tag{7.11}$$

In these expressions c_{se} and c_{si} stand for the thermal velocities of the different plasma species, defined through $c_{se,si}^2 = \kappa T_{e,i}/m_{e,i}$. Solving of (7.8)–(7.11) for the different electron and ion variables yields

$$\delta n_e = \frac{\varepsilon_0 k^2\omega_{pe}^2}{q_e(\omega_{\nu e}\omega_{\gamma e} - k^2c_{se}^2)}\delta U + i\frac{kN_e\gamma_{ed}}{\omega_{\nu e}\omega_{\gamma e} - k^2c_{se}^2}\delta u_d - i\frac{\mu_e\omega_{\gamma e}}{\omega_{\nu e}\omega_{\gamma e} - k^2c_{se}^2}\delta q_d, \tag{7.12}$$

$$\delta u_e = \frac{kq_e\omega_{\nu e}}{m_e(\omega_{\nu e}\omega_{\gamma e} - k^2c_{se}^2)}\delta U + i\frac{\gamma_{ed}\omega_{\nu e}}{\omega_{\nu e}\omega_{\gamma e} - k^2c_{se}^2}\delta u_d - i\frac{kc_{se}^2\mu_e}{N_e(\omega_{\nu e}\omega_{\gamma e} - k^2c_{se}^2)}\delta q_d, \tag{7.13}$$

$$\delta n_i = \frac{\varepsilon_0 k^2\omega_{pi}^2}{q_i(\omega_{\nu i}\omega_{\gamma i} - k^2c_{si}^2)}\delta U + i\frac{kN_i\gamma_{id}}{\omega_{\nu i}\omega_{\gamma i} - k^2c_{si}^2}\delta u_d - i\frac{\mu_i\omega_{\gamma i}}{\omega_{\nu i}\omega_{\gamma i} - k^2c_{si}^2}\delta q_d, \tag{7.14}$$

$$\delta u_i = \frac{kq_i\omega_{\nu i}}{m_i(\omega_{\nu i}\omega_{\gamma i} - k^2c_{si}^2)}\delta U + i\frac{\gamma_{id}\omega_{\nu i}}{\omega_{\nu i}\omega_{\gamma i} - k^2c_{si}^2}\delta u_d - i\frac{kc_{si}^2\mu_i}{N_i(\omega_{\nu i}\omega_{\gamma i} - k^2c_{si}^2)}\delta q_d. \tag{7.15}$$

For the dust grains we have that

$$\delta n_d = \frac{kN_d}{\omega_d}\delta u_d, \tag{7.16}$$

$$\delta u_d = \frac{kQ_d}{m_d\omega_{\gamma d}}\delta U + i\frac{\gamma_{de}}{\omega_{\gamma d}}\delta u_e + i\frac{\gamma_{di}}{\omega_{\gamma d}}\delta u_i. \tag{7.17}$$

Inserting these results into the linearized and Fourier transformed equation of Poisson (7.5) gives us a global expression of the form

$$A\delta U + B\delta u_d + C\delta q_d = 0, \tag{7.18}$$

with

$$A = \varepsilon_0 k^2 \left\{ \frac{\omega_{pe}^2}{\omega_{\nu e}\omega_{\gamma e} - k^2 c_{se}^2} + \frac{\omega_{pi}^2}{\omega_{\nu i}\omega_{\gamma i} - k^2 c_{si}^2} - 1 \right\}, \tag{7.19}$$

$$B = \frac{kN_d Q_d}{\omega_d} + i\frac{kN_e q_e \gamma_{ed}}{\omega_{\nu e}\omega_{\gamma e} - k^2 c_{se}^2} + i\frac{kN_i q_i \gamma_{id}}{\omega_{\nu i}\omega_{\gamma i} - k^2 c_{si}^2}, \tag{7.20}$$

$$C = N_d - i\frac{\mu_e q_e \omega_{\gamma e}}{\omega_{\nu e}\omega_{\gamma e} - k^2 c_{se}^2} - i\frac{\mu_i q_i \omega_{\gamma i}}{\omega_{\nu i}\omega_{\gamma i} - k^2 c_{si}^2}. \tag{7.21}$$

Similarly the global conservation of charge (7.6) gives that

$$D\delta U + E\delta u_d + F\delta q_d = 0, \tag{7.22}$$

with

$$D = \varepsilon_0 k^2 \left\{ \frac{\nu_e \omega_{pe}^2}{\omega_{\nu e}\omega_{\gamma e} - k^2 c_{se}^2} + \frac{\nu_i \omega_{pi}^2}{\omega_{\nu i}\omega_{\gamma i} - k^2 c_{si}^2} \right\}, \tag{7.23}$$

$$E = ik\frac{N_e q_e \nu_e \gamma_{ed}}{\omega_{\nu e}\omega_{\gamma e} - k^2 c_{se}^2} + ik\frac{N_i q_i \nu_i \gamma_{id}}{\omega_{\nu i}\omega_{\gamma i} - k^2 c_{si}^2}, \tag{7.24}$$

$$F = iN_d\omega_d + q_e\mu_e + q_i\mu_i - i\frac{q_e \nu_e \mu_e \omega_{\gamma e}}{\omega_{\nu e}\omega_{\gamma e} - k^2 c_{se}^2} - i\frac{q_i \nu_i \mu_i \omega_{\gamma i}}{\omega_{\nu i}\omega_{\gamma i} - k^2 c_{si}^2}. \tag{7.25}$$

Finally, there remains to insert (8.30) and (8.31) into (7.17) to get

$$G\delta U + H\delta u_d + J\delta q_d = 0, \tag{7.26}$$

with

$$G = \frac{kQ_d}{m_d} + ik\frac{q_e \omega_{\nu e}\gamma_{de}}{m_e(\omega_{\nu e}\omega_{\gamma e} - k^2 c_{se}^2)} + ik\frac{q_i \omega_{\nu i}\gamma_{di}}{m_i(\omega_{\nu i}\omega_{\gamma i} - k^2 c_{si}^2)}, \tag{7.27}$$

$$H = -\omega_{\gamma d} - \frac{\omega_{\nu e}\gamma_{de}\gamma_{ed}}{\omega_{\nu e}\omega_{\gamma e} - k^2 c_{se}^2} - \frac{\omega_{\nu i}\gamma_{di}\gamma_{id}}{\omega_{\nu i}\omega_{\gamma i} - k^2 c_{si}^2}, \tag{7.28}$$

$$J = \frac{kc_{se}^2 \mu_e \gamma_{de}}{N_e(\omega_{\nu e}\omega_{\gamma e} - k^2 c_{se}^2)} + \frac{kc_{si}^2 \mu_i \gamma_{di}}{N_i(\omega_{\nu i}\omega_{\gamma i} - k^2 c_{si}^2)}. \tag{7.29}$$

The dispersion law is then

$$\begin{vmatrix} A & B & C \\ D & E & F \\ G & H & J \end{vmatrix} = 0, \tag{7.30}$$

clearly very complicated. Without loss of generality, we assume henceforth that $U_d = 0$.

7.3 Modes in a non-magnetized plasma

For high-frequency modes in a Maxwellian proton-electron plasma, assuming that $m_d \to \infty$ and thereby neglecting the dust dynamics, the dispersion law (7.30) becomes:

$$\begin{vmatrix} A & C \\ D & F \end{vmatrix} = 0 \tag{7.31}$$

$$\Leftrightarrow \quad \left[\frac{\omega_{pe}^2}{\mathcal{D}_e} + \frac{\omega_{pi}^2}{\mathcal{D}_i} - 1\right]\left[i\omega - \alpha_e - \alpha_i + i\frac{\alpha_e\nu_e(\omega + i\nu_e)}{\mathcal{D}_e} + i\frac{\alpha_i\nu_i(\omega + i\nu_i)}{\mathcal{D}_i}\right]$$
$$- \left[\frac{\nu_e\omega_{pe}^2}{\mathcal{D}_e} + \frac{\nu_i\omega_{pi}^2}{\mathcal{D}_i}\right]\left[1 + i\frac{\alpha_e(\omega + i\nu_e)}{\mathcal{D}_e} + i\frac{\alpha_i(\omega + i\nu_i)}{\mathcal{D}_i}\right] = 0, \tag{7.32}$$

with:

$$\mathcal{D}_\alpha = (\omega - kU_\alpha + i\nu_\alpha)^2 - k^2c_{s\alpha}^2. \tag{7.33}$$

For the non-drifting case, this dispersion relation can be written as:

$$\omega^5 + ia_1\omega^4 + a_2\omega^3 + ia_3\omega^2 + a_4\omega + ia_5 = 0, \tag{7.34}$$

with real coefficients a_i, and this equation describes damped Langmuir and damped dust ion-acoustic modes with solutions like $\omega = \pm\omega_1 - i\omega_2$, coupled to a pure imaginary mode ($\omega = -i\omega_3$). For the dust-acoustic modes the dynamics of the dust grains must be included and in that case we need to analyze the full dispersion law (7.30).

The dispersion relations can be solved numerically, but it is instructive to find analytic approximations for the different branches.

7.3.1 Parameters

We can easily calculate the different charging parameters (see **chapter 6**) when we assume that only primary charging is present.

Nondrifting plasma

In the nondrifting case the different parameters can be written as:

$$\nu_e = \gamma_{ed} = \frac{N_d|I_{e0}|}{eN_e} \tag{7.35}$$

$$\nu_i = \gamma_{id} = \frac{N_d|I_{e0}|}{eN_i} \tag{7.36}$$

$$\mu_e = \frac{N_d|I_{e0}|}{C\kappa T_e} \tag{7.37}$$

$$\mu_i = -\frac{N_d|I_{e0}|}{C\kappa T_i - eQ_d} \tag{7.38}$$

with

$$|I_{e0}| = 2\sqrt{2\pi}a^2 ec_{se} N_e \exp\chi. \tag{7.39}$$

Using the following new notations:

$$N = \frac{N_e}{N_i} \qquad T = \frac{T_e}{T_i} \qquad \chi = \frac{e\Phi_0}{\kappa T_e} \qquad \mu = \frac{m_e}{m_i}, \tag{7.40}$$

the equations (6.6) and (7.5) yield:

$$\frac{N\sqrt{T}\exp(\chi)}{\sqrt{\mu}} - 1 + \chi T = 0, \tag{7.41}$$

$$-N + 1 + \chi P = 0. \tag{7.42}$$

Once T and

$$P = \frac{4\pi\varepsilon_0\kappa}{e^2}\frac{N_d a T_e}{N_i} \tag{7.43}$$

are given, these equations will give $N(P,T)$ and $\chi(P,T)$.

With the standard definition of plasma frequency $\omega_p = \sqrt{\omega_{pe}^2 + \omega_{pi}^2}$ and Debyelength $1/\lambda_D^2 = 1/\lambda_{de}^2 + 1/\lambda_{di}^2$ it can be calculated that:

$$\nu_e = \omega_p \times N_d a^2 \lambda_D \times 2\sqrt{2\pi}\sqrt{\frac{T+N}{N+\mu}}\exp(\chi), \tag{7.44}$$

$$\nu_i = \omega_p \times N_d a^2 \lambda_D \times 2\sqrt{2\pi}N\sqrt{\frac{T+N}{N+\mu}}\exp(\chi), \tag{7.45}$$

$$\alpha_e = \frac{e\mu_e}{N_d} = \omega_p \times \frac{a}{\lambda_D} \times \sqrt{\frac{N^2}{2\pi(N+\mu)(T+N)}}\exp(\chi), \tag{7.46}$$

$$\alpha_i = -\frac{e\mu_e}{N_d} = \omega_p \times \frac{a}{\lambda_D} \times \sqrt{\frac{N^2}{2\pi(N+\mu)(T+N)}\frac{T}{1-\chi T}}\exp(\chi), \tag{7.47}$$

or with the proper definition of the functions F_i (Appendix B):

$$\nu_e = \omega_p \times N_d a^2 \lambda_D \times F_1(P,T), \tag{7.48}$$

$$\nu_i = \omega_p \times N_d a^2 \lambda_D \times F_2(P,T), \tag{7.49}$$

$$\alpha_e = \omega_p \times \frac{a}{\lambda_D} \times F_3(P,T), \tag{7.50}$$

$$\alpha_i = \omega_p \times \frac{a}{\lambda_D} \times F_4(P,T). \tag{7.51}$$

Influence of drift velocities

As indicated in section 4.2.1, we need to use the expressions (4.17) and (4.16) for nonvanishing values of $w_\alpha = U_\alpha/c_{s\alpha}$. Assuming that $w_e \ll 1$ as is the case for most applications, we can use (7.39) substituted in (7.35) and (7.36) provided that χ is recovered by using the appropriate expressions for the charging currents.

So formally the expressions for ν_e, ν_i and μ_e remain the same. However

$$\mu_i = -\frac{N_d|I_{e0}|}{C\kappa T_i\left\{\frac{1}{2} + w_i^2 + w_i \exp(-w_i^2)/[\sqrt{\pi}\mathrm{erf}\ (\mathrm{w_i})]\right\} - eQ_d} \tag{7.52}$$

7.3.2 Langmuir modes

When we suppose that a small region of an equilibrium plasma is perturbed, so that some plasma particles are displaced from their equilibrium position, an imbalance of charges will be created. This imbalance will give rise to electrostatic fields, which will pull the particles back. If they were massless, the electrostatic force would restore charge neutrality. However, the particle inertia keeps them moving and they will overshoot their equilibrium position. This results in an oscillatory motion around the equilibrium position at a frequency $\omega_{p\alpha}$, mainly maintained by the lightest particles; the electrons. In the case of a dusty plasma these Langmuir oscillations couple to the charge relaxation mechanism and become damped.

When we consider $\nu_e, \nu_i, \alpha_e, \alpha_i, kU_e, kU_i$ and kc_{si} as small frequencies compared to the different plasma frequencies, we can solve the dispersion relation (7.31):

$$\begin{aligned} \omega = \pm\delta\omega_p &- \frac{i\nu_e}{2}\frac{2-2\delta^2-x}{1-2\delta^2+\varepsilon x} - \frac{i\nu_i}{2}\frac{(\varepsilon-\delta^2)(1-x)}{\delta^2(1-2\delta^2+\varepsilon x)} \\ &+kU_e\frac{1-x-\delta^2}{(1-2\delta^2+\varepsilon x)} + kU_i\frac{\varepsilon+x-\delta^2}{(1-2\delta^2+\varepsilon x)} \end{aligned} \tag{7.53}$$

with

$$(\delta^2-1)(\delta^2-\varepsilon x) = \varepsilon x^2, \tag{7.54}$$

and $x = \omega_{pe}^2/\omega_p^2 = N/(N+\mu) \leq 1$ and $\varepsilon = k^2c_{se}^2/\omega_p^2$. We restrict the analysis to solutions with a frequency close to the plasma frequency ($\delta \geq 1$). We look also for solutions for which $\varepsilon < 1$, because within the multi-fluid treatment the phase velocity should be larger than the thermal veocity. For most three component dusty plasmas $x \approx 1$, but when all electrons reside on the grain $x \to 0$.

In the driftless case (7.53) can be rewritten with the help of (7.54) as:

$$\begin{aligned} \omega = \pm\delta\omega_p &- \frac{i\nu_e}{2}\frac{\varepsilon x^3(\varepsilon x+\delta^2)}{(\varepsilon x-\delta^2)^2\left[(1-\delta^2)^2+\varepsilon x^2\right]} \\ &- \frac{i\nu_i}{2}\frac{(\delta^2-\varepsilon)(\delta^2-1)(1-x)}{\delta^2\left[(1-\delta^2)^2+\varepsilon x^2\right]}, \end{aligned} \tag{7.55}$$

and this describes a damping. This damping mechanism may be understood as follows [Bhatt, 1997]. Fluctuations in the electric potential will occur due to electron density fluctuations as in usual plasmas (1), but also due to electron density variations due to the capture/release of electrons by the grains (2), and due to the dust charge fluctuations itself (3). When only (1) and (3) are considered (no RHS in the electron continuity equation or a Vlasov approach), the modes become unstable [Ma and Yu, 1994], [Li et al., 1994], lacking the stabilizing effect of (2). In the *fully consistent description* however, the effect of (2) plays a crucial role. The damping rate due to (2) is twice the instability rate due to (1) and (3), and therefore damping occurs. This damping is clearly a consequence of the coupling between the Langmuir and charge relaxation mechanism.

This dispersion relation becomes for very small thermal effects $\varepsilon \ll 1$:

$$\omega = \pm\omega_p + kU_e x - \frac{i\nu_e}{2}x + kU_i(1-x) - \frac{i\nu_i}{2}(1-x). \tag{7.56}$$

The two last terms in this dispersion relation come from the ions, and they can be shown to be an order μ smaller than the first two terms, and hence we can neglect them.

For $x \approx 1$ we recover, neglecting terms of order μ:

$$\omega = \pm\sqrt{1+\varepsilon}\,\omega_p + kU_e - \frac{i\nu_e}{2}\frac{1+2\varepsilon}{1+\varepsilon}. \tag{7.57}$$

In order to evaluate the importance of this charge exchange damping, we must compare this damping rate with the rates obtained from a kinetic theory. This theory predicts an additional Landau-damping [Stix, 1992]. It can easily be shown that there can exist a domain $k_{cr1} \leq k \leq k_{cr2}$ for which classical Landau damping exceeds charge exchange damping.

With hindsight, it is easy to sketch in general terms what happens. We could have found (7.57) by simply assuming that not only the dust grains, but also the ions contribute to the static non-neutral background as in the classical Langmuir mode derivation. Only the dust charge variation and the electron density variations will sustain the Langmuir modes, while the ions only contribute to the equilibrium charge of the grains. The system can then be described by the continuity and momentum equations for the electrons, the charge variation equation and Poisson's equation.

$$\delta n_e = \frac{kN_e}{\omega_{\nu e}}\delta u_e - i\mu_e\delta q_d, \tag{7.58}$$

$$\delta u_e = \frac{kc_{se}^2}{N_e\omega_{\nu e}}\delta n_e + \frac{kq_e}{m_e\omega_{\nu e}}\delta U, \tag{7.59}$$

$$-iN_d\omega\delta q_d = q_e\nu_e\delta n_e + q_e\mu_e\delta q_d, \tag{7.60}$$

$$k^2\varepsilon_0\delta U = q_e\delta n_e + N_d\delta q_d. \tag{7.61}$$

The corresponding dispersion relation can be written in a form:

$$(\omega+i\nu_e)^2 - k^2c_{se}^2 - ikU_e\nu_e - \omega_{pe}^2\left(1+i\frac{\nu_e}{\omega}\right) + k^2U_e^2 - 2kU_e\omega = \frac{\alpha_e\nu_e}{\omega+i\alpha_e}\left(\frac{\omega_{pe}^2}{\omega^2} - \omega - i\nu_e\right) + i\frac{kU_e\nu_e\omega}{\omega+i\alpha_e}. \tag{7.62}$$

When the drift is neglected, this dispersion relation is the same as equation (17) of Bhatt [1997], and it is not surprising that the result from Bhatt [1997] is recovered for (7.57).

For a drifting plasma our result is different from Bhatt's because they included the variation of the attachment frequency in their model. When $N \approx 1$ and hence $x \approx 1, U_e = U_i = U$, (7.31) can be solved for small $\alpha_e, \alpha_i, \nu_e, \nu_i$ and kc_{si} and non-resonant modes:

$$\omega = kU \pm \sqrt{\omega_{pe}^2 + k^2 c_{se}^2} - i\frac{\nu_e}{2}\frac{\omega_{pe}(1+2\varepsilon) \pm 2kU\sqrt{1+\varepsilon}}{\omega_{pe}(1+\varepsilon) \pm kU\sqrt{1+\varepsilon}} \tag{7.63}$$

This dispersion relation simplifies to (7.57) where $x \to 1$ for the limit $U \to 0$, and for the limit $\varepsilon \to 0$ in the lowest order of ν_e and kU. When $U > 0$, the mode for which $\omega \approx kU + \sqrt{\omega_{pe}^2 + k^2 c_{se}^2}$ is damped, while a weak instability can occur for the $\omega \approx kU_e - \sqrt{\omega_{pe}^2 + k^2 c_{se}^2}$ mode when

$$\left(\frac{1}{2} + \frac{3}{4}\varepsilon\right)\omega_{pe} < kU < \left(1 + \frac{1}{2}\varepsilon\right)\omega_{pe}. \tag{7.64}$$

When $U < 0$, the mode for which $\omega \approx kU - \sqrt{\omega_{pe}^2 + k^2 c_{se}^2}$ is damped, while a weak instability can occur for the $\omega \approx kU + \sqrt{\omega_{pe}^2 + k^2 c_{se}^2}$ mode when

$$-\left(1 + \frac{1}{2}\varepsilon\right)\omega_{pe} < -kU < -\left(\frac{1}{2} + \frac{3}{4}\varepsilon\right)\omega_{pe}. \tag{7.65}$$

The instability is clearly a consequence of the coupling between the charging process and the streaming.

7.3.3 Dust ion-acoustic modes

If ion motions are considered, sound waves driven by long-range electrostatic forces can exist. These waves involve the motion of the more massive ions, and therefore their frequency is lower than those of the Langmuir waves discussed above.

In the ω-range for which $k^2 c_{se}^2 \gg k^2 c_{se}^2 \omega_{pi}^2/(\omega_{pe}^2 + k^2 c_{se}^2) + k^2 c_{si}^2 = \omega_{dia}^2$ ion-acoustic waves can be generated. When we assume that the charging frequencies $\nu_e, \nu_i, \alpha_e, \alpha_i$ are small frequencies compared to ω_{dia}, than we can solve the dispersion relation (7.31) in the lowest order of the small quantities:

$$\begin{aligned}\omega = \omega_o &- \frac{i}{2}\frac{k^2\lambda_{de}^2\omega_{pi}^2}{\omega_o(\omega_o - kU_i)(1 + k^2\lambda_{de}^2)^2}\nu_e \\ &- \frac{i}{2}\left\{2 - \frac{k^2\lambda_{de}^2\omega_{pi}^2}{\omega_o(\omega_o - kU_i)(1 + k^2\lambda_{de}^2)}\right\}\nu_i.\end{aligned} \tag{7.66}$$

with

$$\omega_o = kU_i \pm \sqrt{\frac{k^2\lambda_{de}^2\omega_{pi}^2}{1 + k^2\lambda_{de}^2} + k^2 c_{si}^2} = kU_i \pm \omega_{dia} \tag{7.67}$$

Non-drifting plasma

For a non-drifting plasma, (7.66) becomes:

$$\omega = \omega_o - \frac{i}{2}\frac{\lambda_{de}^2}{(1+k^2\lambda_{de}^2)(\lambda_{de}^2+\lambda_{di}^2+k^2\lambda_{di}^2\lambda_{de}^2)}\nu_e - \frac{i}{2}\frac{\lambda_{de}^2+2\lambda_{di}^2+2k^2\lambda_{de}^2\lambda_{di}^2}{\lambda_{de}^2+\lambda_{di}^2+k^2\lambda_{di}^2\lambda_{de}^2}\nu_i, \tag{7.68}$$

and again damping occurs, because of the coupling of the ion-acoustic mode and the grain charging mechanism. This dispersion relation can further be simplified for an isothermal plasma for which $\lambda_{de}^2/\lambda_{di}^2 = \nu_e/\nu_i$. It can be shown that

$$\omega = \omega_o - \frac{i\nu_e}{2}\frac{1+N+2N^2+N\eta^2+4N^2\eta^2+2N^2\eta^4}{2(1+\eta^2)(1+N+N\eta^2)} \tag{7.69}$$

with $\eta = k\lambda_{de}$. This relation is valid as long as $\omega \gg \nu_e$ or $k \gg \nu_e/(\omega_{pi}\lambda_{de})$.

Dispersion law (7.68) includes the special case for which $N_e \approx N_i$ and $T_e \approx T_i$. Indeed, for such a situation $N \approx 1$, and the imaginary part of the frequency is $\mathrm{Im}(\omega) = -\nu_e = -\nu_i$, for both very short and very long wavelengths. A minimum damping of $(\sqrt{8}-1)/2\nu_e = 0.91\nu_e$ appears for $k\lambda_{de} = \sqrt[4]{2}$.

Dust ion-acoustic instability

A new, dust ion-acoustic drift driven instability can be analyzed using equation (7.66). When $kc_{si} \ll \omega_0$, the dispersion relation is simplified to:

$$\omega = \omega_0 - \frac{i}{2}\frac{1}{1+k^2\lambda_{de}^2}\frac{\pm\omega_{dia}}{kU_i \pm \omega_{dia}}\nu_e - \frac{i}{2}\frac{2kU_i \pm \omega_{dia}}{kU_i \pm \omega_{dia}}\nu_i \tag{7.70}$$

For $k\lambda_{de} \ll 1$, we recover:

$$\omega = kU_i \pm k\lambda_{de}\omega_{pi} - \frac{i}{2}\frac{1}{1\pm\eta}\nu_e - \frac{i}{2}\frac{1\pm 2\eta}{1\pm\eta}\nu_i, \tag{7.71}$$

with $\eta = U_i/(\lambda_{de}\omega_{pi})$

It is readily verified that the mode $\omega = kU_i + \omega_{dia}$ remains stable, while the $\omega = kU_i - \omega_{dia}$ mode can become unstable [Bhatt and Pandey, 1994]. It can be shown that for a two component plasma ($N = 0$), one recovers a purely growing mode, while for a normal dusty plasma, the instability appear as long as $\eta < \eta_o = (1-N)/2$. For a specific value of the drift velocity $\eta = \eta_o$, a stable mode exists. This conclusion is qualitatively the same as the one of Bhatt and Pandey [1994]. However, the damping for high η values is finite for our approach, while a infinitely strong damping is encountered in the approach of Bhat and Pandey [1994].

7.3.4 Dust-acoustic modes

For still lower phase velocities, the dust dynamics can no longer be neglected, and the dust participates in the wave motion. The modes that occur in the range: $kc_{se} \gg kc_{si} \gg \omega - kU_\alpha \gg kc_{sd}$, were called dust-acoustic modes.

When we use the expressions for the different coefficients and take the limit for $m_e \to 0$ and $m_i \to 0$ in (6.44), we recover the dispersion relation found by Melandsø et al. [1993], which can be written as:

$$(\alpha - i\omega)\left(A^2\omega_{pd}^2 - \omega^2\right) = A^2\beta\omega^2, \tag{7.72}$$

with the definitions

$$\alpha = \alpha_e + \alpha_i, \qquad \beta = \frac{\nu_e}{k^2\lambda_e^2} + \frac{\nu_i}{k^2\lambda_i^2}, \qquad A^2 = \frac{k^2\lambda_D^2}{1 + k^2\lambda_D^2}. \tag{7.73}$$

The nature of the damping can be readily verified from (7.72); the dust-acoustic mode couples with the zero frequency mode due to the charging mechanism. (7.72) is only valid when all the finite mass effects of the plasma particles can be neglected. This was carried out by Melandsø et al. [1993], by using Boltzmann distributions for the plasma particles, and therefore sidesteps the issue of sink and source terms in continuity and momentum equations. These terms become important at both ends of the wavelength domain, because for these k-values the damping rate will be less than γ_{de} and γ_{di} in (7.72), but equal to their sum in the self-consistent approach.

Low dust density

When the charging frequencies $\nu_e, \nu_i, \alpha_e, \alpha_i, \gamma_{ed}, \gamma_{id}, \gamma_{de}$ and γ_{di} are small frequencies compared to ω:

$$\begin{aligned}\omega = \pm A\omega_{pd} &- i\frac{\nu_e}{2}\frac{A^2}{k^2\lambda_{de}^2} - i\frac{\gamma_{ed}}{2}\frac{A^2 m_e Q_d}{k^2\lambda_{de}^2 m_d q_e} - i\frac{\gamma_{de}}{2}\left\{1 + \frac{A^2 N_d Q_d}{k^2\lambda_{de}^2 N_e q_e}\right\} \\ &- i\frac{\nu_i}{2}\frac{A^2}{k^2\lambda_{di}^2} - i\frac{\gamma_{id}}{2}\frac{A^2 m_i Q_d}{k^2\lambda_{di}^2 m_d q_i} - i\frac{\gamma_{di}}{2}\left\{1 + \frac{A^2 N_d Q_d}{k^2\lambda_{di}^2 N_i q_i}\right\}.\end{aligned} \tag{7.74}$$

We can easily see that for large k values, the damping is described by:

$$\omega = \pm A\omega_{pd} - i\frac{\gamma_{de} + \gamma_{di}}{2}, \tag{7.75}$$

as indicated by Meuris and Verheest [1996].

With the use the expressions for the different coefficients for an isotropic proton electron plasma with only primary charging (7.30) we get:

$$\begin{aligned}\omega = \pm A\omega_{pd} &- i\frac{\nu_e}{2}\left\{\frac{N_e m_e}{N_d m_d} + \frac{A^2}{k^2\lambda_{de}^2}\left(1 + 2\frac{Q_d m_e}{q_e m_d}\right)\right\} \\ &- i\frac{\nu_i}{2}\left\{\frac{N_i m_i}{N_d m_d} + \frac{A^2}{k^2\lambda_{di}^2}\left(1 + 2\frac{Q_d m_i}{q_i m_d}\right)\right\}.\end{aligned} \tag{7.76}$$

High dust density

For intermediate k-values (7.72) adequately describes the dust-acoustic mode, even for high dust densities. From the general structure of (7.72), we see that the solutions are of the form: $\omega = \pm\omega_1 - i\omega_2$ together with a pure imaginary mode $\omega = -i\omega_3$. However, equation (7.72) can have **three** pure imaginary modes. In that case the dust-acoustic mode disappears, in a finite k interval, and a bifurcation occurs.

The marginal k-values are those for which (7.72) has a double and a simple pure imaginary root. These k values are give by the real valued solution of:

$$4\alpha(\alpha + A^2\beta)^3 + A^2(8\alpha^2 - 20A^2\alpha\beta - A^4\beta^2)\omega_{pd}^2 + 4A^4\omega_{pd}^4 = 0. \tag{7.77}$$

For low $k\lambda_D \ll 1$ and $\omega \ll \alpha$ of (7.72), is given by:

$$\omega^2 = \omega_{pd}^2 \frac{\alpha_e + \alpha_i}{\nu_e/\lambda_{de}^2 + \nu_i/\lambda_{di}^2} k^2, \tag{7.78}$$

as stated by Melandsø et al. [1993].

7.3.5 Zero-frequency modes

The charging mechanism gives rise to a zero-frequency damped mode. When we solve the dispersion relation (7.30) in the lowest order of the small quantities: ν_e, ν_i, α_e, α_i, γ_{de}, γ_{di}, γ_{ed}, γ_{id} and ω, we get for the small wavelength case:

$$\omega = -i(\alpha_e + \alpha_i). \tag{7.79}$$

This corresponds to the charge relaxation at the charge relaxation frequency. For long wavelengths, the situation is more complex, the mode couples to the other modes, as explained before, and no analytical expressions could be recovered.

7.4 Modes in a magnetized plasma

In the presence of a magnetic field, one could more adequately describe a plasma by a model containing an anistropic pressure, because of the intrinsic anisotropy, contained in a magnetized plasma. However, when we stick to our model as a first order description, we can use some results of the previous section. When the modes propagate parallel to an ambient magnetic field, this description remains valid for a classical (non dusty) plasma. Indeed, when $\mathbf{k} \parallel \mathbf{B}_0$, the $\mathbf{u} \times \mathbf{B}$-effects vanish, and the system behaves for these modes as if no ambient field is present. This holds no longer for a dusty plasma, because the expressions will depend on an appropriate charging theory, which is not yet available.

On the other hand, when electrostatic modes propagate perpendicular to an ambient magnetic field, and when the dust dynamics can be neglected, the dispersion relation (7.30) remains formally the same although we must use:

$$\omega_{\gamma\alpha} = \omega + i\gamma_{\alpha d} - \frac{\Omega_\alpha^2}{\omega + i\gamma_{\alpha d}}. \tag{7.80}$$

The dispersion relation can then be used to describe the resonances of the extra-ordinary mode.

7.4.1 Lower-hybrid modes

The dust lower-hybrid resonance will be described in **chapter 9** in the framework of the low frequency dust Alfvén mode.

7.4.2 Upper-hybrid modes

For the extraordinary modes the energy is divided in an electrostatic and an electromagnetic part. The upper-hybrid wave is a purely electrostatic wave and can be seen as the limit of the extraordinary wave, approaching the resonance ($k \to \infty$) while the electromagnetic energy is converted into electrostatic waves.

When we assume that ν_e, ν_i, α_e, α_i, γ_{ed}, γ_{id} and ω_{pi} are small frequencies in a cold, nondrifing plasma, taking into account (7.80), the dispersion relation for the upper hybrid waves is given by:

$$\omega^2 = \omega_{pe}^2 + \Omega_e^2 - \frac{i}{2}\gamma_{ed}\frac{\omega_{pe}^2 + 2\Omega_e^2}{\omega_{pe}^2 + \Omega_e^2} \tag{7.81}$$

7.5 Case studies

The validity of the analysis and previous dispersion laws can be verified by solving the **full** dispersion relation (7.30) numerically. This equation is a polynomial with 17 solutions. Note that although some of the analytical results are obtained from the more simple model (7.31), the numerical results are solutions of (7.30). Note that the parameters were derived as if only primary charging is important. This is not be the case for the real situation in the rings, but to a first approximation, this will hold.

		E-ring	Spokes
N_d	(m^{-3})	10^2	10^6
N_i	(m^{-3})	10^7	10^7
T_e	(K)	5×10^5	5×10^5
T_i	(K)	5×10^5	5×10^5
λ_{De}	(m)	23.3	101
λ_{Di}	(m)	15.4	15.4
λ_D	(m)	12.9	15.3
a	(m)	10^{-6}	10^{-6}
N		0.438	0.0233
χ		-1.87	-0.000326
$N_d a^2 \lambda_D$		1.2810^{-9}	15.2×10^{-6}
$N_d a \lambda_D^2$		0.017	233

Table 7.1: Data used in the case studies

7.5.1 Saturn's E-ring: a dust-in-plasma

Neglecting the relative plasma dust drift and the magnetic field, we obtain the following parameters:

$$\nu_e = \gamma_{ed} = 2.11 \times 10^{-4}\ \mathrm{s}^{-1} \tag{7.82}$$
$$\nu_i = \gamma_{id} = 0.92 \times 10^{-4}\ \mathrm{s}^{-1} \tag{7.83}$$
$$\alpha_e = 3.09 \times 10^{-4}\ \mathrm{s}^{-1} \tag{7.84}$$
$$\alpha_i = 1.08 \times 10^{-4}\ \mathrm{s}^{-1} \tag{7.85}$$
$$\gamma_{de} = 2.01 \times 10^{-15}\ \mathrm{s}^{-1} \tag{7.86}$$
$$\gamma_{di} = 3.69 \times 10^{-12}\ \mathrm{s}^{-1} \tag{7.87}$$
$$\omega_p = 118 \times 10^3 \mathrm{s}^{-1} \tag{7.88}$$

The resulting solutions $\omega(k)$ are shown in Figures 7.1-7.3, for the Langmuir-mode, the dust-ion acoustic mode and the dust-acoustic mode respectively.

The Langmuir modes are perfectly described by (7.57) for the k-domain considered. The Langmuir damping is larger than the charge exchange damping for k values outside the domain [0.01, 1.60]. Because Landau damping decays exponentially for both smaller and larger wavelengths, we may safely neglect it outside this interval.

The dust ion-acoustic modes are described by (7.69) because ω_{dia} is much larger than the small frequencies in (7.69).

The dust-acoustic mode does not disappear in the k-interval considered. As long as $A\omega_{pd}$ is an order of magnitude larger than the small frequencies, we may use (7.74). For larger wavelengths, (7.72) is valid. Note that this dispersion relation is not valid for higher k values, because $\gamma_{d\alpha}$-effects are going to play.

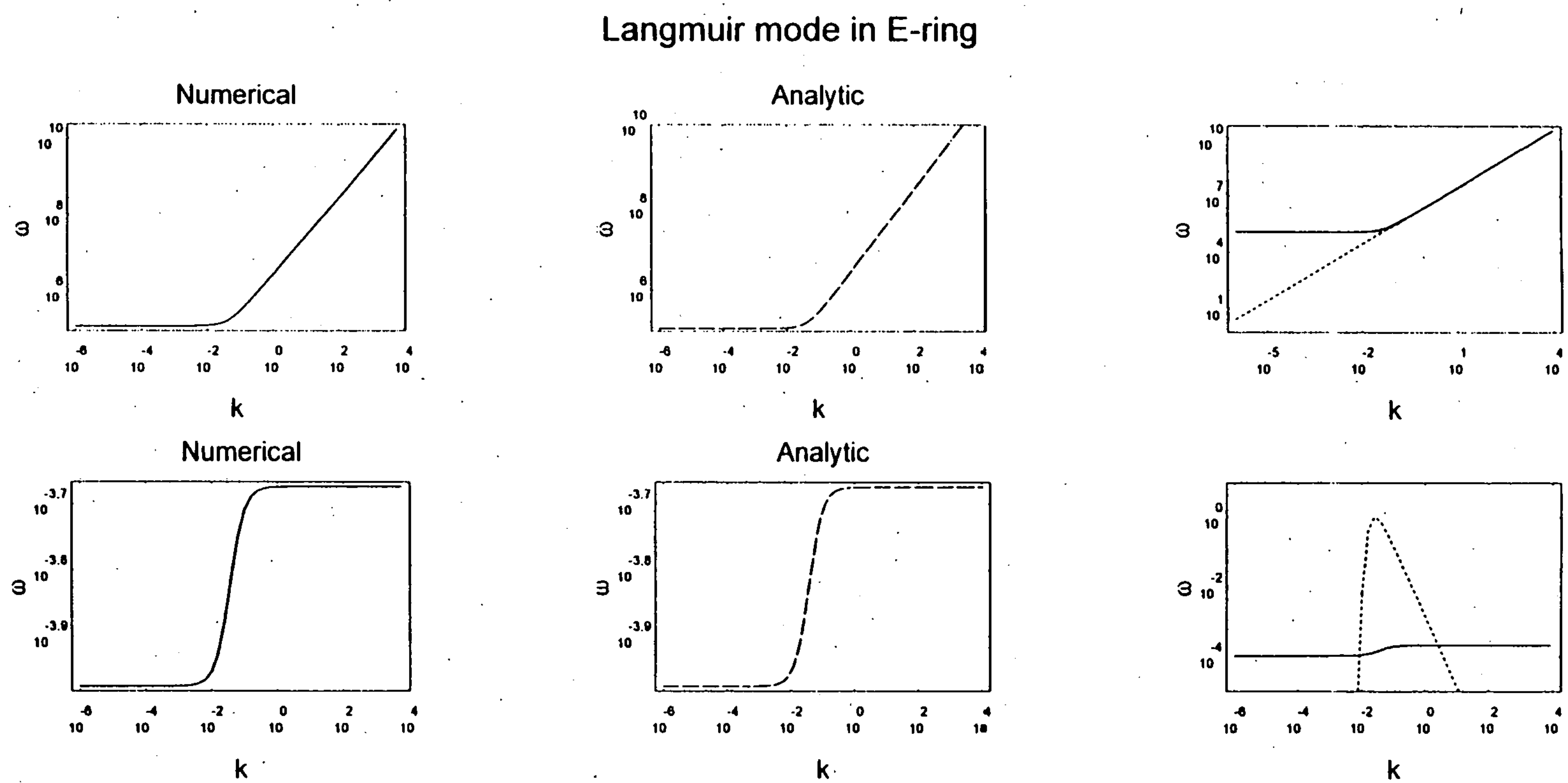

Figure 7.1: The real (first row) and imaginary part (second row) of the dispersion law, for the Langmuir modes for data corresponding with the E-ring. The numerical results were obtained by solving the full dispersion relation (7.30), while the analytical result is the solution of (7.56). In the last figure the Landau damping is shown.

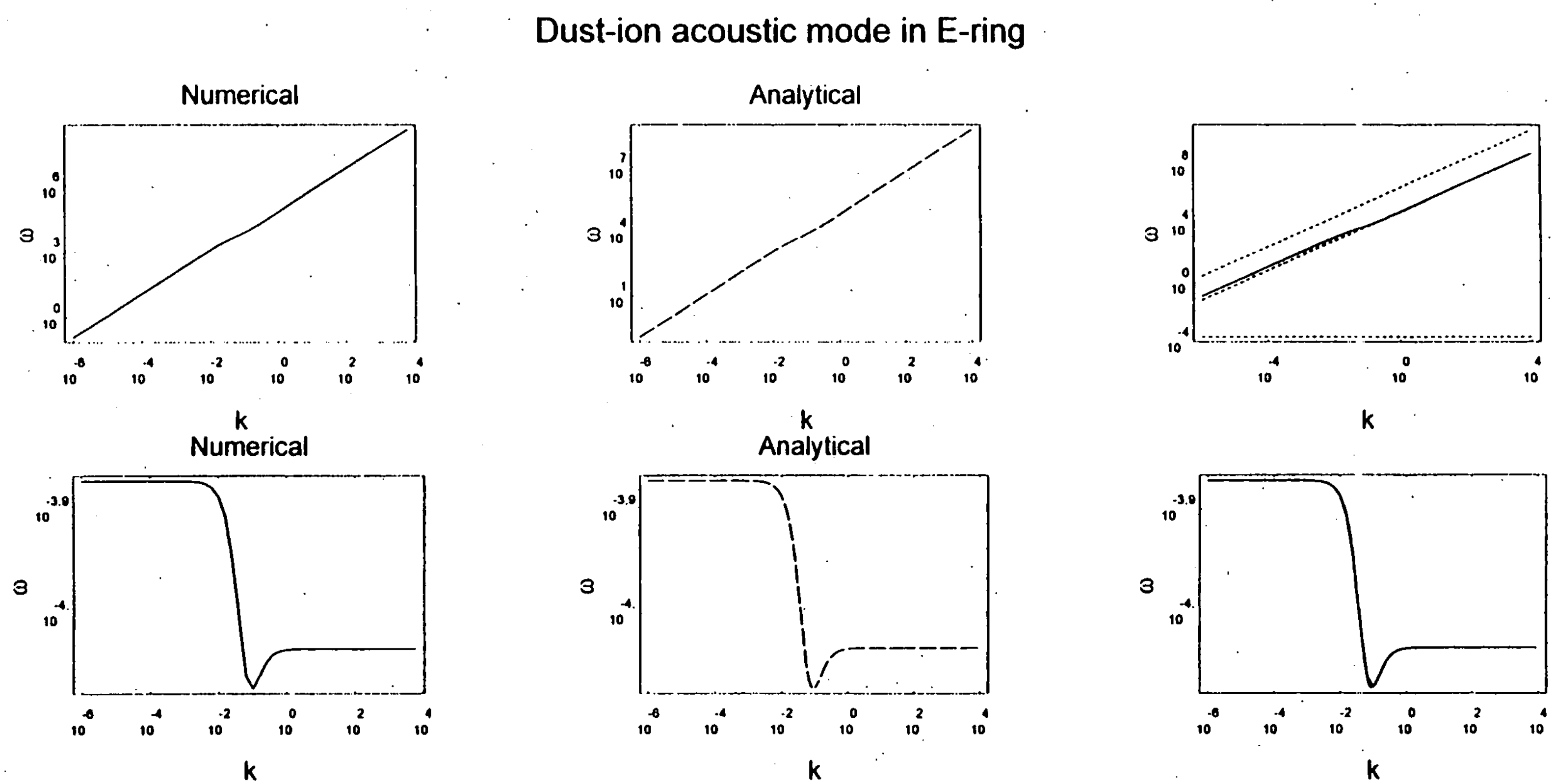

Figure 7.2: The real (first row) and imaginary part (second row) of the dispersion law, for the dust-ion acoustic modes for data corresponding with the E-ring. The numerical results were obtained by solving the full dispersion relation (7.30), while the analytical result is the solution of (7.69). In the overview figure of the real part, the largest frequency ν_e is shown.

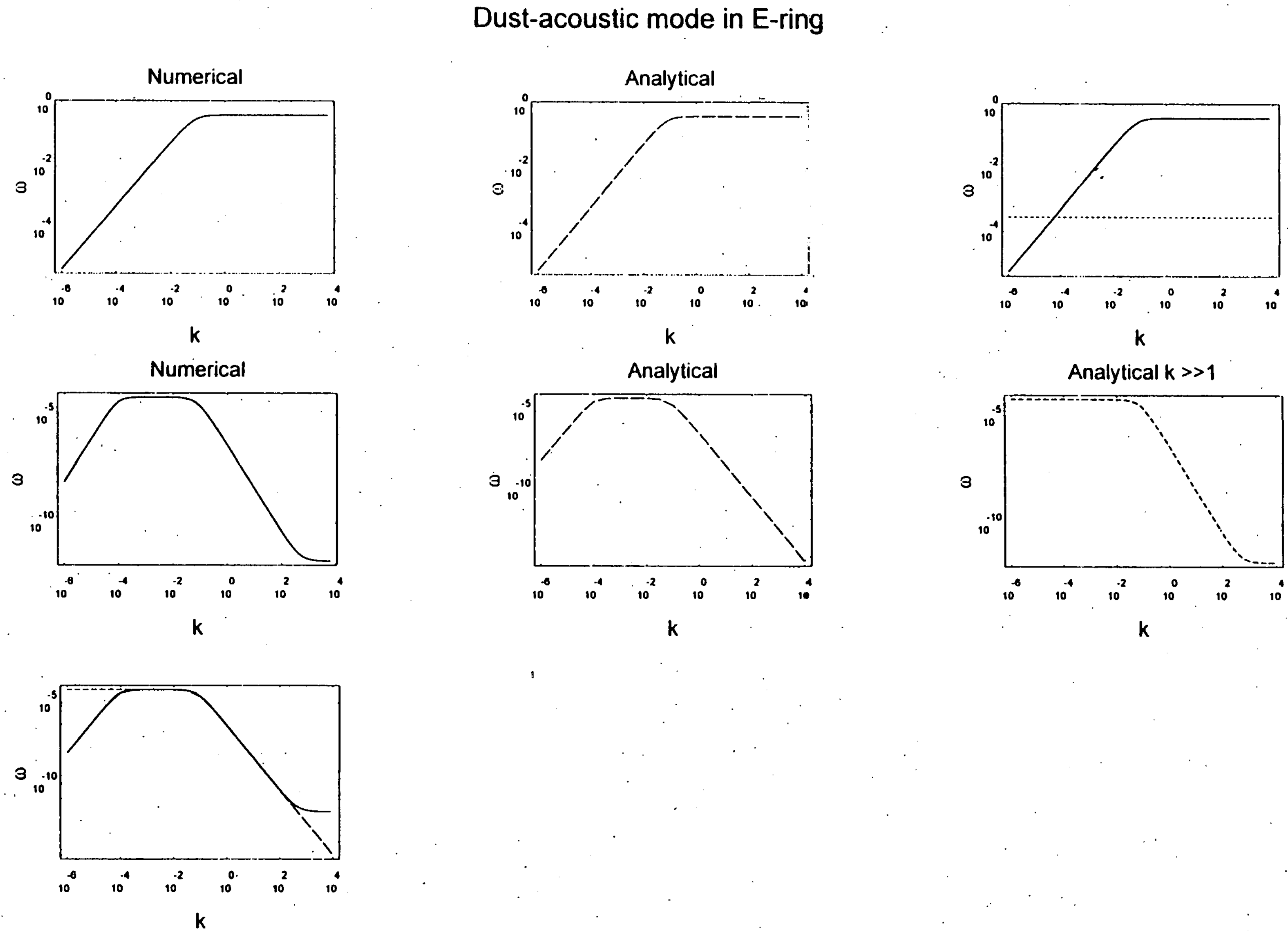

Figure 7.3: The real (first row) and imaginary part (second and third row) of the dispersion law, for the dust-acoustic modes for data corresponding with the E-ring. The numerical results were obtained by solving the full dispersion relation (7.30), while the analytical result is the solution of the Melandsø relation (7.72). The limit for large k (7.74) is also shown.

7.5.2 Saturn's spokes: a dusty plasma

Neglecting the relative plasma dust drift and the magnetic field, we come to the following charging frequencies:

$$\nu_e = 13.8\ s^{-1} \tag{7.89}$$
$$\nu_i = 0.322\ s^{-1} \tag{7.90}$$
$$\alpha_e = 1.07 \times 10^{-4}\ s^{-1} \tag{7.91}$$
$$\alpha_i = 1.07 \times 10^{-4}\ s^{-1} \tag{7.92}$$
$$\gamma_{de} = 7.00 \times 10^{-16}\ s^{-1} \tag{7.93}$$
$$\gamma_{di} = 1.29 \times 10^{-12}\ s^{-1}. \tag{7.94}$$

The resulting solutions $\omega(k)$ are shown in Figures 7.4-7.6, for the Langmuir-mode, the dust-ion acoustic mode and the dust-acoustic mode respectively. A detailed view of the damping rate of the dust-acoustic mode solution is given in Figure 7.7.

The Langmuir modes are perfectly described by (7.57) for the k-domain considered. The Langmuir damping is at least an order of magnitude stronger than the classical Landau damping, so that the latter might be neglected.

The dust ion-acoustic modes can be described by (7.69), as long as $\omega_{dia} \gg \nu_e$. When this is no longer the case, the mode disappears, and the situation becomes more complex.

For the dust-acoustic mode, the situation is as follows. In the k-interval [0.187, 0.411], the dust-acoustic mode vanishes because of a mode bifurcation and three purely damped modes appear. For wavelengths shorter than this critical interval, we find ourselves in the small wavelength regime, for which Re(ω)=ω_{pd}. For longer wavelengths, we recover equation (7.78) for the real part of the mode, until a k value is reached for which the mode disappears.

The dust-acoustic damping can be described by (7.74) for small wavelengths, while (7.72) gives the numeric solution for intermediate k-values. This equation is not valid for very small wavelengths as indicated by Meuris and Verheest [1996].

7.6 Conclusions and new results

- Although previous results ([Ma and Yu, 1994], [Li et al., 1994]) deduced that the presence of dust grains would make the Langmuir mode unstable, we showed that in a self-consistent approach the opposite is true. Langmuir modes are damped by the presence of dust grains. This was recently shown by Bhatt [1997], using rather ad hoc assumptions. We derived the same result from a more complete theory.
- It was shown for the first time in the self-consistent approach that the dust ion-acoustic modes are damped due to their coupling to the charging mechanism. The damping rate is given by equation 7.68.

- The standard dispersion relation first derived by Melandsø et al. [1993], which described the coupling of the dust-acoustic mode and the charging mechanism, is not adequate to describe both small and long wavelength modes. In that case a fully consistent approach is needed that includes the sink/source terms in the momentum equations. When Melandsø's equation is valid, three pure imaginary modes can appear. In that case the coupling of the dust-acoustic mode and the charging process leads to the disappearance of the dust-acoustic mode in a small k-interval.

- Although modes in a magnetized plasma need a fully developed charging model, we could derive results for modes propagating parallel to the magnetic field, and the results for upper-hybrid waves. The damping rate for the latter is derived as a function of the ad hoc parameters.

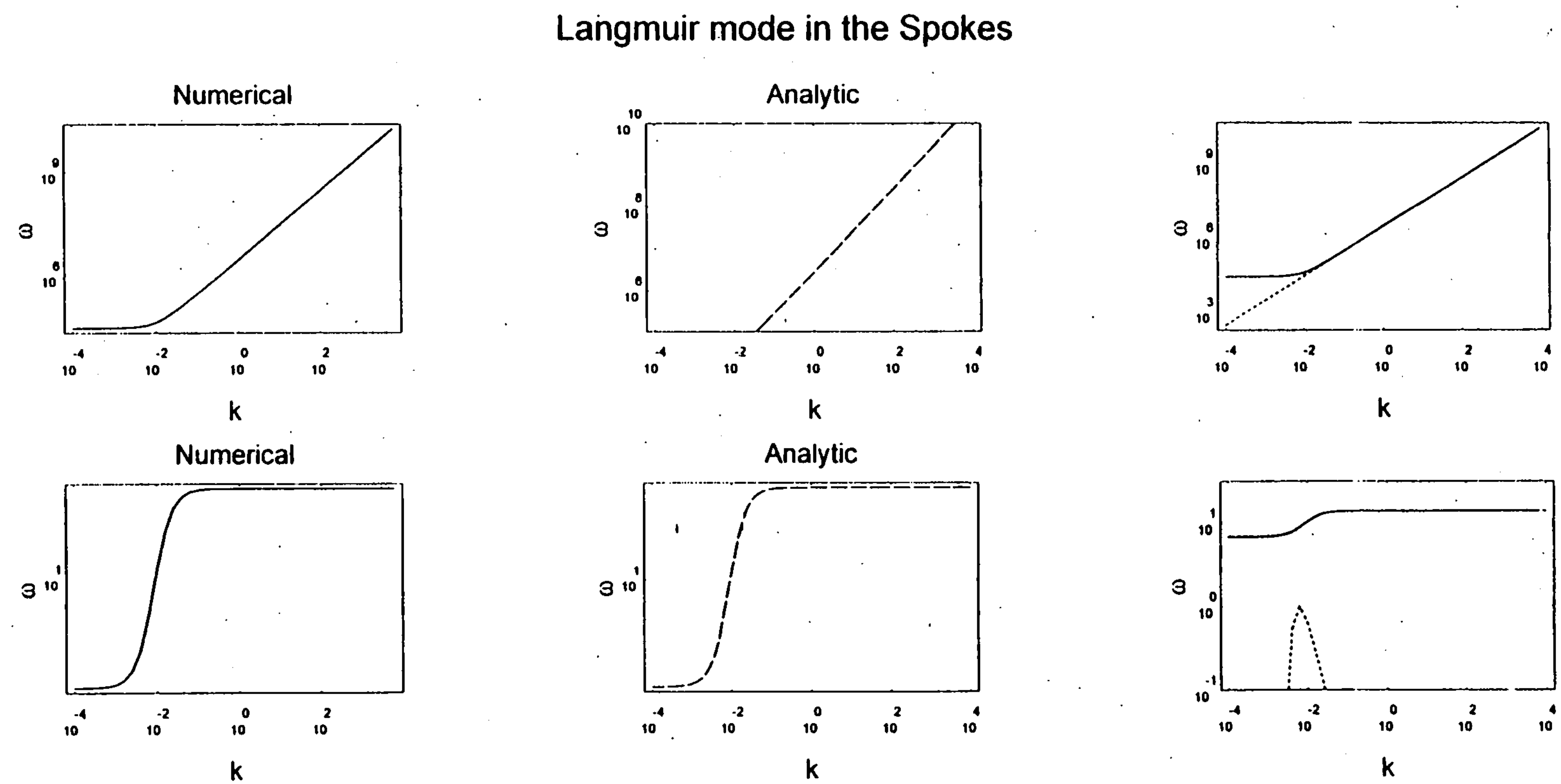

Figure 7.4: The real (first row) and imaginary part (second row) of the dispersion law, for the Langmuir modes for data corresponding with the spokes region. The numerical results were obtained by solving the full dispersion relation (7.30), while the analytical result is the solution of (7.56). In the last figure the Landau damping is shown.

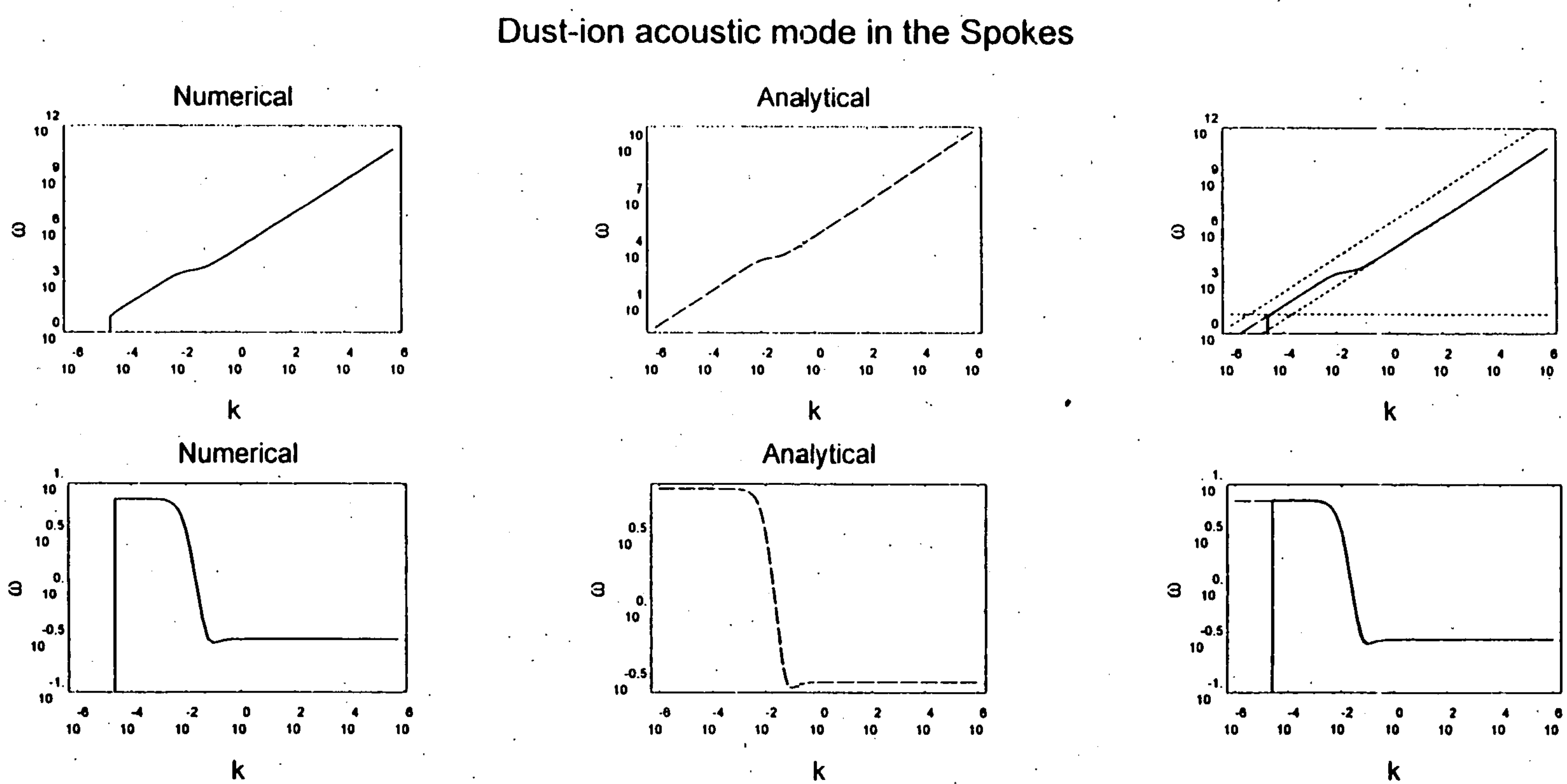

Figure 7.5: The real (first row) and imaginary part (second row) of the dispersion law, for the dust-ion acoustic modes for data corresponding with the spokes region. The numerical results were obtained by solving the full dispersion relation (7.30), while the analytical result is the solution of (7.69). In the third figure of the first row k c_{se} and k c_{si} are drawn, together with ν_e. When the real frequency is of the order of ν_e the mode vanished.

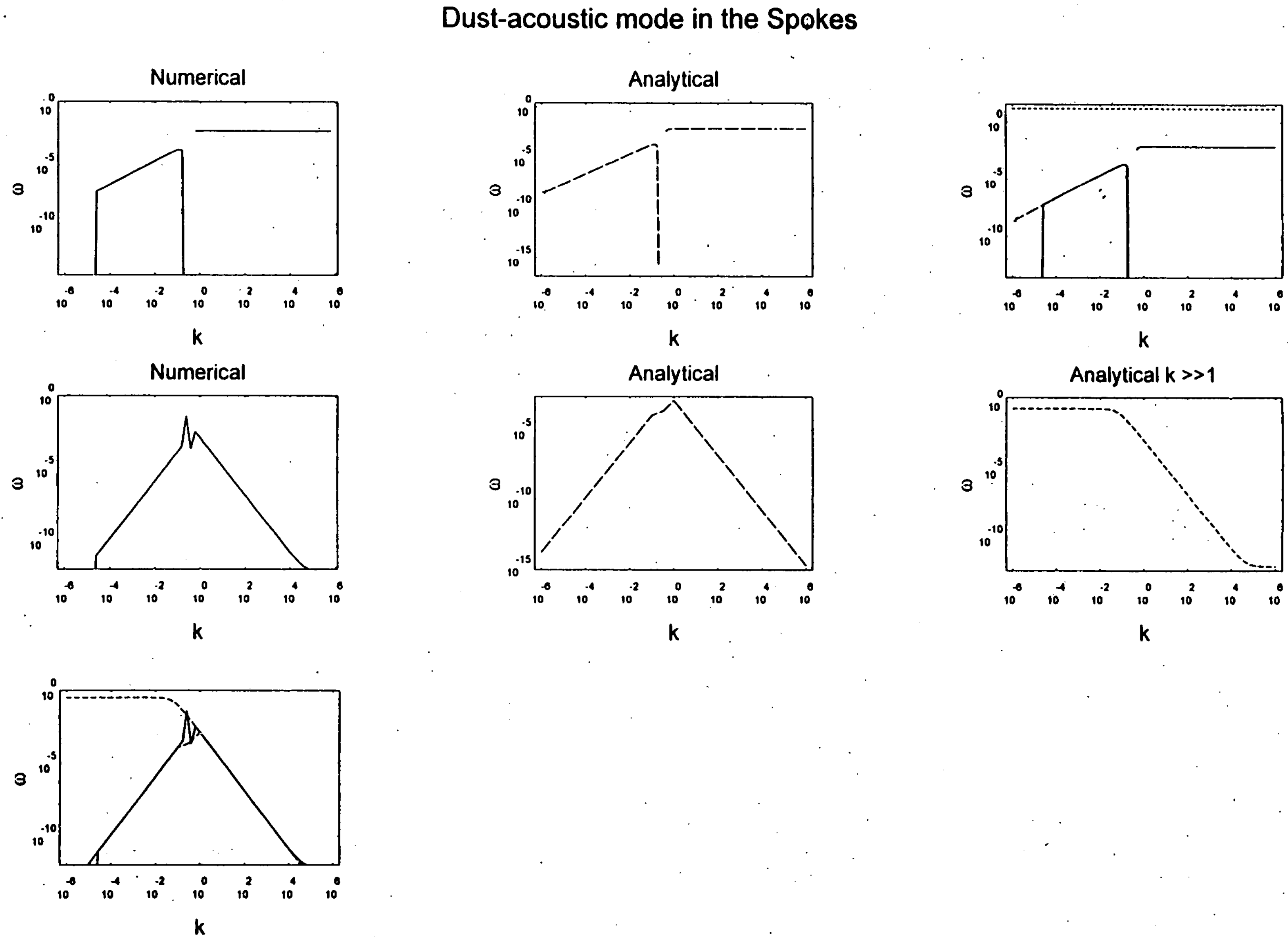

Figure 7.6: The real (first row) and imaginary part (second and third row) of the dispersion law, for the dust-acoustic modes for data corresponding with the spokes region. The numerical results were obtained by solving the full dispersion relation (7.30), while the analytical result is the solution of the Melandsø relation (7.72). The limit for large k (7.74) is also shown. In the k-range [0.19; 0.41], the dust-acoustic mode disappears and a blowup of this particular area is shown in Figure 7.7.

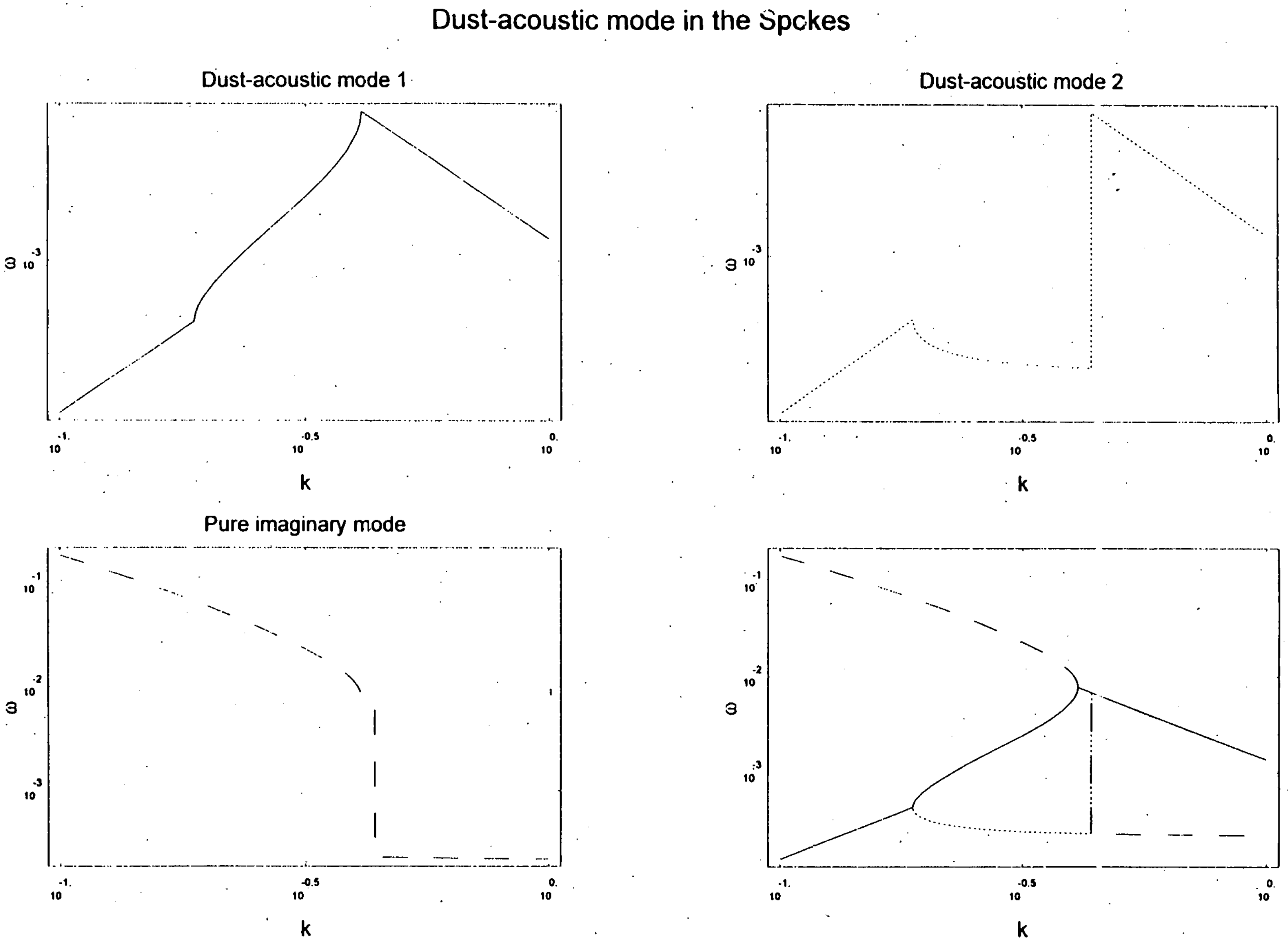

Figure 7.7: The imaginary part of the dispersion law, for the dust-acoustic modes for data corresponding with the spokes region. The results were obtained by solving the Melandsø relation (7.72). Within the k-range [0.187, 0.411], three pure imaginary solutions are present, outside this range, the two dust-acoustic branches have the same damping rate.

7.7 Appendix B: Tabulation of functions

		Log[T]						
		-3	-2	-1	0	1	2	3
Log[P]	-3	1,000	0,999	0,998	0,997	0,998	0,999	0,999
	-2	0,997	0,986	0,976	0,975	0,981	0,988	0,993
	-1	0,972	0,870	0,783	0,770	0,822	0,883	0,934
	0	0,854	0,419	0,181	0,108	0,161	0,319	0,540
	1	0,756	0,252	0,082	0,028	0,016	0,028	0,076
	2	0,740	0,235	0,075	0,024	0,008	0,005	0,008
	3	0,738	0,234	0,074	0,023	0,007	0,003	0,001

Table 7.2: Tabulation of the function $N[P, T]$

		Log[T]						
		-3	-2	-1	0	1	2	3
Log[P]	-3	-0,303	-1,439	-2,390	-2,502	-1,908	-1,235	-0,683
	-2	-0,300	-1,427	-2,370	-2,484	-1,896	-1,229	-0,680
	-1	-0,276	-1,303	-2,166	-2,302	-1,779	-1,168	-0,656
	0	-0,146	-0,581	-0,819	-0,892	-0,839	-0,681	-0,460
	1	-0,024	-0,075	-0,092	-0,097	-0,098	-0,097	-0,092
	2	-0,003	-0,008	-0,009	-0,010	-0,010	-0,010	-0,010
	3	0,000	-0,001	-0,001	-0,001	-0,001	-0,001	-0,001

Table 7.3: Tabulation of the function $\chi[P, T]$

		Log[T]						
		-3	-2	-1	0	1	2	3
Log[P]	-3	3,7	1,2	0,5	0,6	2,5	14,7	80,1
	-2	3,7	1,2	0,5	0,6	2,5	14,8	80,6
	-1	3,8	1,4	0,6	0,8	3,1	16,7	85,1
	0	4,3	2,8	2,7	6,6	17,2	45,0	136,2
	1	4,9	4,7	6,8	27,2	111,3	271,3	523,7
	2	5,0	5,1	7,6	32,2	168,0	685,2	1684,5
	3	5,0	5,1	7,7	32,8	177,1	897,5	3522,9

Table 7.4: Tabulation of the function $F_1[P,T]$

		Log[T]						
		-3	-2	-1	0	1	2	3
Log[P]	-3	3,70	1,19	0,48	0,58	2,46	14,64	80,07
	-2	3,70	1,19	0,48	0,58	2,47	14,65	80,02
	-1	3,70	1,19	0,48	0,59	2,52	14,72	79,54
	0	3,70	1,19	0,50	0,71	2,76	14,33	73,47
	1	3,70	1,19	0,56	0,77	1,80	7,48	39,61
	2	3,70	1,19	0,56	0,77	1,38	3,22	13,71
	3	3,70	1,19	0,57	0,77	1,32	2,31	5,20

Table 7.5: Tabulation of the function $F_2[P,T]$

		Log[T]						
		-3	-2	-1	0	1	2	3
Log[P]	-3	0,29438	0,09409	0,03485	0,02309	0,01784	0,01154	0,00637
	-2	0,29517	0,09529	0,03552	0,02337	0,01790	0,01154	0,00636
	-1	0,30261	0,10779	0,04304	0,02633	0,01855	0,01161	0,00632
	0	0,34447	0,22049	0,14097	0,05086	0,02162	0,01137	0,00584
	1	0,38894	0,36265	0,24318	0,05940	0,01428	0,00595	0,00315
	2	0,39749	0,38730	0,25739	0,05955	0,01094	0,00256	0,00109
	3	0,39842	0,38991	0,25885	0,05956	0,01051	0,00183	0,00041

Table 7.6: Tabulation of the function $F_3[P,T]$

		Log[T]						
		-3	-2	-1	0	1	2	3
Log[P]	-3	0,00029	0,00093	0,00281	0,00659	0,00888	0,00927	0,00931
	-2	0,00030	0,00094	0,00287	0,00671	0,00897	0,00932	0,00934
	-1	0,00030	0,00106	0,00354	0,00797	0,00987	0,00986	0,00962
	0	0,00034	0,00219	0,01303	0,02688	0,02302	0,01645	0,01266
	1	0,00039	0,00362	0,02410	0,05414	0,07199	0,05551	0,03373
	2	0,00040	0,00387	0,02571	0,05898	0,09956	0,12852	0,09992
	3	0,00040	0,00390	0,02588	0,05950	0,10402	0,16685	0,20710

Table 7.7: Tabulation of the function $F_4[P,T]$

Chapter 8

Electromagnetic modes

8.1 Introduction

The modes occurring in a plasma containing oscillating electric and magnetic fields are addressed as *electromagnetic*. For the description of these modes in a dusty plasma, an additional problem exists. As explained in **chapter 4** there is no model available yet to adequately describe the dust charging in a magnetized plasma. Therefore, the dust charge perturbations are in most of the cases neglected [Shukla, 1996]. This might not be valid for wave frequencies lower than the characteristic dust charging frequencies and therefore, we take a different view. Although there is for the moment no self-consistent model available describing the dust grain charging in a magnetized plasma, we can assume that such a model will result in source/sink terms in continuity and momentum equations. With the use of these ad hoc parameters, a proper analysis of the modes can be made.

Electromagnetic modes propagating along the ambient magnetic field will be called *parallel*, while the remainder will consist of *perpendicular and oblique* modes. This distinction was made because the behavior of electromagnetic dust modes for the *cold* parallel case is easier to describe. Indeed, in that case, dust charge fluctuations, like density fluctuations, give rise to first order current perturbations parallel to the propagation direction, and parallel modes decouple from the rest of the modes in a cold plasma description, even in the presence of dust grain perturbations.

For a good understanding, the model equations are repeated here:

$$\frac{\partial n_\alpha}{\partial t} + \nabla \cdot (n_\alpha \mathbf{u}_\alpha) = -\nu_\alpha (n_\alpha - N_\alpha) - \mu_\alpha (q_d - Q_d), \tag{8.1}$$

$$\frac{\partial n_d}{\partial t} + \nabla \cdot (n_d \mathbf{u}_d) = 0 \tag{8.2}$$

$$\left(\frac{\partial}{\partial t} + \mathbf{u}_\alpha \cdot \nabla\right) \mathbf{u}_\alpha = -\frac{q_\alpha}{m_\alpha}(\mathbf{E} + \mathbf{u}_\alpha \times \mathbf{B}) + \frac{1}{n_\alpha m_\alpha} \nabla p_\alpha$$

$$
\begin{aligned}
& - \gamma_{\alpha d}(\mathbf{u}_\alpha - \mathbf{U}_\alpha - \mathbf{u}_d + \mathbf{U}_d), & (8.3)\\
\left(\frac{\partial}{\partial t} + \mathbf{u}_d \cdot \nabla\right) \mathbf{u}_d = & - \frac{q_d}{m_d}(\mathbf{E} + \mathbf{u}_\alpha \times \mathbf{B}) + \frac{1}{n_d m_d}\nabla p_d \\
& - (\gamma_{de} + \gamma_{di})(\mathbf{u}_d - \mathbf{U}_d) + \gamma_{de}(\mathbf{u}_e - \mathbf{U}_e) + \gamma_{di}(\mathbf{u}_i - \mathbf{U}_i), & (8.4)\\
\nabla \times \mathbf{E} + \frac{\partial \mathbf{B}}{\partial t} = & \; \mathbf{0}, & (8.5)\\
\varepsilon_0 \nabla \cdot \mathbf{E} = & \sum_\alpha n_\alpha q_\alpha + n_d q_d, & (8.6)\\
c^2 \nabla \times \mathbf{B} = & \; \frac{\partial \mathbf{E}}{\partial t} + \frac{1}{\varepsilon_0}\left[\sum_\alpha n_\alpha q_\alpha \mathbf{u}_\alpha + n_d q_d \mathbf{u}_d\right], & (8.7)\\
\nabla \cdot \mathbf{B} = & \; 0. & (8.8)
\end{aligned}
$$

To describe nonlinear electromagnetic waves in the low-frequency limit (section 8.2.2), we first determine a global equation by multiplying the perpendicular projection of (8.3) by $n_\alpha m_\alpha$, summing the results over all species and eliminating sums containing $n_\alpha q_\alpha$ with the help of Maxwell's equations (8.7) or, only for section 8.2.2, assuming quasi-neutrality:

$$\sum_\alpha n_\alpha q_\alpha = 0. \qquad (8.9)$$

This procedure gives:

$$\sum_\alpha n_\alpha m_\alpha \frac{\partial \mathbf{u}_{\alpha\perp}}{\partial t} + \sum_\alpha n_\alpha m_\alpha u_{\alpha\parallel} \frac{\partial \mathbf{u}_{\alpha\perp}}{\partial z} = \frac{B_0}{\mu_0}\frac{\partial \mathbf{B}_\perp}{\partial z} - \sum_\alpha n_\alpha m_\alpha \gamma_{\alpha d}(\mathbf{u}_{\alpha\perp} - \mathbf{u}_{d\perp}). \qquad (8.10)$$

It needs to be stressed that, although the coefficients ν_α and $\gamma_{\alpha\beta}$ are *ad hoc* parameters, we can find an order of magnitude by using the results from Table 7.2. Indeed, for non-magnetized dust grains, we can see that in the limit $N_d \to 0$ we find that $\gamma_{ed} = \gamma_{id}$. On the other hand, when the number of free electrons is small ($N_e \to 0$), we might expect that $\sqrt{m_e}\gamma_{ed} \approx \sqrt{m_i}\gamma_{id}$. These results were obtained in the absence of ANY magnetic field. However, as we have seen before (Section 4.4), this might expected to remain valid as long as the grain size is smaller than the mean gyration radius, which is the case in most space plasma applications. These results need to be re-examined when a better theory becomes available.

8.2 Parallel modes

The electromagnetic modes propagating parallel to an ambient magnetic field in a cold plasma consist of left-hand (L) and right-hand (R) circularly polarized modes. Because dust-related effects come into play in low-frequency phenomena, we are mostly interested in the low-frequency Alfvén branches and the whistler modes. At the linear level we describe a new whistler mode [Verheest and Meuris, 1995], in a regime where the dust is assumed to be immobile. The influence of dust in the comet-solar wind interaction is studied [Reddy et al., 1996; Verheest and Meuris, 1997]. A nonlinear treatment of the low-frequency branch concludes this section [Verheest and Meuris, 1996a].

8.2.1 Linear parallel modes in an immobile background

We consider dust grains embedded in a plasma with a number of plasma populations. The dust grains are assumed to be very massive, so the dust dynamics must not be taken into account. Left- or right-circularly polarized, parallel electromagnetic modes are described by Verheest and Meuris [1995]:

$$\omega^2 = k^2c^2 + \sum_\beta \frac{\omega_{p\alpha}^2(\omega - kU_\beta)}{\omega - kU_\beta - i\gamma_{\beta d} \pm \Omega_\beta}. \tag{8.11}$$

Here $\Omega_\beta = q_\beta B_0/m_\beta$ are the signed gyrofrequencies of the plasma particles. Note that for propagation parallel to the ambient magnetic field, the specific form of the sink/source terms in the continuity equation does not play any role. The summation index β varies over all plasma species.

We assume that for all plasma species

$$|\omega - kU_\beta - i\gamma_{\beta d}| \ll |\Omega_\beta|. \tag{8.12}$$

If this is the case, the dispersion relation can be written as:

$$\begin{aligned}
\omega^2 &= k^2c^2 \pm \sum_\beta \frac{\omega_{p\alpha}^2}{\Omega_\beta^2}(\omega - kU_\beta)(\Omega_\beta \mp \omega \pm kU_\beta \pm i\gamma_{\beta d}) \\
\Leftrightarrow \qquad \omega^2 &= k^2c^2 - \omega^2 \sum_\beta \frac{\omega_{p\alpha}^2}{\Omega_\beta^2} \pm \omega \sum_\beta \frac{\omega_{p\alpha}^2}{\Omega_\beta} + 2\omega k \sum_\beta \frac{\omega_{p\alpha}^2 U_\beta}{\Omega_\beta^2} + i\omega \sum_\beta \gamma_{\beta d}\frac{\omega_{p\alpha}^2}{\Omega_\beta^2} \\
&\mp k \sum_\beta \frac{\omega_{p\alpha}^2 U_\beta}{\Omega_\beta} - k^2 \sum_\beta \frac{\omega_{p\alpha}^2 U_\beta^2}{\Omega_\beta^2} - ik \sum_\beta \frac{\omega_{p\alpha}^2 U_\beta \gamma_{\beta d}}{\Omega_\beta^2}.
\end{aligned}$$

With the definition

$$\overline{J_\beta} = \left(\sum_\beta N_\beta m_\beta J_\beta\right) \Big/ \left(\sum_\beta N_\beta m_\beta\right), \tag{8.13}$$

the conservation of current for the plasma as a whole in equilibrium

$$\sum_\beta N_\beta q_\beta U_\beta = 0, \tag{8.14}$$

and the identity

$$\overline{(U_\beta - \overline{U_\beta})^2} = \overline{U_\beta^2} - \left(\overline{U_\beta}\right)^2, \tag{8.15}$$

we rewrite the dispersion relation as:

$$\omega^2\left(1 + \frac{V_A^2}{c^2}\right) - k^2V_A^2 \pm \omega\frac{V_A^2\omega_{pd}^2}{c^2\Omega_d} - 2\omega k\overline{U_\beta} - i\omega\overline{\gamma_{\beta d}} + k^2\overline{U_\beta^2} + ik\overline{U_\beta\gamma_{\beta d}} = 0.$$

For our applications, we might assume that $V_A \ll c$ and hence we come to:

$$\boxed{(\omega - k\overline{U_\beta})^2 - \omega\left(i\overline{\gamma_{\beta d}} \mp \frac{N_d Q_d B_0}{\sum_\beta N_\beta m_\beta}\right) - k^2\left(V_A^2 - \overline{(U_\beta - \overline{U_\beta})^2}\right) + ik\overline{\gamma_{\beta d} U_\beta} = 0. \qquad (8.16)}$$

Here the Alfvén velocity is defined as:

$$V_A^2 = \frac{B_0^2}{\sum_\beta N_\beta m_\beta}, \tag{8.17}$$

and we repeat that the summation must be carried out over the plasma species **excluding** the dust.

If there were no dust, one would be led to the usual Alfvén modes in a drifting plasma. So with $\gamma_{\beta d}$ and N_d zero the dispersion law (8.16) becomes:

$$(\omega - k\overline{U_\beta})^2 - k^2\left(V_A^2 - \overline{(U_\beta - \overline{U_\beta})^2}\right) = 0. \tag{8.18}$$

If there is no relative drift, this dispersion law describes parallel Alfvén waves as can readily be verified. In the presence of different relative drift velocities there is a possibility of beam-induced firehose-type instabilities due to the parallel flow alone, like in many astrophysical applications.

To have a feeling of the order of magnitude of the different terms we look at an electron-proton plasma where the plasma mass is provided by the protons. We compare the two terms of the coefficient of ω in (8.16).

$$\begin{aligned}
& \overline{\gamma_{\beta d}} : \frac{N_d |Q_d| B_0}{\sum_\beta N_\beta m_\beta} \\
\Leftrightarrow \quad & \gamma_{id} : \frac{N_d |Q_d| B_0}{N_i m_i} \\
\Leftrightarrow \quad & \frac{I_{i0}}{q_i} : |Z_d| \Omega_i
\end{aligned}$$

The first term is for our applications of the order of 1 Hz while the second term is at least Z_d times this order of magnitude, and therefore much bigger. On the other hand, we might compare the last term with the cross term of the first bracket in (8.16). This gives us:

$$\begin{aligned}
& 2\omega k\overline{U_\beta} : k\overline{\gamma_{\beta d} U_\beta} \\
\Leftrightarrow \quad & \omega : \overline{\gamma_{\beta d} U_\beta}/\overline{U_\beta} \\
\Leftrightarrow \quad & \omega : \gamma_{id}\left(1 + \frac{m_e N_i}{m_i N_e}\right).
\end{aligned} \tag{8.19}$$

For most applications (except for dusty plasmas with a negligible free electron density), $m_e N_i/(m_i N_e) \ll 1$, and we recover that except for very small frequencies ($\omega \approx \gamma_{\beta d}$) the last term accounts for a lower order effect.

We may conclude that (8.16) gives the dispersion law for parallel electromagnetic modes in a dusty plasma with variable dust grain charges. The dust dynamics are neglected and assumption (8.12) holds. However, for low and extra low-frequencies, the dust alters the modes considerably.

Whistler waves

The mere presence of the dust leads to the appearance of a new kind of whistler wave. Indeed, let us start with dispersion law (8.16). If there were no dust and no equilibrium drifts one would be led to the usual Alfvén modes:

$$\omega = k_\| V_A. \tag{8.20}$$

Next comes the pure influence of the dust presence, without any streaming or charging effects, yielding

$$\omega^2 \pm \frac{N_d Q_d B_0}{\sum_\alpha N_\alpha m_\alpha}\omega - k^2 V_A^2 = 0. \tag{8.21}$$

At the lowest frequencies we are considering this gives a frequency

$$\omega = \frac{k^2 V_A^2 \sum_\alpha N_\alpha m_\alpha}{N_d |Q_d| B_0} = \frac{|\Omega_d| k^2 c^2}{\omega_{pd}^2} \tag{8.22}$$

or equivalently

$$\frac{\omega}{|\Omega_d|} = \frac{c^2 k^2}{\omega_{pd}^2}. \tag{8.23}$$

The mode with dispersion relation (8.22) or (8.23) is the generalization of the right-hand whistler mode in an electron plasma where the ions form an immobile neutralizing background, with dispersion law

$$\frac{\omega}{|\Omega_e|} = \frac{c^2 k^2}{\omega_{pe}^2}. \tag{8.24}$$

This is also known as the Eckersley approximation [Booker, 1984], valid for modes for which $\Omega_i \ll \omega \ll |\Omega_e|$. Here, with the dust treated as immobile, we are looking at low frequencies in the sense that $\omega \ll \Omega_i \ll |\Omega_e|$.

In what follows we are going to look at a three component plasma consisting of protons and electrons and negatively charged dust. We compute from the equilibrium conditions that

$$N_e = N N_i \quad \Longrightarrow \quad U_e = \frac{U_i}{N}, \tag{8.25}$$

with $N = N_e/N_i$ denoting the fractional density of the electrons compared to the protons. This number is below unity in the presence of dust grains, as these are usually negatively charged. It can readily be verified that the electrons and the ions drift in the same direction, which we can take for simplicity as along the positive static magnetic field, and we can calculate that:

$$\begin{aligned}
\overline{U_\alpha} &= \frac{N_e m_e U_e + N_i m_i U_i}{N_e m_e + N_i m_i} = \frac{m_e + m_i}{N m_e + m_i} U_i \simeq U_i \\
\overline{(U_\alpha - \overline{U_\alpha})^2} &= \frac{(1-N)^2 m_e m_i}{N(N m_e + m_i)^2} U_i^2 \simeq \frac{(1-N)^2 m_e}{N m_i} U_i^2.
\end{aligned} \tag{8.26}$$

The latter quantity is usually very small compared to V_A^2, except for unrealistically high drift velocities in the dust frame of reference and therefore we can neglect this term. We used the approximation that $m_e \ll m_i$.

With the foregoing in mind we see that (8.16) can be solved for the low-frequency branch as

$$\mathrm{Re}\,\omega = -\frac{\Omega_d k^2 c^2}{\omega_{pd}^2} = \frac{k^2 V_A^2}{(1-N)\Omega_i}, \tag{8.27}$$

similar to what we found in (8.22), with however in general an imaginary part to it,

$$\mathrm{Im}\,\omega = \frac{\overline{\gamma_{\alpha d}} k^2 V_A^2}{(1-N)^2\Omega_i^2} - \frac{k\overline{\gamma_{\alpha d} U_\alpha}}{(1-N)\Omega_i} = \frac{\overline{\gamma_{\alpha d}}\ \mathrm{Re}\,\omega - k\overline{\gamma_{\alpha d} U_\alpha}}{(1-N)\Omega_i}. \tag{8.28}$$

Before we discuss growth or damping we look at the case when the streaming and the charging effects balance each other. Then perfectly stable modes are possible, which requires that

$$\overline{\gamma_{\alpha d}}\ \mathrm{Re}\,\omega = k\overline{\gamma_{\alpha d} U_\alpha}, \tag{8.29}$$

or more explicitly that the ion streaming be such that

$$\frac{kU_i}{\mathrm{Re}\ \omega} = \frac{N m_e \gamma_{ed} + m_i \gamma_{id}}{m_e \gamma_{ed} + m_i \gamma_{id}}. \tag{8.30}$$

The evaluation of the right-hand side of this equation depends on the values for $\gamma_{\alpha d}$. This quantity is of order unity, provided the relative responses of the electrons and the ions are comparable, as can be expected for N_d small. On the other hand for large N_d -values, we might expect that $\sqrt{m_e}\gamma_{ed} \simeq \sqrt{m_i}\gamma_{id}$ and the quantity is of the order unity. This also holds for the cases between these two limiting cases. We can conclude that there exists a new kind of whistler mode described by the dispersion law (8.23). This mode is damped provided that Re $\omega < kU_i$, while instability occurs for Re $\omega > kU_i$.

The assumption that $\omega \ll \Omega_i$ becomes:

$$k \ll 4 \times 10^{-9}\sqrt{Z_d N_d} = 4 \times 10^{-9}\sqrt{N_i(1-N)}. \tag{8.31}$$

This restricts the dust charge to places where the dust charge is very high as might be the case in the spokes of Saturn or close to a comet. On the other hand, these modes might occur also in laboratory plasmas where the dust charges are appreciably higher.

Linear instabilities in solar wind interaction with dusty cometary plasmas

A natural application of our beam-plasma model is the low-frequency instability due to the pick-up of cometary ions by the solar wind. It is known that in cometary environments enhanced Alfvén wave turbulence occurs due to the mass loading of the solar wind by the cometary ions. These plasma populations can be considered as beam plasmas, because of their high relative streaming velocities which exceed the thermal velocity. Although one could in principle consider both electrostatic and electromagnetic instabilities, the low-frequency electromagnetic fluctuations seem to dominate. The higher-frequency instabilities have a large growth rate but saturate at very low levels of turbulence, and hence are not efficient in destroying the ion beams and in assimilating the beam ions into the main flow [Verheest and Lakhina, 1991].

We consider a cometary plasma with dust, ions and electrons and a solar wind plasma consisting of protons and electrons. With the indices s, c and d we will refer to solar wind particles (electrons and protons), to cometary plasma particles (electrons and protons or cometary water group ions assumed to be singly charged) and average cometary dust grains. A second subscript e or i refers to the corresponding electrons and ions. We work in the cometary reference frame, in which all cometary material is essentially at rest in equilibrium, neglecting the small parallel outflow velocities of such particles ($\sim$ 1 km/s). On the other hand, the beam velocity U will be the projection of the solar wind velocity ($\sim$ 300 km/s) on the direction of the solar wind magnetic field.

We start with dispersion law (8.16), with now:

$$\overline{\gamma_{\alpha d}} = \sum_{\alpha \neq d} \rho_\alpha \gamma_{\alpha d} \Big/ (\rho_{se} + \rho_{si} + \rho_{ce} + \rho_{ci}), \tag{8.32}$$

$$\overline{U_\alpha} = \frac{\rho_{se} + \rho_{si}}{\rho_{se} + \rho_{si} + \rho_{ce} + \rho_{ci}} U = \sigma U, \tag{8.33}$$

$$\overline{\gamma_{\alpha d} U_\alpha} = \frac{\rho_{se}\gamma_{sed} + \rho_{si}\gamma_{sid}}{\rho_{se} + \rho_{si} + \rho_{ce} + \rho_{ci}} U, \tag{8.34}$$

$$\overline{(U_\alpha - \overline{U_\alpha})^2} = \frac{(\rho_{se} + \rho_{si})(\rho_{ce} + \rho_{ci})}{(\rho_{se} + \rho_{si} + \rho_{ce} + \rho_{ci})^2} U^2 = \sigma(1-\sigma)U^2. \tag{8.35}$$

The Alfvén velocity as defined earlier by the summation of all plasma particles can be rewritten in function of $V_{A,sw}$, which is the solar wind Alfvén velocity such that:

$$V_A^2 = \sigma V_{A,sw}^2. \tag{8.36}$$

No dust grains

When no dust grains ($N_d = 0$) are present, the dispersion relation becomes:

$$\omega^2 - 2\sigma k U \omega + \sigma k^2 V_{A,sw}^2 (M^2 - 1) = 0, \tag{8.37}$$

$$\Leftrightarrow \quad (\omega - \sigma k U)^2 + \sigma k^2 V_{A,sw}^2 (-M^2\sigma + M^2 - 1) = 0, \tag{8.38}$$

with M denoting the Alfvénic Mach number $M = U/V_{A,sw}$, and so unstable modes appear when:

$$\sigma < \sigma_{cr} = 1 - \frac{V_{A,sw}^2}{U^2} < 1. \tag{8.39}$$

The solutions of the dispersion law are given by:

$$\omega_1^0 = \sigma kU \pm ikU\sqrt{\sigma(\sigma_{cr} - \sigma)} \qquad \text{for} \qquad \sigma \leq \sigma_{cr} \tag{8.40}$$

$$\omega_2^0 = \sigma kU \pm kU\sqrt{\sigma(\sigma - \sigma_{cr})} \qquad \text{for} \qquad \sigma \geq \sigma_{cr}. \tag{8.41}$$

This means that unstable modes occur, when the fraction of the plasma mass density of solar wind origin is smaller than a threshold value. It means that the mass of the loaded cometary plasma will induce the instability.

No dust charge variation

Next we will look at the influence of the mere presence of the dust grains without dust charge variations. Therefore we neglect the terms in $\gamma_{\alpha d}$ in (8.16) and obtain:.

$$(\omega - k\sigma U)^2 \pm \omega \frac{N_d Q_d B_0}{\sum_\alpha N_\alpha m_\alpha} - \sigma k^2 \left(V_{A,sw}^2 - (1-\sigma)U^2\right) = 0. \tag{8.42}$$

When we introduce the notations:

$$A = \frac{N_d |Q_d| B_0}{\sum_\alpha N_\alpha m_\alpha}, \tag{8.43}$$

$$k_1 = \frac{A}{2U(\sqrt{\sigma} + \sqrt{\sigma_{cr}})\sqrt{\sigma}}, \tag{8.44}$$

$$k_2 = \frac{A}{2U|\sqrt{\sigma} - \sqrt{\sigma_{cr}}|\sqrt{\sigma}}, \tag{8.45}$$

we can rewrite this equation as:

$$\omega^2 - [2\sigma kU \pm \mathrm{Sgn}(\mathrm{Q_d})A]\,\omega + k^2\sigma V_{A,sw}^2(M^2 - 1) = 0. \tag{8.46}$$

The discriminant of (8.46) can then be written for negative dust as:

$$\Delta = 4\sigma U^2(\sigma - \sigma_{cr})(k \pm k_1)(k \mp k_2), \qquad \text{if } \sigma < \sigma_{cr},$$
$$\Delta = 4\sigma U^2(\sigma - \sigma_{cr})(k \pm k_1)(k \pm k_2), \qquad \text{if } \sigma > \sigma_{cr},$$

while for positive dust:

$$\Delta = 4\sigma U^2(\sigma - \sigma_{cr})(k \mp k_1)(k \pm k_2), \qquad \text{if } \sigma < \sigma_{cr},$$
$$\Delta = 4\sigma U^2(\sigma - \sigma_{cr})(k \mp k_1)(k \mp k_2), \qquad \text{if } \sigma > \sigma_{cr},$$

and we come to the following conclusions:

No charged dust	Negatively (positively) charged dust
$\sigma \geq \sigma_{cr}$ stable or marginally stable modes	RHCP (LHCP) becomes unstable for $k_1 < k < k_2$
$\sigma < \sigma_{cr}$ unstable modes due to cometary ion pickup	RHCP (LHCP) mode is stable for $k < k_2$ LHCP (RHCP) mode is stable for $k < k_1$

Numerical evaluation and conclusions

To estimate the relevance of the previous calculation, appropriate values should be put into the expressions (8.44) and (8.45). We consider a typical solar wind plasma (electrons and protons) with plasma density $N_{sw,p} = 6 \times 10^6\mathrm{m}^{-3}$ ($\rho_{sw} = 1 \times 10^{-20}\mathrm{kgm}^{-3}$) an energy of 10 eV with an ambient magnetic field of 9 nT. The solar wind velocity is given by $U = 400 \times 10^3\mathrm{ms}^{-1}$ and the solar wind magnetic field. $V_{A,sw} \approx 80 \times 10^3\mathrm{ms}^{-1}$ and hence $M = 5, \sigma_{cr} = 0.96$.

One expects the variation of the cometary ion density N_i to be similar to that of the neutral gas density. The ion mass of the cometary ion group ions is taken to be 16.8 times the proton mass. Observations of comet Halley by the Giotto spacecraft would indicate that N_i varies as d^{-2} outside the contact surface. At $d = 1.5 \times 10^8$m, the ion density is given by $27 \times 10^6\mathrm{m}^{-3}$ [Balsiger et al., 1986] or $10 \times 10^6\mathrm{m}^{-3}$ [Mukai et al., 1986]. The parameter σ is therefore given as a function of d (in units of 10^9 m) by:

$$\sigma = \frac{d^2}{D + d^2}, \tag{8.47}$$

with $D = 0.756$ and $D = 2.04$ for Mukai et al. [1986] and Balsiger et al. [1986] respectively. This means that at a distance of 10^9m, we can use values of $\sigma \approx 0.3 - 0.6$. These values are smaller than σ_{cr}, and hence instabilities are expected.

For the dust density we use the measurement in the mass channels ranging from 10^{-13} to 10^{-20} kg for the VEGA spacecraft carried out by Vaisberg et al. [1986]. They arrived at a dust density of order $10^{-3}\mathrm{m}^{-3}$ at a distance of 10^8m. The dust is assumed to be charged to 7000 elementary charges, and the sign of the dust charge is not really relevant for the rest of this discussion.

When we put these numbers in (8.44) and (8.45), we come for a typical value of $\sigma = 0.5$:

$$k_1 = 5 \times 10^{-14}\mathrm{m}^{-1} \tag{8.48}$$

$$k_2 = 3 \times 10^{-13}\mathrm{m}^{-1}. \tag{8.49}$$

These length scales associated with these wavenumbers are bigger than the cometary structure itself, and therefore such modes can not exist. We must conclude that the presence of dust grains does not influence the mass loading mechanism of the solar wind significantly.

8.2.2 Nonlinear parallel modes in an immobile background

The nonlinear description of these modes were obtained in a more complete multispecies approach with a not *a priori* specified number of plasma species. We address an interesting intermediate regime, where the linear electromagnetic waves are not affected, but the dust charging influences the slower nonlinear development [Verheest and Meuris, 1996b]. The usual stretching of coordinates and time is [Mio et al., 1976; Mjølhus and Wyller, 1986]

$$\xi = \varepsilon(z - Vt), \qquad \tau = \varepsilon^2 t. \tag{8.50}$$

Variables connected with parallel effects have the following series expansions around a homogeneous equilibrium:

$$\begin{aligned}
n_\alpha &= N_\alpha + \varepsilon n_{\alpha 1} + \varepsilon^2 n_{\alpha 2} + \cdots, \\
q_\alpha &= Q_\alpha + \varepsilon q_{\alpha 1} + \varepsilon^2 q_{\alpha 2} + \cdots, \\
u_{\alpha\parallel} &= U_\alpha + \varepsilon u_{\alpha\parallel 1} + \varepsilon^2 u_{\alpha\parallel 2} + \cdots, \\
E_\parallel &= \varepsilon E_{\parallel 1} + \varepsilon^2 E_{\parallel 2} + \cdots,
\end{aligned} \tag{8.51}$$

whereas those connected with transverse aspects of the waves are developed as

$$\begin{aligned}
\mathbf{u}_{\alpha\perp} &= \varepsilon^{\frac{1}{2}} \mathbf{u}_{\alpha\perp 1} + \varepsilon^{\frac{3}{2}} \mathbf{u}_{\alpha\perp 2} + \cdots, \\
\mathbf{B}_\perp &= \varepsilon^{\frac{1}{2}} \mathbf{B}_{\perp 1} + \varepsilon^{\frac{3}{2}} \mathbf{B}_{\perp 2} + \cdots, \\
\mathbf{E}_\perp &= \varepsilon^{\frac{1}{2}} \mathbf{E}_{\perp 1} + \varepsilon^{\frac{3}{2}} \mathbf{E}_{\perp 2} + \cdots.
\end{aligned} \tag{8.52}$$

Substitution of the stretching (8.50) and the perturbation expansions (8.51)-(8.52) into the equations (8.1–8.3–8.5–8.7) and the quasi-neutrality condition

$$\sum_\alpha n_\alpha q_\alpha = 0, \tag{8.53}$$

gives a sequence of equations, upon equating the coefficients of the various powers of $\varepsilon^{\frac{1}{2}}$. To orders $\frac{3}{2}$ and $\frac{5}{2}$ the global equation (8.10) gives

$$\sum_\alpha N_\alpha m_\alpha (U_\alpha - V) \frac{\partial \mathbf{u}_{\alpha\perp 1}}{\partial \xi} = \frac{B_0}{\mu_0} \frac{\partial \mathbf{B}_{\perp 1}}{\partial \xi}, \tag{8.54}$$

and

$$\begin{aligned}
&\sum_\alpha N_\alpha m_\alpha \frac{\partial \mathbf{u}_{\alpha\perp 1}}{\partial \tau} + \sum_\alpha N_\alpha m_\alpha (U_\alpha - V) \frac{\partial \mathbf{u}_{\alpha\perp 2}}{\partial \xi} \\
&\quad + \sum_\alpha m_\alpha \left(n_{\alpha 1}(U_\alpha - V) + N_\alpha u_{\alpha\parallel 1} \right) \frac{\partial \mathbf{u}_{\alpha\perp 1}}{\partial z} \\
&\quad = \frac{B_0}{\mu_0} \frac{\partial \mathbf{B}_{\perp 2}}{\partial \xi} - \sum_\alpha \sum_\beta N_\alpha m_\alpha \gamma_{\alpha\beta} (\mathbf{u}_{\alpha\perp 1} - \mathbf{u}_{\beta\perp 1}),
\end{aligned} \tag{8.55}$$

so that we shall need to determine the dependent variables only to second order. Furthermore, the coefficients related to the different aspects of the fluctuating dust charges like ν_α, μ_α and $\gamma_{\alpha\beta}$ are supposed to be small, so that the linear waves can be considered as stable and the influence of these coefficients only comes into play at the nonlinear level:

$$\nu_\alpha \sim \mu_\alpha \sim \gamma_{\alpha\beta} \sim \frac{\partial}{\partial \tau}. \tag{8.56}$$

Because of this ordering, the results to lowest orders are reminiscent to what was found in the cold-plasma parallel case for ordinary multispecies treatments [Verheest, 1990]. Starting with the continuity equations (6.2) we find

$$u_{\alpha\|1} = \frac{V - U_\alpha}{N_\alpha} n_{\alpha 1}, \tag{8.57}$$

and from Faraday's equation (8.5) to order $\frac{3}{2}$ and the perpendicular equations of motion (8.3) to lowest order

$$\mathbf{u}_{\alpha\perp 1} = \frac{U_\alpha - V}{B_0} \mathbf{B}_{\perp 1}. \tag{8.58}$$

We can now derive from (8.54) the dispersion law as

$$\sum_\alpha N_\alpha m_\alpha (V - U_\alpha)^2 = \frac{B_0^2}{\mu_0}. \tag{8.59}$$

If all equilibrium drifts vanish, V is nothing but the global Alfvén velocity V_A. At the next order we find that

$$\mathbf{u}_{\alpha\perp 2} = \frac{U_\alpha}{B_0}\mathbf{B}_{\perp 2} + \frac{u_{\alpha\|1}}{B_0}\mathbf{B}_{\perp 1} + \frac{(V - U_\alpha)^2}{B_0 \Omega_\alpha}\mathbf{e}_z \times \frac{\partial \mathbf{B}_{\perp 1}}{\partial \xi} + \frac{1}{B_0}\mathbf{E}_{\perp 2} \times \mathbf{e}_z. \tag{8.60}$$

With the help of this we find from a combination of the parallel equations and charge neutrality that

$$\begin{aligned} n_{\alpha 1} &= \frac{N_\alpha}{2B_0^2} B_{\perp 1}^2 - \frac{\omega_{p\alpha}^2 N_d q_{d1}}{Q_\alpha (V - U_\alpha)^2} \Big/ \sum_\beta \frac{\omega_{p\beta}^2}{(V - U_\beta)^2}, \\ u_{\alpha\|1} &= \frac{V - U_\alpha}{2B_0^2} B_{\perp 1}^2 - \frac{\omega_{p\alpha}^2 N_d q_{d1}}{N_\alpha Q_\alpha (V - U_\alpha)} \Big/ \sum_\beta \frac{\omega_{p\beta}^2}{(V - U_\beta)^2}. \end{aligned} \tag{8.61}$$

Although the interplay between the nonlinear effects and the dust charging is clear, direct influences of fluctuating dust charges will drop out, when we insert all known expressions in (8.55) and eliminate $\mathbf{B}_{\perp 2}$ and $\mathbf{E}_{\perp 2}$ with the help of Faraday's law (8.5) to order $\frac{5}{2}$. This yields a nonlinear evolution equation

$$A\frac{\partial \mathbf{B}_{\perp 1}}{\partial \tau} + \frac{1}{4\mu_0}\frac{\partial}{\partial \xi}\left(B_{\perp 1}^2 \mathbf{B}_{\perp 1}\right) + C\mathbf{e}_z \times \frac{\partial^2 \mathbf{B}_{\perp 1}}{\partial \xi^2} + D\mathbf{B}_{\perp 1} = \mathbf{0}, \tag{8.62}$$

the coefficients of which are

$$A = \sum_\alpha N_\alpha m_\alpha (V - U_\alpha), \tag{8.63}$$

$$C = \sum_\alpha \frac{N_\alpha m_\alpha (V - U_\alpha)^3}{2\Omega_\alpha}, \tag{8.64}$$

$$D = \frac{1}{2}\sum_\alpha \sum_\beta \left[N_\alpha m_\alpha \gamma_{\alpha\beta} - N_\beta m_\beta \gamma_{\beta\alpha}\right] U_\beta. \tag{8.65}$$

From the vector form (8.62) we can derive the usual scalar form of the modified derivative nonlinear Schrödinger equation by projection and combination of $\phi = B_{x1} + iB_{y1}$ as

$$A\frac{\partial \phi}{\partial \tau} + \frac{1}{4\mu_0}\frac{\partial}{\partial \xi}\left(|\phi|^2\phi\right) + iC\frac{\partial^2 \phi}{\partial \xi^2} + D\phi = 0. \tag{8.66}$$

If the charging effects conserve momentum between any two species, as true collisional effects do, then $N_\alpha m_\alpha \gamma_{\alpha\beta} = N_\beta m_\beta \gamma_{\beta\alpha}$ holds, and D vanishes exactly. This also occurs when there are no equilibrium drifts of the different plasma species along the external magnetic field. In both cases all reference to fluctuating dust charges is lost at the order considered and we are left to discussing the ordinary DNLS equation in multispecies plasma, with its attendant soliton solutions. Here we can fall back on existing multispecies descriptions [Verheest, 1990; Verheest and Buti, 1992; Verheest, 1992; Deconinck et al., 1993a; Deconinck et al., 1993b]. We note from these works that the inclusion of pressure and temperature effects vastly complicates the expressions for the coefficients of the DNLS equations, without altering the structural form of the equation. Hence, we will expect similar conclusions to hold also for the DNLS-like equation (8.66) when the source term does not vanish.

When the charging and discharging effects do not conserve momentum between any two species then $D \neq 0$. In that case one is reduced to a discussion of the DNLS-like equation (8.66) which contains a source term. If we integrate (8.66) over all ξ, as is normally done to investigate conservation laws of the ordinary DNLS equation, we find that

$$A\frac{\partial}{\partial \tau}\int_{-\infty}^{+\infty}\phi d\xi + \left[\frac{1}{4\mu_0}|\phi|^2\phi + iC\frac{\partial \phi}{\partial \xi}\right]_{\xi=-\infty}^{\xi=+\infty} + D\int_{-\infty}^{+\infty}\phi d\xi = 0. \tag{8.67}$$

Since all ϕ vanish at infinity, we conclude that

$$\int_{-\infty}^{+\infty}\phi d\xi = \left[\int_{-\infty}^{+\infty}\phi d\xi\right]_{\tau=0}\exp\left\{-\frac{D}{A}\,\tau\right\}. \tag{8.68}$$

There is no stable solution possible, and certainly no conserved densities, in the traditional sense of soliton theory. And the presence of fluctuating dust grains introduces additional damping (growth) of the modes.

8.3 Perpendicular and oblique modes

In a multispecies plasma with an ambient magnetic field along the z-axis, we consider a perpendicular mode along the positive x-axis. The electromagnetic modes propagating perpendicularly to an ambient magnetic field in a cold plasma consist of the ordinary (O) and the extra-ordinary (X) mode. The X mode is elliptically polarized with the polarization plane perpendicular to the ambient magnetic field, but not necessarily perpendicular to the direction of propagation. The O mode is linearly polarized with the electric vector vibrating parallel to the ambient magnetic field. Linearizing and Fourier transforming the set of basic equations (8.1–8.8) in a warm plasma, neglecting the charge variation for the moment, yields the dispersion law for perpendicular modes as

$$\det[D_{ij}] = 0, \tag{8.69}$$

the elements of the dispersion tensor being given by

$$\begin{aligned}
D_{xx} &= \omega^2 - c^2k^2 - \sum_\alpha \omega_{p\alpha}^2 - \sum_\alpha \frac{\omega_{p\alpha}^2 k^2 U_\alpha^2}{\omega^2 - k^2c_{s\alpha}^2 - \Omega_\alpha^2}, \\
D_{xy} = D_{yx} &= \sum_\alpha \frac{\omega_{p\alpha}^2 k U_\alpha \Omega_\alpha}{\omega^2 - k^2c_{s\alpha}^2 - \Omega_\alpha^2}, \\
D_{xz} = D_{zx} &= -\sum_\alpha \frac{\omega_{p\alpha}^2 k U_\alpha}{\omega^2 - k^2c_{s\alpha}^2 - \Omega_\alpha^2}, \\
D_{yy} &= \omega^2 - c^2k^2 - \sum_\alpha \frac{\omega_{p\alpha}^2(\omega^2 - k^2c_{s\alpha}^2)}{\omega^2 - k^2c_{s\alpha}^2 - \Omega_\alpha^2}, \\
D_{yz} = D_{zy} &= \sum_\alpha \frac{\omega_{p\alpha}^2 \Omega_\alpha}{\omega^2 - k^2c_{s\alpha}^2 - \Omega_\alpha^2}, \\
D_{zz} &= 1 - \sum_\alpha \frac{\omega_{p\alpha}^2}{\omega^2 - k^2c_{s\alpha}^2 - \Omega_\alpha^2}.
\end{aligned} \tag{8.70}$$

The low-frequency, long-wavelength limit of (8.69) leads to the definition of the generalized magnetosonic velocity V_S through

$$V_S^2 = \frac{\omega^2}{k^2} = \frac{c^2 + \sum_\alpha \frac{\omega_{p\alpha}^2 c_{s\alpha}^2}{\Omega_\alpha^2}}{1 + \sum_\alpha \frac{\omega_{p\alpha}^2}{\Omega_\alpha^2}} = V_A^2 + \left(1 - \frac{V_A^2}{c^2}\right) \frac{\sum_\alpha \gamma_\alpha P_\alpha}{\sum_\alpha N_\alpha m_\alpha}. \tag{8.71}$$

We have used the definition of the Alfvén velocity obtainable from (8.71) by dropping all temperature or pressure effects.

The O and X mode decouple when there is no relative drift between the plasma populations. Indeed when $U_\alpha = 0$, we recover a separate dispersion relation for the O mode ($D_{xx} = 0$) and for the X-mode ($D_{yy}D_{zz} - D_{yz}^2 = 0$).

In the presence of charge variation the two modes couple even for a cold non-drifting plasma and an analytical description becomes soon very messy. We restrict our analysis to the description of modes in the absence of charge fluctuations. In this way a dusty plasma can be regarded as a multispecies plasma where the dust is considered as a (very massive) plasma population. At the linear level we describe perpendicular modes in the frequency regime between the dust and ion gyrofrequency. The nonlinear description of magnetosonic modes is developed for the isotropic [Meuris and Verheest, 1997] and the anisotropic pressure tensor [Meuris, 1997]. Finally a nonlinear description is given for oblique modes in a cold plasma [Verheest and Meuris, 1996a].

8.3.1 Linear magnetosonic mode

The dispersion relation for the X mode in a warm, driftless plasma becomes:

$$\left(\omega^2 - k^2c^2 - \sum_\alpha \frac{\omega_{p\alpha}^2\omega^2}{\omega^2 - \Omega_\alpha^2}\right)\left(1 - \sum_\alpha \frac{\omega_{p\alpha}^2}{\omega^2 - \Omega_\alpha^2}\right) - \left(\sum_\alpha \frac{\omega_{p\alpha}^2\Omega_\alpha}{\omega^2 - \Omega_\alpha^2}\right)^2 = 0. \tag{8.72}$$

We will be interested in the frequency regime for which $\omega \ll \Omega_\alpha$. In this regime (8.72) can be written as:

$$\left(\omega^2 - k^2c^2 + \frac{c^2\omega^2}{V_A^2} - \frac{\omega_{pd}^2\omega^2}{\omega^2 - \Omega_d^2}\right)\left(1 + \frac{c^2}{V_A^2} - \frac{\omega_{pd}^2}{\omega^2 - \Omega_d^2}\right) - \left(\frac{\omega_{pd}^2}{\Omega_d} + \frac{\omega_{pd}^2\Omega_d}{\omega^2 - \Omega_d^2}\right)^2 = 0, \tag{8.73}$$

with V_A, the plasma Alfvén velocity, defined by:

$$V_A^2 = \frac{B_0^2}{\mu_0 \sum_\alpha N_\alpha m_\alpha}. \tag{8.74}$$

When the frequency is lower than the dust gyro-frequency, we recover the classical Alfvén limit:

$$\frac{k^2c^2}{\omega^2} = 1 + \frac{c^2}{V_{Ad}^2}, \tag{8.75}$$

where V_{Ad} stands for the dust Alfvén velocity, defined by:

$$V_{Ad}^2 = \frac{B_0^2}{\mu_0 \sum_{\alpha,d} N_\alpha m_\alpha} \approx \frac{B_0^2}{\mu_0 N_d m_d} \ll V_A^2, \tag{8.76}$$

provided that the mass of the system is mostly in the dust grains ($N_d m_d \gg N_i m_i$) as is usually the case.

On the other hand, because of the large difference in q_α/m_α-value for the dust and plasma population, there exists a new and interesting frequency regime for which $\Omega_d \ll \omega \ll \Omega_\alpha$. When we assume that $c \gg V_A$, which is valid for most space plasma applications, dispersion law (8.72) becomes:

$$(\omega^2 - k^2V_A^2 - \omega_{DLH}^2)(\omega^2 - \omega_{DLH}^2) = \frac{\omega^2\omega_{DLH}^4}{\Omega_d^2}. \tag{8.77}$$

with

$$\omega_{DLH}^2 = \frac{\omega_{pd}^2V_A^2}{c^2} = \frac{V_A^2}{V_{Ad}^2}\Omega_d^2. \tag{8.78}$$

It is clear that $\omega_{DLH}^2 \gg \Omega_d^2$. In that case the dispersion relation simplifies to

$$\omega^4 - (k^2V_A^2 + \frac{\omega_{DLH}^4}{\Omega_d^2})\omega^2 + k^2V_A^2\omega_{DLH}^2 = 0. \tag{8.79}$$

This dispersion relation contains two low-frequency modes.

		E-ring	Spokes
N_d	(m^{-3})	10^2	10^6
N_i	(m^{-3})	10^7	10^7
T_e	(K)	5×10^5	5×10^5
T_i	(K)	5×10^5	5×10^5
a	(m)	10^{-6}	10^{-6}
B_0	(T)	0.4×10^{-6}	4×10^{-6}
N		0.438	0.0233
χ		-1.87	-0.000326
ω_{pd}	(s^{-1})	0.48	0.0083
ω_{DLH}	(s^{-1})	0.00432	7.5×10^{-4}
Ω_d	(s^{-1})	0.9×10^{-6}	1.6×10^{-9}
V_{Ad}	(ms^{-1})	564	56
V_A	(ms^{-1})	2.7×10^6	27×10^6

Table 8.1: Data used in the case studies

- The low frequency solution of (8.79) for which $\omega \ll \omega_{DLH}$ can be described by neglecting the term in ω^4. The dispersion law can than be written in the following form, similar to the Alfvén modes in a usual proton electron plasma with a frequency lower than the lower-hybrid frequency [Booker, 1984]. The role of the resonance frequency is played by the *dust lower-hybrid frequency* ω_{DLH} [Salimullah, 1995]:

$$\frac{n^2}{n_{Ad}^2} = \frac{1}{1 - (\omega^2/\omega_{DLH}^2)}, \tag{8.80}$$

with

$$n^2 = \frac{k^2c^2}{\omega^2}, \qquad n_{Ad}^2 = \frac{c^2}{V_{Ad}^2}. \tag{8.81}$$

This resonance described the coupling between the plasma motion of the dust grains, and the low-frequency Alfvén mode of the surrounding plasma.

The dispersion law (8.80) makes it possible for very low-frequency dust Alfvén waves to propagate perpendicular to the magnetic field, in the range where $\Omega_d \ll \omega \ll \omega_{DLH}$. The frequency ω_{DLH} plays the role of the lower-hybrid frequency in a dusty plasma.

- The dispersion law (8.79) contains another low-frequency mode. Because $\frac{\omega_{DLH}^2}{\Omega_d} \gg \omega_{DLH}$, we can safely neglect the last term of (8.79), and the dispersion law becomes in a good approximation:

$$\omega^2 = k^2V_A^2 + \frac{\omega_{DLH}^4}{\Omega_d^2}. \tag{8.82}$$

These modes however must obey the assumption $\omega \ll \Omega_i$ and therefore they can only occur, provided that $N_d|Q_d| \ll N_iq_i$, which is highly unlikely for the applications we have in mind.

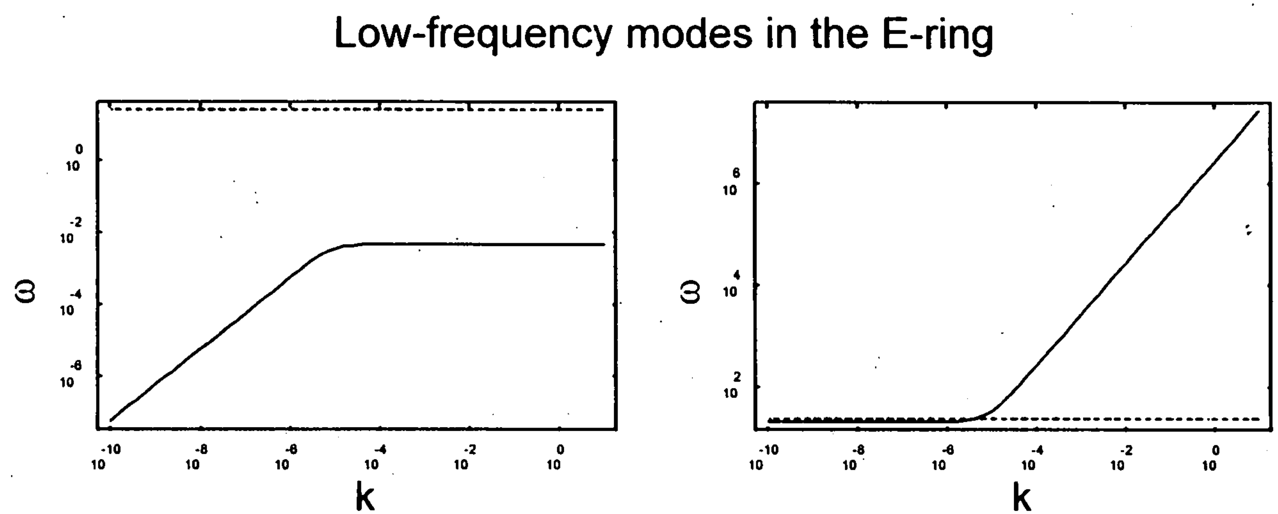

Figure 8.1: The dispersion relation for low-frequency modes corresponding with E-ring. The numerical results were obtained by solving the dispersion relation (8.77). The dashed line stands for the ion gyrofrequency Ω_i.

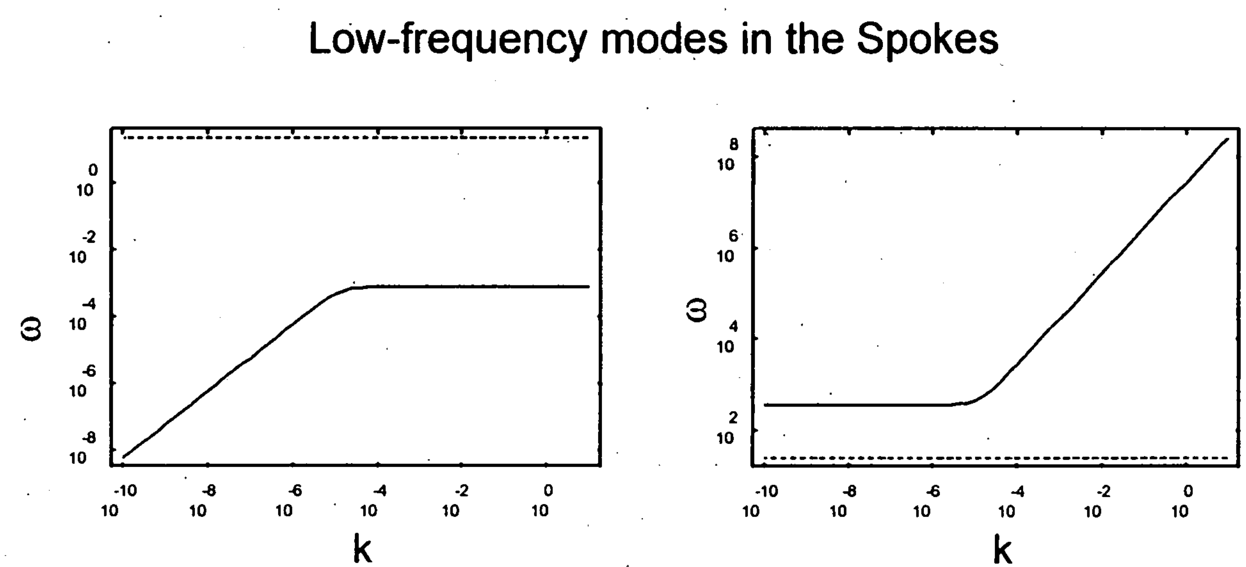

Figure 8.2: The dispersion relation for low-frequency modes corresponding with the spoke region. The numerical results were obtained by solving the dispersion relation (8.77). The dashed line stands for the ion gyrofrequency Ω_i.

Two case studies were carried out, with the data of Table 8.1 and both low-frequency modes were recovered. The dispersion relation is shown in figures 8.1 and 8.2. The dashed curve in these figures corresponds to the ion gyrofrequency. It is clear that the dust Alfvén waves obey the assumption $\omega \ll \Omega_i$ while this is not the case for the other low-frequency mode, and hence the second mode is for these particular choice of the plasma particles unphysical !

8.3.2 Nonlinear perpendicular modes in a warm magnetized multi-ion plasma

The nonlinear multispecies analysis of the magnetosonic modes is carried out using a self-consistent reductive perturbation treatment [Meuris and Verheest, 1997]. As the full dispersion law (8.69) only contains even powers of k and ω, the correction in k to the linear phase velocity will be quadratic, rather than linear as in the case of parallel propagation, resulting in the standard Korteweg–de Vries (KdV) stretching

$$\xi = \varepsilon^{1/2}(z - V_S t), \qquad \tau = \varepsilon^{3/2} t. \tag{8.83}$$

One could let the equations determine the way in which the dependent variables are to be expanded, but it turns out that the standard KdV expansions for perpendicular propagation are adhered to. Hence we take

$$\begin{aligned}
n_\alpha &= N_\alpha + \varepsilon n_{\alpha 1} + \varepsilon^2 n_{\alpha 2} + \cdots, \\
p_\alpha &= P_\alpha + \varepsilon p_{\alpha 1} + \varepsilon^2 p_{\alpha 2} + \cdots, \\
u_{\alpha x} &= U_\alpha + \varepsilon u_{\alpha x1} + \varepsilon^2 u_{\alpha x2} + \cdots, \\
u_{\alpha z} &= \varepsilon u_{\alpha z1} + \varepsilon^2 u_{\alpha z2} + \cdots, \\
B_x &= \varepsilon B_{x1} + \varepsilon^2 B_{x2} + \cdots, \\
E_y &= \varepsilon E_{y1} + \varepsilon^2 E_{y2} + \cdots,
\end{aligned} \tag{8.84}$$

whereas the remainder of the nonzero quantities are expanded as

$$\begin{aligned}
u_{\alpha y} &= \varepsilon^{3/2} u_{\alpha y1} + \varepsilon^{5/2} u_{\alpha y2} + \cdots, \\
B_y &= \varepsilon^{3/2} B_{y1} + \varepsilon^{5/2} B_{y2} + \cdots, \\
E_x &= \varepsilon^{3/2} E_{x1} + \varepsilon^{5/2} E_{x2} + \cdots, \\
E_z &= \varepsilon^{3/2} E_{z1} + \varepsilon^{5/2} E_{z2} + \cdots,
\end{aligned} \tag{8.85}$$

and of course $B_z = 0$ due to (8.8). Substitution of the stretching (8.83) and the perturbation expansions (8.84) and (8.85) into the equations (8.1–8.8) gives a sequence of equations, upon equating the coefficients of the various powers of ε.

We first solve (8.5) for the components of the electric field as a function of the magnetic field:

$$\begin{aligned}
E_{y1} &= -V_S B_{x1}, \\
\frac{\partial E_{y2}}{\partial \xi} &= \frac{\partial B_{x1}}{\partial \tau} - V_S \frac{\partial B_{x2}}{\partial \xi}.
\end{aligned} \tag{8.86}$$

Then the equations of continuity (8.1) and of motion (8.3) are solved to lowest order for $n_{\alpha 1}$ and the components of $\mathbf{u}_{\alpha 1}$. These variables are expressed as a function of the field components as follows:

$$
\begin{aligned}
n_{\alpha 1} &= \frac{N_\alpha B_{x1}}{B_0}, \\
\frac{\partial u_{\alpha x1}}{\partial \xi} &= -\frac{q_\alpha B_{y1}}{m_\alpha}, \\
u_{\alpha y1} &= \frac{E_{z1}}{B_0} + \frac{V_S^2 - c_{s\alpha}^2}{B_0 \Omega_\alpha}\frac{\partial B_{x1}}{\partial \xi} + \frac{U_\alpha B_{y1}}{B_0}, \\
u_{\alpha z1} &= \frac{V_S B_{x1}}{B_0}.
\end{aligned}
\tag{8.87}
$$

The x–component of Ampère's law (8.7) gives us to order $\varepsilon^{3/2}$ that

$$B_{y1} = 0, \tag{8.88}$$

while the y–component of (8.7) vanishes, keeping the definition of V_S in (8.71) in mind. The z–component and Poisson's equation (7.5) vanish to first order due to charge and current neutrality.

The next step is to solve the y–component of the equation of motion (8.3) to second order in ε for

$$u_{\alpha z2} = -\frac{E_{y2}}{B_0} - \frac{V_S B_{x1}^2}{B_0^2} - \frac{V_S m_\alpha}{q_\alpha}\frac{\partial u_{\alpha y1}}{\partial \xi}, \tag{8.89}$$

use the expression for $u_{\alpha y1}$ and substitute this into the z–component of Ampère's law (8.7) to second order. This gives a relation

$$E_{z1} = -\frac{\displaystyle\sum_\alpha \frac{\omega_{p\alpha}^2 (V_S^2 - c_{s\alpha}^2)}{\Omega_\alpha^3}}{\displaystyle 1 + \sum_\alpha \frac{\omega_{p\alpha}^2}{\Omega_\alpha^2}} \frac{\partial B_{x1}}{\partial \xi}, \tag{8.90}$$

which will allow us to rework the expression for $u_{\alpha y1}$. Finally we solve the z–component of (8.3) to order $\varepsilon^{5/2}$ for $u_{\alpha y2}$, together with the continuity equation (8.1) to that order and the polytropic law to order ε^2, substitute that in Ampère's law (8.7), and eliminate all references to B_{x2} and E_{y2} via (8.95). The result is a nonlinear KdV equation

$$A\frac{\partial B_{x1}}{\partial \tau} + C B_{x1}\frac{\partial B_{x1}}{\partial \xi} + D\frac{\partial^3 B_{x1}}{\partial \xi^3} = 0, \tag{8.91}$$

with coefficients

$$
\begin{aligned}
A &= 2V_S\left(1 + \sum_\alpha \frac{\omega_{p\alpha}^2}{\Omega_\alpha^2}\right)^2, \\
C &= \frac{1}{B_0}\left(1 + \sum_\alpha \frac{\omega_{p\alpha}^2}{\Omega_\alpha^2}\right)\sum_\alpha \frac{\omega_{p\alpha}^2 (3V_S^2 + (\gamma_\alpha - 2)c_{s\alpha}^2)}{\Omega_\alpha^2}, \\
D &= \left(1 + \sum_\alpha \frac{\omega_{p\alpha}^2}{\Omega_\alpha^2}\right)\sum_\alpha \frac{\omega_{p\alpha}^2 (V_S^2 - c_{s\alpha}^2)^2}{\Omega_\alpha^4} - \left(\sum_\alpha \frac{\omega_{p\alpha}^2 (V_S^2 - c_{s\alpha}^2)}{\Omega_\alpha^3}\right)^2.
\end{aligned}
\tag{8.92}
$$

This form generalizes known results for perpendicular magnetosonic modes in a standard hydrogen plasma [Kakutani et al., 1968] and in two-ion plasmas [Toida and Ahsawa, 1994]. In particular, whereas quasi-neutrality indeed follows, the displacement current has a non negligible influence, both on the definition of the magnetosonic velocity V_S and of the coefficients in the KdV equation (8.120). Moreover, we have incorporated polytropic pressure variations, whereas the cited results were strictly for cold plasmas only.

8.3.3 Nonlinear perpendicular modes in an anisotropic magnetized multi-ion plasmas

When we use an anistropic plasma model, the problem becomes more complicated [Meuris, 1997]. Indeed, the equation of motion (8.3) must be replaced by

$$\left(\frac{\partial}{\partial t} + u_{\alpha z}\frac{\partial}{\partial z}\right)\mathbf{u}_\alpha + \frac{1}{n_\alpha m_\alpha}\frac{\partial}{\partial z}(\mathbf{e}_z \cdot \mathsf{P}_\alpha) = \frac{q_\alpha}{m_\alpha}(\mathbf{E} + \mathbf{u}_\alpha \times \mathbf{B}), \tag{8.93}$$

while the evolution of the pressure tensor P is described by (6.20)

$$\begin{aligned}\frac{\partial \mathsf{P}_\alpha}{\partial t} + \frac{\partial}{\partial z}(u_{\alpha z}\mathsf{P}_\alpha) + \mathsf{P}_\alpha \cdot \mathbf{e}_z\frac{\partial \mathbf{u}_\alpha}{\partial z} + \left[\mathsf{P}_\alpha \cdot \mathbf{e}_z\frac{\partial \mathbf{u}_\alpha}{\partial z}\right]^T & \\ + \frac{q_\alpha}{m_\alpha}\left[\mathbf{B} \times \mathsf{P}_\alpha + (\mathbf{B} \times \mathsf{P}_\alpha)^T\right] &= 0, \end{aligned} \tag{8.94}$$

in which the divergences of the heat-flow tensors and the sink/source term S_α has been neglected.

Korteweg-de Vries equation

Because we can expect a KdV-equation, we start with the standard KdV-stretching (8.83). One could let the equations determine the way in which the dependent variables are to be expanded, but it turns out that the standard KdV expansions for perpendicular propagation are adhered to. Hence we take for n_α, $u_{\alpha x}$, $u_{\alpha z}$, B_x, E_y, $P_{\alpha xx}$, $P_{\alpha yy}$, $P_{\alpha zz}$, $P_{\alpha xz}$ the expansion $f_\alpha = F_\alpha + \varepsilon f_{\alpha 1} + \varepsilon^2 f_{\alpha 2} + \cdots$ whereas the remainder of the quantities, are expanded as $f_\alpha = \varepsilon^{3/2} f_{\alpha 1} + \varepsilon^{5/2} f_{\alpha 2} + \cdots$ and of course $B_z = 0$ due to (8.8). Substitution of the stretching (8.83) and the perturbation expansions into the equations (8.1–8.8) gives a sequence of equations, upon equating the coefficients of the various powers of ε. We first solve the eqution of Faraday for the components of the electric field as a function of the magnetic field:

$$E_{y1} = -V_S B_{x1}, \tag{8.95}$$

$$\frac{\partial E_{y2}}{\partial \xi} = \frac{\partial B_{x1}}{\partial \tau} - V_S\frac{\partial B_{x2}}{\partial \xi}, \tag{8.96}$$

$$E_{x1} = V_S B_{y1}, \tag{8.97}$$

To order ε, the pressure equation result in $P^{(1)}_{\alpha yy} = P^{(1)}_{\alpha zz}$ and $P^{(1)}_{\alpha xz} = 0$. The yy and zz–components in the order $\varepsilon^{3/2}$ gives us the expressions:

$$P^{(1)}_{\alpha yy} = P^{(1)}_{\alpha zz} = \frac{2P_{\alpha\perp}}{V_S} u_{\alpha z1} \tag{8.98}$$

$$P^{(2)}_{\alpha yz} = -\frac{m_\alpha P_{\alpha\perp}}{2q_\alpha B_0}\frac{\partial u_{\alpha z1}}{\partial \xi} \tag{8.99}$$

Then the equations of continuity and of motion are solved to lowest order for $n_{\alpha 1}$ and the components of $\mathbf{u}_{\alpha 1}$. These variables are expressed as a function of the field components as follows:

$$n_{\alpha 1} = \frac{N_\alpha B_{x1}}{B_0}, \tag{8.100}$$

$$\frac{\partial u_{\alpha x1}}{\partial \xi} = -\frac{q_\alpha B_{y1}}{m_\alpha}, \tag{8.101}$$

$$u_{\alpha y1} = \frac{E_{z1}}{B_0} + \frac{V_S^2 - 2c^2_{s\alpha\perp}}{B_0\Omega_\alpha}\frac{\partial B_{x1}}{\partial \xi} + \frac{U_\alpha B_{y1}}{B_0}, \tag{8.102}$$

$$u_{\alpha z1} = \frac{V_S B_{x1}}{B_0}. \tag{8.103}$$

The x–component of Ampère's law gives us to order $\varepsilon^{3/2}$ that

$$B_{y1} = 0, \tag{8.104}$$

while the y–component of Ampère's law gives us the dispersion relation:

$$1 - \frac{V_S}{c^2} - \frac{V_S^2}{c^2}\sum_\alpha \frac{\omega^2_{p\alpha}}{\Omega^2_\alpha} + 2\sum_\alpha \frac{\omega^2_{p\alpha}c^2_{s\alpha\perp}}{\Omega^2_\alpha c^2} = 0. \tag{8.105}$$

The z–component and Poisson's equation vanish to first order due to charge neutrality.

The next step is to solve the z–component of the equation of motion to second order in ε for

$$u_{\alpha z2} = -\frac{E_{y2}}{B_0} - \frac{V_S B^2_{x1}}{B_0^2} - \frac{V_S m_\alpha}{q_\alpha B_0}\frac{\partial u_{\alpha y1}}{\partial \xi} + \frac{1}{q_\alpha N_\alpha B_0}\frac{\partial P^{(2)}_{\alpha yz}}{\partial \xi}, \tag{8.106}$$

use the previous expressions and substitute this into the z–component of Ampère's law to second order. This gives a relation

$$E_{z1} = -\frac{\displaystyle\sum_\alpha \frac{\omega^2_{p\alpha}(V_S^2 - \frac{3}{2}c^2_{s\alpha\perp})}{\Omega^3_\alpha}}{\displaystyle 1 + \sum_\alpha \frac{\omega^2_{p\alpha}}{\Omega^2_\alpha}}\frac{\partial B_{x1}}{\partial \xi}, \tag{8.107}$$

which will allow us to rework the expression for $u_{\alpha y1}$. The pressure equation can provide us with an expression for $P^{(2)}_{\alpha zz}$. Indeed, when we combine de yy–component and the

zz–component at order $\varepsilon^{5/2}$ and the yz–component of the order ε^2, we find:

$$\begin{aligned} P_{\alpha zz}^{(2)} = & \frac{P_{\alpha\perp}}{B_0^2} B_{x1}^2 + \frac{2P_{\alpha\perp}}{B_0} B_{x2} - \frac{3m_\alpha P_{\alpha\perp}}{2B_0^2 q_\alpha} \frac{\partial E_{z1}}{\partial \xi} \\ & + \left(\frac{2m_\alpha P_{\alpha\perp}^2}{B_0^3 N_\alpha q_\alpha^2} - \frac{5m_\alpha^2 P_{\alpha\perp} V_S^2}{4B_0^3 q_\alpha^2} \right) \frac{\partial^2 B_{x1}}{\partial \xi^2}. \end{aligned} \tag{8.108}$$

Finally we solve the z–component of to order $\varepsilon^{5/2}$ for $u_{\alpha y2}$, substitute that in Ampère's law, and eliminate all references to B_{x2} and E_{y2} via the dispersion relation and Faraday's law. This results in a Korteweg-de Vries equation.

$$A \frac{\partial B_{x1}}{\partial \tau} + C B_{x1} \frac{\partial B_{x1}}{\partial \xi} + D \frac{\partial^3 B_{x1}}{\partial \xi^3} = 0, \tag{8.109}$$

with coefficients

$$\begin{aligned} A &= 2V_S \left(1 + \sum_\alpha \frac{\omega_{p\alpha}^2}{\Omega_\alpha^2} \right)^2 > 0, \\ C &= \frac{3V_S^2}{B_0} \left(1 + \sum_\alpha \frac{\omega_{p\alpha}^2}{\Omega_\alpha^2} \right) \sum_\alpha \frac{\omega_{p\alpha}^2}{\Omega_\alpha^2} > 0, \\ D &= \left(1 + \sum_\alpha \frac{\omega_{p\alpha}^2}{\Omega_\alpha^2} \right) \sum_\alpha \frac{\omega_{p\alpha}^2 (2c_{s\alpha\perp}^4 - \frac{11}{4} c_{s\alpha\perp}^2 V_S^2 + V_S^4)}{\Omega_\alpha^4} - \left(\sum_\alpha \frac{\omega_{p\alpha}^2 (V_S^2 - \frac{3}{2} c_{s\alpha\perp}^2)}{\Omega_\alpha^3} \right)^2. \end{aligned} \tag{8.110}$$

The corresponding linear dispersion law, defining the magnetosonic velocity V_S, is derived during the calculation:

$$V_S^2 = \left(c^2 + 2 \sum_\alpha \frac{\omega_{p\alpha}^2 c_{s\alpha\perp}^2}{\Omega_\alpha^2} \right) \Big/ \left(1 + \sum_\alpha \frac{\omega_{p\alpha}^2}{\Omega_\alpha^2} \right), \tag{8.111}$$

and $c_{s\alpha\perp}^2 = \kappa T_{\alpha\perp}/m_\alpha$. Here $\omega_{p\alpha}$ and Ω_α denote the plasma and gyrofrequency for species α respectively.

8.3.4 Nonlinear oblique modes in a cold magnetized multi-ion plasmas

We model a homogeneous, cold plasma immersed in a uniform magnetic field, and composed of electrons and different types of ions, the number and characteristics of which are not yet specified. For oblique waves or structures propagating along the z–axis, all quantities depend only on z and t, the static magnetic field being taken as $\mathbf{B}_0 = B_0(\sin\vartheta\ \mathbf{e}_x + \cos\vartheta\ \mathbf{e}_z)$ [Verheest and Meuris, 1996a].

The general Alfvén velocity V_A is to be determined later from the linear dispersion requirements. As has been argued several times before, at that time for strictly or very nearly parallel propagation [Verheest, 1992; Deconinck et al., 1993a,b], one can let the equations determine consistently how the dependent variables are to be expanded and hence start for all variables from

$$f = F + \varepsilon f_1 + \varepsilon^2 f_2 + \cdots. \tag{8.112}$$

The only nonzero equilibrium quantities (denoted by capital letters like F) are the densities and the components of the static field. It is also prudent not to impose quasi-neutrality and/or neglect the displacement current from the outset, as is often done in a low-frequency approach.

Substitution of the stretching (8.83) and the perturbation expansions (8.112) into the equations (8.1–8.8) gives a sequence of equations, to be solved iteratively. Although we will not give the details here, one could proceed very systematically by trying to start for low-frequency waves from nonzero $\mathbf{E}_1$ and $\mathbf{B}_1$. Then, after some straightforward but tedious algebra, one would arrive at a true bifurcation point in third order, such that

$$B_{x1} B_0 \sin\vartheta = 0. \tag{8.113}$$

In other words, for really oblique propagation ($\vartheta \neq 0$ and $\sin\vartheta$ finite), we need $B_{x1} = 0$, and as a consequence all first-order variables vanish. The expansion thus starts at order ε^2 in our scheme (the usual KdV ordering, if one replaces the traditional $\varepsilon^{1/2}$ by ε itself), except for quantities like $u_{\alpha y}$, B_y, E_x and E_z, which will only start at order ε^3. This means that the polarization is singled out, for which the wave magnetic field is to lowest order perpendicular to the direction of wave propagation, in the plane spanned by the wavevector and the static field. The linear wave electric field is perpendicular to that plane. For the special case of perpendicular wave propagation, this polarization corresponds to the low-frequency branch of the extraordinary mode.

On the other hand, for strictly or nearly parallel propagation the expansion has to start at order ε for the perpendicular variables and at order ε^2 for the parallel quantities. In that case, because of the different stretching of the independent variables, it leads to vector equivalents of the derivative nonlinear Schrödinger (DNLS) equation [Verheest, 1990] or modifications thereof for slightly oblique propagation [Deconinck et al., 1993].

To lowest nonzero order we find in the ordering chosen that

$$\begin{aligned}
n_{\alpha 2} &= \frac{N_\alpha B_{\perp 0}}{B_0^2}\, B_{x2}, \\
u_{\alpha x2} &= -\frac{V_A B_{\parallel 0}}{B_0^2}\, B_{x2}, \\
u_{\alpha z2} &= \frac{V_A B_{\perp 0}}{B_0^2}\, B_{x2}, \\
u_{\alpha y3} &= \frac{V_A^2}{\Omega_\alpha B_0} \frac{\partial B_{x2}}{\partial \xi} + \frac{E_{z3}}{B_{\perp 0}}.
\end{aligned} \tag{8.114}$$

The vanishing of Ampère's law (8.7) to lowest nontrivial (third) order yields the proper definition of V_A, through

$$V_A^2 = c^2 \left(1 + \sum_\alpha \frac{\omega_{p\alpha}^2}{\Omega_\alpha^2}\right)^{-1}. \tag{8.115}$$

The global equation (8.10) is then also fulfilled to this order, whereas to order ε^4 it shows that

$$\sum_\alpha N_\alpha m_\alpha u_{\alpha y3} = \frac{1}{\mu_0 B_{\perp 0}} \left(\frac{B_{\parallel 0}^2}{V^2} - \frac{B_0^2}{c^2}\right) E_{z3}. \tag{8.116}$$

Together with the expression for $u_{\alpha y3}$ this yields

$$E_{z3} = -\frac{V_A^4}{c^2 \sin^2 \vartheta} \sum_\alpha \frac{\omega_{p\alpha}^2}{\Omega_\alpha^3} \frac{\partial B_{x2}}{\partial \xi}, \tag{8.117}$$

allowing us to rework $u_{\alpha y3}$ as

$$u_{\alpha y3} = \frac{V_A^2}{B_0} \left(\frac{1}{\Omega_\alpha} - \frac{V_A^2}{c^2 \sin^2 \vartheta} \sum_\beta \frac{\omega_{p\beta}^2}{\Omega_\beta^3}\right) \frac{\partial B_{x2}}{\partial \xi}. \tag{8.118}$$

To order ε^5 we will use the global equation (8.10) in the combination of $B_{\parallel 0}$ times its x–component minus $B_{\perp 0}$ times its z–component. We then eliminate quantities like

$$\begin{aligned} B_{\parallel 0} u_{\alpha x2} - B_{\perp 0} u_{\alpha z2} &= -V_A B_{x2}, \\ B_{\parallel 0} u_{\alpha x4} - B_{\perp 0} u_{\alpha z4} &= E_{y4} + u_{z2} B_{x2} + \frac{m_\alpha V_A}{q_\alpha} \frac{\partial u_{\alpha y3}}{\partial \xi} \end{aligned} \tag{8.119}$$

with the help of the y–component of the equations of motion (8.3) to orders 2 and 4 and earlier expressions. Rearranging the different terms with the help of the dispersion law (8.115) and Faraday's law (8.5) to order 5 finally yields a KdV equation

$$A \frac{\partial B_{x2}}{\partial \tau} + C B_{x2} \frac{\partial B_{x2}}{\partial \xi} + D \frac{\partial^3 B_{x2}}{\partial \xi^3} = 0, \tag{8.120}$$

with coefficients

$$\begin{aligned} A &= \frac{2c^4}{V_A^7}, \\ C &= \frac{3c^2 \sin \vartheta}{B_0 V_A^4} \sum_\alpha \frac{\omega_{p\alpha}^2}{\Omega_\alpha^2}, \\ D &= \left(1 + \sum_\alpha \frac{\omega_{p\alpha}^2}{\Omega_\alpha^2}\right) \sum_\alpha \frac{\omega_{p\alpha}^2}{\Omega_\alpha^4} - \frac{1}{\sin^2 \vartheta} \left(\sum_\alpha \frac{\omega_{p\alpha}^2}{\Omega_\alpha^3}\right)^2. \end{aligned} \tag{8.121}$$

This generalizes known results both for oblique modes in a standard hydrogen plasma [Kakutani et al., 1968], and for perpendicular modes in bi-ion plasmas [Toida and Ohsawa, 1994]. At the same time, we have consistently checked how far the usual assumptions concerning low-frequency modes are obeyed in multispecies plasmas of arbitrary composition. Whereas quasi-neutrality indeed follows to the orders needed, the displacement current could have a non negligible influence, both on the definition of the Alfvén velocity V_A and of the coefficients (8.121) in the KdV equation (8.120).

The remarkable property is that the nonlinearity is strongest at strictly perpendicular propagation, and vanishes if one tries to take the parallel limit. Furthermore, as pointed out already by Kakutani et al. [1968], the coefficient of the dispersive term is usually negative for most of the range of oblique propagation, positive for strictly perpendicular modes and changes sign close to perpendicular propagation. It blows up if one tries to take the parallel limit, except for special plasmas as we shall discuss below. This also shows that the case of strictly or very nearly parallel propagation has to be considered separately, leading to a completely different type of nonlinear behaviour [Verheest, 1990].

We now briefly discuss the behaviour of the coefficient D for specific plasmas, and determine in particular the critical angle ϑ_0 where D changes sign. Assuming traditionally that $V_A \ll c$, we find that

$$\sin^2 \vartheta_0 \simeq 1 - \frac{m_e}{m_i} \tag{8.122}$$

in a classical hydrogen plasma with the usual small mass ratio. This gives a critical angle $\vartheta = 88°$. A typical multi-ion plasma is the solar wind, which besides the protons and electrons carries between several to 10% alpha particles, compared to the proton densities, in addition to other minor constituents. Taking for fully ionized helium $q_\alpha = 2e$ and $m_\alpha = 4m_i$ and leaving out the really minor species, one obtains

$$\sin^2 \vartheta_0 \simeq 1 - \frac{4N_i N_\alpha}{N_i^2 + 20N_i N_\alpha + 64N_\alpha^2}. \tag{8.123}$$

The critical angles where D changes sign are around 80° at 1%, 72° at 5% and 70° at 10% alpha particles. Hence increasing the helium number density increases the range of angles around perpendicular propagation where the dispersion is positive.

On the other hand, in an electron-positron plasma ($m_e = m_p$) we see that

$$D = \left(1 + \frac{2\omega_p^2}{\Omega^2}\right) \frac{2\omega_p^2}{\Omega^4} \tag{8.124}$$

is always positive. A relevant question is then of whether in other plasmas a similarly positive dispersion can occur. That would require the vanishing of part of D, such that

$$\sum_\alpha \frac{\omega_{p\alpha}^2}{\Omega_\alpha^3} = 0. \tag{8.125}$$

In a plasma composed of electrons and different kinds of positive ions this cannot occur, as for the usual mass ratios one finds that

$$\sum_\alpha \frac{\omega_{p\alpha}^2}{\Omega_\alpha^3} = \frac{1}{\varepsilon_0 e B_0^3} \sum_{i \neq e} N_i (m_i^2 - m_e^2) > 0, \tag{8.126}$$

the sum being over the (positive) ion species. However, in a plasma which contains at least one species of negative ions, the condition can be fulfilled at critical densities. Taking for simplicity one positively charged ion species (with label 1) and one negatively charged ion species (with label 2), both with unit charges (which amounts to expressing the mass as per unit charge), we get from (8.125) that

$$N_2 = \frac{m_1^2 - m_e^2}{m_2^2 - m_e^2} N_1 \simeq \frac{m_1^2}{m_2^2} N_1. \tag{8.127}$$

An example of this would be an Ar^+–F^- plasma mixture [Nakamura et al., 1985], where the critical density works out as $N_F \simeq 4.4 N_{Ar}$, given that $m_{Ar} = 39.9 m_{\text{proton}}$ and $m_F = 19.0 m_{\text{proton}}$. One can easily generalize the above reasoning for more positive and/or negative constituents.

Except for the special cases of electron-positron plasmas (where also several other waves decouple) or plasmas with negative ions at critical densities, the critical angle is rather close to 90°. Hence the dispersive term has a negative coefficient D for most of the range of oblique waves, and turns positive in a narrow range around perpendicular propagation. Whenever that happens, the solitons solutions to (8.120)

$$B_{x2} = \frac{3MA}{C} \operatorname{sech}^2 \left[\frac{1}{2} \sqrt{\frac{A|M|}{|D|}} (\xi - M\tau) \right] \tag{8.128}$$

will change from subalfvénic ($M < 0$), rarefactive ($B_{x2} < 0$) to superalfvénic ($M > 0$), compressive ($B_{x2} > 0$) in nature.

Chapter 9

Self-gravitational plasmas including dust mass distribution

In plasma physics we may fortunately neglect the gravitational forces. The reason why can be easily resolved numerically. When we compare the gravitational (F_g) and electric forces (F_e) for classical plasma particles, we find that the quantity

$$\frac{F_e}{F_g} = \left(\frac{q_\alpha}{m_\alpha}\right)^2 \frac{1}{4\pi\varepsilon_0 G} \tag{9.1}$$

is of the order of 10^{36} and 10^{42} for protons and electrons respectively. Evidently, the enormous domination of electric forces over gravitation — because of the relative small charge-to-mass ratios — makes it absolutely senseless to take into account the plasma-plasma gravitational interaction. The situation changes when we consider particles for which the charge-to-mass ratio is larger, as is the case for dust grains. For micron-sized grains, the charge needed to balance both forces consists of 5×10^{-4} elementary charges. On the other hand, for one elementary charge, we get the same situation if $a \approx 100\mu$m. When we take a more realistic value of 1000 elementary charges, the critical dust size becomes $a \approx 1$ mm. On the other hand, when we assume that all grain sizes $a \ll \lambda_D$, we can express mass and charge of a dust particle as follows:

$$m(a) = \frac{4}{3}\pi\rho a^3 \sim a^3, \tag{9.2}$$

$$q(a) = 4\pi\varepsilon_0 a V_0 \sim a. \tag{9.3}$$

It can easily be calculated that $F_e = F_g$ is fulfilled for grains for which

$$\left(\frac{V_0}{\rho a^2}\right)^2 = \frac{4\pi G}{9\varepsilon_0}, \tag{9.4}$$

of for a typical ice grain for which $\rho = 1000$ kgm^{-3}:

$$a_{\{\mathrm{m}\}} = 0.018 \times V_{0\{\mathrm{V}\}}^{1/2}. \tag{9.5}$$

This means that for spherical grains embedded in a proton-electron plasma with temperature (T), there exist a critical radius $a_{cr,\{\mathrm{m}\}} = 0.05 \times T_{\{\mathrm{eV}\}}^{1/2}$, for which the gravitational and electromagnetic forces balance each other. We may conclude that although for micron-sized grains the self-gravitation is small, it comes into play for millimetre sized grains and larger.

In reality however, as shown in **chapter 2**, most astrophysical objects demonstrate a broad spectrum of grain sizes. The smallest grains will be mostly influenced by electric forces, while the larger grains will mostly feel a gravitational force. Therefore self-gravitation is intertwined with the form of the grain size distribution. Also, as we will see later in this chapter, small low-frequency long-wavelength deviations from an equilibrium solution of a dusty plasma system are affected by the self-gravitation of the system.

Reverting to the general picture, the behaviour of a self-gravitating plasma is described by the model of **chapter 6**. However, to include the gravitational forces, we change the equation of motion to

$$\frac{\partial \mathbf{u}_\alpha}{\partial t} + \mathbf{u}_\alpha \cdot \nabla \mathbf{u}_\alpha = -\frac{1}{n_\alpha m_\alpha}\nabla p_\alpha + \frac{q_\alpha}{m_\alpha}(\mathbf{E} + \mathbf{u}_\alpha \times \mathbf{B}) - \nabla\psi. \tag{9.6}$$

Here ψ stands for the gravitational potential described by an additional Poisson equation:

$$\nabla^2\psi = 4\pi G \sum_\alpha n_\alpha m_\alpha. \tag{9.7}$$

Because of their high masses, one could be tempted to include only the contribution of the dust grains in (9.7), but that is an unnecessary restriction at this stage.

The problem of condensation of neutral grains due to self-gravitation was first studied by Jeans [1929] and named after him (*Jeans instability*). This is a process in which a slight rearrangement of a uniform distribution of mass by the effect of self-gravitation leads to a further localized condensation of grains. The Jeans instability was originally defined for a neutral gas cloud [Jeans, 1929].

We consider a nearly spatially uniform distribution of uncharged grains (with mass density $\sum_\alpha N_\alpha m_\alpha$) with a slightly overdense region of radius L. This overdense region will collapse if the random velocity v_{rms} of the particles, due to their thermal motions is insufficient to carry them out of the dense region before collapse can occur. A test particle at rest on the edge of the dense sphere will get accelerated by the gravitational forces and the time for this particle to reach the center of the density enhancement can be estimated as [Mace et al., 1997]

$$\tau_c = \sqrt{\frac{3\pi}{32G\sum_\alpha N_\alpha m_\alpha}}. \tag{9.8}$$

On the other hand, the timescale τ_e for particles with random speed v_{rms} to escape the overdense region is of the order

$$\tau_e = \frac{L}{v_{rms}}. \tag{9.9}$$

The critical radius for which the region is stable ($\tau_c = \tau_e$), is given by the Jeanslength, defined by:

$$L_J = \sqrt{\frac{3\pi v_{rms}^2}{32G\sum_\alpha N_\alpha m_\alpha}} \approx \frac{v_{rms}}{\omega_J}, \tag{9.10}$$

where

$$\omega_J^2 = \sum_\alpha \omega_{J\alpha}^2 = 4\pi G \sum_\alpha N_\alpha m_\alpha, \tag{9.11}$$

which defines the proper Jeans length for each particle population α. The Jeans instability occurs, provided that the Jeans frequency exceeds the thermal frequency, or when the characteristic length of the overdense region becomes large than the Jeans length ([Avinash and Shukla, 1994; Mace et al., 1997]). In the case of charged grains unusual and interesting deviations from the corresponding processes of neutral grains are expected.

As a general remark, in what follows we will write $\omega_{p\alpha}\omega_{J\alpha}$ as coming from $N_\alpha q_\alpha$, and hence whenever we encounter a single $\omega_{p\alpha}$ it has to be interpreted as including the sign of the charge. It can readily be verified that:

$$\frac{F_e}{F_g} = \frac{\omega_{p\alpha}^2}{\omega_{J\alpha}^2}. \tag{9.12}$$

This chapter is structured as follows. In the first section, we will study the influence of a reasonable dust size distribution on the plasma and Jeans frequencies ([Meuris et al., 1997], [Meuris, 1997]). Then the electrostatic ([Meuris et al., 1997]) and electromagnetic modes ([Mace et al., 1997], [Verheest et al., 1997]) are considered in section 2 and 3 respectively.

9.1 Influence of a mass distribution on the characteristic frequencies

When we assume that (9.2) and (9.3) hold, we can describe the different dust species in a discontinuous model, where each different q_d/m_d value can be seen as a different dust species. To keep the discussion tractable, we start with two different dust species, with respective grain sizes a_1 and a_2, and densities N_{d1} and N_{d2}. The average size is logically given by

$$\overline{a} = \frac{N_{d1}a_1 + N_{d2}a_2}{N_{d1} + N_{d2}}. \tag{9.13}$$

We can use (9.2) and (9.3) to define

$$\begin{aligned} m_{d1} &= m(a_1), & q_{d1} &= q(a_1) \\ m_{d2} &= m(a_2), & q_{d2} &= q(a_2) \\ \overline{m}_d &= m(\overline{a}) \sim \overline{a}^3, & \overline{q}_d &= q(\overline{a}) \sim \overline{a}. \end{aligned} \tag{9.14}$$

On the other hand, when the number of different m_d/q_d ratios for the different dust grain species increases, a continuous model is reached. For many astrophysical applications the mass distribution is given by a power law, for charged dust grains with radii a in a given range $[a_{min}, a_{max}]$. The differential density distribution goes like

$$n(a)da = Ka^{-\beta}da. \tag{9.15}$$

This kind of distribution is very common in space plasmas (see chapter 2). We find values of $\beta = 4.6$ for the F-ring of Saturn [Showalter et al., 1993], while for the G-ring values of $\beta = 7$ and $\beta = 6$ or smaller were obtained [Gurnett et al., 1983; Showalter et al., 1992; Meyer-Vernet et al., 1997]. For cometary environments, we recall a value of $\beta = 3.4$ [McDonnell et al., 1987].

On the other hand, for dusty plasma experiments (dusty crystals and charging experiments) the dust size distribution is often found to be normally distributed:

$$n(a)da = \frac{N_{tot}}{\sqrt{\pi}\sigma \mathrm{Erf}[\varepsilon/\sigma]} \exp\left[\frac{(a-\overline{a})^2}{\sigma^2}\right] da, \tag{9.16}$$

where N_{tot} denotes the total density of dust grains, σ the width of the distribution and ε the domain $[\overline{a}$-ε, $\overline{a}$+$\varepsilon]$ in which the particle sizes can be found. We assume that $\varepsilon/\sigma > 2$, and therefore $\mathrm{Erf}[\varepsilon/\sigma] \approx 1$.

Plasma frequency

- For the discrete model we define the following plasma frequencies

$$\begin{aligned} \omega_{pd1}^2 &= \frac{N_{d1}q_{d1}^2}{\varepsilon_0 m_{d1}}, \\ \omega_{pd2}^2 &= \frac{N_{d2}q_{d2}^2}{\varepsilon_0 m_{d2}}, \\ \overline{\omega_{pd}^2} &= \frac{(N_{d1}+N_{d2})\overline{q_d}^2}{\varepsilon_0 \overline{m_d}}. \end{aligned} \tag{9.17}$$

Because of (9.13), the total charge (Q_t) that resides on the dust grains is the same for the case where all dust grains have the same mean radius, $Q_t = (N_{d1}+N_{d2})4\pi\varepsilon_0 V_0 \overline{a}$, as for the dust distribution $Q_t = (N_{d1}a_1 + N_{d2}a_2)4\pi\varepsilon_0 V_0$.

We can introduce the quantities

$$\delta = \frac{a_1}{a_2}, \qquad \nu = \frac{N_{d2}}{N_{d1}}. \tag{9.18}$$

To model a realistic power law, we have to assume that there are more grains of smaller size than larger ones, and hence $\delta < 1$, $\nu < 1$. The following ratio is investigated:

$$
\begin{aligned}
R_d &= \sum_d \omega_{pd}^2 \Big/ \overline{\omega_{pd}^2} \\
&= 1 + \frac{\nu(1-\delta)^2}{\delta(1+\nu)^2} > 1
\end{aligned} \tag{9.19}
$$

This ratio is larger than one for arbitrary δ and ν, and hence explicit use of two dust species increases the ratio R_d. Of course the same reasoning holds *a fortiori* for three or more dust species, by repeating the type of argument whenever two dust species are replaced by their averages.

- For the power law mass distribution we define that

$$
\omega_{pd}^2 = \int_{a_{min}}^{a_{max}} \frac{n(a)q^2(a)}{\varepsilon_0 m(a)} da, \tag{9.20}
$$

and

$$
\overline{a} = \int_{a_{min}}^{a_{max}} n(a) a da \Big/ \int_{a_{min}}^{a_{max}} n(a) da. \tag{9.21}
$$

Again, because of this definition, the total charge that resides on the dust grains remains the same for both models. Following the previous calculation, we derive

$$
\begin{aligned}
R_c &= \omega_{pd}^2 \Big/ \frac{N_{tot}\overline{q_d}^2}{\varepsilon_0 \overline{m}_d} \\
&= \frac{(a_{max}^{-\beta} - a_{min}^{-\beta})(a_{max}^{-\beta+2} - a_{min}^{-\beta+2})}{(a_{max}^{-\beta+1} - a_{min}^{-\beta+1})^2} \frac{(\beta-1)^2}{\beta(\beta-2)} \\
&= \frac{(c^{-\beta}-1)(c^{-\beta+2}-1)}{(c^{-\beta+1}-1)^2} \frac{(\beta-1)^2}{\beta(\beta-2)},
\end{aligned} \tag{9.22}
$$

with N_{tot} the total number density of dust grains, given by:

$$
N_{tot} = \int_{a_{min}}^{a_{max}} n(a) da, \tag{9.23}
$$

and $c = a_{max}/a_{min}$. Numerical values for $R_c(\beta, c)$ are shown in Table 9.1.

	$c = 10^0$	$c = 10^1$	$c = 10^2$	$c = 10^3$	$c = 10^4$
$\beta = 1$	1	1.53	4.62	20.9	118
$\beta = 2$	1	1.41	2.35	3.46	4.60
$\beta = 3$	1	1.22	1.32	1.33	1.33
$\beta = 4$	1	1.12	1.12	1.12	1.12
$\beta = 5$	1	1.07	1.07	1.07	1.07
$\beta = 6$	1	1.04	1.04	1.04	1.04
$\beta = 7$	1	1.03	1.03	1.03	1.03

Table 9.1: The expression $R_c(\beta, c)$ as a function of different β and c.

The ratio R_c turns out to be larger than 1 in the range $(1 < \beta, 1 < c)$, which means that also for the continuous case, a power law size distribution increases the dust plasma frequency.

- For large β, the ratio goes to 1, and the influence of the dust distribution vanishes. In that case the influence of c on the result may be neglected.
- However, for smaller β, the ratio R_c reaches higher values and increases with c.

- Along the same paths, we define for a normal distribution

$$\omega_{pd}^2 = \int_{\bar{a}-\varepsilon}^{\bar{a}+\varepsilon} \frac{n(a)q^2(a)}{\varepsilon_0 m(a)} da, \tag{9.24}$$

and

$$\begin{aligned} \bar{a} &= \int_{\bar{a}-\varepsilon}^{\bar{a}+\varepsilon} n(a) a da \Big/ \int_{\bar{a}-\varepsilon}^{\bar{a}+\varepsilon} n(a) da, \\ &= \int_{\bar{a}-\varepsilon}^{\bar{a}+\varepsilon} n(a) a da \Big/ N_{tot}, \end{aligned} \tag{9.25}$$

and calculate the following ratio:

$$R_n = \omega_{pd}^2 \Big/ \frac{N_{tot}\overline{q_d}^2}{\varepsilon_0 \overline{m_d}}. \tag{9.26}$$

The numerical results are given in Table 9.2. We can see that, although changes due to the normal distribution are small, R_n turns out to be bigger than 1, and hence the plasma frequency increases with a normal dust size distribution.

It can be shown that even for variances in the dust grain size of 30 %, the resulting change in the dust plasma frequency is only 5 %.

$\sigma/\bar{a}$	5 %	10 %	20 %	30 %
$R_n(\sigma/\bar{a})$	1.001	1.005	1.02	1.05

Table 9.2: The expression $R_n(\sigma/\bar{a})$ as a function of different $\sigma/\bar{a}$.

- When we consider the dispersion relation for the dust-acoustic mode with a dust size distribution [Rao et al., 1990]:

$$\omega^2 = \frac{k^2\lambda_D^2}{1+k^2\lambda_D^2} \sum_d \omega_{pd}^2, \tag{9.27}$$

we see that the frequency will get changed by the distribution. The overall Debye length remains the same for a mono-sized dust, as for a dust size distribution. Indeed, because of the definition of the mean dust grain radius, the total number of charges on the dust grains remains the same for the two models. Therefore the number of free electrons, and hence the Debye length will not change. The change in phase velocity of the dust-acoustic modes relies therefore totally on the difference in dust plasma frequency, and the previous results can be used.

Jeans frequency

- For the discrete model we define the following Jeans frequencies

$$\begin{aligned} \omega_{Jd1}^2 &= 4\pi G N_{d1} m_{d1}, \\ \omega_{Jd2}^2 &= 4\pi G N_{d2} m_{d2}, \\ \overline{\omega_{Jd}^2} &= 4\pi G (N_{d1} + N_{d2}) \overline{m_d}. \end{aligned} \tag{9.28}$$

We again introduce the quantities

$$\delta = \frac{a_1}{a_2}, \qquad \nu = \frac{N_{d2}}{N_{d1}}, \tag{9.29}$$

but now investigate the following ratio:

$$\begin{aligned} S_d &= \sum_d \omega_{Jd}^2 \Big/ \overline{\omega_{Jd}^2} \\ &= 1 + \frac{(\delta - 1)^2 \nu (1 + 2\delta + 2\nu + \delta\nu)}{(\delta + \nu)^3} > 1 \end{aligned} \tag{9.30}$$

This ratio is larger than one for arbitrary δ and ν, and hence explicit use of two dust species increases the ratio S_d and *a fortiori* for three or more dust species.

- For the power law mass distribution we now define that

$$\omega_{Jd}^2 = 4\pi G \int_{a_{min}}^{a_{max}} n(a) m(a) da, \tag{9.31}$$

with again

$$\bar{a} = \int_{a_{min}}^{a_{max}} n(a) a da \Big/ \int_{a_{min}}^{a_{max}} n(a) da. \tag{9.32}$$

Following the previous calculation, we derive

$$\begin{aligned} S_c &= \omega_{Jd}^2 \Big/ (4\pi G N_{tot} \overline{m_d}) \\ &= \frac{(a_{max}^{-\beta+4} - a_{min}^{-\beta+4})(a_{max}^{-\beta+1} - a_{min}^{-\beta+1})^2}{(a_{max}^{-\beta+2} - a_{min}^{-\beta+2})^3} \frac{(\beta - 2)^3}{(\beta - 4)(\beta - 1)^2} \\ &= \frac{(c^{-\beta+4} - 1)(c^{-\beta+1} - 1)^2}{(c^{-\beta+2} - 1)^3} \frac{(\beta - 2)^3}{(\beta - 4)(\beta - 1)^2}. \end{aligned} \tag{9.33}$$

and $c = a_{max}/a_{min}$. Numerical values for $S_c(\beta, c)$ are shown in Table 9.3.

The ratio S_c turns out to be larger than 1 in the range $(1 < \beta, 1 < c)$, which means that also for the continuous case, a power law size distribution increases the Jeans frequency.

  - For large β, the ratio goes to 1, and the influence of the dust distribution vanishes. Nevertheless, for realistic values of β given above the effect can be considerable.

	$c=10^0$	$c=10^1$	$c=10^2$	$c=10^3$	$c=10^4$
$\beta=1$	1	2.42	7.30	16.0	28.5
$\beta=2$	1	3.28	50.2	1520	64200
$\beta=3$	1	3.02	25.5	250	2490
$\beta=4$	1	2.10	4.09	6.12	8.16
$\beta=5$	1	1.52	1.68	1.68	1.69
$\beta=6$	1	1.27	1.28	1.28	1.28
$\beta=7$	1	1.16	1.16	1.16	1.16

Table 9.3: The expression $S_c(\beta, c)$ as a function of different β and c.

  - For smaller β, the ratio S_c reaches higher values and increases with c.

- Along the same paths, we define for a normal distribution

$$\omega_{Jd}^2 = 4\pi G \int_{\overline{a}-\varepsilon}^{\overline{a}+\varepsilon} n(a)m(a)da, \tag{9.34}$$

  and calculate the following ratio:

$$S_n = \omega_{pd}^2 \Big/ (4\pi G N_{tot}\overline{m_d}). \tag{9.35}$$

  The numerical results are given in Table 9.4. We can see that although changes due to the normal distribution are small, S_n turns out to be bigger than 1, and hence the Jeans frequency increases with a normal dust size distribution.

  It can be shown that even for variances in the dust grain size of 30 %, the resulting change in the Jeans frequency is only 13 %.

$\sigma/\overline{a}$	5 %	10 %	20 %	30 %
$S_n(\sigma/\overline{a})$	1.004	1.02	1.06	1.13

Table 9.4: The expression $S_n(\sigma/\overline{a})$ as a function of different $\sigma/\overline{a}$.

Ratio of plasma and Jeans frequency

Now that we know that both plasma and Jeans frequency increase when we consider a mass distribution, it is worth looking at their ratio:

- We need to investigate the following ratio:

$$\begin{aligned} T_d &= \frac{\sum_d \omega_{Jd}^2}{\sum_d \omega_{pd}^2} \Big/ \frac{\overline{\omega}_{Jd}^2}{\overline{\omega}_{pd}^2} \\ &= \frac{(N_{d1}a_1^3 + N_{d2}a_2^3)(N_{d1}+N_{d2})^4 a_1 a_2}{(N_{d1}a_1 + N_{d2}a_2)^4 (N_{d1}a_2 + N_{d2}a_1)} \end{aligned}$$

$$
\begin{aligned}
&= \frac{(\delta^3+\nu)(1+\nu)^4\delta}{(\delta+\nu)^4(1+\delta\nu)} \\
&= 1+\frac{\nu(1-\delta)^2\left\{\delta^2(1-\delta)+\nu^2(2\delta+4\delta^2-\nu)+R'\right\}}{(\delta+\nu)^4(1+\delta\nu)},
\end{aligned} \tag{9.36}
$$

with

$$
R' = \delta\left[1+\delta+\nu(2+\delta)(2+\nu^2)\right] > 0. \tag{9.37}
$$

As can be seen this ratio is larger than one under the assumptions made, and therefore the Jeans frequency will increase faster than the plasma frequency.

- For the continous case and the normal distribution, we can compare the Tables 9.1–9.4 to come to the same conclusion.

9.2 Electrostatic modes

Following Bliokh and Yaroshenko [1985], we linearize and Fourier transform the continuity equation (6.2), the Poisson equations (6.26) and (9.7), (9.6) neglecting the charge variation. This assumes that there exists some kind of equilibrium solution for the different variables. Because there is no such thing as negative masses, there is no way to make the gravitational potential disappear in the zeroth order, as is the case for the electrostatic potential. However, we might gain some important physical insight by invoking *Jeans swindle* and ignoring the zeroth order of the potential field of gravity in looking at local perturbations. This is justified as long as the scale for changes in the gravitational potential in the equilibrium system is much larger than the scale of the perturbations.

We get the general dispersion law as [Meuris et al., 1997]

$$
\begin{aligned}
&\left(1-\sum_\alpha \frac{\omega_{p\alpha}^2}{(\omega-kU_\alpha)^2-k^2c_{s\alpha}^2}\right)\left(1+\sum_\alpha \frac{\omega_{J\alpha}^2}{(\omega-kU_\alpha)^2-k^2c_{s\alpha}^2}\right) \\
&+\left(\sum_\alpha \frac{\omega_{p\alpha}\omega_{J\alpha}}{(\omega-kU_\alpha)^2-k^2c_{s\alpha}^2}\right)^2 = 0.
\end{aligned} \tag{9.38}
$$

Before discussing (9.38) in more detail, we emphasize that if *all* species are cold ($c_{s\alpha}=0$) and not streaming ($U_\alpha = 0$), the last (squared) term vanishes exactly and there is a full decoupling between electrostatic and Jeans modes, regardless of the composition of the plasma [Bliokh et al., 1995]. This is because $\omega_{p\alpha}\omega_{J\alpha} \sim N_\alpha q_\alpha$ includes the sign of the charges, as stated already in the introduction of this chapter.

We suppose that both the electrons and the (positive) ions can be treated as inertialess Boltzmann species. The condition is now that phase velocities are much smaller than the electron and ion thermal velocities, Re $\omega/k \ll c_{si}, c_{se}$. Defining A as standing for

$$
A = \frac{k^2\lambda_D^2}{1+k^2\lambda_D^2}, \tag{9.39}
$$

with λ_D the Debye length, we find from the dispersion law (9.38) without additional approximations a simple biquadratic equation:

$$\omega^4 + \left(\omega_{Jd}^2 - A\ \omega_{pd}^2\right)\omega^2 - \frac{A}{2}\sum_d\sum_{d'}(\omega_{pd}\omega_{Jd'} - \omega_{pd'}\omega_{Jd})^2 = 0. \tag{9.40}$$

As the product of the roots of (9.40) for ω^2 is negative, we always have a real solution for ω^2, corresponding to a stable mode, as well as a purely imaginary mode ($\omega^2 < 0$). The roots are given by

$$\frac{\omega^2}{\omega_{pd}^2} = \frac{1}{2}\left(A - B \pm \sqrt{(A-B)^2 + 2AC}\right), \tag{9.41}$$

with

$$B = \frac{\omega_{Jd}^2}{\omega_{pd}^2}, \tag{9.42}$$

$$C = \frac{1}{\omega_{pd}^4}\sum_d\sum_{d'}(\omega_{pd}\omega_{Jd'} - \omega_{pd'}\omega_{Jd})^2. \tag{9.43}$$

Both coefficients would be very small for typical micron-sized dust grains, and it is only for highly charged millimetre-sized dust that $B \simeq 1$. For the discussion of the modes we remark that

$$2B - C = \frac{2}{\omega_{pd}^4}\left(\sum_d \omega_{pd}\omega_{Jd}\right)^2 > 0, \tag{9.44}$$

so that we find simple bounds for the discriminant in (9.41) from

$$(A-B)^2 \leq (A-B)^2 + 2AC = (A+B)^2 - 2A(2B-C) < (A+B)^2. \tag{9.45}$$

In addition, we get from the special case $A = B < 1$ a critical wavenumber given by

$$k_c = \frac{1}{\lambda_D}\sqrt{\frac{\omega_{Jd}^2}{\omega_{pd}^2 - \omega_{Jd}^2}}, \tag{9.46}$$

and can introduce the dust-acoustic frequency ω_{da} by

$$\omega_{da}^2 = A\omega_{pd}^2 = \frac{k^2\lambda_D^2\omega_{pd}^2}{1 + k^2\lambda_D^2}. \tag{9.47}$$

The description of the modes goes as follows (see also Table 9.5):

- When $A > B$ or $\omega_{da} > \omega_{Jd}$, the plasma effects dominate, with a permissible k range determined by $k_c < k$. In the solution of (9.41) the square root with the plus sign gives a *generalized dust-acoustic wave* [Rao et al., 1990], at a higher frequency due to the dust distribution.

  The minus sign in front of the square root gives rise to an unstable mode, the frequency of which vanishes when C and the dust mass distribution go to zero. Hence we will call this new mode a *dust distribution instability*.

		Stable modes ($\omega^2 > 0$)	Unstable modes $\omega^2 < 0$
$B < 1$	$k < k_c$	New stable mode $0 \le \omega^2 < \omega_{da}^2$	Jeans instability $-\omega_{Jd}^2 < \omega^2 \le \omega_{da}^2 - \omega_{Jd}^2 < 0$
	$k = k_c$	New stable mode $\omega^2 = \omega_{pd}\omega_{Jd}\sqrt{C/2}$	Dust distribution instability $\omega^2 = -\omega_{pd}\omega_{Jd}\sqrt{C/2}$
	$k_c < k$	Dust-acoustic mode $0 < \omega_{da}^2 - \omega_{Jd}^2 \le \omega^2 < \omega_{da}^2$	Dust distribution instability $-\omega_{Jd}^2 < \omega^2 \le 0$
$B \ge 1$	all k	New stable mode $0 \le \omega^2 < \omega_{da}^2$	Jeans instability $-\omega_{Jd}^2 < \omega^2 \le \omega_{da}^2 - \omega_{Jd}^2 < 0$

Table 9.5: Overview of the different modes included in equation (9.40)

- In the special case that $A = B$ or $k = k_c$, the dust distribution leads to stable and unstable modes, with

$$\omega^2 = \pm\,\omega_{pd}\omega_{Jd}\sqrt{\frac{C}{2}}. \tag{9.48}$$

  Without dust distribution these are all zero-frequency modes.

- For the case $A < B$ the self-gravitational effects dominate, and the square root with the plus sign gives a new stable mode, which does not exist without dust mass distribution. For the limits on k we have to distinguish between the possibilities that $A < B < 1$, with then $k < k_c$, whereas for $A < 1 \le B$ there are no restrictions on k. This latter case is highly unlikely for the usually considered micron-sized grains.

  The mode with the minus sign in front of the square root is a modified Jeans mode, and the dust mass distribution increases its growth rate.

9.3 Electromagnetic modes

Parallel electromagnetic modes will not couple to the self-gravitation. It can be seen from (9.6) that the self-gravitation comes only into play for $\mathbf{u}_\alpha \parallel \mathbf{k}$, even in the presence of thermal effects. This means that only the electrostatic modes are changed as mentioned earlier. The dispersion relation for the parallel electromagnetic modes remains unchanged and so the results from section 8.2 are appropriate.

The description of perpendicular modes is less straightforward. Linearization and Fourier transformation of (6.2), (9.6) the Poisson equation (9.7) and Maxwell's equations in a warm, magnetized self-gravitational plasma (neglecting charge dluctuations) yields

$$\begin{pmatrix} D_{xx} & D_{xy} & D_{xz} & D_{x\psi} \\ D_{yx} & D_{yy} & D_{yz} & D_{y\psi} \\ D_{zx} & D_{zy} & D_{zz} & D_{z\psi} \\ D_{\psi x} & D_{\psi y} & D_{\psi z} & D_{\psi\psi} \end{pmatrix} \cdot \begin{pmatrix} E_x \\ E_y \\ E_z \\ \psi \end{pmatrix} = 0, \tag{9.49}$$

from which the general dispersion law follows as

$$\det[D_{ij}] = 0. \tag{9.50}$$

The elements of the dispersion tensor are (up to scaling factors) given by

$$\begin{aligned}
D_{xx} &= 1 - \sum_\alpha \frac{\omega_{p\alpha}^2}{\omega^2 - k^2 c_{s\alpha}^2 - \Omega_\alpha^2}, \\
D_{xy} = D_{yx} &= \sum_\alpha \frac{\omega_{p\alpha}^2 \Omega_\alpha}{\omega^2 - k^2 c_{s\alpha}^2 - \Omega_\alpha^2}, \\
D_{xz} = D_{zx} &= -\sum_\alpha \frac{\omega_{p\alpha}^2 k U_\alpha}{\omega^2 - k^2 c_{s\alpha}^2 - \Omega_\alpha^2}, \\
D_{x\psi} = D_{\psi x} &= \sum_\alpha \frac{\omega_{p\alpha}\omega_{J\alpha}}{\omega^2 - k^2 c_{s\alpha}^2 - \Omega_\alpha^2}, \\
D_{yy} &= \omega^2 - c^2k^2 - \sum_\alpha \frac{\omega_{p\alpha}^2(\omega^2 - k^2 c_{s\alpha}^2)}{\omega^2 - k^2 c_{s\alpha}^2 - \Omega_\alpha^2}, \\
D_{yz} = D_{zy} &= \sum_\alpha \frac{\omega_{p\alpha}^2 k U_\alpha \Omega_\alpha}{\omega^2 - k^2 c_{s\alpha}^2 - \Omega_\alpha^2}, \\
D_{y\psi} = D_{\psi y} &= -\sum_\alpha \frac{\omega_{p\alpha}\omega_{J\alpha}\Omega_\alpha}{\omega^2 - k^2 c_{s\alpha}^2 - \Omega_\alpha^2}, \\
D_{zz} &= \omega^2 - c^2k^2 - \sum_\alpha \omega_{p\alpha}^2 - \sum_\alpha \frac{\omega_{p\alpha}^2 k^2 U_\alpha^2}{\omega^2 - k^2 c_{s\alpha}^2 - \Omega_\alpha^2}, \\
D_{z\psi} = D_{\psi z} &= \sum_\alpha \frac{\omega_{p\alpha}\omega_{J\alpha} k U_\alpha}{\omega^2 - k^2 c_{s\alpha}^2 - \Omega_\alpha^2}, \\
D_{\psi\psi} &= -1 - \sum_\alpha \frac{\omega_{J\alpha}^2}{\omega^2 - k^2 c_{s\alpha}^2 - \Omega_\alpha^2}.
\end{aligned} \tag{9.51}$$

9.3.1 Driftless, unmagnetized plasma

In the absence of equilibrium drifts along the external magnetic field ($U_\alpha = 0$), the dispersion law splits in two parts. One describes the high-frequency O-mode, with dispersion $D_{zz} = 0$ or

$$\omega^2 = c^2k^2 + \sum_\alpha \omega_{p\alpha}^2, \tag{9.52}$$

for which thermal or self-gravitational effects do not come into play. The remainder of (9.50) then describes a generalized X-mode. In what follows, we will be concerned with the latter.

If, in addition, the plasma is also unmagnetized, then a further factorization is possible, into another times (9.52), and [Bliokh and Yaroshenko, 1985; Meuris et al., 1997]

$$\left(1 - \sum_\alpha \frac{\omega_{p\alpha}^2}{\omega^2 - k^2 c_{s\alpha}^2}\right)\left(1 + \sum_\alpha \frac{\omega_{J\alpha}^2}{\omega^2 - k^2 c_{s\alpha}^2}\right) + \left(\sum_\alpha \frac{\omega_{p\alpha}\omega_{J\alpha}}{\omega^2 - k^2 c_{s\alpha}^2}\right)^2 = 0. \tag{9.53}$$

This has interesting long-wavelength or, equivalently, low-temperature limits, in the sense that for $k \to 0$ or $c_{s\alpha} \to 0$ a decoupling occurs between the high-frequency limit, the usual electrostatic plasma oscillations, with dispersion

$$\sum_\alpha \frac{\omega_{p\alpha}^2}{\omega^2 - k^2 c_{s\alpha}^2} \simeq 1, \tag{9.54}$$

and the low-frequency ordinary Jeans instability, obeying

$$1 + \sum_\alpha \frac{\omega_{J\alpha}^2}{\omega^2 - k^2 c_{s\alpha}^2} \simeq 0. \tag{9.55}$$

The latter is also the only global mode surviving in a neutral gas, barring the individual sound modes of the constituents ($\omega/k = c_{s\alpha}$). In the next sections, we will look at low-frequency, long-wavelength modes in magnetized plasmas, trying to connect the Jeans instability to the magnetosonic modes.

9.3.2 Alfvén–Jeans modes

A first regime is where the wave frequency is assumed to be smaller than all relevant gyrofrequencies, $\omega \ll |\Omega_\alpha|$, in a driftless plasma. The proper ordering to take is $\omega, kc_{s\alpha}, \omega_{J\alpha} \ll |\Omega_\alpha|$ and then (9.51) yields for the X-mode to lowest significant order:

$$\begin{aligned}
D_{xx} &= \frac{c^2}{V_A^2}, \\
D_{xy} &= D_{yx} = 0, \\
D_{x\psi} = D_{\psi x} &= -\frac{c}{V_A}\left(\sum_\alpha \frac{\omega_{J\alpha}^2}{\Omega_\alpha}\right)\left(\sum_\alpha \omega_{J\alpha}^2\right)^{-\frac{1}{2}}, \\
D_{yy} &= \frac{c^2}{V_A^2}\left(\omega^2 - k^2 V_A^2 - k^2 \langle c_s^2\rangle\right), \\
D_{y\psi} = D_{\psi y} &= \frac{c}{V_A}\left(\sum_\alpha \omega_{J\alpha}^2\right)^{\frac{1}{2}}, \\
D_{\psi\psi} &= -1.
\end{aligned} \tag{9.56}$$

In these expressions, the Alfvén velocity V_A is defined for the plasma as a whole through

$$V_A^2 = \frac{B_0^2}{\mu_0 \sum_\alpha N_\alpha m_\alpha}, \tag{9.57}$$

and $V_A \ll c$ as usual. In addition, we have introduced a mass-weighted average for the square of the thermal velocities by putting

$$\langle c_s^2\rangle = \left(\sum_\alpha N_\alpha m_\alpha c_{s\alpha}^2\right)\left(\sum_\alpha N_\alpha m_\alpha\right)^{-1}. \tag{9.58}$$

It is now readily seen that the X-mode obeys

$$\omega^2 = k^2(V_A^2 + \langle c_s^2 \rangle) - \sum_\alpha \omega_{J\alpha}^2, \tag{9.59}$$

retaining only quadratic terms in the different small frequencies. Without self-gravitational effects, the Alfvén–Jeans mode described by (9.59) reduces to a generalized magnetosonic mode. On the other hand, due to the self-gravitational effects it goes over for very small wavenumbers into a modified form of the Jeans instability. It is worth remarking that opposition to the gravitational collapse comes not only from the usual thermal effects, but also from the external magnetic field which cannot easily be squeezed. Hence we have a restoring force against gravitation even in the complete absence of thermal effects, for (wave)lengths which are not too large [Mace et al., 1997].

9.3.3 Influence of neutral dust or gas

It is worth mentioning that the inclusion of cold neutral dust or gas is straightforward, as it only couples to the plasma motion through the gravitational Poisson equation. For the Alfvén–Jeans mode, we have to replace $D_{\psi\psi}$ in (9.56) by

$$D_{\psi\psi} \simeq -1 - \sum_g \frac{\omega_{Jg}^2}{\omega^2}, \tag{9.60}$$

so that the dispersion law can be written as

$$\omega^2 = k^2(V_A^2 + \langle c_s^2 \rangle)\left(1 + \sum_g \frac{\omega_{Jg}^2}{\omega^2}\right) - \sum_\alpha \omega_{J\alpha}^2 - \sum_g \omega_{Jg}^2. \tag{9.61}$$

The index g refers to the neutral gas components of the mixture of plasma, charged dust and neutral gas, whereas of course α labels the charged constituents, of both plasma and charged dust. As the product of the roots of (9.61) for ω^2 is negative, there is always a positive solution for ω^2, corresponding to a stable mode, and a negative solution, giving purely growing modes. The solution of this dispersion law are:

$$\frac{\omega^2}{V_S^2} = \frac{1}{2}\left(k^2 - k_{cr}^2 \pm \sqrt{\frac{4k^2}{V_S^2}\sum_g \omega_{Jg}^2 + (k^2 - k_{cr}^2)^2}\right), \tag{9.62}$$

with

$$k_{cr}^2 = \frac{\sum_\alpha \omega_{J\alpha}^2 + \sum_g \omega_{Jg}^2}{V_S^2}, \tag{9.63}$$

$$V_S^2 = V_A^2 + \langle c_s^2 \rangle. \tag{9.64}$$

The critical wavenumber k_{cr} will increase when neutral gas is added, the other parameters remaining equal. The description of the modes goes then as follows:

- When $k > k_{cr}$, the plasma effects dominate and the plus sign in (9.62) gives a generalized Alfvén–(Jeans) mode. The gas will increase the frequency as is shown in Appendix C.

  The minus sign introduces a new unstable mode, the frequency of which vanishes with the gas Jeans frequency. When the charged dust density is much smaller than the neutral gas density we obtain the ordinary Jeans instability

$$\omega^2 \simeq -\sum_g \omega_{Jg}^2. \tag{9.65}$$

- In the marginal case $k = k_{cr}$, stable as well as unstable modes occur, described by

$$\omega^2 = \pm \left[\left(\sum_\alpha \omega_{J\alpha}^2 + \sum_g \omega_{Jg}^2 \right) \sum_g \omega_{Jg}^2 \right]^{1/2}. \tag{9.66}$$

  Without neutral gas these are zero-frequency modes.

- When $k < k_{cr}$, the gravitational effects dominate, and the minus sign gives a generalized (Alfvén)–Jeans mode. The gas will render the mode more unstable (Appendix C) as might be expected. Indeed, additional neutral gas component(s) increase(s) the total mass of the system and this makes it easier for the Jeans instability to occur.

  The plus sign describes a stable mode vanishing with the gas Jeans frequency. In the long wavelength limit ($k^2 \ll k_{cr}^2$) this becomes

$$\omega^2 = k^2 V_S^2 \left(\sum_g \omega_{Jg}^2 \right) \left(\sum_\alpha \omega_{J\alpha}^2 + \sum_g \omega_{Jg}^2 \right)^{-1} \tag{9.67}$$

9.3.4 Dust Alfvén modes

The next regime to be considered is wave frequencies above the dust gyrofrequency, and for simplicity we will only consider one (average) charged dust grain species. There exists an interesting frequency regime $\Omega_d^2 \ll \omega^2 \ll \omega_{DLH}^2$ between the dust gyrofrequency and the so called *dust lower-hybrid frequency* (ω_{DLH}) (Salimullah, 1995), defined by

$$\omega_{DLH}^2 = \frac{\omega_{pd}^2 V_A^2}{c^2}. \tag{9.68}$$

Note that in this section, for reasons which will become clear below, the Alfvén velocity is defined over the ordinary plasma species only, for which we will reserve the species index p, so that

$$V_A^2 = \frac{B_0^2}{\mu_0 \sum_p N_p m_p}. \tag{9.69}$$

The regime below ω_{DLH} exists provided that $\Omega_d^2 \ll \omega_{DLH}^2$, which is fulfilled provided the mass of the system is mostly in the dust grains ($\sum_p N_p m_p \ll N_d m_d$). On the other hand, the discussion for $\omega_{DLH}^2 \ll \Omega_d^2$ is implicitly included in the preceding section.

For the dust Alfvén mode (9.51) yields to the lowest order:

$$
\begin{aligned}
D_{xx} &= \frac{c^2}{V_A^2} - \frac{\omega_{pd}^2}{\omega^2} \simeq - \frac{c^2\omega_{DLH}^2}{\omega^2 V_A^2}, \\
D_{xy} &= \frac{\omega_{pd}^2}{\Omega_d} + \frac{\omega_{pd}^2\Omega_d}{\omega^2} \simeq \frac{c^2\omega_{DLH}^2}{\Omega_d V_A^2}, \\
D_{x\psi} &= -\sum_p \frac{\omega_{pp}\omega_{Jp}}{\Omega_p^2} + \frac{\omega_{pd}\omega_{Jd}}{\omega^2} \simeq \frac{c\omega_{DLH}\omega_{Jd}}{\omega^2 V_A}, \\
D_{yy} &= \frac{c^2}{V_A^2}\left(\omega^2 - k^2V_A^2 - k^2\langle c_s^2\rangle - \omega_{DLH}^2\right), \\
D_{y\psi} &= \sum_p \frac{\omega_{pp}\omega_{Jp}}{\Omega_p} - \frac{\omega_{pd}\omega_{Jd}\Omega_d}{\omega^2} \simeq - \frac{c\omega_{DLH}\omega_{Jd}\Omega_d}{\omega^2 V_A}, \\
D_{\psi\psi} &= -1 + \sum_p \frac{\omega_{Jp}^2}{\Omega_p^2} - \frac{\omega_{Jd}^2}{\omega^2} \simeq -1 - \frac{\omega_{Jd}^2}{\omega^2}.
\end{aligned}
\tag{9.70}
$$

The average sound speed has been computed as a mass average over the plasma species only. Within the frequency regime considered and because $V_A \ll c$, only the dust related terms are left, except in D_{yy}. In this case the dispersion becomes:

$$
\omega^2 = k^2(V_A^2 + \langle c_s^2\rangle)\frac{\Omega_d^2}{\omega_{DLH}^2} - \omega_{Jd}^2 = k^2(V_{Ad}^2 + c_{DA}^2) - \omega_{Jd}^2. \tag{9.71}
$$

The conclusions are comparable to the *Alfvén–Jeans* modes described earlier, in the now expanded frequency domain beyond the dust gyrofrequency. The modifications are that the Alfvén velocity now is the dust Alfvén velocity, hence the name of the mode, and a dust-acoustic velocity c_{DA} has been introduced through

$$
c_{DA}^2 = \frac{\sum_p N_p m_p c_{sp}^2}{N_d m_d}. \tag{9.72}
$$

There are deviations from the standard definition [Rao et al., 1990], but these are not really of major importance here.

The inclusion of cold neutral dust or gas can be considered by replacing $D_{\psi\psi}$ in (9.70) by:

$$
D_{\psi\psi} \simeq -1 - \frac{\omega_{Jd}^2}{\omega^2} - \sum_g \frac{\omega_{Jg}^2}{\omega^2}. \tag{9.73}
$$

This leads to the dispersion relation:

$$
\omega^2 = k^2(V_{Ad}^2 + c_{DA}^2)\left(1 + \sum_g \frac{\omega_{Jg}^2}{\omega^2}\right) - \omega_{Jd}^2 - \sum_g \omega_{Jg}^2, \tag{9.74}
$$

which is formaly the same as (9.61), and hence the analysis of the previous section remains valid.

9.4 Conclusions and new results

Although the gravitational force is usually much lower than the electrostatic forces, the small low-frequency long-wavelength deviations from an equilibrium solution (which was not specified) of a dusty plasma system are affected by the self-gravitation of the system. Whereas for neutral grains only thermal effects can stabilize the system against Jeans collapse, dusty plasmas containing charged grains can be stabilized by plasma waves.

Indeed, when no magnetic field is present, the Jeans collapse will be restricted by the dust-acoustic modes, and a *dust-acoustic–Jeans length* can be derived:

$$L_{DAJ} = \frac{\lambda_D\sqrt{\omega_{pd}^2 - \omega_{Jd}^2}}{\omega_{Jd}} \approx \frac{\lambda_D\omega_{pd}}{\omega_{Jd}}, \tag{9.75}$$

which restricts the lengths of a stable system. The dust-acoustic frequency generalizes the mean rms value of the velocity of the particles for the specific case where the mass can be found in the dust grains, and the thermal effects are due to the plasma.

The introduction of a size (mass) distribution for the dust grains, will increase both plasma and Jeans frequencies, but the Jeans frequency increases faster than the plasma frequency and hence the Jeans instability occurs for smaller systems in a dusty plasma with a dust size distribution. The dust-acoustic wave frequency will increase when different dust grain sizes are taken into account.

On the other hand, when an ambient magnetic field is present, the parallel electromagnetic modes are not affected by the self-gravity and hence the relevant length scale for parallel modes remains as it was. For (perpendicular) magnetosonic modes, we introduce the *Alfvén–Jeans length* as:

$$L_{AJ} = \frac{\sqrt{V_A^2 + \langle c_s^2\rangle}}{\omega_{Jd}}. \tag{9.76}$$

This length restricts the magnitude of a stable system in the direction perpendicular to an ambient magnetic field. Besides the thermal effects, also the dust Alfvén modes will stabilize the Jeans collapse.

9.5 Appendix C

Consider the function

$$f(k,x,y) = k^2 - y - x \pm \sqrt{4k^2x + (k^2 - y - x)^2}, \tag{9.77}$$

with

$$x = \frac{\sum_g \omega_{Jg}^2}{V_S^2} > 0 \tag{9.78}$$

$$y = \frac{\sum_\alpha \omega_{J\alpha}^2}{V_S^2} > 0 \tag{9.79}$$

We can readily find that:

$$\frac{\partial f}{\partial x}(k,x,y) = -1 \pm \frac{k^2 + y + x}{\sqrt{4k^2x + (k^2 - y - x)^2}}. \tag{9.80}$$

For the minus sign, this is always negative, while for the plus sign the opposite is true:

$$\begin{aligned} & \sqrt{4k^2x + (k^2 - y - x)^2} < k^2 + y + x \\ \Rightarrow \quad & 4k^2x + (k^2 - y - x)^2 < (k^2 + y + x)^2 \\ \Rightarrow \quad & -4yk^2 < 0. \end{aligned} \tag{9.81}$$

Chapter 10

General conclusions

In the second chapter of this thesis we have given a review of the data available for the three most promising dusty space plasma environments: the rings of the giant planets and cometary and interplanetary environments. To be complete, we have added the charging and dusty crystal experiments in laboratories. This clear view on the data is essential to quantify the available dust charging mechanisms in space plasmas (chapter 4). The charging mechanisms also couple to the collective wave phenomena and therefore this chapter serves as a foundation of the thesis.

The lack and the incompleteness of the available data encouraged us to describe a new dust detection method: the "Radio Dust Analyzer" (RDA). This method uses a simple wire dipole antenna to recover the characteristics (velocity, direction, charge) of a dust particle. Also, some elements of the environmental plasma like the Debye length can be recovered. The signal induced by the charged grain on the antenna is examined and the influence of the different parameters is shown. The noise levels, due to the plasma particle flyby and impact on the antenna, are calculated and compared with the height of the RDA-signal. The frequencies of the RDA-signals are estimated for different space missions: Rosetta, Wind, Cassini and Voyager. Particles that approach the antenna within a distance of one Debye length can be detected and therefore the cross section of the analyzer can be as big as thousand square meters. We do not need any specific information of the nature of the grains, because the composition is irrelevant for the technique. The implementation of this method on a specific space mission requires only a small extra cost when an antenna is already available, which is the case for most of the interplanetary space missions.

Chapter 4 gives a review of the current knowledge on the dust charging theory. Different mechanisms play a role: primary charging currents caused by the capture/emission of plasma particles, secondary electron emission, photo-emission, electrostatic disruption, field emission and centrifugal disruption. The effect of a high dust density in a dust-in-plasma, and the influence of a magnetic field are reviewed. In the presence of a magnetic field, the charging model is far from complete, because in that case collisions may not be neglected.

The fifth chapter gives the most important elements in the charging model for different space plasma environments. The charging process is highly nonlinear and so small changes in the model parameters can induce a large difference in the charging behavior. We have looked at the equilibrium potential and the charging time, but also the dependence of this mechanism on the secondary yield parameters is given. First we have examined the rings of Saturn. It was shown that photo-emission plays a minor role in the charging mechanism. Also the dependence of the dust-plasma drift was studied. The dependence on the secondary yield parameters is especially large in the outer part of the E-ring, where it is even possible that the sign of the equilibrium charge changes for different realistic secondary yield parameters. The charging time is typically of the order of minutes to hours, and therefore smaller than the rotation period of the planet. The primary hot electron current will cause the negative charging mechanism, while the positive charging mechanism in the inner rings consists mainly of reflected thermal electrons, secondary thermal electrons and watergroup ions. When we go farther away from the planet, the importance of the latter will decrease and the positive charging mechanism will consist mainly of the secondary electron currents. For the interplanetary medium, a distinction must be made between the different solar wind activities. In most cases considered, the equilibrium potential will decrease when we increase the heliocentric distance (r_h). For high values of r_h the equilibrium potential becomes a constant. For a maximum solar wind activity however there exists a maximum in the equilibrium potential for grains closer to the sun than the Earth. We showed that, although the plasma parameters depend in a rather complicated way on (r_h), the charging time goes roughly like r_h^2. We must add that for cometary environments a detailed analysis of the grain charging mechanisms is premature. The availability of the data is restricted to "snapshots" taken by *in situ* spacecraft at a limited number of comets. An additional problem is that the plasma parameters vary from comet to comet depending on the nucleus size, composition and structure, and for a given comet vary with solar distance, with time, and with distance to the nucleus and hence the range of variation of the parameters is large. There where attempts to explain the charging of dust grains in comets (e.g. [Boenhardt en Fechtig, 1987]), but they were based on a rather simplified model, taking only the primary electrons and the photo-emission into account, without specifying quantitatively why the other charging mechanisms where neglected.

The remainder of the thesis describes waves and instabilities in dusty plasmas in space. In chapter 6 we have explained why we can use a multi-fluid model. This model has the advantage over a kinetic approach that the interpretation is easier. The multi-fluid model is also adequate enough for the space applications we consider. The dust component was described as an additional fluid species. Later on, in chapter 9, additional dust components and a mass-distribution were added, including self-gravitation. The multi-fluid model has been adapted with extra sink/source terms. These terms will describe the liberation/capture of the plasma particles by the dust population. For a simple Maxwellian plasma, analytical results are given for parameters describing the source/sink terms.

The seventh chapter described the coupling between the electrostatic waves and the charging mechanism in a three-component plasma. We have shown that the presence of the dust will damp the Langmuir oscillations. This is in contrast to earlier papers that did not use a self-consistent approach. This damping was quantified for zero-frequency, dust-acoustic, ion-acoustic and Langmuir modes, by means of *ad hoc* parameters that must be recalculated for different space plasma environments. This made it possible to come to results independent of the charging model. For two dusty plasma environments a numerical solution of the dispersion relation is given.

Chapter 8 describes electromagnetic waves. A specific frequency domain is examined where the dust grains must be regarded as immobile, due to their large mass, while the frequency of the modes is lower than the plasma gyrofrequencies. In this regime, a new kind of *whistler* mode exists, equivalent with the Eckersley approximation in a classical plasma. This whistler mode can be stable, depending on the equilibrium between the charging mechanism and the drift velocity of the different plasma constituents. This frequency regime makes it possible to conclude that the solar wind interaction with a dusty cometary plasma is not influenced by the dust grains. Further on, we have developed a nonlinear description of parallel electromagnetic modes with the dust considered as a static background. We come to a modified nonlinear evolution equation (a modified derivative nonlinear Schrödinger equation), without stable soliton solutions. So the presence of dust grains will cause damping/growth of the otherwise stable soliton structures. Perpendicular and oblique propagation were analyzed in the second part of this chapter. The linear low-frequency magneto-acoustic mode propagates perpendicular to the ambient magnetic field with a phase velocity equal to the dust Alfvén velocity (in a cold plasma). This Alfvén velocity is much lower than the plasma Alfvén velocity, because the dust grains determine the mass density of the dusty plasma. The nonlinear description of the magneto-acoustic modes was carried out for a warm plasma with an isotropic pressure, as well as for a anisotropic pressure plasma. For both cases a Korteweg-de Vries equation was obtained. An analysis of obliquely propagating modes in a cold plasma follows. This shows that parallel propagating modes need another approach than oblique modes. The (quasi-)parallel case has been given earlier [Verheest, 1990; Deconinck et al., 1993a, b]. Oblique propagation was given in this work. We have recovered a Korteweg-de Vries equation, generalizing the work of others.

The influence of self-gravitation and mass-distribution is examined in chapter 9. Although the gravitational force is usually much lower than the electrostatic forces, the small low-frequency long-wavelength deviations from an equilibrium solution (which was not specified) of a dusty plasma system is affected by the self-gravitation of the system. Whereas for neutral grains only thermal effects can stabilize the system against Jeans collapse, dusty plasmas containing charged grains can be stabilized by plasma waves. When no magnetic field is present, the Jeans collapse will be opposed by the dust-acoustic modes, restricting the lengths of a stable system. The dust-acoustic frequency generalizes the mean *rms* value of the velocity of the particles for the specific case where the mass can be found in the dust grains, and the thermal effects are due to the plasma. The Jeans instability occurs for smaller systems in a dusty plasma with a dust size distribution. On the other hand, when an ambient magnetic field is present, the parallel electromagnetic modes are not affected by the self-gravity and hence the relevant length scale for parallel modes remains as it was. For (perpendicular) magnetosonic modes, we introduce the *Alfvén–Jeans length* which restricts the magnitude of a stable system in the direction perpendicular to an ambient magnetic field. Besides the thermal effects, also the dust Alfvén modes will stabilize the Jeans collapse. This means that opposition to the gravitational collapse comes not only from the usual thermal effects but also from the external magnetic field which cannot easily be squeezed.

References

J.E. Allen, Probe theory – The orbital motion approach, *Physica Scripta*, **45**, 497–503, 1992

E. Amata, V. Formisano, P. Torrente, R. Giovi, The plasma parameters during inbound and outbound legs of the Giotto trajectory, *Cometary plasma processes*, Geophysical Monograph, edited by A.D. Johnstone, AGU, 131–138, 1991

M.G. Aubier, N. Meyer-Vernet, B.M. Pedersen, Shot noise from grain and particle impacts in Saturn's ring plane, *Geoph. Res. Letters*, **10**, 5–8, 1983

K. Avinash, A. Sen, An electromagnetic model of kinks and braids in Saturn's rings, *Phys. Scripta*, **T63**, 106–110, 1996

K. Avinash, P.K. Shukla, A purely growing instability in a gravitating dusty plasma, *Phys. Lett. A*, **189**, 470–472, 1994

H. Balsiger, K. Altwegg, F. Buehler, S.A. Fuselier, J. Geiss, R. Goldstein, A.J. Lazarus, A. Meier, M. Neugebauer, U. Rettenmund, The composition and dynamics of cometary ions in the outer coma of Halley, *ESLAB Symposium on the Exploration of Halley's comet, Heidelberg*, ESA SP-250, 99–103, 1986

A. Barkan, N. D'Angelo, R.L. Merlino, Charging of dust grains in a plasma, *Phys. Rev. Letters*, **73**, 3093–3096, 1994

A. Barkan, N. D'Angelo, R.L. Merlino, Laboratory experiments on electrostatic ion cyclotron waves in a dusty plasma, *Planet. Space Sci.*, **43**, 905–908, 1995

A. Barkan, N. D'Angelo, R.L. Merlino, Experiments on ion-acoustic waves in dusty plasmas, *Planet. Space Sci.*, **44**, 239–242, 1996

J.W. Belcher, R.L. McNutt Jr., J.D. Richardson, R.S. Selesnick, E.C. Sittler Jr., F. Bagenal, The plasma environment of Uranus, *Uranus*, edited by J.T. Bergstralh, E.D. Miner, M.S. Matthews, University of Arizona Press, Tucson, 780–830, 1991

J. R. Bhatt, Langmuir waves in a dusty plasma with variable grain charge, *Phys. Rev. E*, **55**, 1166–1169, 1997

J. R. Bhatt, B. P. Pandey, Self-consistent charge dynamics and collective modes in a dusty plasma, *Phys. Rev. E.*, **50**, 3980–3983, 1994

P. Bliokh, V. Sinitsin, V. Yaroshenko, *Dusty and self-gravitational plasmas in space*, Kluwer academic publishers, Dordrecht, 1995

P. Bliokh, V. Yaroshenko, *Electrostatic waves in Saturn's rings*, *Sov. Astron.*, **29**, 330–336, 1985

H. Boehnhardt, H. Fechtig, Electrostatic charging and fragmentation of dust near P/Giacobini–Zinner and P/Halley, *Astron. Astrophys.*, **187**, 824–828, 1987

H.G. Booker, *Cold plasma waves*, Nijhoff, Dordrecht, 1984

L. F. Burlaga, R. P. Lepping, K. W. Behannon, L. W. Klein, *J. Geophys. Res.*, **89**, 10659–10668, 1984

J. A. Burns, M. R. Showalter, G. E. Morfill, The ethereal rings of Jupiter and Saturn, *Planetary Rings*, edited by R. Greenberg, A. Brahic, University of Arizona Press, Tucson, 73–199, 1984

A. C. Calder, J. G. Laframboise, Terminal properties of a spherical RF electrode in an isotropic Vlasov plasma: Results of a computer simulation, *Radio Sci.*, **20**, 989–999, 1985

J. Choi, M.J. Kushner, A particle-in-cell simulation of dust charging and shielding in low pressure glow discharges, *IEEE Trans. Plas. Sci.*, **22**, 151–158, 1994

V.W. Chow, D.A. Mendis, M. Rosenberg, Role of grain size and particle velocity distribution in secondary electron emission in space plasmas, *J. Geophys. Res.*, **98**, 19065–19076, 1993

J.H. Chu, L. I, *Physica A*, **205**, Coulomb lattice in a weakly ionized colloidal plasma, 183–190, 1994

R.N. Clark, Ganymede, Europa, Callisto and Saturn's Rings: compositional analysis from reflectance spectroscopy, *Icarus*, **44**, 388–409, 1980

R.N. Clark, T.B. McCord, The rings of Saturn: New near-infrared reflectance measurements and a 0.326-4.08 μm summary, *Icarus*, **43**, 161–168, 1980

S.A. Collins, T.V. Johnson, A.F. Cook, J.N. Cuzzi, J.B. Pollack, G.E. Danielson, G.E. Hunt, D. Morrison, T. Owen, B.A. Smith, First Voyager view of the rings of Saturn, *Nature*, **288**, 439–442, 1980

C. Cui, J. Goree, Fluctuations of the charge on a dust grain in a plasma, *IEEE Trans. Plas. Sci.*, **22**, 151–158, 1994

R.D. Daryanani, Potential distribution around dust particles in plasmas, *PhD-thesis*, Oxford University, 1996

U. de Angelis, The physics of dusty plasmas, *Physica Scripta*, **45**, 465–474, 1992

B. Deconinck, P. Meuris, F. Verheest, Oblique nonlinear Alfvén waves in strongly magnetized beam plasmas. Part 1. Nonlinear vector evolution equation, *J. Plasma Phys.* **50**, 445–455, 1993a

B. Deconinck, P. Meuris, F. Verheest, Oblique nonlinear Alfvén waves in strongly magnetized beam plasmas. Part 2. Soliton solutions and integrability, *J. Plasma Phys.* **50**, 457–476, 1993b

N. Divine, Five populations of interplanetary meteroids, *J. Geophys. Res.*, **98**, 17029–17048, 1993

B.T. Draine, E.E. Salpeter, On the physics of dust grains in hot gas, *Astroph. J.*, **231**, 77–94, 1979

L.W. Esposito, A. Brahic, J.A. Burns, E.A. Marouf, Particle properties and processes in Uranus' rings, *Uranus*, edited by J.T. Bergstralh, E.D. Miner, M.S. Matthews, University of Arizona Press, Tucson, 410–468, 1991

L.W. Esposito, J.N. Cuzzi, J.B. Holberg, E.A. Marouf, G.L. Tyler, C.C. Porco, Saturn's rings: structure, dynamics and particle properties, *Saturn*, edited by T. Gehrels, M.S. Matthews, University of Arizona Press, Tucson, 463–545, 1984

C. Ferrari, A. Brahic, Azimuthal brightness asymmetries in plantery rings. I: Neptune's arcs and narrow rings, *Icarus*, **111**, 193–210, 1994

K. R. Flammer, The global interaction of comets with the solar wind, *Comets in the post-Halley era*, Edited by R.L. Newburn Jr., M. Neugebauer, J. Rahe, Kluwer, Dordrecht, 1125–1144, 1991

M. Fulle, Dust from short period comet P/Schwassmann-Wachmann 1 and replenishment of the interplanetary dust cloud, *Nature*, **359**, 42–44, 1992

M. Fulle, G. Cremonese, K. Jockers, H. Rauer, The dust tail of comet Liller 1988 V, *Astron. Astrophys.*, **253**, 615–624, 1992

C.K. Goertz, Dusty plasmas in the solar system, *Rev. Geophys.*, **27**, 271–292, 1989

C.K. Goertz, G. Morfill, A model for the formation of spokes in Saturn's rings, *Icarus*, **53**, 219–229, 1983

B.E. Goldstein, M. Neugebauer, J.L. Phillips, S. Bame, J.T. Gosling, D. Mccomas, Y.-M. Wang, N.R. Sheeley, S.T. Suess, Ulysses plasma parameters: latitudinal, radial, and temporal variations, *Astron. Astrophys.*, **316**, 296–303, 1996

J.R. Göller, E. Grün, Calibration of the Galileo/Ulysses dust detectors with different projectile materials and at varying impact angles, *Planet. Space Sci.*, **37**, 1197–1206, 1989

R. Grard, H. Laakso, A. Pedersen, J.G. Trotignon, Y. Mikhaïlov, Observations of the plasma environment of comet Halley during the Vega flybys, *Ann. Geoph*, **7**, 141–150, 1989

E. Grün, H. Fechtig, R.H. Giese, J. Kissel, D. Linkert, D. Maas, J.A.M. Mcdonnell, G.E. Morfill, G. Schwehm, H.A. Zook, The Galileo dust detector, *Astron. Astrophys. Suppl. Ser.*, **92**, 411–423, 1992

E. Grün, G.E. Morfill, D.A. Mendis, Dust-magnetosphere interactions, *Planetary Rings*, edited by R. Greenberg, A. Brahic, University of Arizona Press, Tucson, 275–332, 1984

E. Grün, G.E. Morfill, R.J. Terrile, T.V. Johnson, G. Schwehm, The evolution of Spokes in Saturn's B Ring, *Icarus*, **54**, 227–252, 1983

E. Grün, N. Pailer, H. Fechtig, J. Kissel, Orbital and physical characteristics of micrometeroids in the inner solar system as observed by Helios 1, *Planet Space Sci.*, **28**, 333–349, 1980

E. Grün, P. Staubach, M. Baguhl, D.P. Hamilton, H.A. Zook, S. Dermott, H. Fechtig, B.A. Gustafson, M.S. Hanner, M. Horányi, J. Kissel, B.A. Lindblad, D. Linkert, G. Linkert, I. Mann, J.A.M. McDonnell, G.E. Morfill, C. Polanskey, G. Schwehm, R. Srama., South-North and Radial Traverses Through the Interplanetary Dust Cloud, *Icarus*, in press, (http://galileo.mpi-hd.mpg.de/~gruen/NStraverse/template.html), 1997

E. Grün, H.A. Zook, H. Fechtig, R.H. Giese, Collisional balance of the meteoritic complex, *Icarus*, **62**, 244–272, 1985

D.A. Gurnett, T.F. Averkamp, F.L. Scarf, E. Grün, Dust particles detected near P/Giacobini–Zinner by the ICE plasma wave instrument, *Geoph. Res. Letters*, **13**, 291–294, 1986

D.A. Gurnett, E. Grün, D. Gallagher, W.S. Kurth, F.L. Scarf, Micron-sized particles detected near Saturn by the Voyager plasma wave instrument, *Icarus*, **53**, 236–254, 1983

D.A. Gurnett, W.S. Kurth, L.J. Granroth, S.C. Allendorf, R.L. Poynter, Micron-sized particle impacts detected near Neptune by the Voyager 2 plasma wave instrument, *J. Geophys. Res.*, **96**, 19177–19186, 1991

D.A. Gurnett, W.S. Kurth, F.L. Scarf, J.A. Burns, J.N. Cuzzi, E. Grün, Micron-sized particle impacts detected near Uranus by the Voyager 2 plasma wave instrument, *J. Geophys. Res.*, **92**, 14959–14968, 1987

G.A. Harrower, Energy spectra of secondary electrons from Mo and W for low primary energies, *Phys. Rev.*, **104**, 52, 1956

O. Havnes, Charges on dust particles, 4, (9), *Adv. Space Res.*, **4**, 75–83, 1984

O. Havnes, T.K. Aanesen, F. Melandsø, On dust charges and plasma potentials in a dusty plasma with dust size distribution, *J. Geophys. Res.*, **95**, 6581–6585, 1990

R.C. Hazelton, E.J. Yadlowsky, Measurements of dust grain charging in a laboratory plasma, *IEEE Trans. Plas. Sci.*, **22**, 91–96, 1994

J.R. Hill, D.A. Mendis, Electrostatic disruption of a charged conducting spheroid, *Can. J. Physics*, **59**, 897–901, 1981

M. Horányi, Charged dust dynamics in the solar system, *Annu. Rev. Astron. Astrophys.*, **34**, 383–418, 1996

M. Horányi, T.E. Cravens, The structure and dynamics of Jupiter's ring, *Nature*, **381**, 293–295, 1996

M. Horányi, D.A. Mendis, The electrodynamics of charged dust in the cometary environment, *Comets in the post-Halley era*, Edited by R.L. Newburn Jr., M. Neugebauer, J. Rahe, Kluwer, Dordrecht, 1093–1104, 1991

H.L.F. Houpis, E.C. Whipple Jr., Electrostatic charge on a dust size distribution in a plasma, *J. Geophys. Res.*, **98**, 12057–12068, 1987

D.H. Humes, Results of Pioneer 10 and 11 Meteoroid Experiments: Interplanetary and near-Saturn, *J. Geophys. Res.*, **85**, 5841–5852, 1980

L. I, W.-T. Juan, C.-H. Chiang, J.H. Chu, Microscopic particle motion in strongly coupled dusty plasmas, *Science*, **272**, 1626–1628, 1996

H. Ikezi, Coulomb solid of small particles in plasmas, *Phys. Fluids*, **29**, 1764–1766, 1986

D.S. Intriligator, J.H. Wolfe, Results of the plasma analyzer experiment on Pioneers 10 and 11, *Jupiter*, edited by Tom Gehrels, University of Arizona Press, 848–869, 1976

J.H. Jeans, Astronomy and Cosmogeny, *Cambridge University Press*, 1929

E.K. Jessberger, J. Kissel, Chemical properties of cometary dust and a note on carbon isotopes, *Comets in the post-Halley era*, Edited by R.L. Newburn Jr., M. Neugebauer, J. Rahe, Kluwer, Dordrecht, 1075–1092, 1991

S. Jurac, A. Baragiola, R.E. Johnson, E.C. Sittler Jr., Charging of ice grains by low-energy plasmas: Application to Saturn's E-ring, *J. Geophys. Res.*, **100**, 14821–14831, 1995

T. Kakutani, H. Ono, T. Taniuti, C.-C. Wei, *J. Phys. Soc. Japan*, **24**, 1159, 1968

J.G. Laframboise, L.J. Sonmor, Current collection by probes and electrodes in space magnetoplasmas: a review, *J. Geophys. Res.*, **98**, 337–357, 1993

J.M. Lesceux, J. Lemaire, N. Meyer-Vernet, Electric dipole antennae used as micrometeroid detectors, *Planet. Space Sci.*, **37**, 1291–1301, 1987

F. Li, O. Havnes, F. Melandsø, Longitudinal waves in a dusty plasma, *Planet. Space Sci.*, **42**, 401–407, 1994

J.-X. Ma, M.Y. Yu, Langmuir wave instability in a dusty plasma, *Phys. Rev. E*, **50**, R2431–R2434, 1994

R.L. Mace, F. Verheest, M.A. Hellberg, Jeans stability of dusty space plasmas, *Phys. Letters A*, submitted, 1997

E.P. Mazets, R.Z. Sagdeev, R.L. Aptekar, S.V. Golenetskii, Y.A. Guryan, A.V. Dyachkov, V.N. Ilyinskii, V.N. Panov, G.G. Petrov, A.V. Savvin, I.A. Sokolov, D.D. Frederiks, N.G. Khavenson, V.D. Shapiro, V.I. Shevchenko, Dust in comet Halley from Vega observations, *ESLAB Symposium on the Exploration of Halley's comet, Heidelberg*, ESA SP-250, 3–10, 1986

J.A.M. McDonnell, W.M. Alexander, W.M. Burton, E. Bussoletti, G.C. Evans, S.T. Evans, J.G. Firth, R.J.L. Grard, S.F. Green, E. Grün, M.S. Hanner, D.W. Hughes, E. Igenbergs, J. Kissel, H. Kuczera, B.A. Lindblad, Y. Langevin, J.-C. Mandeville, S. Nappo, G.S.A. Pankiewicz, C.H. Perry, G.H. Schwehm, Z. Sekanina, T.J. Stevenson, R.F. Turner, U. Weishaupt, M.K. Wallis, J.C. Zarnecki, The dust distribution within the inner coma of comet P/Halley 1982i: –Encounter by Giotto's impact detector, *Astron. Astrophys.*, **187**, 719–741, 1987

J.A.M. McDonnell, R. Beard, S.F. Green, G.H. Schwehm, Cometary coma particulate modelling for the ROSETTA mission aphelion rendezvous, *Ann. Geophys.*, **10**, 150–156, 1992

J.A.M. McDonnell, J. Kissel, E. Grün, R.J.L. Grard, Y. Langevin, R.E. Olearczyk, C.H. Perry, J.C. Zarnecki, Giotto's dust impact detection system DIDSY and particulate impact analyzer PIA: interim assessment of the dust distribution and properties within the coma, In "Dust in comet Halley from Vega observations, in Proceedings of the international symposium Heidelberg", Germany, **2**, 25–38, 1986

J.A.M. McDonnell, P.L. Lamy, G.S. Pankiewicz, Physical properties of cometary dust, *Comets in the post-Halley era*, Edited by R.L. Newburn Jr., M. Neugebauer, J. Rahe, Kluwer, Dordrecht, 1043–1073, 1991

F. Melandsø, T.K. Aslaksen, O. Havnes, A new damping effect for the dust-acoustic wave, *Planet. Space Sci.*, **41**, 321–325, 1993

A. Melzer, T. Trottenberg, A. Piel, Experimental determination of the charge on dust particle forming Coulomb lattices, *Phys. Letters A*, **191**, 301–308, 1994

D.A. Mendis, A postencounter view of comets, *Ann. Rev. Astron. Astroph.*, **26**, 11–49, 1988

D.A. Mendis, H.L.F. Houpis, J.R. Hill, The gravito-electrodynamics of charged dust in planetary magnetospheres, *J. Geophys. Res.*, **87**, 3449–3455, 1982

D.A. Mendis, M. Rosenberg, Cosmic dusty plasma, *Annu. Rev. Astron. Astroph.*, **32**, 419–463, 1994

P. Meuris, The influence of a dust mass (size) distribution on the dust-acoustic mode, *Planet. Space Sci.*, **12**, 1171–1174, 1997

P. Meuris, Nonlinear magnetosonic modes in multi-species dusty plasmas, Proceedings of the "First International Workshop on Dusty Plasmas", World Scientific Publishing, Singapore, in press, 1997

P. Meuris, F. Verheest, Korteweg–de Vries equation for magnetosonic modes in dusty plasmas, *Physics Letters A*, **219**, 299–302, 1996

P. Meuris, F. Verheest, Electrostatic instabilities due to charge fluctuations in dusty plasmas, *The Physics of Dusty Plasmas*, Ed. P.K. Shukla, D.A. Mendis and V.W. Chow, World Scientific Publishing, Singapore, 159–170, 1996

P. Meuris, F. Verheest, G.S. Lakhina, Influence of dust mass distributions on generalized Jeans-Buneman instabilities in dusty plasmas, *Planet. Space Sci.*, **45**, 449–454, 1997

P. Meuris, N. Meyer-Vernet, J. Lemaire, The detection of dust grains by a wire dipole antenna: the Radio Dust Analyzer, *J. Geophys. Res.*, **101**, 24471–24477, 1996

N. Meyer–Vernet, "Flip-flop" of electric potential of dust grains in space, *Astron. Astroph.*, **105**, 98–106, 1982

N. Meyer–Vernet, Some constraints on particles in Saturn's Spokes., *Icarus*, **57**, 422–431, 1984

N. Meyer-Vernet, M.G. Aubier, B.M. Pedersen, Voyager-2 at Uranus: Grain impacts in the ring plane, *Geophys. Res. Lett.*, **13**, 617-620, 1986

N. Meyer-Vernet, A. Lecacheux, B.M. Pedersen, Constraints on Saturn's E ring from the Voyager 1 radio astronomy instrument, *Icarus*, **123**, 113–128, 1996

N. Meyer-Vernet, A. Lecacheux, B.M. Pedersen, Constraints on Saturn's G ring from the Voyager 2 radio astronomy instrument, *Icarus*, submitted to Icarus, 1997

N. Meyer-Vernet, C. Perche, Tool kit for antennae and thermal noise near the plasma frequency, *J. Geophys. Res.*, **94**, 2405–2415, 1989

K. Mio, T. Ogino, K. Minami, S. Takeda, Modified nonlinear Schrödinger equation for Alfvén waves propagating along the magnetic field in cold plasmas, *J. Phys. Soc. Japan*, **41**, 265–271, 1976

E. Mjølhus, J. Wyller, Alfvén solitons, *Physica Scripta* **33**, 442–451, 1986

G.E. Morfill, C.K. Goertz, Plasma clouds in Saturn's rings, *Icarus*, **55**, 111–123, 1983

H. Mott-Smith, I. Langmuir, *Phys. Rev.*, **28**, 727, 1926

T. Mukai, On the charge distribution of interplanetary grains, *Astron. Astrophys.*, **99**, 1–6, 1981

T. Mukai, M. Kitayama, W. Miyake, T. Terasawa, K. Hirao, Plasma characteristics around comet Halley observed by Suisei, *ESLAB Symposium on the Exploration of Halley's comet, Heidelberg*, ESA SP-250, 71–75, 1986

Y. Nakamura, J.L. Ferreira, G.O. Ludwig, *J. Plasma Phys.*, **33**, 237, 1985

N. F. Ness, Intrinsic magnetic fields of the planets: Mercury to Neptune, *Phil. Trans. R. Soc. Lond. A*, **349**, 249–260, 1994

N. F. Ness, M. H. Acuña, J. E. P. Connerney, Neptune's magnetic field and field-geometric properties, *Neptune and Triton*, edited D. P. Cruickshank, University of Arizona Press, Tucson, 141–168, 1995

N.F. Ness, J.E.P. Connerney, R.P. Lemming, M. Schultz, G.H. Voigt, *Uranus*, edited by J.T. Bergstralh, E.D. Miner, M.S. Matthews, University of Arizona Press, Tucson, 739–779, 1991

F.M. Neubauer, The magnetic field structure of the cometary plasma environment, *Comets in the post-Halley era*, Edited by R.L. Newburn Jr., M. Neugebauer, J. Rahe, Kluwer, Dordrecht, 1075–1092, 1991

T.G. Northrop, Dusty plasmas, *Physica Scripta*, **45**, 474–490, 1992

M.E. Ockert, J.N. Cuzzi, C.C. Porco, T.V. Johnson, Uranian ring photometry: results from Voyager 2, *J. Geophys. Res.*, **92**, 14696–14978, 1987

E.J. Öpik, Interplanetary dust and terrestrial accretion of meteoritic matter, *Irish Astron.*, **4**, 84–135, 1956

L.W. Parker, B.L. Murphy, Potential buildup on an electron-emitting ionospheric satellite, *J. Geophys. Res.*, **72**, 1631–1636, 1967

G.K. Parks, *Physics of space plasmas: an introduction*, University of Washington, Seattle, Washington, 1991

B.M. Pedersen, N. Meyer-Vernet, M.G. Aubier, P. Zarka, Dust distribution around Neptune: grain impacts near the ring plane measured by the Voyager planetary radio astronomy experiment, *J. Geophys. Res.*, **96**, 19187–19196, 1991

C.C. Porco, P.D. Nicholson, J.N. Cuzzi, J.J. Lissauer, L.W. Esposito, Neptune's ring system, *Neptune and Triton*, edited D. P. Cruickshank, University of Arizona Press, Tucson, 141–168, 1995

N.N. Rao, Low-frequency waves in magnetized dusty plasmas, *J. Plasma Phys.* **49**, 375–393, 1993

N.N. Rao, Magnetoacoustic modes in a magnetized dusty plasma, *J. Plasma Phys.* **53**, 317–334, 1995

N.N. Rao, P.K. Shukla, M.Y. Yu, Dust-acoustic waves in dusty plasmas, *Planet. Space Sci.* **38**, 543–546, 1990

R.V. Reddy, G.S. Lakhina, F. Verheest, P. Meuris, Alfvén modes in dusty cometary and planetary plasmas, *Planet. Space Sci.*, **44**, 129–135, 1996

J.D. Richardson, An extended plasma model for Saturn, *Geoph. Res. Letters*, **22**, 1177–1180, 1995

J.D. Richardson, J.W, Belcher, A. Szabo, R.L. McNutt Jr., The plasma environment of Neptune, *Neptune and Triton*, edited D. P. Cruickshank, University of Arizona Press, Tucson, 279–340, 1995

J.D. Richardson, E.C. Sittler Jr., A plasma density model for Saturn based on Voyager Observations, *J. Geophys. Res.*, **95**, 12019–12031, 1990

K. Richter, W. Curdt, H.U. Keller, Velocity of individual large dust particles ejected from Comet P/Halley, *Astron. Astroph.*, **250**, 548–555, 1991

J. Rubinstein, J.G. Laframboise, The theory of a spherical probe in a collisionless magnetoplasma, *Phys. Fluids*, **25**, 1174–1182, 1982

M. Salimullah, Low-frequency dust-lower-hybrid modes in a dusty plasma, *Phys. Lett. A*, **215**, 296–298, 1996

I.P. Shkarofsky, T.W. Johnston, M.P. Bachynski, The particle kinetics of plasmas, Addison–Wesley, Reading Massachusetts, 1966

M.R. Showalter, Dust in planetary ring systems, *Origin and evolution of interplanetary dust.*, Ed. A.C. Levasseur-Regourd and H. Hasegawa, 349–356, 1991

M.R. Showalter, J.A. Burns, J.N. Cuzzi, J.B. Pollack, Discovery of Jupiter's gossamer ring, *Nature*, **316**, 526–528, 1985

M.R. Showalter, J.A. Burns, J.N. Cuzzi, J.B. Pollack, Jupiter's ring system: new results on structure and particle properties, *Icarus*, **69**, 458–498, 1987

M.R. Showalter, J.N. Cuzzi, Structure and particle properties of Saturn's E-ring, *Icarus*, **94**, 451–473, 1991

M.R. Showalter, J.N. Cuzzi, Seeing ghosts: photometry of Saturn's G-ring, *Icarus*, **103**, 124–143, 1993

M.R. Showalter, J.B. Pollack, M.E. Ockert, L.R. Doyle, J.B. Dalton, A photometric study of Saturn's F-ring, *Icarus*, **100**, 394–411, 1992

P.K. Shukla, Low-frequency modes in dusty plasmas, *Physica Scripta*, **45**, 504–507, 1992

P.K. Shukla, Waves in dusty plasmas, *The Physics of Dusty Plasmas*, Ed. P.K. Shukla, D.A. Mendis and V.W. Chow, World Scientific Publishing, Singapore, 107–121, 1996

J.A. Simpson, D. Rabinowitz, A.J. Tuzzolino, L.V. Ksnfomality, R.Z. Sagdeev, Halley's comet dust particle mass spectra, flux distributions and jet structures derived from measurements on the Vega-1 and Vega-2 spacecraft, In *ESA Proceedings of the 20th ESLAB Symposium on the Exploration of Halley's Comet*, Volume 2: Dust and Nucleus pp 11–16, 1986

P.D. Singh, A.A. De Almeida, W.F. Hübner, Dust release rates and dust-to-gas mass ratios of eight comets, *Astron. J.*, **104**, 848–858, 1992

P.D. Singh, W.F. Hübner, D.D. Costa, J.C. Landaberry, J.A. de Freitas Pacheco, Gas and dust release rates and color of dust in comets P/Halley (1986 III), P/Giacobini-Zinner (1985 XIII), and P/Hartley-Good(1985 XVII), *Planet. Space Sci.*, **45**, 455–467, 1997

N. Singh, B.I. Vashi, L.C. Leung, Three-dimensional numerical simulation of current collection by a probe in a magnetized plasma, *Geoph. Res. Letters*, **21**, 833–836, 1994

E.C. Sittler Jr., K.W. Ogilvie, J.D. Scudder, Survey of low-energy electrons in Saturn's magnetosphere: Voyagers 1 and 2, *J. Geophys. Res.*, **88**, 8847–8870, 1983

M.S. Sodha, S. Guha, Physics of colloidal plasmas, *Adv. Plasma Phys.*, **4**, 219–309, 1971

L.J. Sonmor, J.G. Laframboise, Exact current to a spherical electrode in a collisionless, large-Debye-length magnetoplasma, *Phys. Fluids B*, **3**, 2472–2490, 1991

E.J. Sternglass, *Sci. Pap.* 1772, Westinghouse Res. Lab., Pittsburgh, 1954

T.H. Stix, *Waves in plasmas*, American Institute of Physics, New York, 1992

E. Stoffels, W. Stoffels, Electrons, ions and dust in a radio-frequency discharge, *PhD-thesis*, T.U. Eindhoven, Koninklijke Bibliotheek, Den Haag, 1994

H. Thomas, G. E. Morfill, V. Demmel, J. Goree, B. Feuerbacher, D. Möhlmann, Plasma crystal–Coulomb crystallization in a dusty plasma, *Phys. Rev. Lett.*, **72**, 652–656, 1994

M.F. Thomsen, C.K. Goertz, T.G. Northrop, J.R. Hill, On the nature of particles in Saturn's spokes, *Geoph. Res. Letters*, **9**, 423–426, 1982

M. Toida, Y. Ohsawa, *J. Phys. Soc. Japan*, **26**, 573, 1994

D. Tsintikidis, D. Gurnett, L.J. Granroth, S.C. Allendorf, W.S. Kurth, A revised analysis of micron-sized particles detected near Saturn by the Voyager 2 plasma wave instrument, *J. Geophys. Res.*, **99**, 2261–2270, 1994

D. Tsintikidis, W.S. Kurth, D. Gurnett, D.D. Barbosa, Study of dust in the vicinity of Dione using the Voyager 1 plasma wave instrument, *J. Geophys. Res.*, **100**, 1811–1822, 1995

R.K. Varma, P.K. Shukla, V. Krishan, Electrostatic oscillations in the presence of grain-charge perturbations in dusty plasmas, *Phys. Rev. E*, **47**, 3612–3616, 1993

O.L. Vaisberg, V.N. Smirnov, L.S. Gorn, M.V. Iovlev, M.A. Balikchin, S.I. Klimov, S.P. Savin, V.D. Shapiro, V.I. Shevchenko, Dust coma structure of comet Halley from SP-1 detector measurements, *Nature*, **321**, 274–276, 1986

F. Verheest, Nonlinear parallel Alfvén waves in cometary plasmas, *Icarus*, **86**, 273–282, 1990

F. Verheest, Parallel solitary Alfvén waves in warm multispecies beam–plasma systems. Part 2. Anisotropic pressures, *J. Plasma Phys.* **47**, 25–37, 1992

F. Verheest, Waves and instabilities in dusty space plasmas, *Space Sci. Rev.*, **77**, 267–302, 1996

F. Verheest, B. Buti, Parallel solitary Alfvén waves in warm multispecies beam–plasma systems. Part 1, *J. Plasma Phys.*, **47**, 15–24, 1992

F. Verheest, G.S. Lakhina, *J. Gophys. Res.*, Nonresonant low-frequency instabilities in multibeam plasmas–Applications to cometary environments and plasma sheet boundary layers, **96**, 7905–7910, 1991

F. Verheest, P. Meuris, Whistler-like instabilities due to charge fluctuations in dusty plasmas, *Phys. Lett. A*, **198**, 228–232, 1995

F. Verheest, P. Meuris, Korteweg–de Vries equation for oblique modes in magnetized multi–ion plasmas, *J. Phys. Soc. Japan*, **65**, 8, 2522–2525, 1996a

F. Verheest, P. Meuris, Non-linear electromagnetic modes in plasmas with variable dust fscharges, *Phys. Letters A*, **210**, 198–201, 1996b

F. Verheest, P. Meuris, Electromagnetic instabilities in solar wind interaction with dusty cometary plasmas, *Solar Wind Eight*, Ed. D. Winterhalter, J.T. Gosling, S.R. Habbal, W.S. Kurth, M. Neugebauer, AIP Press, New York, 343–346,1997

B. Walsh, M. Horányi, S. Robertson, Measurements of the charging of individual dust grains in a plasma, *IEEE Trans. Plas. Sci.*, **22**, 97–102, 1994

B. Walsh, M. Horányi, S. Robertson, Charging of dust grains in plasma with energetic electrons, *Phys. Rev. Letters*, **75**, 838–841, 1995

E.C. Whipple, Potentials of surfaces in space, *Rep. Prog. Phys.*, **44**, 1197–1250, 1981

G.R. Wilson, The plasma environment, charge state, and currents of Saturn's C and D rings, *J. Geophys. Res.*, **96**, 9689–9701, 1991

W. Xu, N. D'Angelo, R.L. Merlino, Dusty plasmas: The effect of closely packed grains, *J. Geophys. Res.*, **98**, 7843–7847, 1993

Epilogue

"Finish it? Why would I want to finish it?"

Fig. Z. Drawing by W. B. Perk; © 1987, The New Yorker Magazine, Inc.